

Document Version

Final published version

Citation (APA)

Porcarelli, A. (2026). *Highly Strained Lean Premixed Hydrogen Flames: Emissions, Stability and Modelling*. [Dissertation (TU Delft), Delft University of Technology]. <https://doi.org/10.4233/uuid:c41c0f72-499b-4b10-bfaa-3e04841d5f3f>

Important note

To cite this publication, please use the final published version (if applicable). Please check the document version above.

Copyright

In case the licence states “Dutch Copyright Act (Article 25fa)”, this publication was made available Green Open Access via the TU Delft Institutional Repository pursuant to Dutch Copyright Act (Article 25fa, the Taverne amendment). This provision does not affect copyright ownership.

Unless copyright is transferred by contract or statute, it remains with the copyright holder.

Sharing and reuse

Other than for strictly personal use, it is not permitted to download, forward or distribute the text or part of it, without the consent of the author(s) and/or copyright holder(s), unless the work is under an open content license such as Creative Commons.

Takedown policy

Please contact us and provide details if you believe this document breaches copyrights. We will remove access to the work immediately and investigate your claim.

A watercolor illustration of a flame structure. The flame is depicted with a central blue column, surrounded by a yellow and orange ring, and a red and white outer layer. The flame is positioned between two blue, curved, wavy lines that represent the boundaries of a channel or duct. The background is white.

HIGHLY STRAINED LEAN PREMIXED HYDROGEN FLAMES

EMISSIONS, STABILITY AND MODELLING

ALESSANDRO PORCARELLI

**HIGHLY STRAINED LEAN
PREMIXED HYDROGEN FLAMES**

EMISSIONS, STABILITY AND MODELLING

**HIGHLY STRAINED LEAN
PREMIXED HYDROGEN FLAMES**

EMISSIONS, STABILITY AND MODELLING

Dissertation

for the purpose of obtaining the degree of doctor
at Delft University of Technology
by the authority of the Rector Magnificus,
Prof. dr. ir. H. Bijl,
chair of the Board for Doctorates
to be defended publicly on
Thursday, 23rd of April 2026 at 17:30

by

Alessandro PORCARELLI

This dissertation has been approved by the (co)promotors.

Composition of doctoral committee:

Rector Magnificus,	chairperson
Prof. dr. A. Gangoli Rao,	Delft University of Technology, <i>promotor</i>
Dr. I. Langella,	Delft University of Technology, <i>copromotor</i>

Independent members:

Prof. dr. D.J.E.M. Roekaerts,	Delft University of Technology
Prof. dr. N. Chakraborty,	Newcastle University, UK
Dr. A. Attili,	The University of Edinburgh, UK
Dr. N.A.K. Dohan,	Delft University of Technology / Imperial College London, UK
Prof. dr. S.A. Klein,	Delft University of Technology, reserve member

Other members:

Dr. P.E. Lapenna,	Sapienza, University of Rome, Italy
-------------------	-------------------------------------

This research was performed at the Sustainable Aircraft Propulsion (SAP) group within the Flight Performance & Propulsion Section (FPP), Department of Flow Physics and Technology (FPT), Faculty of Aerospace Engineering. The work was funded by the Dutch Ministry of Education and Science via the Sector Plan Scheme.



Keywords: strained combustion, hydrogen combustion, premixed flames, counter-flow flames, NO_x emissions, thermodiffusive instabilities, differential diffusion, preferential diffusion, Large Eddy Simulations (LES), tabulated chemistry models, flamelet models, presumed filtered density function (FDF), filtered tabulated chemistry for LES (F-TACLES)

Printed by: Ipskamp Printing

Cover by: Elena & Erica Geraltini. Snapshot of a turbulent lean premixed hydrogen flame front in strained configuration styled inside an aeroengine case.

Copyright © 2026 by A. Porcarelli ¹

ISBN 978-94-6518-294-0

An electronic version of this dissertation is available at

<https://doi.org/10.4233/uuid:c41c0f72-499b-4b10-bfaa-3e04841d5f3f>.

¹Author e-mail address: alepo98@gmail.com

*Auream quisquis mediocritatem
diligit, tutus caret obsoleti
sordibus tecti, caret invidenda
sobrius aula.*

*Who cherishes the Golden Mean,
avoids the ramshackle squalid dwelling,
likewise avoids, sober,
the enviable mansion.*

Horatius

CONTENTS

Summary	xi
Samenvatting	xiii
1 Introduction	1
1.1 Role of hydrogen combustion in decarbonisation	2
1.2 Opportunities and challenges of highly-strained premixed hydrogen combustion	6
1.3 Research question	9
1.4 Thesis outline	11
2 Theoretical background: Hydrogen premixed combustion	13
2.1 NO_x emissions from hydrogen combustion	14
2.2 Differential and preferential diffusion effects in lean hydrogen flames	18
2.3 Stretch effects	22
2.4 Curvature effects: onset of thermodiffusive instabilities	24
2.5 Flame strengthening by tangential strain rate	27
2.6 Strained premixed flame configurations	29
2.7 Effect of turbulence in thermodiffusively unstable flames	30
2.8 Challenges in tabulated chemistry large eddy simulation models	33
3 NO_x emissions analysis in lean premixed and strained hydrogen flamelets	37
3.1 Introduction	38
3.2 Problem definition	39
3.2.1 2D governing equations and numerical modelling	39
3.2.2 1D governing equations and numerical modelling	40
3.3 Computational setup	41
3.3.1 1D setup	41
3.3.2 2D setup	42
3.4 Results	43
3.4.1 NO_x emissions trends	43
3.4.2 NO formation pathways	47
3.4.3 Analysis of radicals	49
3.4.4 Comparison with methane	52
3.4.5 Effect of pressure	53
3.4.6 Effect of equivalence ratio	55
3.5 Correlation for the integral NO emissions	56
3.5.1 Analytical derivation	56
3.5.2 Semi-empirical estimation of I_{NO}	58
3.6 Summary	60

4	Effect of strain on lean premixed hydrogen flame structure	61
4.1	Introduction	62
4.2	Computational setup and numerical modelling	62
4.3	Results and discussion	64
4.3.1	Radical peaks trends	64
4.3.2	Mixture fraction distribution	65
4.3.3	Mixture fraction transport	66
4.3.4	Flame physical properties	70
4.3.5	Discussion	71
4.4	Summary	72
5	Stability analysis of thermodynamically unstable lean premixed and strained hydrogen flames	75
5.1	Introduction	76
5.2	Computational setup	76
5.2.1	Governing equations	76
5.2.2	2D Setup and numerical details	78
5.2.3	3D Setup and numerical details	79
5.3	Validation	81
5.4	2D simulation results	82
5.4.1	Flame dynamics without imposed perturbations	82
5.4.2	Perturbed flame front dynamics	83
5.4.3	Perturbation growth rate	86
5.4.4	Discussion	90
5.5	3D simulation results	90
5.6	Summary	92
6	Assessment of tabulated chemistry models for lean premixed strained hydrogen flames with low-dimensional manifolds	93
6.1	Introduction	94
6.2	Computational setup and tabulated chemistry models	95
6.2.1	2D laminar setup	95
6.2.2	3D turbulent setup	95
6.2.3	Filtering of DNS dataset	97
6.2.4	Tabulation approach	97
6.3	Results	101
6.3.1	Laminar flames	101
6.3.2	Turbulent flames	109
6.3.3	Choice of fixed strain rate value	117
6.3.4	Unstretched flamelets correction	118
6.4	Summary	120
7	Conclusions and outlook	123
7.1	Fundamental features of strained lean premixed hydrogen flames	124
7.2	Advancements in affordable CFD modelling for lean premixed and strained hydrogen flames	125
7.3	Outlook	126

7.4	Recommendations for future work	126
	Acknowledgements	131
A	Appendix A	147
A.1	Grid convergence study	148
A.2	Flame temperature plot	148
A.3	Reaction rate plot	149
A.4	Radical plots in methane flamelets	149
B	Appendix B	151
B.1	Bilger mixture fraction	152
B.2	Constant Lewis number diffusion model	152
B.3	Influence of reactants temperature	154
B.4	Influence of equivalence ratio.	155
B.5	Karlovitz number calculation and comparison to turbulent flow	156
C	Appendix C	159
C.1	Computational setup boundary conditions	160
C.2	1D flame validation	161
C.3	Time evolution of a sample flame front	162
C.4	Local tangential strain rate in time	162
D	Appendix D	165
D.1	3D turbulent setup combustion regime and additional flame parameters.	166
D.2	Improvement of β -FDF predictions at increasing strain rate	166
D.3	Cross-flame reaction rate plots in the laminar setting obtained with un-stretched flamelets manifold	168
	Curriculum Vitae	171
	List of Publications	173

SUMMARY

In the urgent need to decarbonise energy systems, hydrogen combustion is set to play a key role in hard-to-electrify sectors such as aviation, power generation, and heavy industry. However, the practical deployment of hydrogen combustion faces critical challenges, including high reactivity, high NO_x emissions, and thermodiffusive instabilities, which compromise flame stability and control. While hydrogen premixed flames show a distinctive response to strain compared to other fuels, the fundamental effects of strain on hydrogen flame dynamics and emissions remain poorly understood. Furthermore, lean premixed hydrogen flames feature differential and preferential diffusion effects which lead to the onset of thermodiffusive instabilities. These instabilities, in turn, interact with turbulence and strain. Existing computational fluid dynamics (CFD) models struggle to accurately and affordably predict these distinctive features, thereby limiting the development of safe and low-emissions hydrogen combustion devices in industrial design frameworks. Addressing these gaps is essential for advancing hydrogen combustion technologies, particularly within the aviation and transportation sectors where they are still at a low Technology Readiness Level (TRL).

This thesis aims to contribute to the development of more accurate and affordable CFD tabulated-chemistry large eddy simulation (LES) models of lean premixed hydrogen flames subjected to intensive strain, thereby advancing the capabilities to optimally design hydrogen combustor leveraging strained regimes. First, the fundamental hydrogen flame response to strain is investigated extensively from the point of view of emissions, flame structure, and flame stability through high-fidelity detailed chemistry simulations in simplified laminar settings. Hence, with the help of the insights gathered in the previous phase, novel tabulated chemistry modelling approaches are proposed for LES of strained and turbulent hydrogen flames. The proposed models are tested *a priori* at unfiltered and filtered grids in a turbulent counterflow setup, where strain is established both by shear-driven turbulence and by the configuration.

The main fundamental findings reveal that increasing strain suppresses NO_x emissions across the thermal route, even if the flame reactivity increases, and mitigates preferential diffusion effects by inducing differential species transport in the flame-tangential direction. Furthermore, intensive strain is found to stabilise intrinsic flame instabilities, regardless of the direction of the imposed perturbation and of the tangential velocity gradients established to strain the flame.

Building on these insights, novel tabulated chemistry modelling approaches for LES of lean premixed and strained hydrogen flames are proposed to leverage the discovered low emissions and improved stability enabled by strained regimes. The *a priori* analysis shows that reliable predictions of integral quantities such as the consumption speed can be achieved through the following tabulation approaches when coupled with the β filtered density function (FDF) subgrid closure: (i) a well-established manifold of unstretched premixed flamelets coupled with a novel consumption speed correction based

on the results of the laminar *a priori* analysis, which accounts for the inaccuracies of the thermochemical states provided by this set of flamelets; (ii) a novel manifold of premixed counterflow flamelets at fixed strain rate and varying equivalence ratio, provided that the flamelet strain is chosen within the correct range. Furthermore, again when coupled with the β -FDF closure, an ultra-light manifold made of a single premixed counterflow flamelet (iii) is proved to capture at coarse grids the increased reactivity due to subgrid thermodiffusive instabilities, turbulence and strain, provided that the flamelet strain is close enough to that experienced by the turbulent flame. Among all the models tested, the novel manifold of fixed-strain flamelets at varying equivalence ratio (ii) shows the best performance in reconstructing the local reaction rates at the LES scales. Unlike previous works, the proposed approaches offer improved accuracy without increasing manifold dimensionality, thus maintaining computational efficiency.

Overall, this thesis demonstrates that strained regimes can be leveraged to achieve low emission and stability in hydrogen combustion, and that the design of strained hydrogen combustion devices can be supported by novel modelling approaches enabling accurate and affordable simulations. These advancements contribute to overcoming the low TRL of hydrogen combustion applications, particularly in aviation and power generation, by providing tools to design clean and safe combustion systems.

SAMENVATTING

Er ligt hoge druk op de decarbonisatie van energiesystemen, waarbij waterstofverbranding een sleutelrol kan spelen in moeilijk te elektrificeren sectoren zoals luchtvaart, energieopwekking en zware industrie. Echter, de hoge reactiviteit, NO_x -emissies en thermodiffusieve instabiliteit maken de beheersing van waterstofvlammen, en daarmee praktische toepassingen, uitermate lastig. In vergelijking met andere brandstoffen worden voorgemengde waterstofvlammen op kenmerkende manier beïnvloed door rek, maar de precieze interacties tussen rek, dynamica, en emissies van waterstofvlammen zijn relatief onbekend. Daarnaast komen in zuurstofarme, voorgemengde waterstofvlammen diffusie-effecten voor die uitgroeien tot thermodiffusieve instabiliteiten die vervolgens interacties aangaan met turbulentie en uitstrekking van de flam. Dit soort fenomenen zijn zeer lastig om accuraat te voorspellen met computermodellen zoals numerieke stromingsleer (CFD), wat de ontwikkeling van veilige, schone toepassingen van waterstofverbranding bemoeilijkt. De aanpak van deze hiaten is elementair voor het uitwerken van onderontwikkelde waterstofverbrandingstechnologieën die met name voorkomen in de luchtvaart en transportsector.

Dit proefschrift beoogt bij te dragen aan de ontwikkeling van nauwkeurigere en toepasbare CFD-modellen met behulp van opzoektabelen voor Large Eddy Simulation (LES) van zuurstofarme, voorgemengde waterstofvlammen beïnvloed door intensieve rek, wat de ontwikkeling van optimale ontwerpen van waterstofbranders mogelijk maakt. Ten eerste wordt het effect van rek op waterstofvlammen uitgebreid onderzocht, met betrekking tot emissies, vlamstructuur en vlamstabiliteit met behulp van hoogwaardige, gedetailleerde chemische simulaties in vereenvoudigde laminaire omstandigheden. Met behulp van deze inzichten worden vervolgens nieuwe methoden geconstrueerd voor LES van gerekte en turbulente waterstofvlammen doormiddel van opzoektabelen. De voorgestelde modellen worden *a priori* getest op ongefilterde en gefilterde rasters in een turbulente tegenstroomopstelling, waarbij rek wordt geïntroduceerd door schuifgedreven turbulentie en de configuratie.

De belangrijkste uitkomsten van dit onderzoek zijn dat rek op de vlam de thermische NO_x -emissies onderdrukt, de vlamreactiviteit verhoogt, en dat preferentiële diffusie-effecten erdoor worden verminderd door variabele transport van uitgangsstoffen parallel aan de vlam. Bovendien blijkt intensieve rek intrinsieke vlaminstabiliteiten te verminderen, ongeacht de richting van de opgelegde verstoring en de snelheidsgradiënten die worden toegepast om de vlam te rekken.

Op basis van deze inzichten worden nieuwe modelleringsbenaderingen voor getabelleerde chemie voorgesteld voor LES van zuurstofarme, voorgemengde en gerekte waterstofvlammen, om de interacties tussen rek, emissies en vlamstabiliteit te kunnen exploiteren. De *a priori*-analyse laat zien dat betrouwbare voorspellingen van integrale kenmerken, zoals de consumptiesnelheid, kunnen worden bereikt met de volgende tabelleringsbenaderingen wanneer deze worden gecombineerd met de β -FDF (filtered

density function) subgrid-sluiting: (i) een normaal manifold van ongerekte, voorge-mengde vlammen inclusief een nieuwe correctie voor de consumptiesnelheid gebaseerd op de resultaten van de laminaire *a priori*-analyse, met inachtneming van de onnauw-keurigheden van de thermochemische toestanden die door deze set vlammen worden geleverd; (ii) een nieuw manifold van voorge-mengde tegenstroomvlammen met constante vlamrek en variërende equivalentieverhouding, mits de vlamrek binnen het juiste bereik wordt gekozen. Bovendien blijkt het mogelijk om de verhoogde reactiviteit als ge-volg van subgrid-thermodiffusieve instabiliteiten te berekenen op relatief grove rasters met slechts een enkele voorge-mengde tegenstroomvlam, gekoppeld aan de β -FDF-sluiting, mits de vlamrek voldoende dicht ligt bij die welke door de turbulente vlam wordt ervaren (iii). Van alle geteste modellen vertoont het nieuwe manifold van vlammen met vaste rek en variërende equivalentieverhouding (ii) de beste prestaties bij het reconstrueren van de lokale reactiesnelheden op LES-schaal. In tegenstelling tot eerdere werken bieden de voorgestelde benaderingen een verbeterde nauwkeurigheid zonder de dimensionaliteit van het manifold te vergroten, waardoor de computationele efficiëntie behouden wordt.

Al met al wordt in dit proefschrift aangetoond aan dat vlamrek kan worden geëxploi-teerd voor het verminderen van emissies en het verbeteren van de stabiliteit van water-stofvlammen, en dat deze effecten nauwkeurig kunnen worden berekend doormiddel van goedkope simulaties voor het ontwerp van toepassingen omtrend waterstofverbranding. Met deze vooruitgang is het mogelijk de maturiteit van waterstofverbrandingstoepas-singen in onder andere de luchtvaart en energieopwekking te verhogen door schone en veilige verbrandingssystemen te verwezenlijken.

1

INTRODUCTION

*And if I have the gift of prophecy
and comprehend all mysteries and all knowledge;
if I have all faith so as to move mountains
but do not have charity, I am nothing.*

St. Paul

1.1. ROLE OF HYDROGEN COMBUSTION IN DECARBONISATION

In 2024, global energy demand experienced a significant increase of 2.2%, a notable rise compared to the average annual growth rate of 1.3% observed over the previous decade [1]. This surge was largely attributed to extreme weather conditions and the escalating electricity requirements of technology-driven sectors, such as AI data centers. Electricity generation from renewable energy sources is increasing, both in absolute terms and as a share of total generation, and is expected to grow further under current policy frameworks (see Figure 1.1) [2]. These technologies include solar PV, onshore and offshore

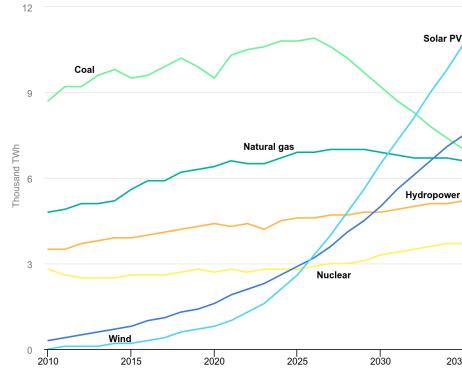


Figure 1.1: World electricity generation in the stated policies scenario [3].

wind, biofuels, and hydro. However, despite this growth, a considerable portion of the energy demand is still fulfilled by fossil fuels, which made up 49.2% of the total energy mix as of 2023 (see Figure 1.2) [4]. Consequently, global carbon dioxide (CO₂) emissions persisted on an upward trajectory, albeit somewhat mitigated by advancements in clean energy [5], reaching a record high of 37.6 gigatonnes in 2024, as illustrated in Figure 1.3 [1]. These trends underscore the urgent need for accelerated advancements in renewable technology. Such progress is essential not only to satisfy the increasing global energy demand but also to decrease CO₂ emissions, which are key drivers of global warming and climate change. Achieving carbon neutrality is thus vital for mitigating climate change and meeting the objectives of the Paris Agreement. This landmark accord, ratified by nearly all nations, aims to strengthen the global response to the climate change threat [8].

Certain sectors, such as aviation and heavy industry, face challenges in achieving direct electrification through renewable sources, and thus struggle to reduce their emissions. In this context, hydrogen emerges as a promising alternative [9, 10]. Hydrogen production encompasses a variety of methods, each associated with different environmental impacts and categorised by distinct 'colours'. Among these, green and blue hydrogen stand out as the most sustainable options and are currently the primary focus of investment and development in the industry [11]. Green hydrogen is produced using renewable energy, while blue hydrogen employs carbon capture and storage (see Figure 1.4). Specifically, green hydrogen has seen substantial investments in electrolyzers [13, 14], which are becoming more efficient, achieving efficiencies of up to around 80% and advancing in

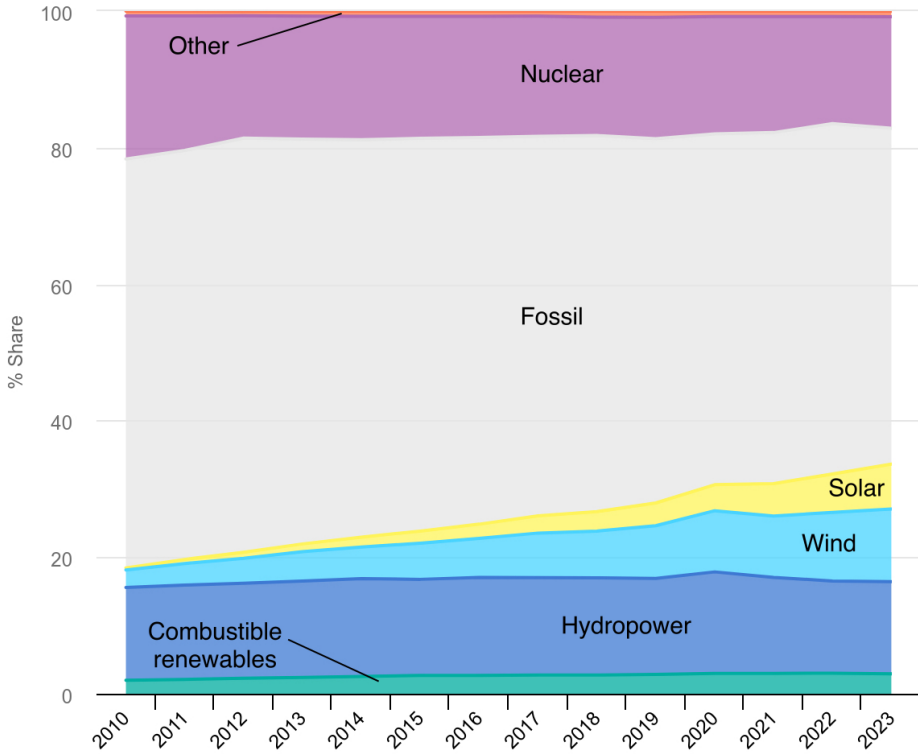
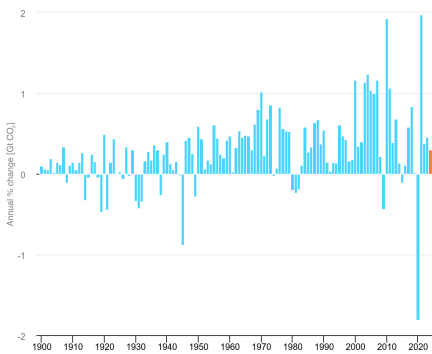
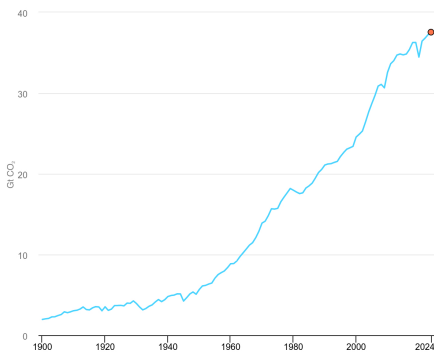


Figure 1.2: OECD share of electricity generation by source [4]. From bottom to top: combustible renewables, hydro, wind, solar, fossil, nuclear, other.



(a) Global CO₂ emissions from energy combustion and industrial processes, 1900-2024 [6].

(b) Annual change in energy-related CO₂ emissions, 1900-2024 [7].

Figure 1.3: Global increase in global CO₂ emissions.

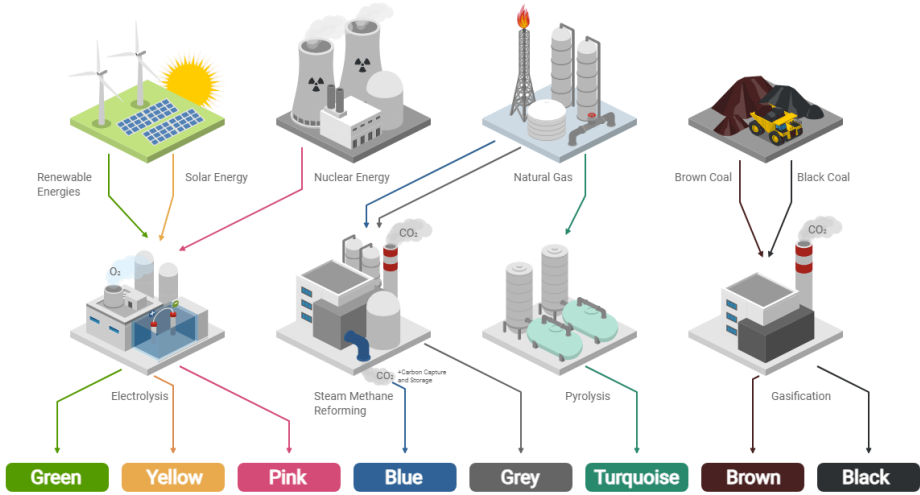


Figure 1.4: The colors of hydrogen [12].

technology readiness levels (TRL) as highlighted by the International Energy Agency [15]. These two types have seen significant investments and numerous project announcements, highlighting their potential to contribute to a sustainable energy future.

Besides the emissions related to its production, hydrogen serves as a carbon-free fuel with diverse applications. It can be utilised directly or serve as an energy storage medium. Hydrogen itself can be stored and used later, providing flexibility for energy systems, especially during periods of excess renewable energy. When converted, hydrogen can react with CO_2 to form methane, offering a method for carbon capture and utilisation [16]. Additionally, hydrogen can be blended with carbon monoxide (CO) to form syngas [17] fuels or with ammonia [18] to create more stable compounds than pure hydrogen for combustion in engines. These alternative fuels and energy carriers are also easier to store compared to pure hydrogen, which requires very high pressure and low temperatures. However, syngas fuels are not fully carbon-free, and the nitrogen oxides (NO_x) emitted from ammonia combustion are toxic. These factors pose health risks and challenges in terms of safe handling and environmental impact, thus limiting their applicability.

Alternatively, hydrogen can be directly employed in fuel cells [19] and combustion processes [20]. Despite their relatively lower efficiency compared to battery-electric engines, hydrogen fuel cells are still being explored for their rapid refuelling and high energy density, making them suitable for electric vehicles, backup power systems, portable applications, and short-range zero-emission aviation. Hydrogen combustion, on the other hand, is increasingly being adopted in sectors that are challenging to decarbonise through electrification, such as industrial heating, power generation, transportation engines, gas turbines, and as a sustainable aviation fuel for long-range flights. In the transportation sector, specifically, ongoing research and development efforts remain crucial. Figure 1.5

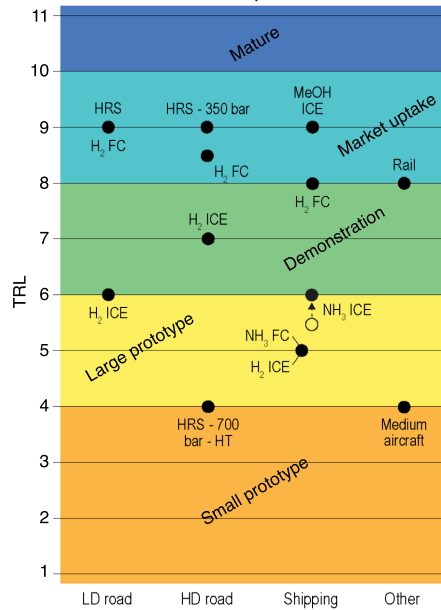


Figure 1.5: Technology Readiness Levels (TRL) for various hydrogen applications within the transportation sector. FC = fuel cell; H₂ = hydrogen; HD = heavy-duty; HRS = hydrogen refueling stations; ICE = internal combustion engine; LD = light-duty; MeOH = methanol; NH₃ = ammonia.

presents a chart that depicts the Technology Readiness Levels (TRL) for various hydrogen applications within this sector [11]. Although notable advancements have been achieved in fuel cell technologies, internal combustion engines and aircraft applications continue to exhibit low TRLs. This underscores the necessity for further research into hydrogen combustion and combustor design to establish the feasibility and effectiveness of these technologies.

The elevated NO_x emissions, resulting from the combustion of hydrogen under ideal air-fuel mixture conditions (stoichiometric) present significant environmental challenges. Additionally, the inherent high reactivity and high flame speed of hydrogen contribute to difficulties in achieving stable combustion [21]. These key factors are responsible for the lower TRL of hydrogen combustion technologies. Indeed, unlike traditional hydrocarbon fuels, hydrogen combustion tends to produce higher levels of NO_x emissions, which are toxic [22]. In the last decades, research efforts have focused on the possibility to burn hydrogen in lean premixed conditions, where the lower adiabatic flame temperature allows to decrease NO_x formation via the thermal route. However, many technological challenges are involved with controlling hydrogen combustion in lean turbulent conditions. In fact, flashback and uncontrolled flame propagation that are typical of this regime [23, 24] are amplified by its propensity to auto-ignite [25, 26] and its very high diffusivity [27]. The latter characteristic is also responsible for differential and preferential diffusion effects which lead to the onset of thermodiffusive instabilities [28]. The instabilities represent a complex physical phenomenon with micro- and macro-scale effects on

the flame front, and are thus particularly challenging to predict accurately with current simulation models used for combustor design [29].

Overall, advancing the TRL of hydrogen combustion is crucial for its role in a carbon-neutral economy. Key challenges include controlling NO_x emissions and ensuring the stability of hydrogen flames. Accurate simulation tools are essential for predicting and stabilising these flames. Addressing these issues will enhance the viability of hydrogen as a clean energy source, contributing significantly to a sustainable and carbon-neutral future.

1.2. OPPORTUNITIES AND CHALLENGES OF HIGHLY-STRAINED PREMIXED HYDROGEN COMBUSTION

One aspect of hydrogen flames that remains not fully understood and has not been extensively researched is their response to strain. Strain measures how the area of a flame surface element changes due to flow non-uniformities [30]. Given that hydrogen flames exhibit a distinct response to strain compared to the well-understood behaviour of hydrocarbon fuels, investigating this area could provide crucial insights into its potential impacts on NO_x emissions and flame stability. This makes strain a valuable focus for advancing hydrogen combustion research.

Considering a simplified two-dimensional flame front, flame strain reduces to the gradient of the flame-tangential velocity with respect to the flame-tangential direction. To visualise this, imagine straining a flame as akin to pulling a rope from both ends, where the rope becomes thinner and stiffer (see Figure 1.6). In this analogy, the rope represents the flame front, and the act of pulling illustrates the effect of tangential velocity gradients imposed by the flow field.

Research has shown that hydrogen's characteristic preferential diffusion effects and strain sensitivity are interdependent, collectively influencing the flame response [31, 32]. Early studies on flames with fuel Lewis numbers below unity, indicating that the fuel's molecular diffusivity is higher than that of temperature, have demonstrated that increased strain rates correlate with observed excess enthalpy relative to undisturbed laminar flames, thereby increasing flame speed [33]. Hydrogen, having a Lewis number below unity, falls into this category. Hydrogen flames have been also proved to align preferentially with extensive tangential strain levels in turbulent strained flames [34, 35], and this particular characteristic can be potentially exploited in the design of novel combustor systems.

While specific studies on the response to strain of pure hydrogen flames are limited, insights from hydrogen blended laminar hydrocarbon flames suggest its potential for practical applications in high strain regimes. Hydrogen addition has been shown to delay the extinction strain rate [36, 37], proving that hydrogen is able to sustain very high strain rates. Furthermore, while the mass burning rate decreases with strain for pure methane flames, a certain amount of hydrogen addition inverts this trend, particularly in lean conditions [38]. Similar considerations hold for the peak heat release rate, which is found to increase with strain in lean hydrogen enriched flames [39]. A positive correlation between strain and heat release rate can also be observed in scatter plots from an existing two-dimensional direct numerical simulation of a turbulent pure-hydrogen lean flame,

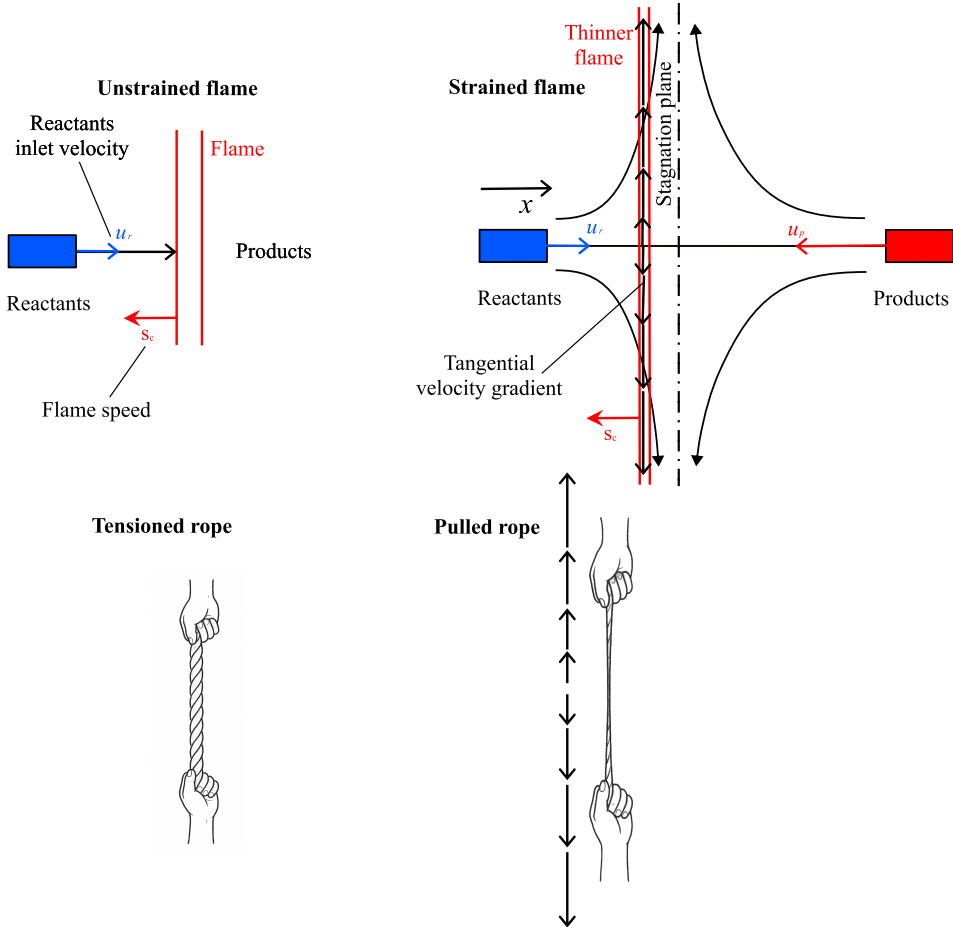


Figure 1.6: Example of unstrained and strained flame. Analogy of straining a flame as akin to pulling a rope from both ends.

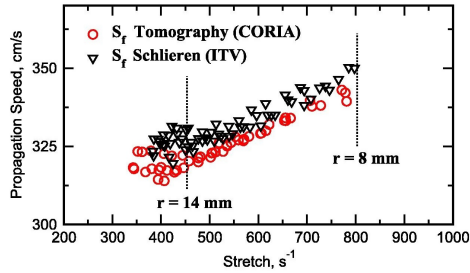


Figure 1.7: Example of flame speed versus stretch graph in curved, laminar, spherically-expanding lean hydrogen flames displaying a negative Markstein length, i.e. the flame speed increases with stretch [44, Figure 2].

where strain was established through turbulence only [35]. All of these observations indicate that hydrogen lean flames strengthen with increasing strain, unlike hydrocarbon fuels that weaken until they reach extinction.

Further studies on hydrogen blends examined syngas fuels (hydrogen and CO mixtures). Here, it was similarly shown that increasing the hydrogen percentage in the fuel at lean conditions affects the laminar flame response to strain. This determines a change of flame temperature, NO_x emissions [40] and consumption speed [21].

However, while several studies have investigated hydrogen blending [21, 36–42], the effect of the discussed distinctive hydrogen burning features at high strain rates in pure hydrogen-air lean premixed flames remains yet to be explored. This is particularly true regarding their impact on NO_x emissions and flame stability, requiring further research to fully understand and harness the potential of hydrogen in combustion applications.

From a broader perspective, when a flame propagates through a non-uniform flow, it undergoes both strain and flame front curvature effects, which together alter the flame area. The fractional rate of change of a flame area element by the combination of strain and curvature is quantified by flame stretch. Specifically, while curvature relates to changes in the flame area due to the shape of the flame front, strain is primarily concerned with how flow non-uniformities impact these changes. Numerous studies [43, 44] have explored the response of spherically expanding lean premixed hydrogen flames to stretch as a whole, where stretch is varying during flame propagation due to decreasing curvature, providing a broader context for understanding their dynamics.

Stretch has been shown to increase the consumption speed under sufficiently lean conditions. This behaviour is opposite to that observed for hydrocarbon flames and implies a change in the sign of the so-called Markstein length for hydrogen. The Markstein length is determined by opposite of the slope of the flame speed versus stretch graph, as illustrated in Figure 1.7. This was highlighted in both numerical [43] and experimental [44] studies of curved laminar spherical flames. Interestingly, this also leads to the observation of super-equilibrium products and super-adiabatic temperatures in relatively highly stretched flames [44]. This characteristic could potentially be exploited to enhance combustion efficiency in low NO_x lean regimes.

Stretching multi-dimensional lean premixed hydrogen flames, combined with differential diffusion effects, is also responsible for the onset of thermodiffusive instabilities.

For cases with an effective Lewis number below unity, such as lean hydrogen-air mixtures, the propagation of these instabilities is intrinsically unstable and thus self-amplifying [45]. Turbulence has been recently shown to further enhance this increase in consumption speed due to the turbulence-enhanced curvature fluctuations, and to lead to super-adiabatic flame temperatures [46]. This phenomenon presents additional challenges not only for flame stabilisation but also for the reliability of existing computational fluid dynamics (CFD) flame simulation tools. These tools, especially within the realm of low-fidelity turbulent simulations such as large-eddy simulations (LES), are crucial for designing safe, efficient, and low-emission combustion systems for practical applications, making their accuracy and reliability of paramount importance.

Building upon the above observations, one aspect that remains unclear is whether the behaviours observed in studies involving flame stretch would manifest under the sole effect of strain. Indeed, unlike curved flame setups, intensive strain rate regimes can be potentially established in practical settings by designing a flow configuration enabling a positive velocity gradient in the tangential direction to the flame, as in a counterflow. More generally, there is a need to understand if straining lean premixed hydrogen flames can be beneficial to simultaneously stabilise the flame while retaining low NO_x emissions, making it a viable solution to advance the development of safe and low-emission hydrogen combustors. Specifically, the impact of strain alone on NO_x emissions in pure hydrogen flames, the lean hydrogen flame structure, and the transport phenomena across the flame are not well understood. Additionally, the role of strain in the onset of thermodiffusive instabilities—whether it stabilises or further destabilises the flame—requires further investigation. Beyond these gaps in fundamental knowledge of strained regimes, the primary limitation in dependable combustor design leveraging such conditions is the unreliability of existing CFD simulation models. Indeed, these models need improvement to accurately predict the characteristics of thermodiffusively unstable, turbulent, and strained hydrogen flames. This highlights the necessity for deeper research into the development of accurate models to bridge this critical limitation in our combustor design capabilities, thereby facilitating advancements in hydrogen combustion technology.

1.3. RESEARCH QUESTION

This dissertation aims to address the knowledge gap discussed in the previous Section by contributing to the development of more accurate low-fidelity models for CFD simulations, thereby advancing the capabilities to optimally design hydrogen combustors leveraging strained regimes. This objective is summarised by the following research question.

What are the optimal modelling strategies for designing lean premixed hydrogen combustion devices that leverage emission reduction and improved stability of highly strained flame regimes?

In order to provide a comprehensive answer to the main research question, a list of key questions is formulated to be addressed throughout the dissertation. Initially, it is essential to determine whether strain suppresses or enhances the formation of nitric oxides

to clarify if this regime can be exploited to mitigate emissions in hydrogen combustor design.

1. What is the effect of increasing strain on NO_x emissions in lean premixed hydrogen flames?

Next, insights are gathered on the response of lean hydrogen flames to the isolated effect of strain, focusing on both cross-flame species diffusive transport phenomena and the overall flame structure. This investigation aims to enhance our understanding of how the transport phenomena promoted by preferential diffusion are influenced by increasing strain, thereby indicating its potential impact on the onset of thermodiffusive instabilities.

2. How does increasing strain influence species diffusive transport and thereby impacts the structure of lean premixed hydrogen flames?

Following a detailed analysis of how strain modifies cross-flame transport phenomena, including diffusion, the dynamic response of strained flames to a forced instability is evaluated. This assessment determines whether strain promotes or inhibits the onset of lean hydrogen's characteristic thermodiffusive instabilities, and thus whether highly strained regimes can create favourable conditions for more stable hydrogen flames in practical applications.

3. What is the effect of increasing strain on the onset of hydrogen's thermodiffusive instabilities in lean premixed conditions?

Finally, having established that strained hydrogen combustion features reduced NO_x emissions and improved stability, the focus shifts to developing low-fidelity CFD simulation tools necessary for designing hydrogen combustion systems that leverage these advantages. Existing CFD-LES models fail to capture the distinctive response of lean premixed hydrogen flames to strain and thus require adjustments.

4. How can existing CFD-LES modelling strategies be improved to account for the distinctive behaviour of lean premixed hydrogen flames at high strain rates?

Overall, this dissertation addresses the main research question by focusing on the assessment of improved modelling strategies essential for designing hydrogen combustors that leverage the benefits of strained combustion regimes. First, it finds novel insights crucial for understanding how strain can enhance the stability and reduce emissions of hydrogen combustors. Indeed, this work demonstrates that strain suppresses NO_x emissions and mitigates preferential diffusion effects, as well as suppresses thermodiffusive instabilities in lean premixed hydrogen flames. Hence, building upon these findings, this work proposes a novel improved model for large-eddy simulations based on strained one-dimensional flamelets and offers a correction for existing models based on unstrained flamelets. These advancements contribute to the development of accurate CFD simulation tools, thereby facilitating the design of hydrogen combustion systems that capitalise on the emission and stability benefits of strained combustion regimes.

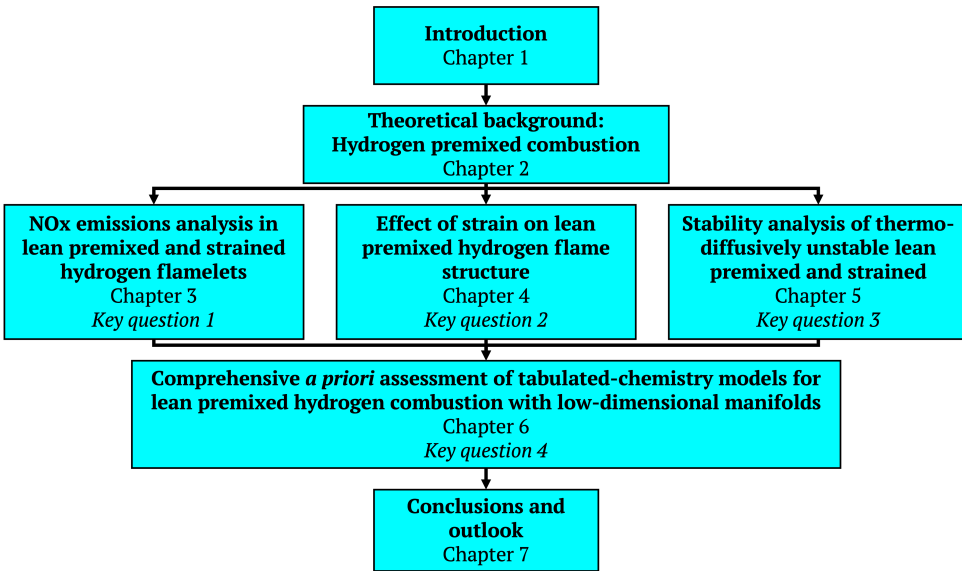


Figure 1.8: Thesis outline

1.4. THESIS OUTLINE

The structure of the thesis is illustrated in Figure 1.8. Chapter 2 delves into the theory of hydrogen flames, highlighting recent breakthroughs in their understanding and modeling, as well as identifying areas that require further investigation.

Chapter 3 addresses key question #1 by investigating NO_x emission trends in lean premixed hydrogen flames subjected to increasing strain rates. This analysis employs simplified 1D and 2D flame configurations to elucidate the impact of strain on emission behaviour.

Chapter 4 delves deeper into the effect of strain on the transport properties and the structure of lean hydrogen 1D flames. This chapter addresses key question #2 by examining how strain influences cross-flame species diffusive transport phenomena and the global flame structure. The insights gained here are crucial for understanding the effect of strain on transport phenomena promoted by preferential diffusion, which can potentially impact flame stability.

Chapter 5 examines key question #3, focusing on how increased strain influences the onset of thermodiffusive instabilities. This chapter assesses the dynamic response of strained flames to forced instabilities in both 2D and 3D lean premixed hydrogen laminar flames, determining whether strain acts as a promoter or inhibitor of these instabilities. The findings are essential for identifying conditions that favor more stable hydrogen flames in practical applications.

Chapter 6 leverages the valuable insights gained from the preceding chapters on the response of hydrogen flames to strain. It applies this knowledge to enhance existing CFD-LES modeling strategies, ensuring they accurately account for the characteristics of lean premixed hydrogen flames at high strain rates. This chapter addresses the final key

question #4.

Chapter 7 concludes the thesis by summarising the key findings and addressing how the central research question has been answered. It evaluates the thesis's contributions to the development of models for designing innovative combustors, which use strain as a mechanism to achieve both flame stabilisation and reduced NO_x emissions. Additionally, this chapter outlines future research directions to further advance our understanding in this field.

2

THEORETICAL BACKGROUND: HYDROGEN PREMIXED COMBUSTION

*Even if there is only one possible unified theory,
it is just a set of rules and equations.
What is it that breathes fire into the equations
and makes a universe for them to describe?*

Stephen Hawking

2.1. NO_x EMISSIONS FROM HYDROGEN COMBUSTION

In the previous chapter, it is introduced that one of the main limitations to the deployment of hydrogen combustion devices is the fact that they produce higher harmful NO_x emissions compared to common hydrocarbon fuels. Understanding the mechanisms behind NO_x formation in hydrogen combustion is crucial for developing strategies to mitigate these emissions and for advancing the viability of hydrogen as a clean fuel source. In this section, the fundamental theoretical background of NO_x emissions from hydrogen combustion in premixed flames is presented, with a focus on highlighting the key differences as compared to a common hydrocarbon fuel like methane.

NO_x is formed through distinct chemical pathways as a result of dissociation reactions that occur during the combustion process. The pathways that are relevant background for this dissertation are described below.

- Thermal NO_x, as first discovered by Zeldovich *et al.* [47], is formed when the temperature is high enough to enable the dissociation of N₂ from air into molecular nitrogen radicals N via the following temperature dependent reaction:



These free N radicals then react with O₂ and OH to form NO. In the cases where the threshold temperature is exceeded (≈ 1700 K), this pathway is often the main contributor to the total NO_x formation.

- Prompt NO_x [48] forms rapidly in the flame front via reactions between hydrocarbon fuel radicals and nitrogen from air. These reactions initially produce HCN, which is subsequently oxidised to form NO.
- NNH-NO_x [49] is formed through an intermediate species, NNH, which itself is produced by the reaction of fuel radicals (such as H or hydrocarbon radicals like CH). Subsequently, NNH reacts with radicals originating from the combustion process, primarily O, to form NO.
- N₂O-NO_x [50] forms mainly via the partial oxidation of nitrogen in fuel-lean, low-temperature combustion reactions, where N₂ first reacts with oxygen to produce N₂O, which then decomposes or further oxidises into NO.

Note that while these pathways primarily describe the formation of nitrogen monoxide (NO), nitrogen dioxide (NO₂) can also be formed in flames through the further oxidation of NO, particularly in cooler, post-flame regions or in the presence of excess oxygen. Yet, the concentration of NO₂ is much lower than that of NO in most practical cases [51]. A simplified sketch of the pathways described is reported in Figure 2.1.

The increase in NO_x emissions in premixed hydrogen flames compared to hydrocarbon flames is attributed to the thermal pathway, as hydrogen features a higher adiabatic flame temperature. This is shown in Figure 2.2, where the adiabatic flame temperature of different fuel/air mixtures are plotted as a function of the equivalence ratio. Indeed, the graph indicates that hydrogen exhibits a significantly higher adiabatic flame temperature compared to other common fuels at all equivalence ratios, with differences exceeding

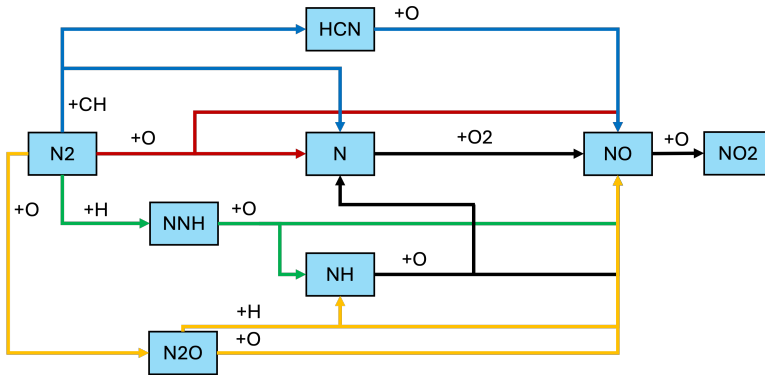


Figure 2.1: Sketch of the main NO_x formation pathways: thermal NO_x (red arrows), prompt NO_x (blue arrows), NNH-NO_x (green arrows) and N₂O-NO_x (yellow lines).

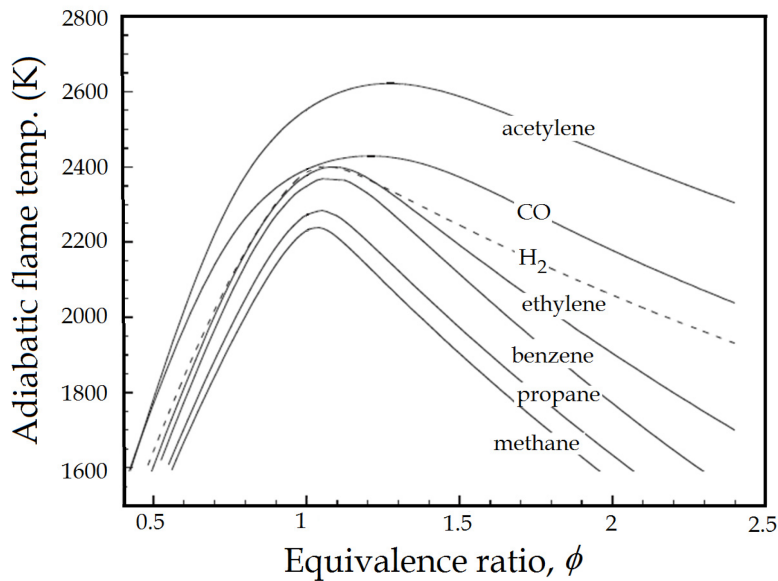


Figure 2.2: Adiabatic flame temperature as a function of the equivalence ratio in premixed flames at atmospheric pressure and reactants temperature $T_r = 300$ K [52, page 41]

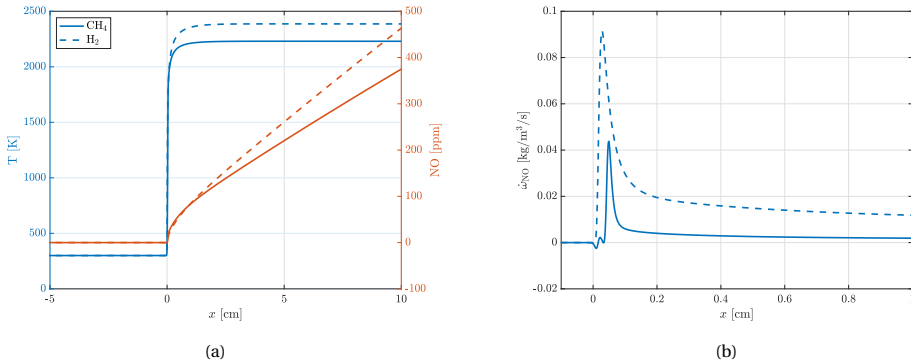


Figure 2.3: Temperature and NO concentration (a) and NO source term $\dot{\omega}_{\text{NO}}$ (b) in a freely propagating premixed flamelet at stoichiometric and atmospheric conditions for hydrogen/air and methane/air fuel mixtures ($T_r = 300$ K).

200K under stoichiometric conditions when compared to methane. This is primarily due to its higher lower heating value (LHV) per kilogram, attributed to its lighter molecular structure.

Figure 2.3 illustrates an example of temperature, NO concentration (in volume ppm), and NO source term profiles across a one-dimensional freely propagating premixed flamelet computed with Chem1D [53] under stoichiometric conditions for both methane/air and hydrogen/air mixtures. As previously discussed, the gap of more than 200K in the products temperature between the two fuels is clearly visible (Fig. 2.3a). This corresponds to a higher concentration of NO in the hydrogen case. It is important to note that the concentration of NO in the products continues to increase downstream as it is progressively formed through the thermal pathway. This is confirmed by the NO source term distribution in Figure 2.3b, which is greater than zero downstream of the flame. Indeed, the dissociation of N_2 through O at high temperature which starts the thermal NO formation pathway is a very slow reaction [47], and thus NO requires a significant amount of time to reach equilibrium, necessitating a very large flamelet domain. Nevertheless, as shown in Figure 2.3a, the gap between the NO concentrations of the two fuels continues to increase, corresponding to a higher NO source term downstream of the flame in the hydrogen case (see Fig. 2.3b). Consequently, a substantial discrepancy in NO emissions at equilibrium between the methane/air and the hydrogen/air flame can be expected.

An example of temperature and NO concentration across a 1D flamelet is further provided for lean conditions ($\phi = 0.6$) in Figure 2.4 for both methane/air and hydrogen/air mixtures. Similarly to the stoichiometric case, there is still a large gap between the flame temperatures and the NO concentration of the two fuels. However, for the methane case the NO concentration remains constant downstream of the flame, suggesting that the pollutant is only formed near the flame through pathways other than the thermal one. Indeed, the temperature is below 1700K, which is the threshold temperature for the N_2 dissociation reaction to be activated. For the hydrogen case, on the other hand, an increasing downstream NO concentration across the thermal pathway is still observed, as

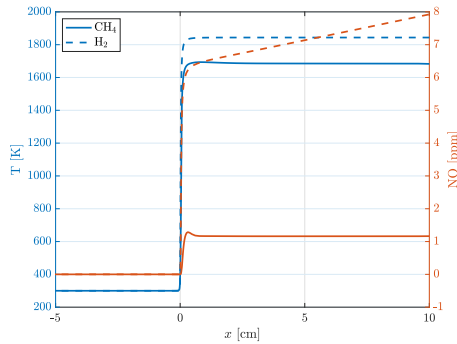


Figure 2.4: Temperature and NO concentration in a premixed flamelet at lean conditions ($\phi = 0.6$) for hydrogen/air and methane/air fuel mixtures at $p = 1$ bar and $T_r = 300$ K.

the temperature is still above 1700K. This finding suggests that to suppress NO formation via the thermal pathway in hydrogen premixed flames, leaner combustion regimes are required compared to methane flames. However, achieving such lean regimes presents significant control challenges, including increased probability of boundary layer flashback [23] and enhanced propensity to develop instabilities due to both hydrodynamic mechanisms [54] and local equivalence ratio oscillations [24]. Additionally, specifically in hydrogen flames, these conditions are characterised by the onset of thermodiffusive instabilities [28], which will be discussed in Section 2.4. Beyond thermal NO_x, the NO formed near the flame front through other pathways is also substantially higher for hydrogen fuel. This can be seen from the higher NO concentration achieved throughout the lean flame front in Figure 2.4 and from the higher NO source term peak in Figure 2.3b for stoichiometric conditions, further remarking the increased challenges in achieving low-emission hydrogen combustion.

Overall, it has been shown that hydrogen flames can potentially feature substantially higher NO_x emissions compared to traditional hydrocarbon fuels like methane. Hydrogen's higher adiabatic flame temperature, primarily due to its elevated lower heating value, leads to increased NO_x formation, particularly through the thermal pathway. This necessitates leaner combustion conditions to mitigate NO_x emissions, which in turn introduces complexities such as potential flashback and flame instabilities. Additionally, lean hydrogen combustion exhibits higher NO formation through non-thermal pathways such as the NNH and N₂O near the flame front, further complicating efforts to achieve low emissions. These factors collectively highlight the challenges to harness hydrogen as a carbon-free fuel while retaining stability and low-NO_x in combustion systems. Addressing these challenges is essential, and this dissertation will explore potential solutions and advancements in this critical area.

2.2. DIFFERENTIAL AND PREFERENTIAL DIFFUSION EFFECTS IN LEAN HYDROGEN FLAMES

In the previous chapter, it was discussed how lean combustion can be a solution to mitigate NO_x emissions in hydrogen flames, while also noting that hydrogen's high diffusivity poses additional challenges for flame control in this typically unstable regime. The high molecular diffusivity of hydrogen leads to differential and preferential diffusion effects. Differential diffusion, refers to hydrogen having a higher molecular diffusivity than the thermal diffusivity, meaning hydrogen diffuses faster than heat. This effect is also referred to as Lewis number effect, where the species Lewis number is defined as the ratio of the mixture's thermal diffusivity and species' molecular diffusivity:

$$\text{Le}_k = \frac{\alpha}{D_k}. \quad (2.2)$$

Preferential diffusion refers to hydrogen diffusing faster than other species in the mixture. This section explores these two phenomena and their effects on the structure of lean premixed flames.

The consumption of common hydrocarbon fuels like methane is chain-breaking, meaning that it consumes radicals. In contrast, the net reaction resulting from the hydrogen consumption chain reads



and is chain-branching, indicating that it generates radicals. These H radicals generated also have a very low Lewis number, meaning that they quickly diffuse upstream (due to Fick's law) faster than temperature. After diffusing upstream, they are burnt across the following intermediate reaction



generating heat release upstream in lower temperature flame regions, as temperature did not diffuse upstream as quickly as the radicals [29]. This can be observed in Figure 2.5, which illustrates the percentage of heat release rate and H radical mass fraction relative to their peaks as a function of temperature across a premixed freely propagating flamelet at two lean equivalence ratios. The figure compares a full multicomponent transport model with an artificial model where differential and preferential diffusion effects are suppressed by setting all Lewis numbers to unity. Indeed, at the same temperature, there are low temperature regions where the flame exhibits a higher percentage of its peak H mass fraction in the case with differential diffusion, and reaches a higher percentage of its peak heat release. When differential diffusion is artificially turned off, on the other hand, the heat release generation concentrates more in higher temperature regions.

In combination with the H radical transport mechanism described in the previous paragraph, the shift of the heat release generation towards lower temperature regions must be also attributed to differential diffusion of molecular hydrogen H_2 . Indeed, H_2 diffuses downstream of the preheat zone faster than temperature diffuses upstream due to its low Lewis number. This leads hydrogen concentration to start decreasing

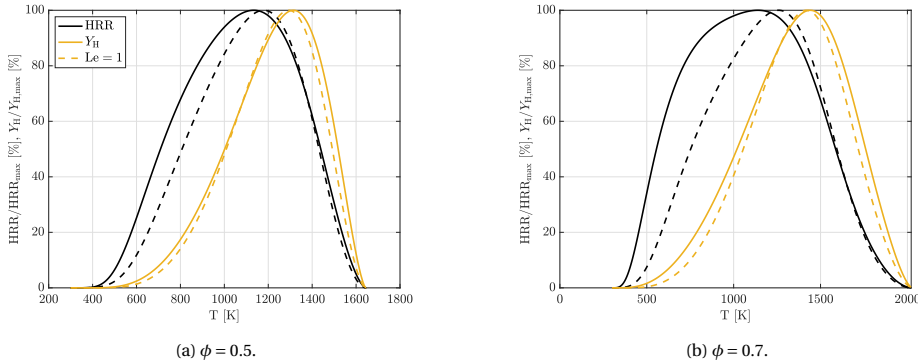


Figure 2.5: Percentage of heat release rate (HRR) and H mass fraction (Y_{H}) relative to its peak as a function of temperature T across a premixed freely propagating flamelet at $\phi = 0.5$ (a) and $\phi = 0.7$ (b). The figure compares a full multicomponent transport model (solid lines) with an artificial model where all Lewis numbers are set to unity (dashed lines) at atmospheric pressure and reactants temperature $T_r = 300$ K.

significantly more upstream compared to an artificial case where Lewis numbers are set to unity, because hydrogen starts to ‘feel’ its concentration gradient in the flame more upstream than heat, thus diffusing opposite to this gradient. This can be observed in Figure 2.6, where the mass fractions of the main species are plotted across two freely propagating lean premixed flamelets together with temperature and heat release rate profiles. While diffusing upstream, however, H_2 is consumed because of consumption reactions being already started in low temperature regions by the presence of H radicals, producing additional H radicals (see Eq. (2.3)) that further empower this phenomenon. These molecular transport mechanisms leading to a shift of heat release towards lower temperatures have several implications on the flame structure which are described in the succeeding paragraphs.

The earlier downstream diffusion of H_2 and subsequent consumption by the presence of H radicals lead to flame thickening. The thermal flame thickness δ_f (sometimes indicated as δ for simplicity in the next chapters) is defined as

$$\delta_f = \frac{T_p - T_r}{\left| \frac{\partial T}{\partial x} \right|_{\max}}, \quad (2.5)$$

where subscripts r and p denote the reactants and products side of the premixed flamelet, respectively. In Figure 2.7a, the thermal flame thickness of a hydrogen freely propagating premixed flamelet computed with full transport properties as a function of the equivalence ratio is compared to that obtained in an artificial case where Lewis numbers are set to unity for all species. An increased thickness at all equivalence ratios can be observed in the full transport case due to differential diffusion, with more significant discrepancies with respect to the $Le = 1$ case found in lean conditions. This is caused by the redistribution of the heat release rate by differential diffusion effects, which thickens the preheat region and smears the temperature gradients [29].

Differential diffusion effects also lead to fluctuations of the total enthalpy across the

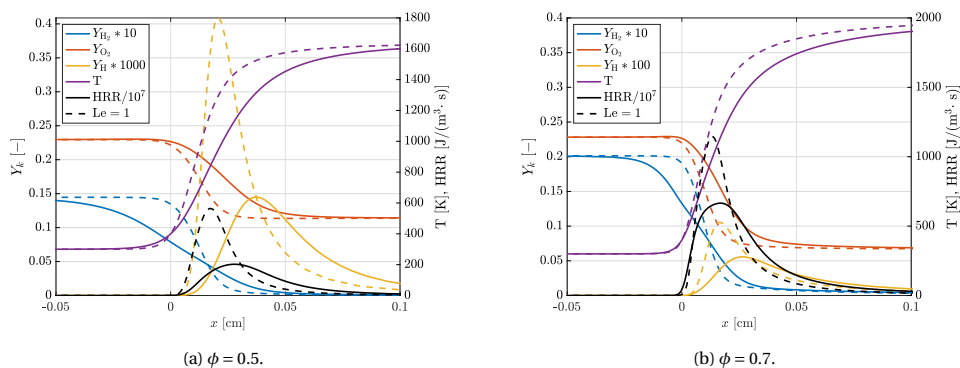


Figure 2.6: Mass fractions of the main species, temperature and heat release rate profiles across two freely propagating lean premixed flamelets at $\phi = 0.5$ (a) and $\phi = 0.7$ (b). The figure compares a full multicomponent transport model (solid lines) with an artificial model where all Lewis numbers are set to unity (dashed lines) at atmospheric pressure and reactants temperature $T_r = 300$ K.

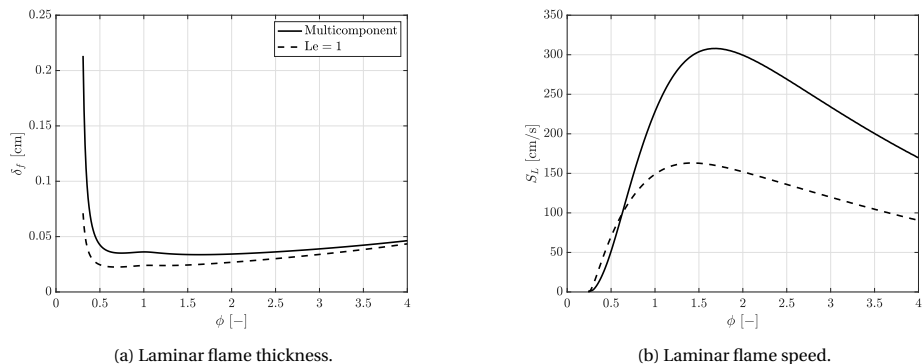


Figure 2.7: Flame thickness δ_f and laminar flame speed S_L as a function of the equivalence ratio ϕ . The figure compares a full multicomponent transport model (solid lines) with an artificial model where all Lewis numbers are set to unity (dashed lines) at atmospheric pressure and reactants temperature $T_r = 300$ K.

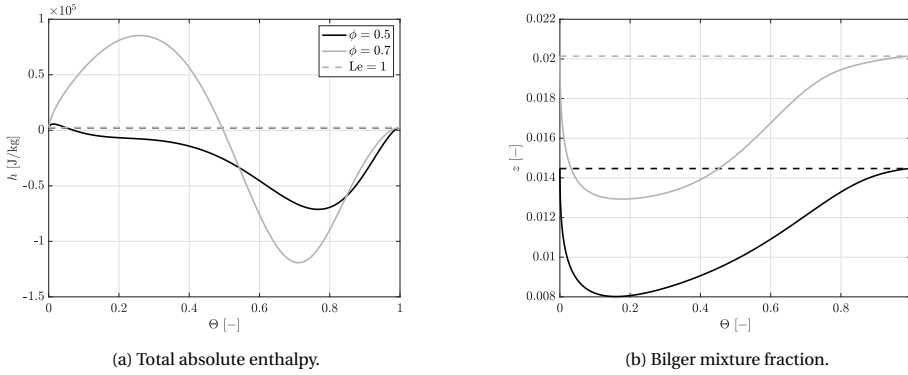


Figure 2.8: Total absolute enthalpy h (a) and Bilger mixture fraction z (b) as function of the temperature based progress variable Θ across two freely propagating lean premixed flamelets at $\phi = 0.5$ and $\phi = 0.7$. The figure compares a full multicomponent transport model (solid lines) with an artificial model where all Lewis numbers are set to unity (dashed lines) at atmospheric pressure and reactants temperature $T_r = 300$ K.

flame, which would be constant in the absence of these effects. The absolute enthalpy of the mixture is defined as the sum of the enthalpy of formation and sensible enthalpy:

$$h = \sum_{k=1}^{N_k} Y_k \Delta h_{f,k}^0 + \int_{298}^T c_{p,mix}(T') dT', \quad (2.6)$$

where Y_k is the mass fraction of the species k , $\Delta h_{f,k}^0$ is the species enthalpy of formation, and $c_{p,mix}$ is the mixture specific heat capacity. This quantity is plotted in Figure 2.8a across two freely propagating lean premixed flamelets as a function of the temperature-based progress variable $\Theta = \frac{T - T_r}{T_p - T_r}$ with both multicomponent transport model and Lewis numbers set to unity. In the leaner case ($\phi = 0.5$), there is a dip of absolute enthalpy across flame. This is attributed to the shift of heat release rate towards lower temperatures. For example, at the peak heat release rate the temperature is lower by 50 K compared to the unity Lewis number case. This leads to a reduction of the sensible enthalpy at the same reaction progress, as it narrows the integration domain in Equation (2.6). When the equivalence ratio is increased to $\phi = 0.7$, an overshoot of enthalpy also appears at low progress variables. This is attributed to the increasing local mass fraction of H radical, which has a very high enthalpy of formation, at richer mixtures. As discussed, the H radical is transported towards lower temperature regions due to differential diffusion, and thus its percentage relative to its peak mass fraction is higher compared to the case without differential diffusion in this region (see Fig. 2.5). This enthalpy fluctuations have a direct effect on the flame speed, as shown in Figure 2.7b. In very lean conditions, the flame speed is observed to be lower compared to the equal unity Lewis number case, due to the lower enthalpy across the flame. Above a threshold equivalence ratio ($\phi \approx 0.6$), instead, the flame speed of the full transport case appears higher. This is because the overshoot of enthalpy at low progress variable becomes increasingly important, leading to higher burning rates.

Preferential diffusion also plays a role in altering the hydrogen flame structure, leading

to fluctuations in the local equivalence ratio or mixture fraction. The Bilger mixture fraction is defined based on the elemental mass fractions of monoatomic hydrogen (\mathcal{Y}_H) and oxygen (\mathcal{Y}_O) [55–57]:

$$z = \frac{\frac{1}{2W_H}(\mathcal{Y}_H - \mathcal{Y}_{H,p}) - \frac{1}{W_O}(\mathcal{Y}_O - \mathcal{Y}_{O,p})}{\frac{1}{2W_H}(\mathcal{Y}_{H,r} - \mathcal{Y}_{H,p}) - \frac{1}{W_O}(\mathcal{Y}_{O,r} - \mathcal{Y}_{O,p})} \quad (2.7)$$

where W_k is the molar mass of element k , and the subscripts r and p indicate reactants and products side of the flamelet. Indeed, hydrogen diffuses downstream of the preheat zone towards the flame faster than oxygen, and thus its concentration starts to decrease more upstream across the flame (see Fig. 2.6). This creates a leaning region, corresponding to a dip in the mixture fraction, as it can be seen in Figure 2.8b. One might argue that this should be compensated by a region of richer mixture fraction downstream. However, as discussed above, hydrogen is also meanwhile consumed, generating products with diffusivities closer to those of the other major species. Hence, the mixture fraction returns to its initial value at the products side without any overshoot. The leaning phenomenon is more pronounced in leaner conditions, contributing to the decreased flame speed in these conditions. Furthermore, a leaner mixture with a decreased hydrogen content also leads to a locally lower mixture heat capacity, as hydrogen has itself a very high heat capacity. Therefore, preferential diffusion also contributes to the local decrease of sensible enthalpy discussed in the previous paragraph.

Overall, this section described differential and preferential diffusion effects and their significant impact on macroscopic flame properties, such as flame thickness and speed, and on local cross-flame characteristics, including flame structure, enthalpy, and equivalence ratio.

2.3. STRETCH EFFECTS

In the previous section, the effects of differential and preferential diffusion have been discussed considering the structure of a one-dimensional lean premixed hydrogen flame, where they establish cross-flame species and heat transport phenomena that trigger a redistribution of heat release, local enthalpy and mixture fraction. In this section, the discussion is extended to the interaction of these cross-flame phenomena with stretch in multi-dimensional flame fronts. The distinctive response to stretch of lean premixed hydrogen flames represents a fundamental aspect in understanding their dynamics and being able to develop accurate simulation models.

Stretch is defined by the fractional rate of change of a flame surface element A propagating in a non-uniform flow [30, 58]:

$$K = \frac{1}{A} \frac{dA}{dt}. \quad (2.8)$$

For a thin flame sheet, a general expression reads [59]:

$$K = -\mathbf{nn} : \nabla \mathbf{u} + \nabla \cdot \mathbf{u} + s_d(\nabla \cdot \mathbf{n}) = (\delta_{ij} - n_i n_j) \frac{\partial u_i}{\partial x_j} + s_d \frac{\partial n_i}{\partial x_i}, \quad (2.9)$$

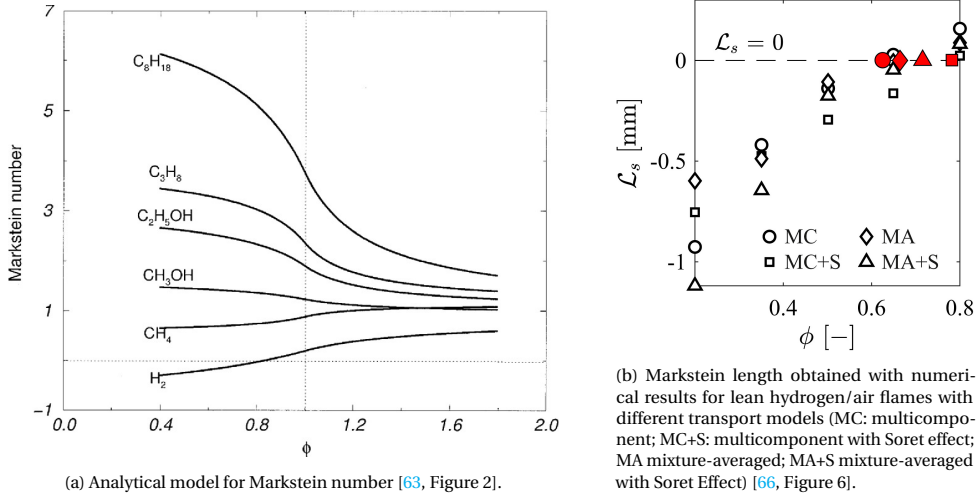


Figure 2.9: Sample Markstein numbers or lengths obtained analytically (a) and numerically (b).

where $\mathbf{n} = -\frac{\nabla c}{|\nabla c|}$ is the unit vector normal to the flame surface, defined positive when pointing towards the fresh gases given a flame progress variable c , and s_d is the flame displacement speed, i.e. the propagating flame front speed relative to the flow. In Equation (2.9), $\mathbf{nn} : \nabla \mathbf{u}$ represents the gradient of the velocity field \mathbf{u} normal to the flame front. By combining the first two terms at the right hand side in Equation (2.9), one obtains $\nabla_t \cdot \mathbf{u}$, which is the tangential component of the gradient operator [60] such that

$$K = \nabla_t \cdot \mathbf{u} + s_d \nabla \cdot \mathbf{n} = K_s + \kappa s_d. \quad (2.10)$$

The first term on the right-hand side in Equation (2.10) represents the change of flame surface area due to tangential strain rate K_s , i.e. velocity gradients in the plane tangential to the flame, while the second term accounts for the change of flame surface area due to curvature $\kappa = \nabla \cdot \mathbf{n}$. Examples of simplified flame configurations featuring solely positive tangential strain rate are stagnation point flames, wall-stabilised flames and counterflow flames [30]. Positively and negatively curved flames are found in spherically expanding flames [44] and Bunsen burners [61], respectively. Tubular burners experience both positive strain and curvature [62].

By means of asymptotic analysis, the effect of stretch on the flame speed S_f was described analytically through the following relation [58]:

$$S_f = S_L - \mathcal{L}K, \quad (2.11)$$

where \mathcal{L} is the Markstein length. Analytical expressions for the Markstein length are available in literature [63, 64] based on the hydrodynamic theory [58, 65], which allow to predict \mathcal{L}/δ_f (referred to as Markstein number) as a function of the equivalence ratio for different fuel/air premixed flames as reported in Figure 2.9a. The Markstein length can be also measured experimentally in spherically expanding flame setups [67] or in a constant volume combustion vessel [68], or determined numerically in strained

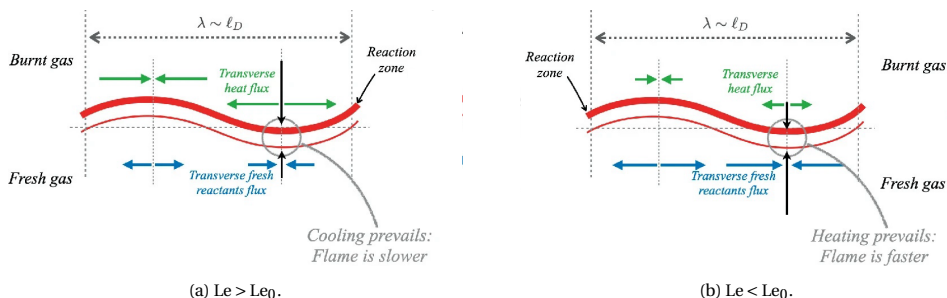


Figure 2.10: Sketch of the thermodiffusive mechanism: stable (a) and unstable (b) cases [28, Figure 13].

counterflow flames [66]. The figure shows that all the analytically evaluated mixtures exhibit a positive Markstein length, except for lean hydrogen/air mixtures. The inversion of Markstein length in lean hydrogen flames was also measured experimentally [44] and computed numerically [69], where the level of detail of the transport model can affect its quantitative prediction as shown in Figure 2.9b [66].

2.4. CURVATURE EFFECTS: ONSET OF THERMODIFFUSIVE INSTABILITIES

In this section, the effects of curvature in lean premixed hydrogen flames are discussed, which is one of the two contributors to stretch as introduced in Section 2.3, and the mechanism leading to the onset of thermodiffusive instabilities is described. As mentioned in Chapter 1, controlling these instabilities presents a distinctive challenge for implementing lean premixed hydrogen flames in practical settings. Hence, understanding their features and the conditions leading to their onset is crucial for developing flame control strategies using reliable simulation tools.

The dynamics of a curved flame front is affected by (i) the flow field modification due to cross-flame density jump driven by thermal expansion; and (ii) transverse convection and diffusion of species and heat. These two phenomena are responsible for the onset of intrinsic flame instabilities: cross-flame thermal expansion (i) leads to hydrodynamic instabilities (or Darrieus-Landau, DL), and mechanism (ii) causes the onset of thermodiffusive instabilities (TD). While any flame subject to hydrodynamic instabilities is unconditionally unstable regardless of the perturbation wavelength [28], diffusion fluxes can lead to thermodiffusively stable or unstable flames, depending on the mixture Lewis number. Bechtold and Matalon [63] analytically defined a critical Lewis number Le_0 , such that when $Le < Le_0$ the flame is intrinsically unstable. Here, Le is an effective Lewis number defined as a function of the Lewis numbers of the deficient and the excess reactant [70]. Examples of thermodiffusively unstable flames where $Le < Le_0$ are sufficiently lean hydrogen/air mixtures, but also rich propane/air mixtures [71].

The mechanism leading to the onset of thermodiffusive instabilities in lean hydrogen flames is described below and sketched in Figure 2.10. As discussed in Section 2.2, H_2 diffuses downstream faster than heat diffuses upstream normally to the flame due to differential diffusion. The curved flame front enables a misalignment between these dif-

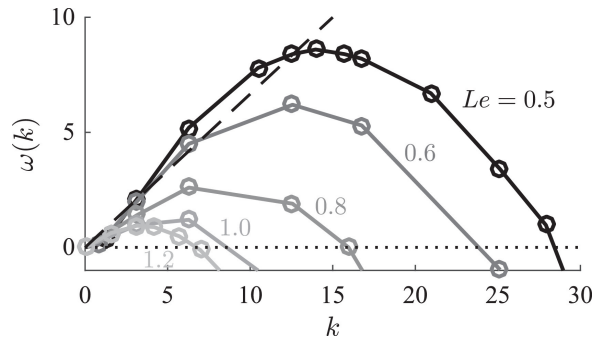
diffusive fluxes (that are normal to the flame surface) and the longitudinal direction. Hence, diffusive fluxes can be decomposed into a longitudinal component, which alters the flame structure as described in Section 2.2, and a transverse component. The transverse component, which becomes more and more important as curvature is increased, impacts the local flame speed as follows:

- in positively curved flame fronts (concave towards the products), the transverse flux of H_2 replenishes the reaction zone faster than the transverse heat flux is able to cool it down (see right hand side of the sketch in Fig. 2.10b). This leads to a so-called ‘focusing’ of hydrogen in the hot reaction zone, leading to super-adiabatic temperatures and enhancing the local reactivity and thus the flame speed. The local increase of flame speed triggers a more pronounced curvature, which leads to a further increase of flame speed.
- in negatively curved flame fronts (concave towards the reactants), the transverse flux of H_2 empties the reaction zone faster than the transverse heat flux is able to heat it up (see left hand side in the sketch in Fig. 2.10b). This leads to a defocusing of hydrogen in the reaction zone, decreasing the local reactivity and thus the flame speed. The local decrease of flame speed triggers a more pronounced negative curvature, further decreasing the flame speed.

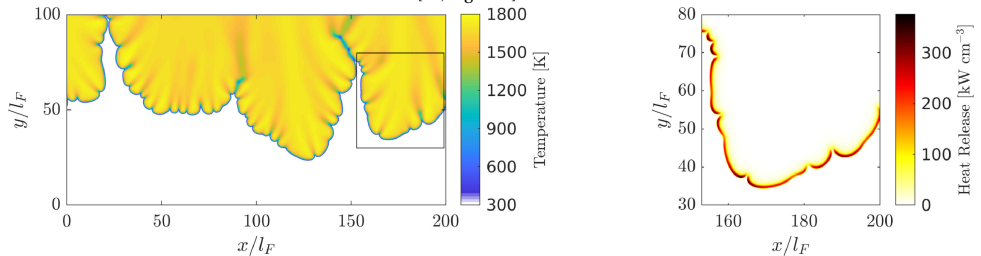
In both positively and negatively curved flame fronts, hydrogen's higher diffusive flux than heat ($Le < Le_0$) drives the self-amplification of the instability in lean hydrogen mixtures, making the flame thermodiffusively unstable. Conversely, when heat fluxes are stronger than species fluxes ($Le > Le_0$), such as in methane/air flames, an opposite mechanism that dampens any perturbation is observed, which makes the flame thermodiffusively stable (see sketch in Fig. 2.10a).

A similar description leading to the onset of thermodiffusive instabilities can be phenomenologically valid considering preferential diffusion effects. Indeed, in a positively (negatively) curved flame front, the flame experiences a transverse flux of H_2 which is greater than that of O_2 leading to a local enrichment (leaning) of the mixture and thus increased (decreased) local reactivity and flame speed with super-equilibrium products. However, by artificially isolating the contributions of differential and preferential diffusion effects, Pitsch [29] attributed the growth of thermodiffusive instabilities solely to the former. Nevertheless, the method used to isolate the two effects employs unreal molecular diffusivities for species other than H_2 , thus introducing artificial differential and preferential diffusion effects which have an unknown impact on the flame structure and the burning rates. In reality, the two effects are inherently connected, as described in Section 2.2, and thus a rigorous method to isolate them can hardly be found. Therefore, while it is probably true that the imbalance of H_2 and H diffusivity with respect to heat diffusivity is the main contributor to thermodiffusive instabilities, both effects play a role.

Well-established theoretical and numerical studies describing the onset of intrinsic flame instabilities are available in literature. In the limit of small amplitude perturbations, an initial regime where the instability grows linearly in time is identified [74], whose growth rate ω depends on the local perturbation mode k [75], allowing to reconstruct the so-called ‘dispersion relation’. An example obtained with numerical simulations is



(a) Linear regime: example of reconstructed dispersion relations with different mixture Lewis numbers [72, Figure 1].



(b) Non-linear regime: snapshot of the temperature field showing small-scale cellular structures and large-scale finger-like structures along the flame front [73, Figure 1]. (l_F : flame thickness).

Figure 2.11: Example of dispersion relation (a) and cellular and finger-shaped flame structures (b) obtained from numerical simulations of lean premixed hydrogen flames.

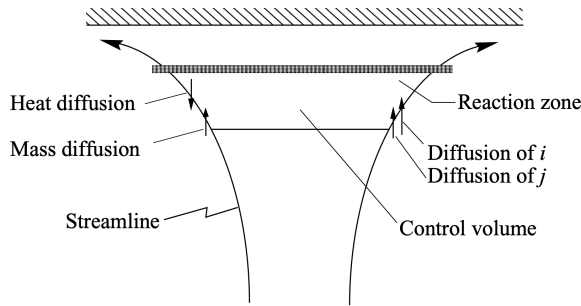


Figure 2.12: Sketch of the stagnation flame configuration with conceptual demonstration of the effects of stretch on the flame response in presence of differential (left hand side) and preferential (right hand side) diffusion effects [52, page 411, Figure 10.3.1a]

reported in Figure 2.11a. The dispersion relation can be reconstructed in freely propagating [58, 64, 65] and spherically expanding [76] premixed flame configuration using analytical models such as the hydrodynamic model, which assumes infinitely thin flame fronts. However, this theory is incomplete for $Le < Le_0$. More simplified theoretical models based on the integral approach also exist, which employ the constant density flow assumption and thus neglect thermal expansion [77–80]. Although these models claim validity for arbitrary Lewis numbers and stretch, more recent works have argued that they are valid only for weak stretch [81] and in the near-unity-Lewis number limit [82]. Additionally, the quantitative predictions of the Markstein length obtained do not agree with the numerical results [69]. The initial linear regime is followed by a non-linear growth regime where the flame displays small-scale cellular structures and large-scale finger-shaped structures [73], as displayed in Figure 2.11b. Since the recent growing focus on hydrogen combustion, the onset of thermodiffusive instabilities in curved flame fronts has been extensively studied numerically under a variety of laminar burning conditions with both one-step [83, 84] and detailed chemistry [73–75, 85] direct numerical simulations (DNS) based on comprehensive transport modelling. Fewer numerical studies exist, on the other hand, considering the effect of tangential strain rate in lean premixed hydrogen flames, which is discussed in the next section.

2.5. FLAME STRENGTHENING BY TANGENTIAL STRAIN RATE

After describing the interaction of curvature and differential/preferential diffusion effects, which lead to the onset of thermodiffusive instabilities, the other contributor to stretch is now considered: the tangential strain rate. Considering a stagnation flame configuration, a control volume is taken enclosing the preheat and the reaction zone of the flame, and delimited by two symmetric streamlines, as reported in Figure 2.12 [52]. As discussed in Section 2.4, diffusive fluxes are normal to the flame front. The preheat zone within the control volume is replenished with H_2 molecules through its lateral boundaries faster than heat leaves the control volume through the same boundaries due to differential diffusion effects. This leads to super-adiabatic temperatures and enhances the reactivity of the flame and thus the flame speed, similarly to a positively curved flame front. Analogously,

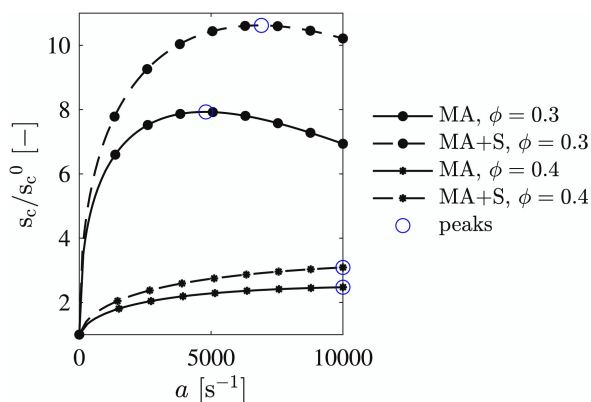


Figure 2.13: Normalised fuel consumption speed s_c with respect to the unstretched flame speed s_c^0 obtained with different transport models as a function of the applied strain rate a in a strained lean premixed hydrogen flame (MA: mixture-averaged; MA+S mixture-averaged with Soret) [66, Figure 5a].

more H_2 is transported into the preheat zone than O_2 through the lateral boundary of the control volume due to preferential diffusion effects, leading to a local flame enrichment and super-equilibrium products, and thus to increased reactivity and flame speed.

The increased reactivity at increased strain due to differential and preferential diffusion effects discussed in the previous paragraph has potentially interesting implications. In fact, unlike hydrocarbon fuels, sufficiently lean hydrogen flames are generally strengthened by strain, and this allows the flame to stabilise beyond the lean flammability limit [86], possibly enabling further reduced NO_x regimes. Furthermore, it was shown by increasing the hydrogen content in hydrogen-enriched flames that the extinction strain rate is substantially delayed [36, 37], suggesting that hydrogen flames can withstand very high strain regimes. This is driven by both hydrogen's fast chemistry and the aforementioned strengthening mechanism by differential/preferential diffusion at increasing strain. Note, however, that this flame strengthening is observed up until a certain level of strain [66], depending on the equivalence ratio, as shown by the consumption speed graph as a function of strain in Figure 2.13. Beyond this threshold, characteristic flow times become of the same order as the very short chemical times and thus the flame starts to exhibit decreasing consumption speed and to weaken, with a similar mechanism to that of hydrocarbon fuels.

As discussed in Chapter 1, although the above findings on the strengthening effect of strain are promising, the isolated impact of strain on lean premixed hydrogen flames—particularly its influence on NO_x emissions, flame structure, transport phenomena, and onset of thermodiffusive instabilities—is not fully understood. Addressing this knowledge gap could reveal pathways to simultaneously enhance flame stability and minimise emissions in hydrogen flames, which are currently the key challenges in hydrogen combustion applications.

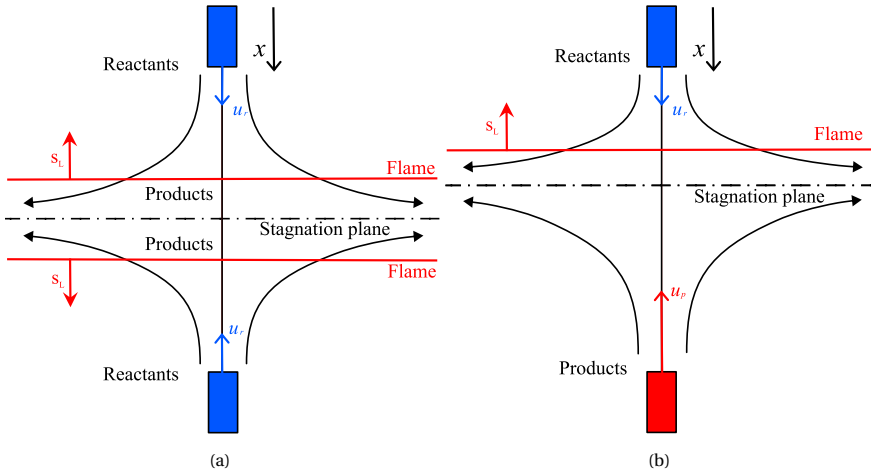


Figure 2.14: Sketch of the reactants-to-reactants or back-to-back (a) and reactants-to-products or fresh-to-burnt (b) counter-flow premixed strained flame configurations, where x is the flamelet longitudinal coordinate, u_r is the inlet velocity of the reactants mixture, u_p is the inlet velocity of the products mixture, and S_L is the laminar flame speed. Curved lines indicate the streamlines of the flow.

2.6. STRAINED PREMIXED FLAME CONFIGURATIONS

In order to study strained premixed flames, the canonical configurations used to establish a strained regime are now examined. Strained premixed flames are most commonly investigated using three canonical setups: the stagnation flame with adiabatic stagnation surface (see Fig. 2.12 in the previous section), the twin flame counterflow (Figure 2.14a), and the reactants-to-products counterflow (Figure 2.14b). The flame obtained from these three configurations features the same characteristics at low strain rates, i.e. when the flame stabilises far from the wall or stagnation plane. However, significant differences arise when the flame is pushed closer to the stagnation surface at higher strain rates, which is the regime of interest in this thesis.

The stagnation flame configuration involves a fresh reactant mixture directed toward an adiabatic wall, which generates a premixed flame at a strain rate determined by the inlet velocity of the reactants (Figure 2.12). By assuming an adiabatic wall, this setup eliminates heat losses, enabling an isolated analysis of strain rate effects on the flame. Furthermore, the flow field in this setup can be accurately described by a potential flow formulation [52], making it an ideal and widely adopted configuration for analytical investigations of the dynamics of strained flames. A particularly relevant example within the framework of this thesis is the stability analysis of strained and thermodiffusively unstable flames conducted by Sivashinsky *et al.* [87] using this configuration—a study that will be discussed further in Chapter 5. However, at the high strain rates that are of interest in this thesis, the flame is pushed very close to the stagnation plane, which can artificially alter the structure of the flame and the predictions of slow pollutants such as NO_x . Furthermore, highly strained flames cannot be practically stabilised so close to a wall due to unavoidable heat losses.

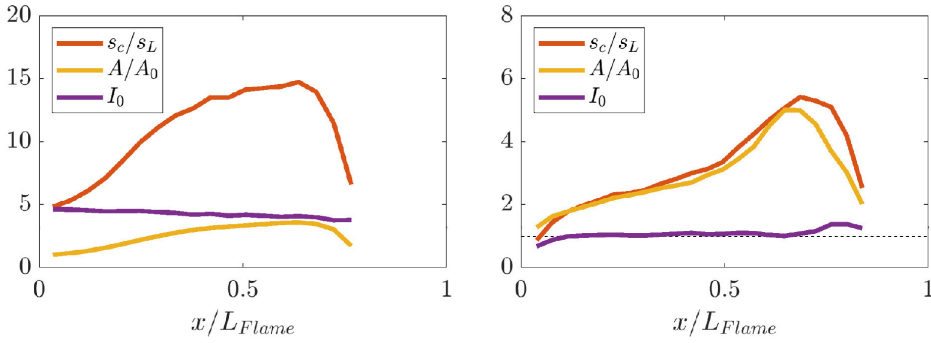
The second configuration consists of a twin counterflow configuration, also referred to as back-to-back or reactants-to-reactants, where two flames are stabilised symmetrically with respect to the flow stagnation plane (Figure 2.14a). Several studies are available where the effects of hydrogen enrichment and strain on lean blow-off, extinction strain, mass burning rate, and NO_x emissions are investigated with this setup [36–38, 40]. Specifically on NO_x emissions that are of interest in this thesis, a technical report from Xie *et al.* [88] underlines a decreasing trend with strain for this configuration in rich pure-hydrogen flames, attributing to the NNH pathway the predominant contribution to NO_x formation at high strain levels. However, the limitation of this configuration is represented by the proximity of the two twin flames to each other, particularly at the high strain rates achievable by purely hydrogen flames. In these conditions, in fact, the combustion reactions have no space to complete, and this has been shown to have a negative impact on the prediction of the extinction strain rate [89, 90]. Minor species are shown not to be fully burnt within the stagnation plane Jackson *et al.* [36, Figures 5 and 6]. Similarly, the reaction rates of NO_x pathways were observed to approach zero within the stagnation plane for lower strain rates by Ning *et al.* [40, see Figures 6–8], but not at higher strain rates. The same was observed to occur to the water rate of production by Xie *et al.* [88, see Figure 2].

The last premixed strained flame configuration consists of a reactants-to-products or fresh-to-burnt counterflow, where a single flame stabilises on the reactants side of the domain (Figure 2.14b). Unlike the other two configurations, the single flame setup without walls allows the combustion reactions to complete even at very high strain rates, as the fuel and the radicals have space to burn completely, eventually migrating across the stagnation plane [52]. This evidence can be found, for instance, in the work of Marzouk *et al.* [39, Figures 4–6]. Although the presence of complete combustion hot products on one of the boundaries can precondition the problem, particularly considering the products temperature, previous studies proved that the extinction strain rate can be accurately predicted in this configuration [91]. As a matter of fact, this configuration has been already employed in analyses of strained syngas and hydrogen-enriched laminar flames [21, 39], and widely discussed for methane flamelets [92, 93], particularly to compare flame speeds of turbulent cases with the strained flamelet speed [35, 90], in the application of LES-FGM models with strained flamelets [94, 95], and to evaluate NO_x emission at varying strain rate [96].

In light of the above discussion, the reactants-to-products counterflow configuration is adopted in the analyses performed in thesis. Indeed, its single flame layout allows the chemical reactions to complete also at very high strain rate—a feature that makes it particularly well suited for analysing the structure, emissions, and stability of lean premixed hydrogen flames under the highly strained conditions which are relevant in the framework of this thesis.

2.7. EFFECT OF TURBULENCE IN THERMODIFFUSIVELY UNSTABLE FLAMES

In the previous sections, the fundamental characteristics of lean premixed hydrogen flames under laminar conditions have been examined, where simplified flow fields fa-



(a) Detailed transport model (thermodiffusively unstable).

(b) Unity Lewis numbers (thermodiffusively stable, differential/preferential diffusion effects artificially turned off).

Figure 2.15: Turbulent flame speed, surface area increase, and stretch factor at different heights above the burner for detailed transport model (a) and unity Lewis numbers (b). [46, Figure 7].

cilitate the analysis and the understanding of the flame features. However, in practical combustion systems, flames are inherently turbulent. This section examines the impact of turbulence on lean premixed hydrogen flames, focusing on its interactions with differential and preferential diffusion, thermodiffusive instabilities, and strain effects.

Even if the typical cellular structures are not directly observable due to the instantaneous flame perturbation by turbulent eddies, intrinsic flame instabilities continue to influence flame dynamics in turbulent conditions. A direct numerical simulation of a lean premixed hydrogen flame in a slot burner configuration first suggested that thermodiffusive instabilities feature a synergistic interaction with turbulence in enhancing the fuel consumption rate per flame surface area [46]. This was shown by decomposing the turbulent flame speed (here quantified with consumption speed s_c) into the laminar unstretched burning velocity s_L , the flame surface area increase in a turbulent flame due to flame corrugation A/A_0 , and the stretch factor I_0 :

$$s_c = s_L \frac{A}{A_0} I_0. \quad (2.12)$$

The stretch factor accounts for increased turbulent flame speed due to variations of the flame structure compared to a laminar unstretched flamelet, such as increased reaction rate or local flame thickness. The contributions of these terms to the turbulent flame speed at increasing height above the burner are reported in Figure 2.15a. These results obtained with a detailed transport model are compared to those obtained in an artificial case where all Lewis numbers are set to unity in Figure 2.15b, thus suppressing differential/preferential diffusion effects. The figures show that when differential/preferential diffusion effects are turned off the stretch factor is close to unity, indicating that the flame structure is similar to that of an unstretched premixed flamelet. Conversely, a substantial contribution of the stretch factor to the turbulent flame speed is found in the case with differential/preferential diffusion due to increased flame reactivity by stretch (see Section 2.3). By observing that this stretch factor ($I_0 \approx 4$) is greater than that computed in a laminar flame, it was suggested that turbulence and thermodiffusive instabilities feature

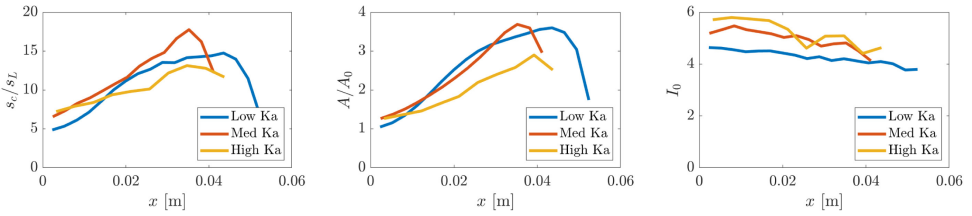


Figure 2.16: Turbulent flame speed, surface area increase, and stretch factor at different heights above the burner for three different Karlovitz number cases [99, Figure 3].

a synergistic effect to enhance the flame speed. The authors attributed this phenomenon to turbulence inducing higher fluctuations of curvature by thermodiffusive instabilities and to an increased average strain rate, which lead to a further increase of local equivalence ratio and thus local reaction rates. The tendency of turbulent flames to increase their overall burning rate and wrinkling with decreasing mixture Lewis number due to thermodiffusive instabilities had already been observed in a DNS study of spherically expanding flames [97], although not yet attributed to this synergistic mechanism. In a later study, this synergistic effect was also observed experimentally [98] on a slot burner configuration similar to that of Berger *et al.* [46].

In a follow up study, Berger *et al.* [99] expanded their analysis by increasing the levels of turbulence through the flame Karlovitz number, defined by $Ka = (\delta_f/\eta)^2$, where η is the Kolmogorov length scale, and which represents a non-dimensional flame stretch [100]. The increase of turbulent flame speed and the contributions of stretch factor and flame surface area at three different Ka are reported in Figure 2.16. The figure shows that the turbulent flame speed peaks at intermediate Karlovitz numbers. Indeed, the flame surface area decreases with increasing Ka due to increased turbulence levels. Although the stretch factor shows a monotonically increasing trend with Ka, the decrease of flame surface counteracts this effect and becomes predominant at the highest Karlovitz case, leading to a lower turbulent flame speed. Furthermore, the monotonically increasing stretch factor is attributed solely to increased mean tangential strain rate by shear-driven turbulence. In fact, curvature fluctuations are shown to progressively vanish with increasing Ka, suggesting a vanishing effect of thermodiffusive instabilities on the stretch factor. Interestingly, the authors compared the conditional means of mixture fraction across the progress variable of the three turbulent simulations to those of three strained laminar flamelets at different strain rates. The comparisons suggested that it is possible to mimic the effect of increasing Ka on the conditional mean of mixture fraction in turbulent flames by increasing strain in a counterflow flamelet, as shown in Figure 2.17. Despite it was already known that stretch and Karlovitz number are closely related by definition [100], this finding considering the mixture fraction profile has implications in tabulated chemistry models for hydrogen combustion which are introduced in the next section and assessed in Chapter 6.

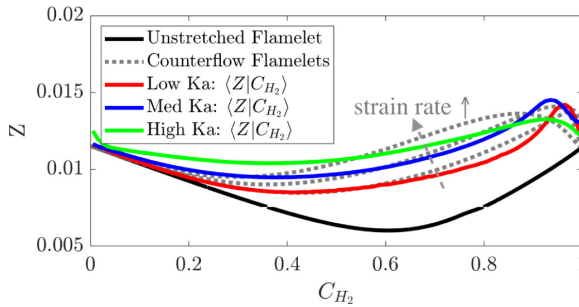


Figure 2.17: Comparison of the conditional mean mixture fraction $\langle Z | c_{H_2} \rangle$ with respect to progress variable in the turbulent flames and the three selected counterflow flames (gray dotted lines) and the unstretched flamelet (black line) [99, Figure 8].

2.8. CHALLENGES IN TABULATED CHEMISTRY LARGE EDDY SIMULATION MODELS

So far, the unique characteristics of hydrogen flames that set them apart from conventional hydrocarbon flames have been described. Developing accurate yet computationally efficient computational fluid dynamics (CFD) models that capture these features is essential for designing safe and low-emission lean premixed hydrogen combustion systems. However, these characteristics pose significant challenges for existing modelling approaches, which are discussed in this section.

Flamelet-based tabulated chemistry models have been extensively explored and applied to practical cases. They are based on the assumption that universal local laminar-like structures appear across a turbulent flame front. By transporting few representative scalars—such as mixture fraction or progress variable—instead of all individual species, they enable a significant reduction of computational cost. The source terms for these variables are found tabulated from one dimensional flamelet calculations as a function of the chosen controlling variables. These tables obtained from 1D flamelets are also referred to as ‘manifolds’. Within the large eddy simulation (LES) framework, additional subgrid models are included to account for turbulence-chemistry interactions at subfilter scales. Examples of subgrid models are the presumed filtered density functions (PDF) [101] and the filtered tabulated chemistry approach for LES (F-TACLES) [102], which will be further described in Chapter 6.

Due to hydrogen’s unique high-diffusivity characteristics, however, existing tabulated chemistry large eddy simulation models assuming unity Lewis number need to be modified to account for differential and preferential diffusion, the possible onset of thermodiffusive instabilities, and for their potential interaction with strain and turbulence [29]. While premixed flames typically feature a constant mixture fraction, hydrogen’s differential/preferential diffusion effects introduce fluctuations, thereby affecting the local reactivity. An example of a scatter plot obtained from a direct numerical simulation (DNS) of a turbulent lean premixed hydrogen flame is provided in Figure 2.18 [46]. This scatter broadens the range of thermochemical states within the flame which need to be accounted for in the flamelet manifold generation.

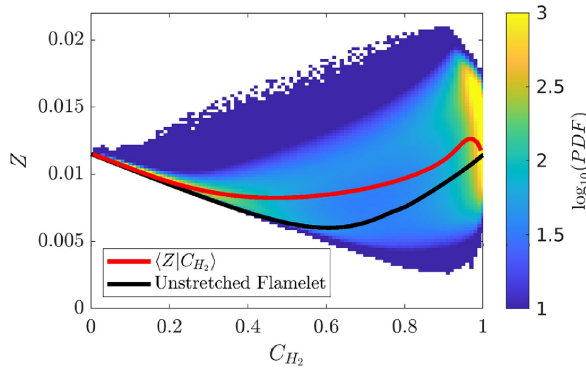


Figure 2.18: Joint probability density function (PDF) of progress variable based on H_2 (c_{H_2}) and mixture fraction Z , along with the conditional mean of Z on c_{H_2} (red line), and the profile of mixture fraction across an unstretched premixed flamelet at the same nominal equivalence ratio (black line) [46, Figure 17].

Various tabulated chemistry formulations based on two controlling variables, namely progress variable and mixture fraction, have been proposed in the literature to account for differential and preferential diffusion at the resolved scales in laminar conditions. Regele *et al.* [71] first introduced a modified mixture fraction equation by including a progress variable dependent source term and considering $Le \neq 1$ for the fuel only. This approach was later extended by Schlup and Blanquart [103] to incorporate a full mixture-averaged transport formulation and including thermal diffusion effects. Another proposed formulation consists of introducing additional terms in the diffusive fluxes of the transported controlling variables [104]. This approach was tested only recently with good success to pure hydrogen flames in partially premixed [105] and fully premixed conditions [106]. Mukundakumar *et al.* [107] proposed a different formulation obtained by inverting the order of the operations performed to reconstruct the diffusive transport terms of the controlling variables, and assuming constant non-unity Lewis numbers. Another approach is the composition space method first introduced for unstretched premixed flamelet manifolds [108] and then extended to strained and curved premixed flamelets [109]. The extended formulation was tested with good success over spherically expanding lean premixed hydrogen flames at atmospheric [110] and elevated [111] pressure, but required a four-dimensional manifold, which is computationally demanding. Reduced manifold formulations have been also attempted for the same modelling framework by using unstretched flamelets with varying reactants temperature [112] and curved (unstrained) flamelets [113].

Further challenges for tabulated chemistry models of lean hydrogen flames arise at subfilter scales due to the presence of thermodiffusive instabilities. Recent studies have addressed these challenges by tabulating data from filtered direct numerical simulations performed over the same flame setup [114], and introducing an algebraic laminar wrinkling factor to correct the filtered consumption speed to model the effect of subgrid thermodiffusive instabilities over resolved scales [72]. While this approach was successful in the framework of one-step chemistry simulations [115], it still needs improvement in a detailed chemistry framework [116].

The accurate modelling challenges posed by subgrid thermodiffusive instabilities in a large eddy simulation framework become even more pronounced in turbulent flames. As discussed in Section 2.7, direct numerical simulations [46] and experiments [98] suggested that thermodiffusive instabilities feature a synergistic interaction with turbulence in enhancing hydrogen reactivity and consumption speed. Although these synergistic effects have been proved to progressively vanish with higher and more practical Karlovitz numbers, the flame reactivity still increases due to hydrogen's response to strain triggering a local flame enrichment [99]. This enrichment can be in principle taken into account in tabulated chemistry frameworks by entering the laminar reaction rate in the table corresponding to the local equivalence ratio experienced by the turbulent flame provided that the subgrid distribution of the local equivalence ratio is accurately modelled, as recently proved *a priori* [117]. In the context of LES with presumed filtered density functions (FDF), extensions of the formulations of Regele *et al.* [71] and Mukundakumar *et al.* [107] have been proposed with discrete success by Berger *et al.* [118], Kai *et al.* [119] and Ferrante *et al.* [120], respectively. In these works the reaction rates were obtained from unstretched premixed hydrogen flamelets with varying equivalence ratio, tabulated as a function of progress variable and mixture fraction. However, a recent *a priori* study performed by Böttler *et al.* [121] indicated that a simple two-dimensional unstretched flamelet manifold exhibits limitations in capturing the local thermochemical states in thermodiffusively unstable and turbulent conditions even at the DNS scale. The authors showed that the local error of the tabulated quantities can be significantly reduced through a novel higher-dimensional flamelet manifold consisting of five control variables and considering around 26000 strained and curved flamelets. However, this solution appears very memory-demanding.

Despite recent progress, further research is essential to develop reliable and computationally efficient tabulated chemistry LES models that accurately capture the interplay of differential/preferential diffusion, thermodiffusive instabilities, strain and turbulence in lean premixed hydrogen flames. This thesis contributes to addressing these challenges in the framework of strained hydrogen flames proposing and testing strategies to improve such models.

3

NO_x EMISSIONS ANALYSIS IN LEAN PREMIXED AND STRAINED HYDROGEN FLAMELETS

To have one basis for life and another for science is apriori a lie.

Karl Marx

3.1. INTRODUCTION

In Chapter 1, the critical role of hydrogen combustion in decarbonisation efforts and the unique challenges and opportunities associated with this technology were discussed. One of the key challenges in hydrogen combustion is the elevated NO_x emissions, which pose substantial environmental and health risks. Given the discussed promising aspects of hydrogen combustion under strain, this chapter aims to explore how intensive strain levels affect NO_x emissions in lean premixed hydrogen flames.

This study presents a numerical investigation of counterflow premixed laminar hydrogen flames, focusing on their behaviour under intensive strain levels and particularly on the effect on NO_x emissions. This is, to best of the authors' knowledge, the first time that such an investigation is conducted. The increase in reaction rate and the observation of super-adiabatic temperatures under stretched regimes discussed in Chapter 2 would suggest a corresponding increase of NO_x emissions. Counter-intuitively, this study highlights that NO_x emissions do not increase with strain, and conversely they are suppressed at lean conditions, particularly at very high strain rates.

Detailed-chemistry one-dimensional and two-dimensional computational fluid dynamics (CFD) analyses are performed to achieve a deeper understanding of the employed counterflow strained flamelet configuration for intensive strain levels. In particular, a detailed analysis of NO_x formation pathways shows that thermal NO_x mechanism is the main contributor to the pollutant decrease with strain. Hence, the way strain affects the main radicals distribution is investigated in order to shed light on the observed emissions pattern. The analysis is also repeated for a higher pressure level, different chemical mechanism, and several lean equivalence ratios to investigate the behaviour of NO_x under different conditions. The response of the hydrogen counterflow flamelet is further compared to that of a methane flame to highlight structural differences between cases with and without differential and preferential diffusion. A correlation is eventually proposed from the outcomes of these analyses, to predict the decay of the integral NO emissions with strain at different equivalence ratios. The physical behaviour of the simplified flames investigated in this study is the first step to shed light on potential features of novel hydrogen combustor systems, where NO_x emissions are controlled by stabilising the flame against intensive strain.

This chapter is organised as follows. The governing equations used for the 1D and 2D cases are introduced in Section 3.2, followed by an overview of the numerical setups in Section 3.3. Emission results for hydrogen in atmospheric lean premixed conditions are then discussed in Section 3.4. First, a comparative analysis of emission trends with strain between 1D and 2D cases is performed (Section 3.4.1), after which NO_x formation pathways (Section 3.4.2) and radicals distribution in the flame (Section 3.4.3) are analysed. The emission behaviour under different conditions of fuel, pressure and equivalence ratio is discussed in Sections 3.4.4, 3.4.5 and 3.4.6, respectively. The proposed correlation along with its derivation is presented in Section 3.5. Finally, conclusions are provided in Section 3.6.

3.2. PROBLEM DEFINITION

3.2.1. 2D GOVERNING EQUATIONS AND NUMERICAL MODELLING

Both one-dimensional and two-dimensional simulations of planar reactants-to-products counterflow flames are performed. This configuration is chosen following the discussion in Section 2.6. For the two-dimensional simulations, the reactingFoam transient compressible solver in OpenFOAM [123] is employed. The reacting Navier Stokes equations [30] are solved for mass, momentum, absolute enthalpy and N species with detailed chemistry. The equation for the mass fraction Y_k of a generic species k is

$$\frac{\partial(\rho Y_k)}{\partial t} + \frac{\partial(\rho u_i Y_k)}{\partial x_i} = -\frac{\partial(\rho V_{k,i} Y_k)}{\partial x_i} + W_k \dot{w}_k, \quad (3.1)$$

where subscripts i denotes direction i , W_k is the molar mass of the specie k , ρ is the mixture density, $V_{k,i}$ is the diffusion velocity vector, and \dot{w}_k is the molar rate of production of species k . Radiation, body forces, and viscous dissipation effects are neglected. The Dufour effect on the heat flux is also neglected for simplicity.

The ideal gas law and the caloric equation of state are used as thermodynamic model, where the species heat capacities are obtained using the JANAF polynomials. Given the lean conditions investigated in the present work, the mixture viscosity is computed with Sutherland's law with the properties of air for simplicity. The mixture conductivity is found from the viscosity with the modified Eucken correlation [124]. A mixture-averaged diffusion model [30] is used to model the diffusion velocity and account for the low Lewis number of the hydrogen fuel as follows:

$$V_{k,i} = -\frac{D_k^M}{X_k} \frac{\partial X_k}{\partial x_i} \approx -\frac{D_k^M}{Y_k} \frac{\partial Y_k}{\partial x_i} \quad (3.2a)$$

$$D_k^M = \frac{1 - Y_k}{\sum_{l,k \neq l}^N X_l / D_{kl}} \quad (3.2b)$$

The binary diffusion coefficients D_{kl} for the species involved in the reactions are found with the Chapman-Enskog correlation [125, 126]. To avoid the system over-determination, the mass fraction of the most abundant species (N_2) is found as $Y_N = 1 - \sum_{k=1}^{N-1} Y_k$ instead of solving its transport equation.

Detailed kinetic data of reactions from GRI-3.0 mechanism [127] are used to obtain consumption and production rate of species. Generally taken as a reference scheme for methane [128], a recent study by Cazerres [129] considered GRI-3.0 as the starting detailed scheme for the generation of reduced mechanisms for the combustion of hydrogen and methane-hydrogen blends. His analysis showed that optimised reductions of GRI-3.0 provide accurate predictions of the burning parameters of these fuels under a broad range of regimes, ultimately concluding that hydrogen combustion chemistry is contained in methane-air combustion schemes. In light of this conclusion, in order to reduce the CPU time, the GRI-3.0 mechanism has been reduced in this study removing all the carbon species and the related reactions. Furthermore, while previous studies highlighted the limitations of the scheme in the prompt NO_x prediction [130, 131], in this study pure hydrogen is considered as fuel and thus no carbon species enabling the

formation across this pathway are present. In order to further speed up the simulations, the TDACChemistryModel in OpenFOAM is also adopted, consisting of the combination of the *in situ* adaptive tabulation (ISAT) algorithm with the dynamic adaptive chemistry (DAC) reduction scheme [132].

3.2.2. 1D GOVERNING EQUATIONS AND NUMERICAL MODELLING

One-dimensional simulations are run with CHEM1D [53], which is a widely-validated code for one-dimensional flame simulations [38]. In one dimension and for a planar reactants-to-products counterflow flame, the set of conservation equations solved in CHEM1D is expressed as follows [133]:

$$\frac{\partial \rho}{\partial t} + \frac{\partial(\rho u_x)}{\partial x} = -\rho K \quad (3.3a)$$

$$\frac{\partial(\rho Y_k)}{\partial t} + \frac{\partial(\rho u_x Y_k)}{\partial x} = -\frac{\partial(\rho V_{x,k} Y_k)}{\partial x} + W_k \dot{w}_k - \rho K Y_k \quad (3.3b)$$

$$\frac{\partial \rho K}{\partial t} + \rho u_x \frac{\partial K}{\partial x} = \frac{\partial}{\partial x} \left(\mu \frac{\partial K}{\partial x} \right) + \rho_p a^2 - \rho K^2 \quad (3.3c)$$

$$\frac{\partial \rho h}{\partial t} + \frac{\partial \rho u_x h}{\partial x} = \frac{\partial q}{\partial x} - \rho K h \quad (3.3d)$$

where the velocity u_x across the longitudinal axis x of the flamelet, the density of the products mixture ρ_p , the applied strain rate a , the local stretch rate K , the specific absolute enthalpy h , and the specific heat flux q have been introduced. Note that the unsteady term in the equations is reported for completeness, but the equations are resolved for steady-state conditions. The system is again closed with the caloric equation of state and the ideal gas law, where in the latter a low Mach-number approximation is introduced. Dirichlet boundary conditions for Y_k and h are imposed at both the reactants and products, where the enthalpy is assigned according to temperature and heat capacity at constant pressure of reactants and products streams, while for K a combination of Dirichlet and Neumann boundary conditions is imposed as follows:

$$\frac{\partial K}{\partial x}(x \rightarrow -\infty) = 0, K(x \rightarrow \infty) = a \quad (3.4)$$

The applied strain rate a is a setup parameter and is defined as the velocity gradient at the products boundary:

$$a = - \left(\frac{du_x}{dx} \right)_p \quad (3.5)$$

The influence of the y -component (flame-tangential) of the flow on the transport of scalars is taken into account with the introduction of the local stretch rate [133]:

$$K(x) = \frac{\partial u_y}{\partial y} \quad (3.6)$$

As a consequence of the continuity equation, the relation between the two parameters above reads $K_{x \rightarrow \infty} = a$. The GRI3.0 is used as chemical mechanism, along with

a mixture-averaged diffusion model (Eq. (3.2)). Empirical laws are used for viscosity and conductivity in CHEM1D, and the binary diffusion coefficients are computed using molecular potentials and are tabulated as a function of temperature in polynomial form. The reader can find further details in [134].

3.3. COMPUTATIONAL SETUP

The combustion of hydrogen is evaluated at atmospheric conditions and at 5 bar. Temperature and species boundary conditions at the reactants and products boundary are prescribed as follows for both 1D and 2D cases. An equivalence ratio of $\phi = 0.7$ is imposed for both streams. The reactants temperature is $T_r = 300$ K, while the products temperature is set to the adiabatic flame temperature of an unstrained hydrogen flamelet with the same equivalence ratio computed with CHEM1D, $T_p = 2021$ K. Mass fractions at the products boundary are imposed from complete combustion. A summary of the temperature and species boundary conditions for both 1D and 2D simulations are reported in Table 3.1.

Table 3.1: Temperature and species boundary conditions for 1D and 2D simulations, for a hydrogen flame at $p = 1$ atm and $\phi = 0.7$.

Quantity	Left boundary (reactants)	Right boundary (products)
T [K]	300	2021
Y_{H_2} [-]	0.02	0
Y_{O_2} [-]	0.228	0.068
$Y_{\text{H}_2\text{O}}$ [-]	0	0.18
Y_{N_2} [-]	0.752	0.752

3.3.1. 1D SETUP

For the one-dimensional simulations, a relatively wide computational domain of $L_{1\text{D}} = 20$ cm is chosen, where L is the length in the streamwise direction. CHEM1D uses an adaptive mesh algorithm, thus ensuring a sufficiently accurate mesh refinement in the flame region at both atmospheric and increased pressure settings. The adaptive grid accounts for 200 points in total. An exponential differential scheme is used for the spatial discretization, and a second-order time integration of the differential equations is performed by the stationary solver. The time step is adjusted automatically by the numerical tool to achieve convergence, and ranges between 10^{-6} s and 10^{-8} s. The only input parameter for the velocity field is represented by the applied strain rate a , defined in Equation (3.5). According to the applied strain rate definition, the higher is a , the higher will be the boundary velocity and the stretch rate experienced by the flame. Also, the velocity field is solved such that the stagnation plane is always found at the center of the domain, i.e. fulfilling the $u(x=0) = 0$ condition. Hence, the boundary velocities are determined by the solver for each strain rate depending on the chosen domain extension at both sides, where the domain extension is irrelevant to the flamelet calculation, provided that the flame is stabilised within the domain and sufficiently far from the boundaries. A broad range of applied strain rates is investigated for 1D simulations, from 100 s^{-1} up to 20000 s^{-1} .

Although these levels of strain are significantly above the extinction strain rate found for methane-air flames (about 2000 s^{-1} at stoichiometric conditions [135]), only near the high side of the above range the hydrogen flames start to exhibit signs of extinctions. The one-dimensional flames are relatively quick to compute, with computational time ranging from few minutes to few hours depending on the applied strain rate.

3.3.2. 2D SETUP

Two-dimensional laminar simulations are performed to enhance the physical understanding of the 1D results, and ultimately to verify the NO_x emission behaviour with strain observed in the 1D simulations. For this reason, only two representative, relatively-high applied strain rates configurations are investigated in the 2D case, $a = 2000 \text{ s}^{-1}$ and $a = 5000 \text{ s}^{-1}$. Although experimental data at such strain levels is not available in the literature for validation purposes, these two-dimensional simulations are essential to extract further information on the behaviour observed for the one-dimensional cases, and allow to identify possible multi-directional effects that could not be observed in the flamelets. An implicit second-order Euler-backward discretization scheme for time marching is used for the 2D simulations, along with a second-order central scheme for the convective term of all resolved quantities. Since OpenFOAM is a finite volume solver and does not offer high-order polynomial schemes, the simulation performed are categorised here as laminar quasi-DNS. For a reacting flow test case, Zirwes *et al.* [136] showed that a flame-resolved quasi-DNS solution with a cubic discretization scheme compares to experimental data within a 1 % error. Their study also showed that quasi-DNS simulations of canonical flows with second order central schemes well match the solutions from higher-order finite differences DNS codes, with an error of 5-10 %. This range of error is acceptable for the purpose of the present 2D analysis of validating the NO_x emissions trends observed in 1D. A variable time step is used ensuring a maximum Courant number of 0.5 for all domain. The simulations are run for a physical time of $t = 0.5 \text{ s}$ for both the applied strain rates investigated, corresponding to more than 100 times the maximum estimated flow-through time inside the domain. A typical computation required 225 and 895 CPU hours respectively for lower and higher strain rate cases.

The higher computational cost of two-dimensional quasi-DNS simulations led to the choice of decreasing the dimension of the domain to $L_{2D} = 2 \text{ cm}$ in both the horizontal and the vertical directions. Nevertheless, this size was sufficient to fully enclose the flame within the domain and ensure a flame position far enough from the boundary for all simulations. The mesh consists of 100 uniform quadrilaterals in the x direction and 40 in the y direction, resulting into a cell spacing of $\Delta x = 0.2 \text{ mm}$ and $\Delta y = 0.5 \text{ mm}$ respectively for the streamwise and flame-tangential directions. The mesh is refined progressively by a factor of 2 for three times in the proximity of the flame. An example for $a = 5000 \text{ s}^{-1}$ is provided in Figure 3.1, and a more comprehensive mesh independence analysis can be found in Appendix A.1. The flame position is determined for every applied strain rate combining preliminary coarse 2D simulations and 1D simulations. The use of a central difference scheme also allows to benefit of additional numerical dissipation that stabilises the solution in the mesh refinement interfaces, where numerical instabilities may arise. Unlike in CHEM1D, where the applied strain rate a was the only input parameter for the velocity field, a uniform velocity at the two inlets is prescribed for the 2D simulations. The

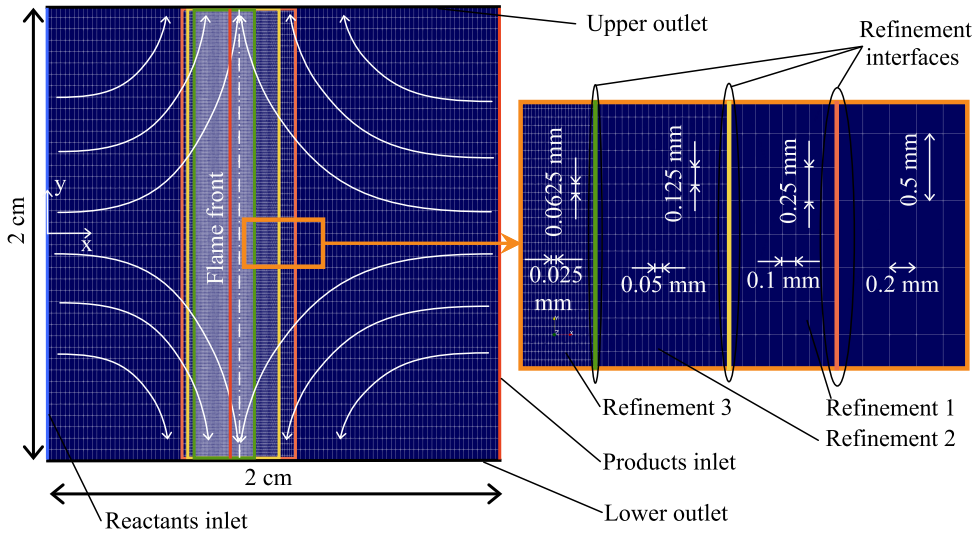


Figure 3.1: Sketch of the two-dimensional setup with mesh refinement for $a = 5000 \text{ s}^{-1}$.

values assigned for the axial velocity at the reactants and products boundaries (indicated respectively by the subscripts 'r' and 'p') are extracted from the 1D simulations, i.e.

$$u_{r,2D} = (u_{1D}(x = -1 \text{ cm}))_{a=\text{const}}, \quad (3.7a)$$

$$u_{p,2D} = (u_{1D}(x = 1 \text{ cm}))_{a=\text{const}}. \quad (3.7b)$$

These values are reported in Table 3.2.

Table 3.2: Inlet velocity boundary conditions assigned at the reactants ($u_{r,2D}$) and products ($u_{p,2D}$) side of two-dimensional simulations for the two values of applied strain rate a .

a [s^{-1}]	$u_{r,2D}$ [m/s]	$u_{p,2D}$ [m/s]
2000	5.31	-21.85
5000	16.84	-53.92

A zero gradient boundary condition is assigned at the upper and lower boundaries. Note that, since the assignment of velocity profiles in the 2D cases does not also imply constant strain rate at the boundary, some discrepancy is expected in the solution along the centerline between 1D and 2D cases. Nevertheless, these differences do not affect the generalities of the analyses to be conducted next.

3.4. RESULTS

3.4.1. NO_x EMISSIONS TRENDS

NO_2 mass fraction peaks were shown to be at least three orders of magnitude smaller than the ones of NO for any of the setups investigated. Therefore, similarly to previous

studies [40], NO emissions will be considered representative of the overall NO_x emissions. The behaviour of Y_{NO} across a hydrogen-air flamelet at an equivalence ratio $\phi = 0.7$, and for different applied strain rates, is shown in Figure 3.2a. It is immediately observable that both the peak and the area under the curves of NO mass fraction decrease significantly as the applied strain is increased, up to a factor of about 5 if one compares the highest ($a = 100\text{s}^{-1}$) and lowest ($a = 10000\text{s}^{-1}$) peaks. It is worth noting that no extinction is observed at the highest strain rates achieved, indicating that pure hydrogen-air flames can sustain very high strain levels, in line with observations in previous studies [36, 37]. Furthermore, as strain increases, the peak value of NO decreases in relative percentage less, e.g. the relative decrease between $a = 5000\text{s}^{-1}$ and $a = 10000\text{s}^{-1}$ is only about 20%. This however does not imply that the overall suppression of NO also reaches a plateau as strain increases, and in fact NO decreases almost linearly (in the logarithmic space) instead, as will be discussed later.

In Figure 3.2b the decrease of the peaks of Y_{NO} in the one-dimensional case, and along the centreline for the two-dimensional simulations, is further highlighted. The differences observed between 1D and 2D results at the same applied strain are the consequence of the different boundary conditions as discussed in Section 3.3.2. As observed in the figure, the suppression of NO peak with strain is confirmed in the 2D case. In order to have an understanding of the overall behaviour of NO in the domain, the density-weighted NO integral is also shown in Figure 3.2c (refer to the left y axis), where the integral is calculated as

$$I_{\text{NO},1\text{D}} = \int_{-L/2}^{L/2} \rho Y_{\text{NO}} dx. \quad (3.8)$$

As observed in the figure, the integral amount of NO decreases almost linearly in the logarithmic space with strain, indicating that strain remains as effective in suppressing NO_x also at very high values. Further curves are shown in Figure 3.2 where two additional chemical mechanisms are used in place of the GRI-3.0 in order to evaluate the effect on the prediction of NO. GRI-2.11 is tested in light of previous studies where it provided generally improved estimations of NO emission [128, 137], along with the recently-published mechanism from Capurso *et al.* [138]. While different, albeit within the same order of magnitude, quantitative values are observed, particularly at higher strain rates for the Capurso *et al.* [138] scheme, the NO decreasing trend is maintained, suggesting that the choice of the mechanism does not affect the generalities of the results presented in this study. Nevertheless, results suggest that the mechanism has to be chosen with care if one aims to obtain quantitative estimations.

One might argue that NO is a slow species which would form downstream of the flame in the hot products region, and this formation in the products side is prevented by the right boundary condition, where $Y_{\text{NO}}(x = L/2) = 0$ is imposed. In fact, in the present configuration Y_{NO} peaks near the stagnation plane to then rapidly drop to fulfill the boundary condition, see Figure 3.2a. On the other hand, the investigation of the 2D simulations, where the NO is free to form in the y direction (tangential to the flame in Figure 2.14b), suggests this not to be the case, i.e. NO is suppressed at high strain by some other means. Hence, the focus is shifted to the understanding of the emission behaviour in the flame-tangential direction of the two-dimensional simulations. One can compute for this purpose the two-dimensional density-weighted NO integral for the 2D setups by

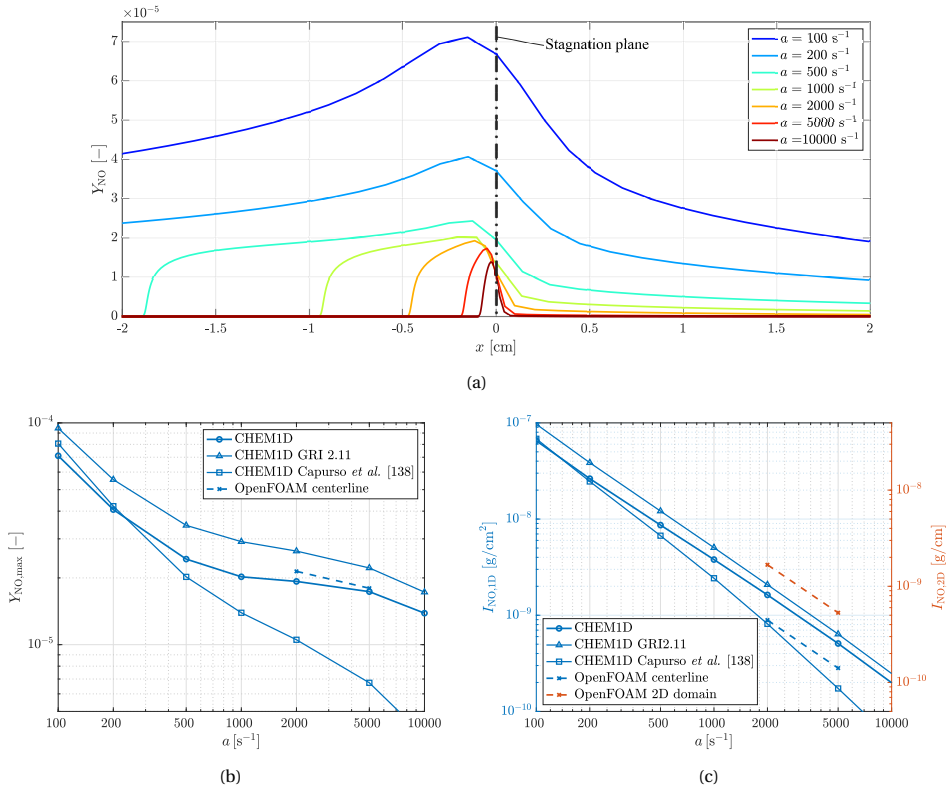


Figure 3.2: (a) NO mass fraction (Y_{NO}) across the longitudinal coordinate x in a one-dimensional hydrogen-air flamelet at equivalence ratio $\phi = 0.7$, for different applied strain rates a . Variation of peak NO mass fraction $Y_{NO,max}$ (b) and density weighted NO integral $I_{NO,1D}$ (c) with strain rate for 1D and 2D simulations of hydrogen-air flames at equivalence ratio $\phi = 0.7$. Wherever the chemical mechanism is not specified in the legend, GRI-3.0 is used.

integrating on the 2D-domain surface as follows:

$$I_{\text{NO},2\text{D}} = \int_A \rho Y_{\text{NO}} dA. \quad (3.9)$$

This integral is also reported in Figure 3.2c (refer to the right y axis). As one can observe, the suppression of NO with strain seems to follow the same linear trend in the logarithmic space as that observed for the 1D simulations. From the analysis of the 2D data it is further observed that

$$I_{\text{NO},2\text{D}} \approx I_{\text{NO},1\text{D}} \cdot L_{2\text{D}}, \quad (3.10)$$

i.e. the 1D integral of NO calculated across the centreline of the 2D solution, multiplied by the vertical dimension, is approximately equal to the 2D integral. These considerations raise confidence on the fact that the suppression of NO_x observed in 1D simulations and in the 2D domain centreline as strain is increased is not compensated by any additional NO formation in the vertical direction. Further evidence on this can be provided by following the NO formation along the same streamline at the two different strain rates investigated for the 2D cases. This is shown in Figure 3.3, where a streamline intersecting the reactants boundary at a vertical position $y = -0.2$ mm is shown. This streamline is chosen such that it crosses the flame, continues in the products stream, and exits the domain without intersecting the stagnation plane. The residence time of a parcel of fluids travelling along this streamline for the case at $a = 5000 \text{ s}^{-1}$ is about $\Delta t = 1.23$ ms. During the same time, a parcel of fluids in the reactants entering the domain for the case at $a = 2000 \text{ s}^{-1}$ at the same vertical position as the $a = 5000 \text{ s}^{-1}$ case, has travelled less distance, as indicated by the pathline shown for this case in Figure 3.3b, and ends up positioned upstream the flame at a relative vertical position $y = -0.53$ mm from the centreline. The integral amount of NO is at this point computed across the flame (streamwise direction) at the section crossing this position, and compared to that evaluated at the exit section for the higher strain (see green lines in Figure 3.3). These values of integral NO are provided in Table 3.3. By investigating this data one can notice that not only the NO integral is

Table 3.3: Density-weighted NO integral values across the sections in green indicated in Figure 3.3, for two different applied strain rates a .

a [s^{-1}]	$y(\Delta y)$ [mm]	$I_{\text{NO}}(y)$ [g/cm^2]
2000	-0.53	$8.39 \cdot 10^{-10}$
5000	-10	$2.82 \cdot 10^{-10}$

lower for the higher strain rates (despite it is computed at a section where it had the same time to form as for the lower strain rate case), but also that the values of integral NO for the two cases are very close to the ones along the centerline reported in the graph in Figure 3.2c. This indicates that there is no additional NO formation in the vertical direction at higher strain rates, and thus the suppression of NO_x at increased strain is not a mere consequence of the decreased residence time. For comparative purposes the flux of NO across the outlet boundary is also shown in Table 3.4 for the two strain rates. This flux is defined as

$$\Phi_{\text{NO}} = \int_{-L/2}^{L/2} \rho u_y Y_{\text{NO}} dx, \quad (3.11)$$

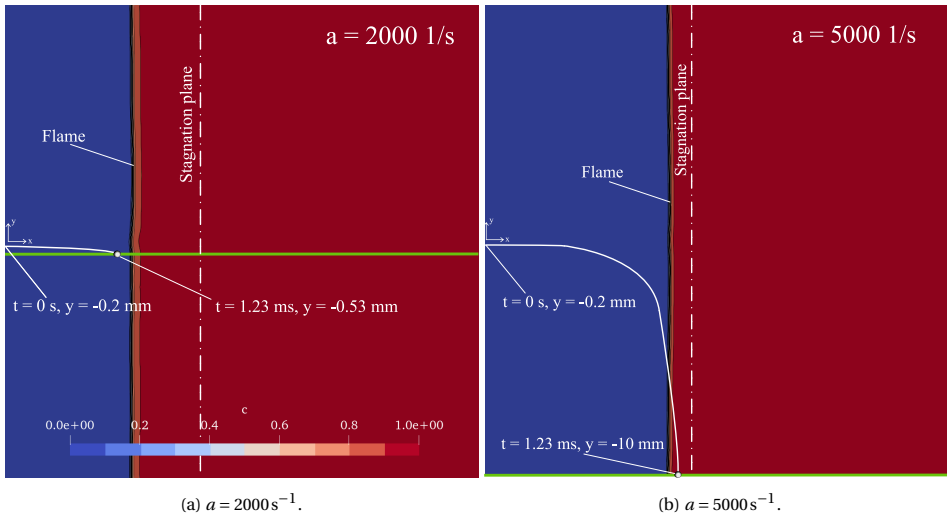


Figure 3.3: Streamlines intersecting the left boundary at vertical coordinate $y = -0.2$ mm for two applied strain rates a are plotted on top of water mass fraction based normalised progress variable contours. Green lines indicate the section along with the integral of NO is computed for the two cases after the same travelling time $t = 1.23$ ms.

While the increased outlet speed for the higher strain rate case (due to the increased inlet

Table 3.4: Flux of NO (per unit width) across the lower outlet surface (refer to Figure 3.1) at two different applied strain rates a .

a [s^{-1}]	y [mm]	$\Phi_{NO}(y)$ [$g/(cm \cdot s)$]
2000	-10	$2.48 \cdot 10^{-4}$
5000	-10	$1.90 \cdot 10^{-4}$

speed) implies also an increase in the total mass flux, a decreased value in the NO flux is still observed for the higher strain rate, which gives further evidence that the decreased residence time at the higher strain rate is not by itself the reason behind the observed suppression of NO_x .

According to the above analyses the observed NO_x suppression with increasing strain is neither a consequence of the specific counterflow configuration and boundary conditions, nor of the decreased resident time of the fluid particles in the domain. The suppression of NO_x must thus be associated to a direct effect of the increased tangential velocity gradients on the hydrogen flame combustion. This will be further investigated in the next section by analysing the NO formation pathways.

3.4.2. NO FORMATION PATHWAYS

The focus is now shifted to the evaluation of the NO formation pathways, with the goal of further understanding the physical reasons behind the observed NO decrease with strain.

As carbon species are not involved in hydrogen combustion, the prompt NO_x formation pathway is not considered, and the only pathways evaluated are thermal NO, NNH-NO, NNH-HNO-NO and N₂O-NO. CHEM1D solutions data are used for the purposes of the present NO formation routes investigations, since the NO emissions behaviour with strain was observed to be the same for the two-dimensional simulations (see Figure 3.2c). Two high applied strain rates setups of $a = 2000 \text{ s}^{-1}$ and $a = 5000 \text{ s}^{-1}$ are analysed. For a sample reaction r involved in a pathway $\nu_A A + \nu_B B \leftrightarrow \nu_C C + \nu_D D$, the forward, $K_{f,r}$, and backward, $K_{r,r}$, reaction coefficients are obtained using the Arrhenius law as [30]:

$$K_{f,r}(T) = A_r T^{\beta_r} e^{\left(\frac{-E_{a,r}}{R_0 T}\right)}, \quad K_{r,r}(T) = \frac{K_{f,r}}{\left(\frac{p_a}{R_0 T}\right)^{\sum_s \nu_s} e^{\left(\frac{\Delta S_r^0}{R_0} - \frac{\Delta H_r^0}{R_0 T}\right)}}, \quad (3.12)$$

where A_r , β_r and $E_{a,r}$ are found in the GRI3.0 mechanism reaction web page [127], and ΔS_r^0 and ΔH_r^0 are respectively the reaction entropy and enthalpy that can be found as a function of temperature with JANAF polynomials. The respective forward and reverse reaction rates are found as

$$\dot{w}_{f,r} = K_{f,r}(x) \cdot [A(x)]^{\nu_A} [B(x)]^{\nu_B}, \quad \dot{w}_{r,r} = K_{r,r}(x) \cdot [C(x)]^{\nu_C} [D(x)]^{\nu_D}. \quad (3.13)$$

where the quantities in square brackets indicate the concentration of the species. Three-body and pressure-dependent reactions have been treated with dedicated formulas [139]. Following the formulation of Ning *et al.* [40], the overall reaction rate (ORR) of the reaction r is obtained by integrating the net reaction rate across the longitudinal (flame-normal) direction:

$$\text{ORR}_r = \int_{-L/2}^{L/2} \dot{w}_r(x) dx. \quad (3.14)$$

Summing the contribution of the ORR for the single reactions along a specific route, a chart diagram indicating the NO formation pathways at $a = 2000 \text{ s}^{-1}$ and $a = 5000 \text{ s}^{-1}$ is obtained, which is shown in Figure 3.4a for the two strain rates. While all the reaction rates involved in the pathways are observed to decrease in magnitude at higher strain, one can notice that this decrease is stronger for the thermal NO pathway. For instance, the highest reduction of NO between the two different strain rates of 45% is observed for the rate of decomposition of N₂ into N. Since the formation of N is what enables the formation of NO across the thermal pathway, this observation suggests that this pathway is the main responsible for the overall NO_x suppression with strain, as highlighted in Section 3.4.1. To further investigate on this, the ORR of the reactions directly producing NO in each pathway is also summed, and the resulting values are presented in the bar chart in Figure 3.4b. The graph shows that the main NO production pathways for a lean hydrogen strained flame are both the thermal and the NNH. Moreover, the histogram confirms that the strongest decrease of NO production at high strain rates is associated to the thermal pathway. One could generally expect this to just be the outcome of a decreased flame temperature with increasing strain rate [140]. Nevertheless, for the flames investigated in the present work, increasing super-adiabatic temperatures are observed as strain is increased (see Appendix A.2), which is in line with previous studies for strained syngas [21] and spherical pure-hydrogen flames [44]. Hence, the reason behind

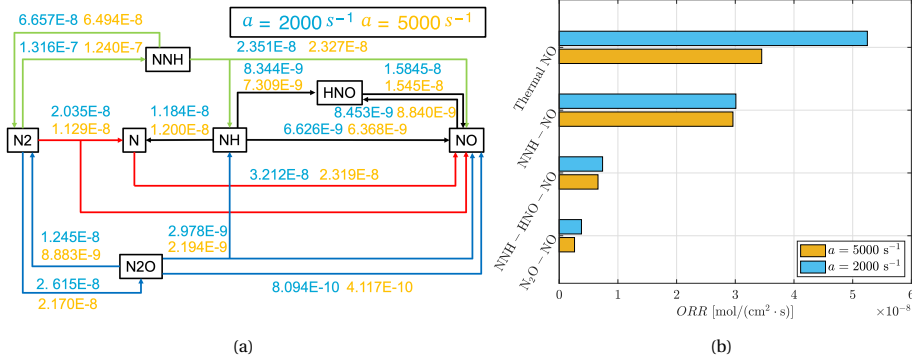


Figure 3.4: (a) Chart diagram showing the overall reaction rates (in mol/(cm²·s)) over each specific reaction route along the NO formation pathways for a hydrogen-air flamelet, and for strain levels $a = 2000 \text{ s}^{-1}$ (light blue values) and $a = 5000 \text{ s}^{-1}$ (yellow values). Thermal NO pathway is highlighted in red, NNH-NO pathway in green, NNH-NO-HNO intermediate pathway in black, and N₂O-NO pathway in blue. (b) Contribution of each NO formation pathway to the total NO formation for strain levels $a = 2000 \text{ s}^{-1}$ (light blue) and $a = 5000 \text{ s}^{-1}$ (yellow).

the observed NO suppression is not imputable to a change in the flame temperature despite the dominant mechanism being the thermal one. The behaviour of radicals is thus investigated next to shed light on the reasons of the observed NO_x suppression.

3.4.3. ANALYSIS OF RADICALS

The investigation in Section 3.4.2 suggests that a more extensive analysis should be performed on the concentration of the radicals involved in the pathway reactions in order to further shed light on the physical explanation behind the phenomenon of NO_x suppression with strain in lean premixed hydrogen flames. Figures 3.5a-3.5d show the distribution of the main radicals participating in the hydrogen-air combustion process as a function of the flame-centered, flame-thickness-normalised longitudinal coordinate, for a range of applied strain rates between $a = 100 \text{ s}^{-1}$ and $a = 10000 \text{ s}^{-1}$. The flame position at different strain rates is defined as $x_0 = x(c = 0.5)$, where the progress variable c is based on $Y_{\text{H}_2\text{O}}$ and is normalised to vary between 0 and 1. The thermal thickness δ is taken as flame thickness (see Eq. (2.5)), and its values at the different strain rates are reported in Table 3.5.

Table 3.5: Thermal thickness δ in a hydrogen-air flamelet at equivalence ratio $\phi = 0.7$ and for different strain rates a .

a [s ⁻¹]	100	200	500	1000	2000	5000	10000
δ [mm]	0.330	0.330	0.329	0.328	0.324	0.312	0.294

For all the radicals except atomic oxygen, the peak of their respective mass fractions is observed to increase with strain. As suggested in previous studies [39, 138], particularly considering the H radical, this phenomenon is the responsible for the increase of the

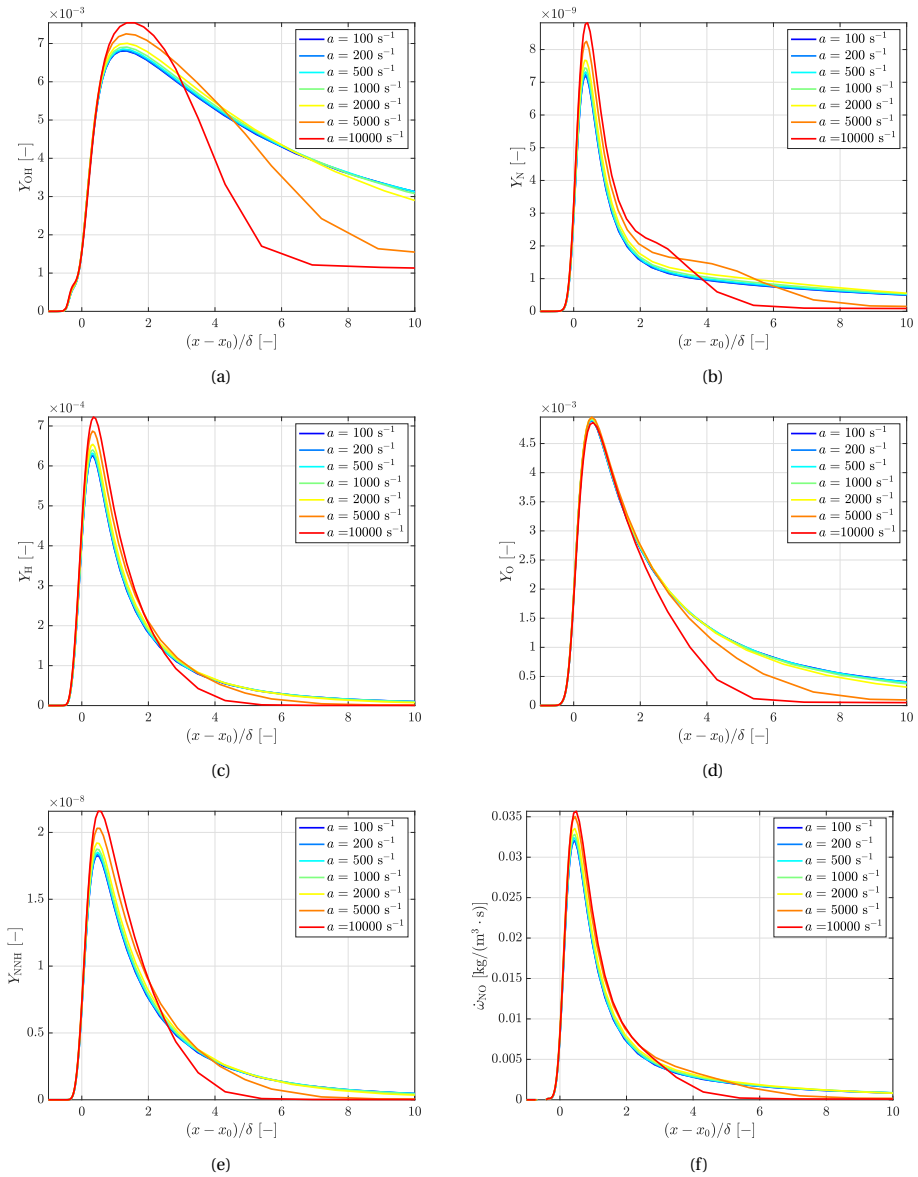


Figure 3.5: Distribution of OH (a), N (b), H (c), O (d), and NNH (e) radicals mass fraction Y_k across a hydrogen-air flamelet at equivalence ratio $\phi = 0.7$ and for different strain rates a . The NO source term ω_{NO} is also shown (f).

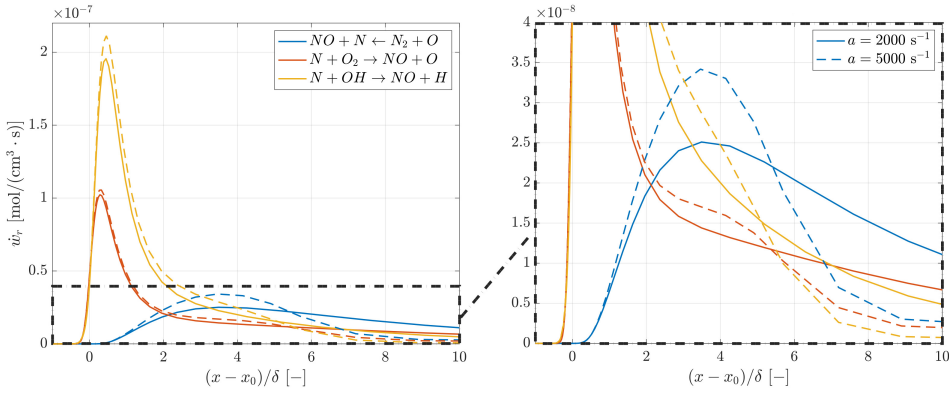


Figure 3.6: Molar rate of thermal NO_x reactions \dot{w}_r across a hydrogen-air flamelet at equivalence ratio $\phi = 0.7$, for two applied strain rates of $a = 2000 \text{ s}^{-1}$ (solid line) and $a = 5000 \text{ s}^{-1}$ (dashed line). A zoom in the region indicated by the dashed rectangular area is shown on the right for clarity.

peak heat release rate and reaction rate with strain. This behaviour is also reported in the Appendix A.3 for clarity using results of the present study and the reaction rate of progress variable, $\dot{\omega}_c$. It is interesting to observe from Figure 3.5 that all the main radicals are consumed immediately downstream of the flame at higher strain rates, which results in lower values of mass fractions downstream of the flame as compared to the cases at lower strain. This is likely due to the stronger convection that characterises the highly-strained regimes, that ‘pushes’ the radicals towards the flame, limiting their diffusion downstream in the hot products.

In Figure 3.5f, the distribution in space of the mass source term of NO, $\dot{\omega}_{\text{NO}}$, at different strain rates is further shown. This quantity is observed to vary with strain, consistently with the variation of radicals involved in NO formation highlighted in the previous paragraph. In fact, while a local increase of NO formation with strain is observed in the proximity of the flame, i.e. in at the location where the peaks of the radicals are found (in particular of H and N), an opposite trend is found more downstream in the hot products region. Since an increased H concentration is known to promote the oxidation of N_2 to NNH [138, 141], the corresponding local increase with strain of $\dot{\omega}_{\text{NO}}$ can be attributed to an enhanced NO formation through the NNH pathway. This consideration is supported by Figure 3.5e, where the peaks of NNH mass fraction is shown to increase accordingly with increasing strain rate. In contrast, the lower availability of radicals at higher strain rates downstream of the flame is probably the main responsible factor determining the decrease of thermal NO formation with strain, observed in Section 3.4.2. In order to better understand this behaviour, the rate of the three reactions involved in the thermal NO route are plotted as a function of space across the flamelet for two different strain rates ($a=2000 \text{ s}^{-1}$ and $a=5000 \text{ s}^{-1}$) in Figure 3.6. Once again, higher peaks of reaction rates are observed at higher strain rates. In particular, the rate increase of the first reaction (blue lines in Figure 3.6) seems to be contributing to the local increase of N concentration observed in Figure 3.5b. On the other hand, the rate of the three reactions drops at higher strain at more downstream positions. Considering again the first of the reactions indicated in the

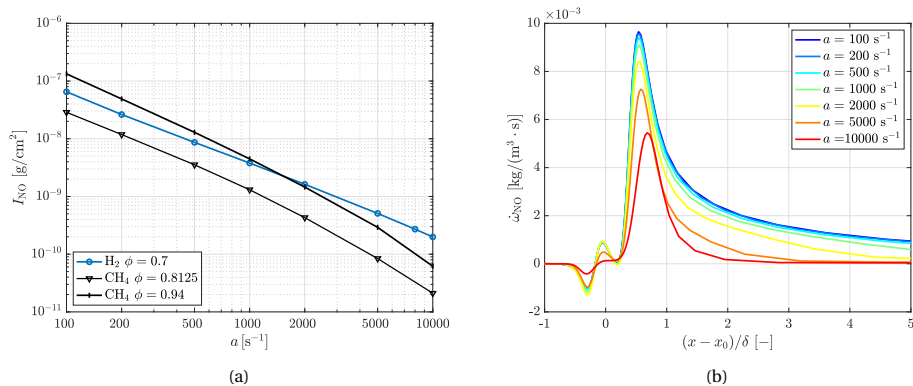


Figure 3.7: (a) Variation of density weighted NO integral I_{NO} with strain a for a methane-air flamelets at two equivalence ratios and hydrogen-air flamelet at $\phi = 0.7$. (b) NO source term ω_{NO} across the flamelet for different strain rates for methane at $\phi = 0.8125$ (same adiabatic flame temperature as hydrogen at $\phi = 0.7$).

figure, less N radicals are formed where $(x - x_0)/\delta > 5$, probably because of a decreased availability of reaction-enabling radicals of atomic oxygen, which is observable in Figure 3.5d. As a consequence, the rates of the second and the third reactions indicated in the figure are limited in this region as well by the lower availability of N radicals. Furthermore, the rate of the third reaction indicated in the figure is also limited by the locally lower OH availability at higher strain highlighted in Figure 3.5a. It can thus be concluded that the amount of O and OH radicals has a direct influence on the rate of NO formation via the thermal route, which is consistent with past experimental studies [141, 142]. Overall, the downstream decrease of the rate of the reactions involved in the NO formation via thermal route at higher strain is the responsible of the observed local decrease of the total NO source term, shown in Figure 3.5f. In light of the overall decrease of NO emissions with strain highlighted in Section 3.4.1, it can be further concluded that the discussed decrease of NO formation rate at more downstream positions overcompensates for the local increase observed closer to the flame, and is itself the responsible for the overall lower emissions of NO at high strain.

3.4.4. COMPARISON WITH METHANE

In the following section, methane-air flamelets are analysed to investigate how specific characteristics of hydrogen's combustion, including both its high diffusivity and increased reactivity caused by chain-branching consumption, contribute to the observed reduction in NO_x emissions. In Figure 3.7a, the density weighted NO integral as a function of strain is plotted for two different methane-air flamelets at two different equivalence ratios. All other parameters are the same as those used for the hydrogen-air case discussed in the previous sections.

The first equivalence ratio, $\phi = 0.8125$, is chosen such that the same adiabatic flame temperature of hydrogen at $\phi = 0.7$ is achieved in the products, $T_{ad} = 2021 \text{ K}$ (see Table 3.1). As for the hydrogen flamelet, increasing the strain is observed to suppress NO, as also suggested in a previous pioneering work [96]. In the methane case, however, strain is

meanwhile weakening the flame. Indeed, the maximum flame temperature decreases for the methane-air flame as the strain increases, and therefore one can expect, unlike for the hydrogen case, that NO decreases because of the temperature. The further condition of $\phi = 0.94$ is evaluated for the methane-air flamelet. This value is chosen in this case in order to obtain the same power in output achieved by a premixed hydrogen flame at $\phi = 0.7$ in a freely propagating configuration, where the power in output P is obtained as the inlet fuel mass flow rate \dot{m}_f multiplied by the fuel lower heating value H_L , $P = \dot{m}_f H_L$. In this case emissions of NO for the hydrogen flame are even quantitatively lower than those for the methane flame for strain rates $a < 1000 \text{ s}^{-1}$. For higher strain rates the curves cross each other and the methane flame exhibits the lower emissions instead. As discussed earlier, however, the steeper decrease in the methane-air case is due to the flame becoming inefficient and the consequent decrease of temperature. One can further observe that, for both the equivalence ratios investigated on the methane-air flamelet, NO_x tends to be suppressed more rapidly at high strain as compared to the hydrogen-air flamelet. This indicates that the methane flame is indeed approaching extinction as the strain rate increases.

Further insights on the reasons behind the more steep decrease of NO in the methane flamelets is provided in Figure 3.7b, where the source term of NO across the flamelet at $\phi = 0.8125$ are plotted for different strain rates. Negative values of $\dot{\omega}_{\text{NO}}$ observed around $(x - x_0)/\delta = 0$ are due to the local formation of NO_2 at the relatively low temperatures at this location. Unlike what observed for hydrogen in Section 3.4.3, both the peak of NO source term decreases with strain. Moreover, $\dot{\omega}_{\text{NO}}$ also decreases with strain in the further downstream region of the domain, similarly to the hydrogen case. These trends are triggered by the distribution of the main radicals, which follows a similarly decreasing trend, as reported in Appendix A.4. It follows that in the case of methane-air combustion the behaviour of the radicals in the tail and downstream of the flame also contribute to the suppression of NO_x but, unlike the hydrogen case, this comes along with a decrease of radicals also in the flame, indicating that the flame is becoming weaker. This explains the steeper decrease with strain of integral NO observed in Figure 3.7 for the methane flamelets, since both flame and postflame regions are contributing to the decrease of NO in this case. In the case of hydrogen instead, the combination of its higher reactivity and high diffusivity triggers the strengthening of the flame with strain, which causes a local increase in the main radicals concentration peaks. In turn, this phenomenon contributes to NO formation, and thus limits the overall NO suppression as strain increases, but at the same time allows the flame to sustain much higher strain levels.

3.4.5. EFFECT OF PRESSURE

The effect of increasing pressure on the hydrogen-air flamelet at $\phi = 0.7$ is investigated in this section. The density-weighted NO integral values are shown in Figure 3.8a for the atmospheric condition investigated earlier and the further condition at $p = 5$ bar. The decrease of NO with strain is observed to be similar for the two pressure conditions, and an almost linear variation is observed in the logarithmic space also for the higher pressure case. Similarly to what observed in Section 3.4.3, for $p = 5$ bar the peaks of the main radicals mass fraction are observed to increase with strain, and radicals are also suppressed more at downstream positions as strain increases (not shown). Another

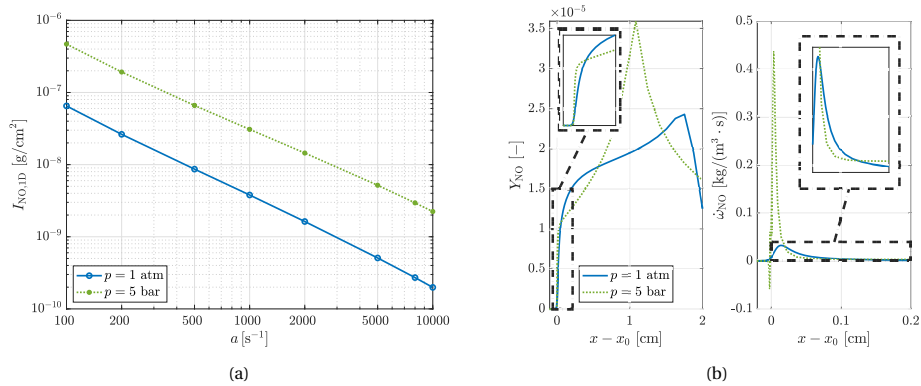


Figure 3.8: (a) Variation of density weighted NO integral I_{NO} with strain a for a hydrogen-air flamelet at $\phi = 0.7$ at $p = 1$ atm and $p = 5$ bar. (b) Distribution of NO mass fraction Y_{NO} and NO source term $\dot{\omega}_{NO}$ across the flamelets for the two pressure conditions for $a = 500$ s⁻¹. The regions indicated by the dashed rectangle are zoomed out for clarity.

observation is that the integral of NO mass fraction increases of about one order of magnitude when pressure is increased to 5 bar. The increase of NO_x emissions with pressure has been already observed for hydrogen enriched flames, e.g. De Persis *et al.* [143], and can be partly attributed to a slight increase of the adiabatic flame temperature. Further insight on the local emissions of NO can be obtained by looking at the distribution of NO mass fraction and its source term at the two pressure conditions in Figure 3.8b. The two flamelets in the figure are compared for a representative strain rate of $a = 500$ s⁻¹. Note that the x axis is not normalised by the flame thickness in this case since the flame thickness varies with the pressure. A higher peak of source term triggers a steeper local increase in the NO mass fraction at higher pressure as one would expect. However, the flame thickness also decreases by a factor of about five for the higher pressure case, which explains why the source term in the latter case approaches zero more quickly as compared to the atmospheric case. This in turn implies a lower local mass fraction of NO in the higher pressure case downstream of the flame. Nevertheless, moving further downstream, the two curves of the source term for the two pressure conditions intersect again (the reaction rate is again higher for the higher pressure case), which causes a steeper increase of NO mass fraction in the products. This behaviour explains the higher integral values of NO observed in Figure 3.8a. Note that the peak of Y_{NO} is located earlier in space in Figure 3.8b (left) for the higher pressure case because the consumption speed is decreased by a factor of almost two, and so the flame stabilises closer to the regions of lower flow speed. Still, the integral value of NO is higher because of its stronger source term on the products side.

The above analysis indicates that the behaviour with strain of the hydrogen flame remains qualitatively the same when pressure increases. Additional analyses for further higher pressure were not conducted here due to the uncertainty deriving from the chemical kinetic mechanism to be used.

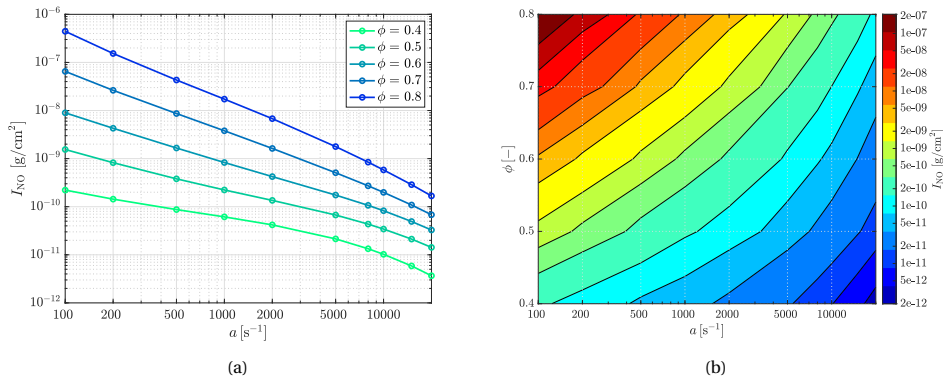


Figure 3.9: (a) Variation of density weighted NO integral I_{NO} with strain a for hydrogen-air flame at different equivalence ratios ϕ . (b) Contour plot of density weighted NO integral I_{NO} as a function of strain a and equivalence ratio ϕ .

3.4.6. EFFECT OF EQUIVALENCE RATIO

The influence of equivalence ratio on the behaviour of NO_x emission with strain is discussed in this section for the hydrogen-air flame. The density-weighted NO integral is plotted as a function of strain for a range of lean equivalence ratios varying from $\phi = 0.4$ to $\phi = 0.8$ in Figure 3.9a. In order to assess whether the flame is approaching extinction at the lowest equivalence ratios, the range of strain rates has been extended up to $a = 20000 \text{ s}^{-1}$. As expected, lower NO values are observed for leaner conditions at the same strain rate due to the lower adiabatic flame temperature. The suppression of NO with strain is confirmed at all the equivalence ratios investigated, but the gradient of this decrease becomes less steep in leaner conditions. This is probably due to the fact that the production of NO via the thermal route, which was observed to be the major contributor for NO suppression with strain, is already lower due to the lower temperatures of the leaner burning regime, and thus strain has a more limited effect in further reducing the NO formation. It is interesting to note that the gradient of decrease of NO with strain is now observed to change significantly for the lower equivalence ratios at the highest strain values. As discussed for the analysis on the methane flame, this indicates that flame extinction conditions are being approached, and it is remarkable that this situation occurs in the hydrogen flame only at very lean regimes ($\phi = 0.4$) and $a > 10000 \text{ s}^{-1}$.

Further insight is provided in the contour plot of Figure 3.9b, showing the combined effect of equivalence ratio and strain on the integral NO emissions. The isolines in this figure in particular indicate couples of values (ϕ, a) for which the integral NO across the flamelet is the same. It can be observed that increasing strain in richer conditions allows to reach outcomes of NO emissions that are comparable to the ones in lean regimes at low strain levels. Considering also that flame extinction is not approached for almost any of the regimes shown in the contour plot, these results indicate that burning hydrogen in potentially unstable, ultra-lean conditions to reduce NO_x emissions may not be necessary as the suppression of NO_x can be compensated by imposing intensive strain rates on the flame.

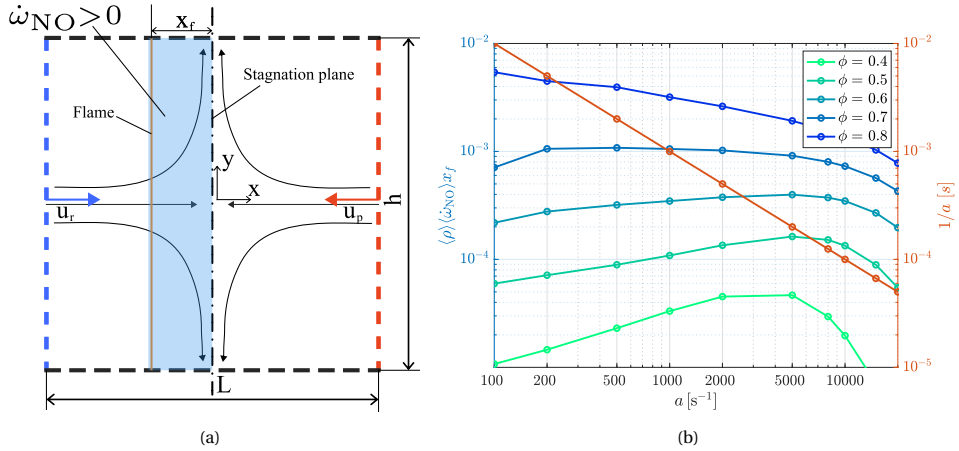


Figure 3.10: (a) Control volume around the counterflow premixed reactants-to-products flame configuration used for the analytical derivation of the correlation for I_{NO} . (b) Variation with strain a of the numerator of Equation (3.25) for the hydrogen-air premixed flame at different equivalence ratios ϕ , as compared to the function $1/a$.

3.5. CORRELATION FOR THE INTEGRAL NO EMISSIONS

A correlation is proposed in this section to estimate the amount of integral NO produced across a flamelet at varying strain rate and equivalence ratio. This correlation is found combining analytical and numerical results, and its derivation is shown next.

3.5.1. ANALYTICAL DERIVATION

The integral formulation of continuity and NO mass fraction conservation equations in a steady flow reads:

$$\int_A \rho(\mathbf{u} \cdot \mathbf{n}) dA = 0; \quad (3.15a)$$

$$\int_A \rho(\mathbf{u} \cdot \mathbf{n}) Y_{NO} dA = \int_V \dot{\omega}_{NO} dV. \quad (3.15b)$$

where \mathbf{u} is the velocity vector, \mathbf{n} is the unity vector normal to a control volume encompassing the flame and pointing outwards, A is the area of the domain boundary and V is the volume of the integration domain. The source term of NO is here considered to be a mass source term, with dimension $[\text{kg}/(\text{m}^3 \cdot \text{s})]$. Let's consider a two-dimensional reactants-to-products domain of arbitrary vertical and horizontal dimensions h and L (see Figure 3.10a). Equation (3.15b) can be re-arranged as follows:

$$2 \int_{-L/2}^{L/2} [\rho u_y Y_{NO}]_{y=\pm h/2} dx = \{\dot{\omega}_{NO}\} x_f h. \quad (3.16)$$

where x_f is the distance between the flame and the stagnation plane, which without loss of generalities for the present derivation is also assumed to be the region of formation of NO, and $\{\dot{\omega}_{NO}\}$ is the mean value of the NO reaction rate over the same region. The flux of

NO across the inlet surfaces is zero consistently to the analysis done in Section 3.4. The source term of NO has non-zero values only within the flame and in the region between the flame and the stagnation plane as mentioned earlier. The continuity equation can also be re-arranged as follows:

$$-(\rho_r u_{x,r} + \rho_p u_{x,p})h + 2\langle \rho u_y \rangle_{\pm h/2} L = 0, \quad (3.17)$$

where $\langle \rho u_y \rangle_{\pm h/2}$ refers to the line average along the streamwise direction at $y = \pm h/2$, and the subscripts r and p respectively refer to reactants and products inlet boundaries. It is further assumed that:

$$\int_{-L/2}^{L/2} [\rho u_y Y_{\text{NO}}]_{y=\pm h/2} dx \approx \langle u_y \rangle \int_{-L/2}^{L/2} [\rho Y_{\text{NO}}]_{y=\pm h/2} dx, \quad (3.18a)$$

$$\langle \rho u_y \rangle \approx \langle \rho \rangle \langle u_y \rangle, \quad (3.18b)$$

where all the averages indicated by the $\langle \cdot \rangle$ operator are evaluated along the streamwise direction at $y = \pm h/2$, and the subscript $\pm h/2$ is omitted from now on for clarity of notation. The above approximations were verified *a posteriori* using the two-dimensional simulations data and observed to remain accurate for the range of conditions explored in this study. By substituting Equation (3.18b) into Equation (3.17) one obtains:

$$\langle u_y \rangle = \frac{\rho_r u_{x,r} + \rho_p u_{x,p}}{2\langle \rho \rangle} \frac{h}{L}. \quad (3.19)$$

By substituting equations (3.18a) and (3.19) into Equation (3.16), the following expression is thus found:

$$\frac{\rho_r u_{x,r} + \rho_p u_{x,p}}{\langle \rho \rangle L} \int_{-L/2}^{L/2} [\rho Y_{\text{NO}}]_{y=\pm h/2} dx = \{\dot{\omega}_{\text{NO}}\} x_f. \quad (3.20)$$

where the vertical dimension h cancels out, indicating that this expression is independent of the vertical direction. This finding is consistent with the discussion in Section 3.4.1, and particularly Equation (3.10), where the 1D density weighted integral of NO was found to be substantially independent on the vertical direction in the two-dimensional simulations performed. The integral on the left-hand-side of Equation (3.20) is by definition the density weighted NO integral I_{NO} evaluated across one-dimensional flamelets in this study, whose prediction is the objective of the present derivation. From Equation (3.20), I_{NO} can thus be expressed as:

$$I_{\text{NO}} = \frac{\langle \rho \rangle \{\dot{\omega}_{\text{NO}}\} x_f L}{\rho_r u_{x,r} + \rho_p u_{x,p}}. \quad (3.21)$$

As discussed in Section 3.3.1, in the investigated counterflow flamelet setup the stagnation plane is always located at $x = 0$. The applied strain rate is thus

$$a = -\left(\frac{du_x}{dx}\right)_p = \frac{u_p}{L/2}. \quad (3.22)$$

Furthermore, Darabiha *et al.* [93] have shown that for the type of flows in the present configuration the following relation between reactants and products inlet velocities can be derived:

$$\rho_p u_{x,p}^2 = \rho_r u_{x,r}^2. \quad (3.23)$$

Combining equations (3.22) and (3.23), $u_{x,p}$ and $u_{x,r}$ can be expressed as a function of the applied strain rate:

$$u_{x,p} = \frac{a}{L/2}; \quad (3.24a)$$

$$u_{x,r} = u_{x,p} \sqrt{\frac{\rho_p}{\rho_r}} = \frac{a}{L/2} \sqrt{\frac{\rho_p}{\rho_r}}. \quad (3.24b)$$

By substituting these relations into Equation (3.21), one obtains:

$$I_{\text{NO}} = \frac{\langle \rho \rangle \{ \dot{\omega}_{\text{NO}} \} x_f L}{\frac{1}{2} a L \left(\rho_r \sqrt{\frac{\rho_p}{\rho_r}} + \rho_p \right)} = \frac{2 \langle \rho \rangle \{ \dot{\omega}_{\text{NO}} \} x_f}{a \left(\sqrt{\rho_p \rho_r} + \rho_p \right)}. \quad (3.25)$$

This relation shows the dependence of I_{NO} on $1/a$ and is consistent with the findings obtained from the simulations presented in Section 3.4. On the other hand, the numerator in Equation (3.25) also is influenced by strain through x_f , because different consumption speeds of the flame at different strain rates imply different flame stabilisation points. The average source term of NO can also be expected to vary with strain, which one might deduce from Figure 3.5f, and similar considerations hold for the averaged density. In order to understand this dependence and the relative contribution on I_{NO} of numerator and denominator in Equation (3.25) as strain increases, the latter two are calculated using the simulations data for the hydrogen-air counterflow flamelets at different equivalence ratios, and shown in Figure 3.10b. It can be seen that $1/a$ is a steeper function of strain than $\langle \rho \rangle \{ \dot{\omega}_{\text{NO}} \} x_f$. The numerator of Equation (3.25) has a stronger dependence on strain only for the leanest condition of $\phi = 0.4$, and therefore at intermediate lean equivalence ratios and moderate-high strains one could conclude that I_{NO} has an almost linear dependence on $1/a$. Nevertheless, in order to quantify the effect of the numerator, particularly for the more extreme conditions of equivalence ratio and strain, a semi-empirical approach is employed, which is described next.

3.5.2. SEMI-EMPIRICAL ESTIMATION OF I_{NO}

In the one-dimensional reactants-to-products counterflow hydrogen flamelets investigated in this study, the combined influence of equivalence ratio and strain on the density weighted NO integral are observed to closely follow the following correlation function

$$I_{\text{NO}}(a, \phi) = \int_{-L/2}^{L/2} \rho Y_{\text{NO}} dx = k(\phi) \cdot a^{l(\phi)}. \quad (3.26)$$

The choice to test a power law as a correlation function followed from the observation in Figure 3.9a that the log plot of I_{NO} versus strain is an almost straight line at different equivalence ratios. The coefficients k and l are empirically found to be an exponential and a linear function of ϕ , respectively:

$$k(\phi) = k_1 \cdot e^{k_2 \phi} \quad (3.27a)$$

$$l(\phi) = l_1 \phi + l_2 \quad (3.27b)$$

The coefficients k_1 , k_2 , l_1 and l_2 are reported in Table 3.6. For the range of equivalence

Table 3.6: Fitting values for the coefficients in the correlation of Equation (3.26).

Coefficient	value	dimension
k_1	$5.413 \cdot 10^{-14}$	$\text{g}/(\text{s} \cdot \text{cm}^2)$
k_2	28.22	-
l_1	-2.036	-
l_2	0.1769	-

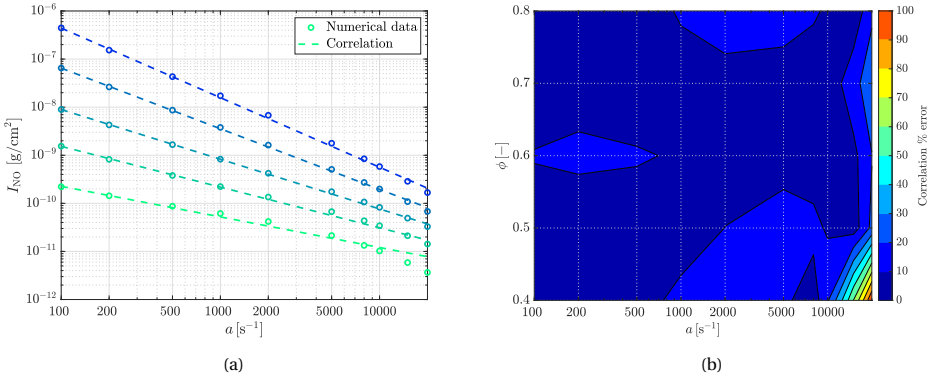


Figure 3.11: (a) Comparison of integral NO I_{NO} with strain obtained from numerical simulations of premixed hydrogen-air flamelets in counterflow at different equivalence ratios ϕ , and the correlation expression of Equation (3.26). (b) Contour plot of the correlation error with respect to numerical data.

ratios investigated, the coefficient l is always negative, enabling I_{NO} to be a decreasing function of strain. Furthermore, the value of l is found to be about $l \approx -1$, implying that the NO integral function behaves almost as a decreasing hyperbolic function of strain:

$$I_{\text{NO}}(a) \sim \frac{1}{a}. \quad (3.28)$$

which is consistent with the analytical findings in Section 3.5.1.

In Figure 3.11a the values for I_{NO} obtained from the correlation of Equation (3.26) using the best fit values of Table 3.6 are compared to those computed from the hydrogen-air premixed counterflow flamelets. The correlation error is also reported in the contour plot in Figure 3.11b. Higher errors are observed only for very high strain and very lean conditions, where extinction might start to be approached and thus the I_{NO} curve with strain starts to depart from a quasi-linear behaviour in the logarithmic space. For all other conditions where the regime is far from extinction, the error is below 10%. It is worth noting that a similar correlation for I_{NO} could be used for methane flames k and l . However, in this case the relation would hold for only a limited region of the domain shown in Figure 3.11b, since the methane flamelet approaches extinction much more easily than the hydrogen flame. The strong reactivity of the hydrogen flame allows instead for the correlation presented here to hold for a wide range of strains and equivalence ratios. The correlation in Equation (3.26) can thus be used to quickly assess in preliminary

analyses how the integral NO emissions vary in lean premixed hydrogen flames with strain rate and equivalence ratio, and eventually aid the design of novel combustion systems where NO_x is suppressed by the combined effect of the latter.

3.6. SUMMARY

Detailed chemistry analyses have been conducted on pure hydrogen-air lean premixed and strained flamelets in a counterflow reactants-to-products configuration. The study investigated a broad range of strain rates, including very high levels rarely considered before in the literature. The main findings are summarised below.

- NO_x is significantly suppressed as the strain rate increases, despite the hydrogen flame becoming more reactive. This is shown for the first time for pure hydrogen fuel and lean flames.
- The NO_x suppression is not a consequence of any numerical setup preconditioning or resident time effect.
- The most substantial decrease of NO_x with strain is observed across the thermal pathway due to the local redistribution of radicals, even though the temperature across the flame does not decrease with strain.
- The impact of high strain effects has also been studied at higher pressure and methane fuel, showing generally similar trends in NO_x suppression, although with different rates of decrease due to an occasionally different radical redistribution mechanism.
- The analysis of multiple lean equivalence ratios further indicates that in place of ultra-lean hydrogen flames, richer mixtures under high strain can result in the same NO_x suppression.

A correlation for the prediction of the density-weighted integral of NO as a function of strain and equivalence ratio has been derived for premixed counterflow hydrogen flames, where the integral value of NO is found to have an almost linear dependence with the reciprocal of the applied strain rate. This correlation can be used for preliminary analyses oriented to the design of low-NO_x, novel combustion systems that can employ a combination of lean flames and high strain. As a final note, one might object that flame emissions at highly turbulent, practical conditions, may result in different behaviours than those discovered and analysed here in simplified laminar flames. Nevertheless, in a submitted and co-authored follow up work, a similar NO_x suppression mechanism by strain is observed through numerical simulations within a more practical turbulent laboratory burner, where the flame is stabilised over a bluff body and mean strain rate is adjusted by increasing the inlet mass flow rate [144].

4

EFFECT OF STRAIN ON LEAN PREMIXED HYDROGEN FLAME STRUCTURE

*Our knowledge can only be finite,
while our ignorance must necessarily be infinite.*

Karl Popper

4.1. INTRODUCTION

In previous chapters, it is established that strain plays a crucial role in hydrogen combustion. Notably, Chapter 3 demonstrated that NO_x emissions decrease with increasing strain in lean premixed hydrogen flames. Building upon this understanding of emissions behaviour, the attention is now turned to the investigation of the flame response to strain in terms of species diffusive transport and global flame structure. Understanding this response is essential for uncovering the potential of strained regimes on flame stability, and for developing reliable computational models that accurately represent the properties of strained flames. In this chapter, laminar one-dimensional flames are examined, which should provide valuable insights into the more complex two-dimensional and three-dimensional behaviours discussed in Chapter 5.

As discussed in Chapters 1 and 2, preferential and differential diffusion effects, along with thermodiffusive instabilities, play crucial roles in the stability of hydrogen lean premixed flames. While the interaction between curvature and differential and preferential diffusion has been extensively studied, the specific effects of flame tangential strain rate—the other contributor to stretch—on hydrogen flame transport properties and structure remain less explored. Chapters 1 and 2 further introduced that hydrogen flames exhibit unique behaviours under strained conditions, such as increased consumption speed and peak heat release rate, as well as delayed lean blow-off. However, the effects of these characteristics of hydrogen flames under strained conditions on cross-flame species diffusive transport phenomena and global flame structure remain unknown.

The purpose of this chapter is to shed light on how strain affects the structure and the transport properties of lean premixed hydrogen flames, with a particular focus on preferential diffusion effects. Results show that, contrary to previous studies where strain is generally identified as a contributor to thermodiffusive instabilities and preferential diffusion effects, the strain rate actually mitigates the importance of cross-flame diffusion. This ultimately limits the impact of preferential diffusion on the flame's global burning properties.

This chapter is organised as follows. The numerical setup and validation are presented in Section 4.2, including details on the chemical mechanisms and transport models employed. In Section 4.3, the flame structure under various strain rates is analysed, in terms of radical peak trends (Sec. 4.3.1), mixture fraction distribution (Sec. 4.3.2), mixture fraction transport (Sec. 4.3.3), with particular attention to preferential diffusion effects and their impact on global flame properties (Sec. 4.3.4). Section 4.3.5 discusses these findings in the context of existing literature, comparing the results with previous studies on strained hydrogen flames. Finally, Section 4.4 summarises the key insights and their implications.

4.2. COMPUTATIONAL SETUP AND NUMERICAL MODELLING

Detailed chemistry one-dimensional analyses are performed for pure-hydrogen, lean premixed, strained laminar flamelets in a reactants-to-products counterflow configuration—the same configuration adopted in Chapter 3 and illustrated in Figure 2.14b. As discussed in Section 2.6, this configuration was selected for its suitability for this type of analysis involving high strain rates. Simulations are run with the one-dimensional solver

CHEM1D [53] for a range of applied strain rates from $a = 100 \text{ s}^{-1}$ to $a = 10000 \text{ s}^{-1}$. The reader is invited to read Appendix B.5 to compare these strain regimes to practical turbulent flows. Detailed kinetic data of reactions from Conaire mechanism [146] are used, along with a multicomponent diffusion model [147] including Soret and Dufour effects and with transport properties computed using the EGLIB library [148]. The reactants temperature is fixed to 300 K so that the most favourable conditions for the observation of preferential diffusion effects are established [73]. For the investigated setup, the set of conservation equations solved and the boundary conditions can be found in Section 3.2.2, Equations (3.3) and (3.4), respectively. Lean conditions are established at an equivalence ratio of 0.5 to maximize preferential diffusion effects while not approaching extinctions at high strain rate. Flamelet results with and without preferential diffusion are compared to be able to assess preferential diffusion effects on the flame structure. In the latter case preferential diffusion is thus deliberately suppressed, i.e. $Le = 1$ is assumed for all species. For clarity of treatment, if one tries to isolate preferential and differential diffusion effects (e.g. see [149]), both the effects would be artificially suppressed in the $Le = 1$ case, while both are retained in the multicomponent case. Since artificially isolating the two different effects is challenging, the analysis and the conclusions of the present work are mostly focused on preferential diffusion effects (occurring due to hydrogen's higher molecular diffusivity with respect to other species), which are the ones triggering a local change of mixture fraction across the flame (see Sec. 4.3.2), and their interplay with strain. Instead, the term 'differential' will be used only in the context of diffusive fluxes to highlight a different flux between fuel and oxidizer.

This study focuses on the strain rate contribution to stretch. In fact, in the investigated stationary and planar 1D configuration, the curvature term in Equation (2.10) is equal to zero and the effect of flame straining can be isolated. There are two related parameters that can identify strain appearing in the governing flamelet equations (Eq. (3.3)). The first is represented by the applied strain rate a , which is a flamelet setup parameter and is defined as the velocity gradient at the products boundary according to Equation (3.5). The local stretch rate K in this type of flamelet, also referred to as local strain rate in this chapter given the planar setup, is instead defined by Equation (3.6) and is introduced in the governing equations to consider the influence of the vertical component of the flow on the transported quantities.

In order to monitor the local leaning and enrichment effect of the flame due to the combination of hydrogen preferential diffusion and strain effects, it is convenient to define the mixture fraction according to Regele *et al.* [71]. Rearranged for the investigated lean premixed counterflow configuration, the definition reads

$$z_{\text{reg}} = \frac{\nu Y_{\text{H}_2} - Y_{\text{O}_2} + Y_{\text{O}_2, \text{air}}}{\nu + Y_{\text{O}_2, \text{air}}} \quad (4.1)$$

where $Y_{\text{O}_2, \text{air}}$ is the mass fraction of oxidizer in air and ν is defined as the mass stoichiometric ratio

$$\nu = \frac{\nu_{\text{O}_2} W_{\text{O}_2}}{\nu_{\text{H}_2} W_{\text{H}_2}}, \quad (4.2)$$

with the stoichiometric coefficient of the species k denoted by ν_k . Note that this definition is simplified version of that provided in Equation (2.7) in Section 2.2, which is convenient

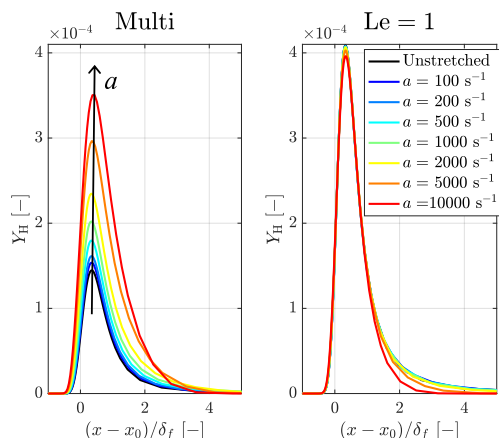


Figure 4.1: Distribution of H radicals mass fraction at different strain rates obtained with multicomponent diffusion model (left) and $Le = 1$ model (right).

for the transport term analysis performed in Section 4.3.3. More details on the two different definitions of mixture fraction are provided in Appendix B.1.

4.3. RESULTS AND DISCUSSION

4.3.1. RADICAL PEAKS TRENDS

The distribution of H radical mass fraction as a function of the flame-centered, flame-thickness-normalised longitudinal flamelet coordinate at different strain rates computed with the multicomponent diffusion model and $Le = 1$ are compared in Figure 4.1. The flame position at different strain rates is defined as $x_0 = x(c = 0.5)$, where the progress variable c is based on the water mass fraction, $c = \frac{Y_{H_2O}}{Y_{H_2O,max}}$, and the thermal thickness δ_f defined in Equation (2.5) is taken as flame thickness. For clarity of treatment, the flame region is indicated where $0.5 < c < 0.9$, and the preheat and post flame zone is referred where $c < 0.5$ and $c > 0.9$, respectively. The peak of radical concentration is observed to increase with strain rate in the case with preferential diffusion. The same trend is observed for other radicals, such as OH, O and N (not shown), and similar evidence was found in Chapter 3 at slightly richer conditions (see Sec. 3.4.3, Figure 3.5). This behaviour is likely to drive the increase of the peak reaction rate and heat release rate with strain [39], and with positive curvature [138, 150] in hydrogen flames.

In contrast, when no preferential diffusion effects are taken into account, the flame appears substantially insensitive to strain, as peaks of Y_H remain about constant. Moreover, the peak values in the unitary Lewis number case are higher than the ones of the case with preferential diffusion. This is consistent with the peaks of reaction rate, as can be observed in Figure 4.2, and with the laminar flame speed found for unstretched flamelets in lean conditions (see Sec. 2.2 in Chapter 2), which are also higher in the unitary Lewis number case. The comparison between Figs. 4.1 and 4.2 thus suggests that the high diffusivity of atomic hydrogen is somewhat limiting its burning potential. Despite this, hydrogen's

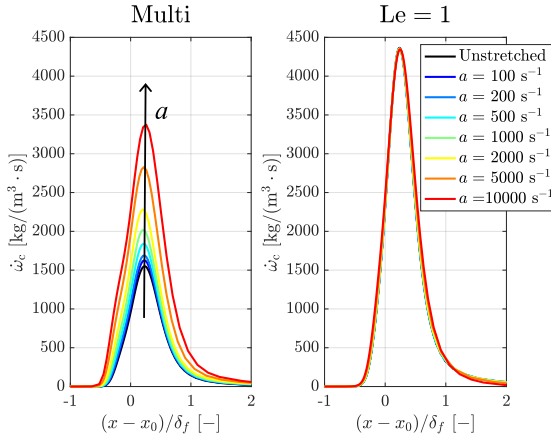


Figure 4.2: Distribution of progress variable reaction rate at different strain rates obtained with multicomponent diffusion model (left) and $Le = 1$ model (right).

peak reaction rate and heat release rate are still significantly stronger than the ones found in hydrocarbon fuels at similar regimes. This is because the set of chemical reactions that are governing hydrogen combustion is such that more free H radicals are generated than consumed in a reaction step, i.e. the consumption of hydrogen is chain-branching, as introduced in Chapter 2 (see Sec. 2.2). The further consumption of these radicals is contributing to the total heat release. This is not the case in hydrocarbon fuels, whose consumption is instead chain-breaking.

4.3.2. MIXTURE FRACTION DISTRIBUTION

The distribution of the mixture fraction as defined in Equation (4.1) across the flamelet, computed with the multicomponent and $Le = 1$ diffusion models, is shown in Figure 4.3. Without preferential diffusion, the mixture fraction is expected to be constant across the flame, and the flamelet results for the $Le = 1$ case confirm this expectation for any strain level. Only minor local oscillations are visible due to the employed simplified definition of the mixture fraction, and this inaccuracy is addressed in Appendix B.1. As suggested in previous studies of unstrained premixed hydrogen flames [71] and introduced in Chapter 2 (see Sec. 2.2), a local dip (i.e. a local decrease of mixture fraction or equivalently a leaner mixture) can be instead expected when preferential diffusion is present, as the different species molecular diffusivities trigger a local imbalance between fuel and oxidizer. A similar dip to the one observed for unstretched flames can also be recognised for strained flames, as shown in Figure 4.3. However, this leaner region is observed to be followed by an overshoot of mixture fraction, and this overshoot becomes stronger as the strain rate imposed to the flame increases indicating that a local enrichment is experienced by the flame. Similar results were also observed in other works under strained [46] and positively curved conditions [138]. Given that this overshoot is not present in freely propagating unstretched flame configurations, the only possible responsible for this outcome is strain. The local enrichment further leads to super-equilibrium values of the combustion

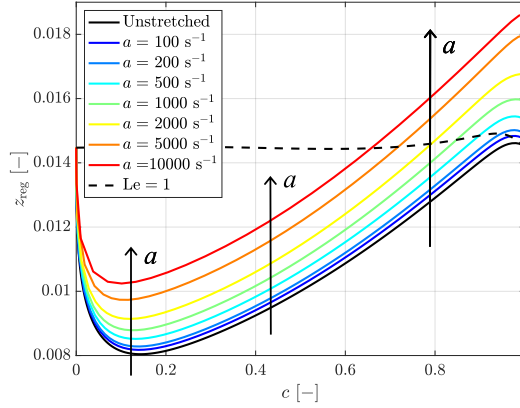


Figure 4.3: Distribution of mixture fraction across the flamelet at different strain rates obtained with multicomponent (solid lines) and $Le = 1$ (dashed lines) diffusion models.

products [46].

It can also be observed from Figure 4.3 that the local decrease of mixture fraction is more limited when strain rate is increased. This suggests that strain somewhat limits the local leaning of the flame that occurs because of preferential diffusion, thus smearing its effect on lean premixed hydrogen flames. Overall, this results in a general enrichment of the mixture within the flame front at higher strain rates, see Figure 4.3. Note that in absence of preferential diffusion, there is not such influence of strain, as z_{Teg} is constant across the flame at any strain rate when the species have equal molecular diffusivities. In the next subsection, the reasons behind the mixture fraction response to strain observed are further investigated quantitatively.

4.3.3. MIXTURE FRACTION TRANSPORT

The transport equation of mixture fraction for a one-dimensional steady counterflow flame is

$$\frac{\partial}{\partial x} (\rho u_x z) = -\frac{\partial J_{x,z}}{\partial x} - \rho K z, \quad (4.3)$$

where $J_{x,z}$ is the diffusive flux of the mixture fraction across the flamelet direction [71]. For simplicity, the analysis is carried on flamelet results obtained with a constant non-unity Lewis number diffusion model (Le_{const}) and neglecting thermal diffusion effects. Following the methodology of Vance et al. [151], the constant Lewis numbers of each species are obtained by fitting the results of the simulation with the multicomponent diffusion model at the same strain rate. Neglecting pressure gradients, the diffusive flux $J_{x,z}$ in Equation (4.3) can be expressed as [71]:

$$J_{x,z} = -\frac{\lambda}{c_p} \frac{\partial z}{\partial x} - \frac{\lambda}{c_p} \left(\frac{1}{Le_{H_2}} - 1 \right) (1-z) \frac{\partial Y_{H_2}}{\partial x} - \frac{\lambda}{c_p} Y_{H_2} \left(\frac{1}{Le_{H_2}} - 1 \right) (1-z) \frac{1}{W} \frac{\partial W}{\partial x}, \quad (4.4)$$

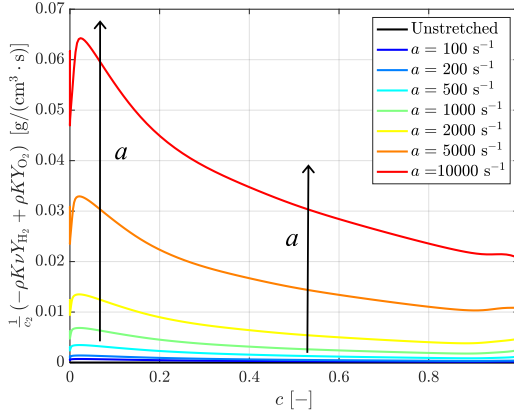


Figure 4.4: Differential strain term across the flamelet as defined in Equation (4.6) for different applied strain rates.

where W is the mixture molar mass, and λ is the thermal conductivity. Note that the choice of the diffusion model does not alter the trends with strain rate of the flame physical properties observed in previous subsections, and will not thus affect the general conclusions (see also Appendix B.2). The strain rate term in Equation (4.3) can be decomposed as follows

$$-\rho K z = -\frac{\rho K}{c_2} (v Y_{\text{H}_2} - Y_{\text{O}_2} + c_1), \quad (4.5)$$

where $c_1 = Y_{\text{O}_2, \text{air}}$ and $c_2 = v + c_1$ are both positive constants. Hence, considering the first two terms on the right-hand-side of Equation (4.5), a ‘differential’ strain term can be defined as

$$\frac{1}{c_2} (-\rho K v Y_{\text{H}_2} + \rho K Y_{\text{O}_2}). \quad (4.6)$$

The differential strain term determines whether the fuel and oxidizer are being transported due to strain in the second dimension of the counterflow following their stoichiometric proportions (for which the differential strain would vanish), or if instead there is an imbalance. An imbalance is eventually what would trigger a local leaning and enrichment of the mixture fraction with changing strain rate. This term is plotted in Figure 4.4 across the flamelet at different strain rates. It is visible that the differential strain rate is positive across the progress variable for any flamelet investigated, and with reference to Equation (4.6) this implies that

$$-\rho K v Y_{\text{H}_2} + \rho K Y_{\text{O}_2} > 0, \quad (4.7)$$

and thus that

$$|\rho K v Y_{\text{H}_2}| < |\rho K Y_{\text{O}_2}|. \quad (4.8)$$

Equation (4.8) shows that more O_2 is transported in the second dimension by strain than H_2 with respect to the mass stoichiometric proportions for hydrogen combustion. This proves that the conditions for an overall mixture enrichment are established because of

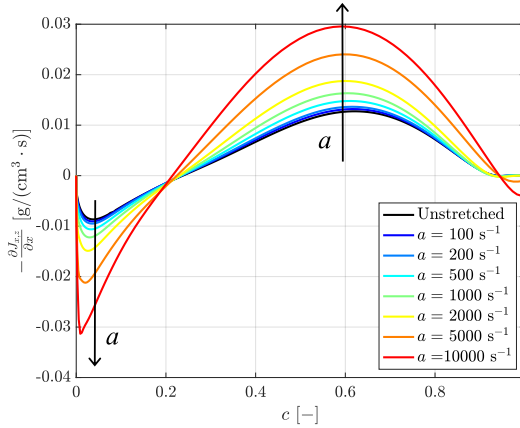


Figure 4.5: Mixture fraction diffusion term across the flamelet as defined at the first term at the right hand side in Equation (4.3) and by Equation (4.4) for different applied strain rates.

the application of strain rate. Furthermore, the figure shows that this effect is amplified when the applied strain rate is increased, because the differential strain term is increasing with applied strain rate, and so is the difference between oxygen and hydrogen being transported in the second dimension (with respect to the stoichiometric case). This is also consistent with the mixture enrichment with strain rate observed in Figure 4.3.

In order to further understand the way the mixture fraction is locally affected by combined strain and preferential diffusion effects, the mixture fraction diffusion term is also shown for different strain rates in Figure 4.5, where the diffusive flux is computed according to Equation (4.4). In the figure, two different regions can be identified. For $c > 0.2$, the diffusion term is positive, which means that the mixture fraction has to increase at this location. Figure 4.5 shows that the higher is the strain rate, the stronger in module the diffusion term becomes at the same location, which is due to the fact that species gradients are steepened by strain. Along with the local enrichment enabled by the strain rate, this is probably the reason why strain triggers super-equilibrium values of z_{reg} at the products side (see Fig. 4.3), leading to super-equilibrium products.

In the second region identified in Figure 4.5, where $c < 0.2$, the diffusion term is negative at all strain rates, which corresponds to a decreasing mixture fraction, as z_{reg} is transported out of this region by diffusion. Furthermore, as the applied strain rate increases, the diffusion term becomes increasingly negative at the same location, which is again due to species gradients being steepened. One could expect that this increase in magnitude should by itself trigger a further local leaning of the burning mixture. However, this is not the case as observed in the plot in Figure 4.3, which instead shows that the mixture is enriched by strain rate all across the flamelet. The reason behind this is that the strain rate term, which triggers an enrichment of the mixture all across the flamelet, overcompensates for the expected leaning of the mixture. This argument is supported by Figure 4.4, which shows that the peak of differential strain rate is positioned in the proximity of where the negative peak of diffusion term is found across the flamelet. To further confirm this argument, the budgets of each term in Equation (4.3) at $c = 0.1$ are

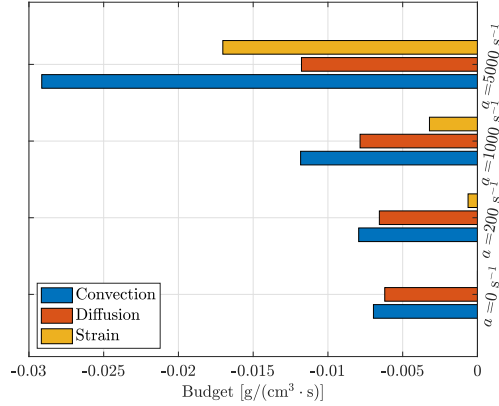


Figure 4.6: Bar chart showing the budget terms of z_{reg} according to Equation (4.3) at $c = 0.1$ and at four different sample applied strain rates.

reported in Figure 4.6 for increasing applied strain rates. In this figure the sum of the diffusion and strain terms is equal to the convection term (which is the term at the left hand side in Equation (4.3)), as one would expect. The figure shows that when the applied strain rate is increased, the relative contribution of the strain rate term in compensating for the convection term also increases with respect to that of the diffusion term. For instance, at $a = 200 \text{ s}^{-1}$, the strain term contributes only marginally (9%) to balance the convection, with the diffusion term being the main contributor (91%). In contrast, at $a = 5000 \text{ s}^{-1}$, the situation is inverted with the strain term balancing the 59% of the convection term and the diffusion term contributing for 41%. To summarise, even though the strain rate is increased, two effects occur in this region where $c < 0.2$. On the one hand, the diffusion term's negative peak intensifies, potentially causing the flame to lean locally. On the other hand, the strain term, previously discussed to cause local flame enrichment, increasingly counteracts this effect. Ultimately, the contribution of the strain term overcompensates the effect of the diffusion term and thus triggers an overall local enrichment of the flame. Note that an enrichment is observed at any strain value (see Fig. 4.3 where $c < 0.2$), albeit less significant at lower strain values, but the relative contribution of the strain term is still lower than that of diffusion for $a < 5000 \text{ s}^{-1}$ according to Figure 4.6, which seems to contradict the previous discussion. Nevertheless, an increase of the strain term is expected to induce more substantial changes in the local mixture fraction compared to a similar increase of the diffusion term. This is because the former is a linear function of z_{reg} , while the latter only acts on its second derivative, thus having a less significant effect on z_{reg} itself. Note also that the gradients shown in Figure 4.6 were computed *a posteriori* and some accuracy error might be expected, although these do not affect the generalities of the discussion above.

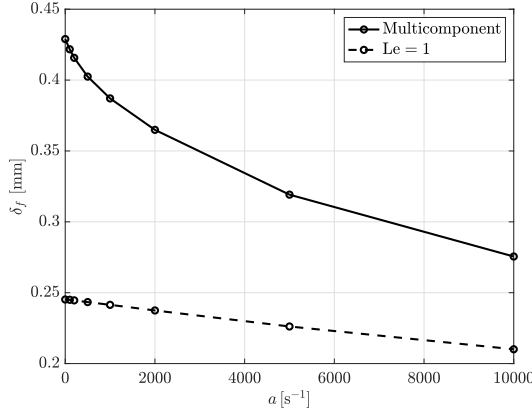


Figure 4.7: Evolution of the thermal flame thickness with strain.

4.3.4. FLAME PHYSICAL PROPERTIES

In order to draw general conclusions on the mutual effect of strain and preferential diffusion on the global performance of hydrogen flames, the effect of the investigated mixture fraction variation on the flame physical properties is discussed in this subsection. The flame thermal thickness as a function of strain for the two cases with and without preferential diffusion is reported in Figure 4.7. As expected, the multicomponent unstretched flame is thicker by a factor $Le_{H_2}^{-1/2}$ [152] with respect to the unstretched $Le = 1$ and this is due to preferential diffusion triggering species redistribution over a wider region at low progress variables, thus relaxing the species gradients across the flamelet. The graph further shows that for both the diffusion models strain reduces the flame thickness due to the stronger flow convection, but that this reduction is steeper in the flamelets computed with the multicomponent model. This could be due to the fact that the strain term in the transport equations is becoming more and more dominant with respect to the diffusion term, as also discussed for the mixture fraction in Section 4.3.3. This means that each fluid element is preferentially being transported in the second dimension (tangentially to the flame) from the strain term rather than being transported in the longitudinal dimension (normal to the flame) by the diffusion term. Hence, preferential diffusion effects, which were smoothing the gradients in unstretched conditions, are now inherently being overcome by strain effects when the applied strain rate is increased. This ultimately explains the steeper flame thickness decrease with strain as compared to the $Le = 1$ case observed in Figure 4.7.

The consumption speed is also reported in Figure 4.8, defined as

$$S_c = -\frac{1}{\rho_r Y_{H_2,r}} \int_{-\infty}^{\infty} \dot{\omega}_{H_2} dx \quad (4.9)$$

. First of all, it can be seen as expected that the flame speed is lower in the multicomponent case compared to the $Le = 1$ case in unstretched conditions because of the mixture being locally leaned by preferential diffusion. Furthermore, the well-known negative hydrogen

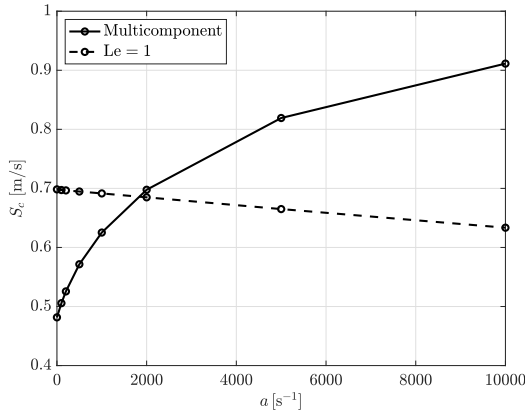


Figure 4.8: Evolution of the consumption speed with strain.

fuel Markstein length can be immediately observed for the case with preferential diffusion turned on by noticing the increasing consumption speed with strain. Of course, this trend is triggered by the mixture being locally enriched with increasing applied strain rate as discussed in Section 4.3.2. It is worth noting that despite the overall burning mixture enrichment observed as strain increases, the peak reaction rate does not achieve the (high) values one would obtain when preferential diffusion effects are suppressed, even at relatively high strain levels (see Fig. 4.2). Nevertheless, due to the combination of thicker flame (see Fig. 4.7) and enhanced burning rate, the consumption speed for $a > 2000 \text{ s}^{-1}$ reaches values above those one would obtain without taking preferential diffusion into account. This means that the flame performance in terms of consumption speed, initially limited by preferential diffusion effects in unstretched conditions due to the flame burning locally leaner, are re-enhanced and even improved by the overall burning mixture enrichment triggered by increasing strain rate.

4.3.5. DISCUSSION

The analyses in Section 4.3.1 and 4.3.4 have indicated that in presence of preferential diffusion effects, certain flame physical and global properties such as peak reaction rate, peak radical concentration, flame thickness, and consumption speed are suppressed, limiting the burning performance in a lean hydrogen flame. However, when strain rate is applied, these properties are restored towards the levels that one would observe if preferential diffusion effects were artificially turned off. This suggests that mean strain rate can play a role in mitigating the limitations imposed by preferential diffusion effects on the flame behaviour. This observation on the physical properties is quantitatively confirmed by inspecting the budget terms of the mixture fraction, which showed that with increasing applied strain rate an element of fluid is more and more preferentially being transported in the second dimension rather than diffusing across the flamelet longitudinal direction, thus limiting the impact of preferential diffusion effects on the flame itself. Furthermore, fuel and oxidizer are being differentially transported in the

second dimension by the strain term such that the burning mixture is enriched. Overall, this results in a mitigation of the flame leaning triggered by preferential diffusion in unstretched conditions, and in a general enrichment of the mixture, which ultimately enables an improvement of the burning performance. Note that the discussed mitigation of preferential diffusion effects by intensive mean applied strain rate can be at first glance linked to a similar mitigation of thermodiffusive instabilities by increasing turbulence level and so Karlovitz number in practical applications. However, it is important to remark that the macroscopic response of the flame to mean strain rate investigated here in laminar conditions should not be confused with the microscopic local flame response to strain due to turbulence, and this is further discussed in Chapter 6 and in Appendix B.5.

As final consideration, it was already shown in Berger et al. [46] that the effect of mean positive strain in a lean turbulent hydrogen flame is to steepen scalar gradients, leading to an enhancement of the mean mixture fraction and higher mean reaction rates within the flame. In their study it is concluded that both strain and curvature amplify the effect of preferential diffusion in lean hydrogen flames. In their case, however, the flame is not subject to strong mean tangential gradients, and only experiences local strain and curvature due to shear-driven turbulence. In light of the analysis presented in this work, and of the broad range of mean strain rate investigated in laminar conditions, it can be rather concluded that mean strain limits the species from differentially diffusing across the flame longitudinal direction, as it instead triggers a preferential species transport on the flame tangential direction. Hence, the way preferential diffusion affects the flame is limited by mean strain, with most of the flame physical properties approaching those one would obtain in the hypothetical case in which preferential diffusion is turned off. By studying laminar bluff body stabilised premixed hydrogen flames, Vance et al. [86] further highlighted that in correspondence of highly stretched regions, the flame stabilises beyond the lean flammability limit. This phenomenon was generically linked to “stronger preferential diffusion effects”, in light of an observed higher elemental hydrogen mass fraction. The findings presented in this study suggest, however, that while the delayed lean blow off is indeed caused by the strengthening of the flame as consequence of the higher local stretch, this phenomenon is due to the species differential diffusive fluxes becoming less significant to the overall species transport, rather than becoming more dominant.

4.4. SUMMARY

Detailed chemistry one dimensional simulations have been conducted on pure hydrogen lean premixed strained flamelets for a broad range of strain rates. Preferential diffusion was turned on and off in the modelling in order to highlight its effect on the flame structure and its interplay with the strain effects. The main findings are summarised below.

- Strain has a mitigating effect on the importance of fluid elements cross-flame diffusion, as they are preferentially being transported on the vertical or flame-tangential direction.
- The weakening impact of fuel/oxidizer differential diffusive fluxes on the flame physical properties and burning performance, which is a consequence of a leaner burning mixture at unstretched conditions, is limited by increasing strain due to the

preferential transport on the flame-tangential direction described at the previous point, which triggers a global flame enrichment.

These findings contradict previous studies where stretch was generally indicated to enhance the effects of preferential diffusion on the flame. Next chapter will focus on expanding the analysis to a two-dimensional and a three-dimensional setup to explore the combined effect of tangential strain rate and local curvature. In particular, the present one-dimensional study suggests that intensive mean applied strain rate may somewhat limit the propagation of thermodiffusive instabilities (triggered by locally curved flame fronts) by establishing a transport of fluid elements in the flame tangential direction which can be significantly stronger than the fluid elements diffusion across the flame normal direction.

5

STABILITY ANALYSIS OF THERMODIFFUSIVELY UNSTABLE LEAN PREMIXED AND STRAINED HYDROGEN FLAMES

*Science is the asymptote of truth;
it approaches unceasingly, and never touches.*

Victor Hugo

5.1. INTRODUCTION

The investigation of lean premixed hydrogen flames under high strain conditions has revealed several promising characteristics. Chapter 3 demonstrated significant reductions in NO_x emissions at elevated strain rates, highlighting the environmental benefits of strained hydrogen combustion. Chapter 4 showed that strain mitigates preferential diffusion effects in one-dimensional flames, suggesting that it might help suppress flame instabilities. In fact, thermodiffusive instabilities are driven by the combination of preferential and differential diffusion effects, although differential diffusion plays a dominant role [29]. As a natural continuation of the analysis performed in the previous chapter, this chapter aims to verify in multi-dimensional laminar flames whether strain has a stabilising effect on flame instabilities. This analysis focuses on laminar conditions and different fixed applied strain rate to understand whether thermodiffusively unstable hydrogen flames can be stabilised through strained configurations in practical combustion systems.

The response of lean premixed strained hydrogen flame fronts to perturbations of varying wavelengths is characterised using detailed chemistry high-fidelity numerical simulations. By varying the applied strain rate in two-dimensional and three-dimensional laminar counterflow configurations, strain's potential to inhibit intrinsic flame instabilities is investigated. In two-dimensional flames, the findings indicate that above a critical strain rate threshold, while perturbations along the direction of strain initially grow, the flame consistently returns to its stable unperturbed state, demonstrating strain's stabilising capability. Furthermore, in three-dimensional flames perturbed polychromatically in the third dimension, a shift of the dispersion relation curve towards smaller growth rates is observed with increasing strain, leading to stabilising growth rates at all modes at the highest strain.

The chapter is organised as follows: Section 5.2 presents the governing equations (Sec. 5.2.1) and the computational setup and numerical details of the two-dimensional (Sec. 5.2.2) and three-dimensional (Sec. 5.2.3) laminar counterflow configurations used in this study. Section 5.3 validates the high-fidelity solver with mixture-averaged transport developed through comparisons with established results for both one-dimensional and two-dimensional flame configurations. Next, results for the two-dimensional setup are discussed in Section 5.4. Section 5.4.1 examines the flame dynamics without imposed perturbations, establishing baseline behaviour at different strain rates. Section 5.4.2 analyses the response of perturbed flame fronts, investigating the evolution of perturbation wavelengths and growth rates (Sec. 5.4.3), and discussing the key findings (Sec. 5.4.4). Results of the three-dimensional perturbed flame fronts analysis are provided next in Section 5.5. Finally, Section 5.6 summarises the key findings and discusses their implications for understanding and controlling thermodiffusive instabilities in strained hydrogen flames.

5.2. COMPUTATIONAL SETUP

5.2.1. GOVERNING EQUATIONS

Detailed-chemistry, two-dimensional, laminar reacting flow simulations are performed using an *in-house* version of reactingFoam. This transient compressible solver in OpenFOAM has been modified to incorporate mixture-averaged transport and temperature-

dependent thermodynamic and transport properties. The reacting Navier-Stokes equations [30] are solved for mass, momentum, sensible enthalpy h and the mass fraction Y_k of $N - 1$ species k . In Einstein's notation, the equation for the generic species k is

$$\frac{\partial(\rho Y_k)}{\partial t} + \frac{\partial(\rho u_i Y_k)}{\partial x_i} = -\frac{\partial(\rho V_{k,i} Y_k)}{\partial x_i} + W_k \dot{w}_k, \quad (5.1)$$

where ρ is the mixture density, $V_{k,i}$ is the diffusion velocity of species k , \dot{w}_k is the molar rate of production of species k , W_k is the molar mass of species k , and subscripts i and j denote the spacial directions. The mass fraction of the N^{th} species is found as $Y_N = 1 - \sum_{k=1}^{N-1} Y_k$. Body forces, viscous dissipation, and pressure gradients are neglected. The low-Mach ideal gas law and the caloric equation of state are used as thermodynamic model, where in the latter the species heat capacities are obtained using the JANAF polynomials. The species viscosities are calculated *a priori* in Chem1D [53] following the standard kinetic theory [154], and are then tabulated as a logarithmic third-order polynomial function of temperature.

A mixture-averaged diffusion model [30] with velocity correction is used to model the diffusion velocity and account for lean hydrogen's preferential and differential diffusion effects:

$$V_{k,i} = -\frac{D_k^M}{X_k} \frac{\partial X_k}{\partial x_i} + V_{c1,i} \approx \frac{D_k^M}{Y_k} \frac{\partial Y_k}{\partial x_i} + V_{c,i}, \quad (5.2a)$$

$$D_k^M = \frac{1 - Y_k}{\sum_{l,k \neq l}^N X_l / D_{kl}} \quad (5.2b)$$

where D_k^M are the mixture-averaged diffusion coefficients and $V_{c,i}$ is the correction velocity:

$$V_{c,i} = \sum_{k=1}^N D_k^M \frac{\partial Y_k}{\partial x_i}. \quad (5.3)$$

Note that the variations of mixture molar mass are relatively small in the present context, therefore the additional term related to the gradients of mixture molar mass in Equation (5.2a) has been omitted for simplicity. The correction velocity follows from the mass conservation to ensure that $\sum_{k=1}^N j_k = \sum_{k=1}^N \rho V_{k,i} Y_k = 0$, where j_k are the species mass fluxes. It is worth noting that, while previous works pointed out that quantitative results may improve by using a multicomponent diffusion model [155, 156], simplified models like the mixture-averaged used in the present work are commonly used for stability analyses and have been shown not to affect the generalities of the conclusions [73–75, 85]. The binary diffusion coefficients species D_{kl} in Equation (5.2) are computed using the approximation of Hirschfelder *et al.* [154] and tabulated in OpenFOAM as a function of temperature [157]. The effect of Soret or thermal diffusion is neglected at this stage to reduce computational cost. Despite this assumption might impact the quantitative predictions of perturbation growth rates, the patterns of intrinsic flame instabilities analysed in this work are not affected by this modelling choice [85].

The heat flux is found as the composition of conductive and diffusive contributions

$$q_i = q_{i,\text{cond}} + q_{i,\text{diff}} = -\lambda \frac{\partial T}{\partial x_i} + \rho \sum_{k=1}^N h_k Y_k V_{k,i}, \quad (5.4)$$

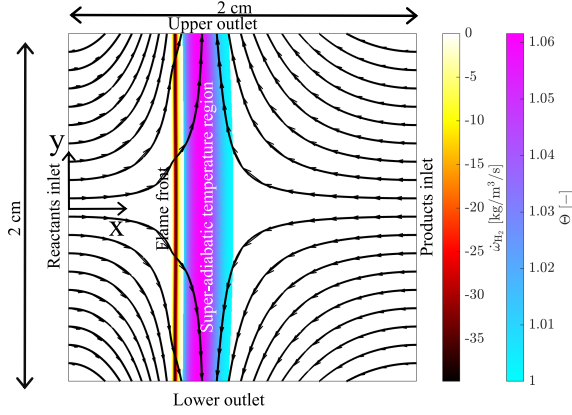


Figure 5.1: Sketch of the two-dimensional laminar reactants-to-products counterflow setup, showing the flame solution of case a1000. The flame front is identified by the contour of hydrogen source term $\dot{\omega}_{\text{H}_2}$, and super-adiabatic temperatures are visible in the region of super-unity temperature progress variable $\Theta = \frac{T - T_r}{T_p - T_r}$.

5

where mass conservation is ensured by the condition $\sum j_k = 0$, leading to the following expression of the diffusive heat flux

$$q_{i,\text{diff}} = \rho \sum_{k=1}^N h_k Y_k V_{k,i} = \rho \sum_{k=1}^{N-1} h_k Y_k V_{k,i} - \rho h_N \sum_{k=1}^{N-1} Y_k V_{k,i}. \quad (5.5)$$

Similarly to the species viscosity, the species conductivity is also determined *a priori* and tabulated as function of temperature. Radiation and Dufour effects are neglected in this study. Detailed kinetic data of reactions and species transport are taken from the Conaire chemical mechanism [146].

5.2.2. 2D SETUP AND NUMERICAL DETAILS

The two-dimensional flame setup consists of a counterflow reactants-to-products configuration as shown in Figure 5.1. As discussed in the previous chapters, such configuration is considered the most suitable to analyse lean premixed hydrogen flames at intensive strain rates. For more details on the setup boundary conditions, the reader is referred to Appendix C.1. Similarly to previous studies performing linear stability analyses of unstretched thermodiffusively unstable flames [74, 75, 85], lean conditions are established at an equivalence ratio $\phi = 0.5$ and the reactants temperature and pressure are fixed respectively to $T_r = 300$ K and $p = 1$ atm. At the products boundary, the temperature is prescribed to adiabatic conditions, $T_p = 1646$ K, and the mixture composition is imposed from complete combustion. The nominal applied strain rate in this study is defined as

$$a = \frac{|u_r| + |u_p|}{L}, \quad (5.6)$$

where L is the domain length in the x direction, and u_r and u_p are the velocities at the reactants and products boundary, respectively. Note that this definition is different to that provided in Equation (3.5) and used in previous chapters in the framework of one-dimensional counterflow flamelets, which is an explicit applied strain rate parameter appearing in the transport equation of the local stretch rate (see Eq. (3.3c)). In this chapter, instead, different nominal strain rates are achieved by prescribing the velocity at the reactants and products boundary, which are reported in Appendix C.1, and thus the definition provided in Equation (5.6) is more appropriate. The domain is fixed to $L_x = L_y = 2 \text{ cm} \approx 50\delta_f$. Note that the zero-gradient boundary condition at the top and bottom of the counterflow domain of this study allows to safely reduce the domain in the flame-tangential direction compared to previous works [72, 158]. Indeed, unlike freely propagating flame setups with periodic boundary conditions, here possible large-scale flame fingers can still develop near the boundaries. Four cases at different applied strain rate are investigated in the present study and reported in Table 5.1 along with their consumption speed S_c (see Eq. (4.9) in Sec. 4.3.4), thermal flame thickness δ_f (see Eq. (2.5) in Sec. 2.2), and the chemical time scale $\tau_f = \delta_f / S_c$.

Table 5.1: Overview of the four simulations investigated in the present work.

Case name	a [s^{-1}]	S_c [m/s]	δ_f [mm]	τ_f [ms]
a500	346.3	0.596	0.402	0.675
a1000	706.85	0.659	0.371	0.563
a2000	1447.5	0.732	0.346	0.472
a5000	3633.5	0.831	0.299	0.360

The computations are performed with an implicit second-order Crank-Nicolson discretization scheme for time marching, combined with a third-order cubic scheme for the convective term of all resolved quantities. A constant time-step is chosen to ensure a maximum CFL number below 0.2. The simulations are first run over a long transient (up to $t = 50\tau_f$) from ignition to a basic steady state (if achieved, see Sec. 5.4.1). Then, a single-wavelength perturbation is applied to the flame front at steady state and is tracked until the crests exit the domain in the upper outlet, corresponding to a physical time of up to $t = 7\tau_f$. The domain for all simulations is discretised using a uniform mesh of 800×800 finite volumes, resulting in a cell spacing $\Delta x = 2.5 \cdot 10^{-5} \text{ m}$. This mesh enables a resolution of the flame structure comparable to prior studies [85], with $n_f = \delta_f / \Delta x$ ranging between 12 and 15.

5.2.3. 3D SETUP AND NUMERICAL DETAILS

The three-dimensional setup consists of the same counterflow reactants-to-products described in the previous section extruded in the third dimension by $L_z = 2 \text{ cm}$, as shown in Figure 5.2, with periodic boundary conditions over the z axis. Note that to reduce the computational cost, L_y is decreased to 1 cm in this case, as there is no imposed perturbation along the y direction. The third dimension is discretised with a uniform mesh of 800 finite volumes, such that a uniform mesh of $800 \times 400 \times 800$ elements with $\Delta x = 2.5 \cdot 10^{-5} \text{ m}$ is achieved in all directions. Due to the high computational cost of three-dimensional simulations (up to 1.2 millions CPU hours), only the two cases at

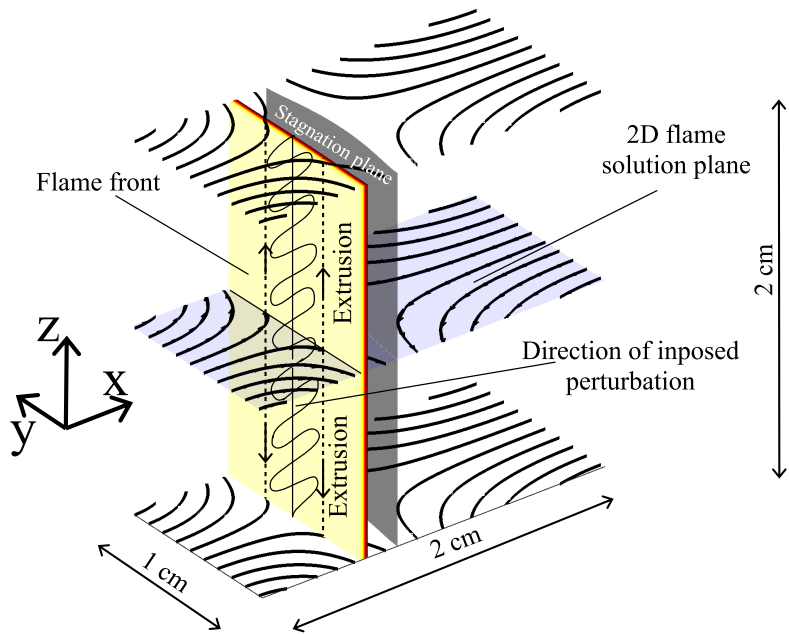


Figure 5.2: Sketch of the three-dimensional counterflow setup.

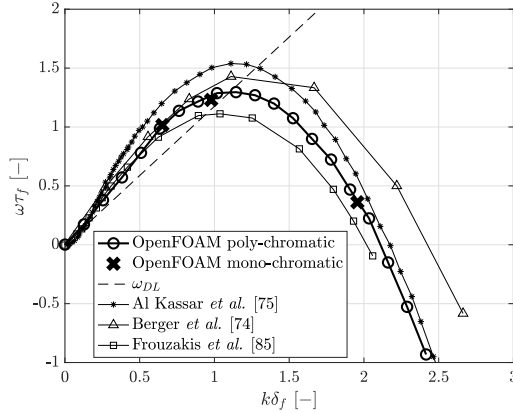


Figure 5.3: Dispersion relation for a freely propagating hydrogen flame obtained from current results, and compared to data from the literature.

the highest strain rates a2000 and a5000 in Table 5.1 are considered. The basic state solution obtained from two-dimensional simulations (see Sec. 5.4.1) is mapped over the 3D domain as starting solution for the simulations. Then, the flame is perturbed across the z direction with a multi-wavelength perturbation with initial amplitude $A_0 = 0.02\delta_f$, and the dispersion relation in the linear regime is reconstructed following the polychromatic methodology in Al Kassar *et al.* [75].

5.3. VALIDATION

Results obtained using the presented methodology in OpenFOAM were preliminarily validated for a one-dimensional freely propagating premixed hydrogen laminar flame at equivalence ratio $\phi = 0.5$, against those obtained from the well-known code Chem1D [53]. Results indicated a maximum difference of 2.4%, 4.5%, and 5.7% respectively for the mixture fraction dip across the domain, flame thickness, and consumption speed. For further details on this preliminary validation over the 1D setup, the reader is referred Appendix C.2.

In order to assess the solver's capability in performing stability analyses in thermodynamically unstable flames, a two-dimensional laminar, freely propagating premixed flame with hydrogen fuel at an equivalence ratio of $\phi = 0.5$ is further simulated on a mesh ensuring 25 cells within the laminar flame thickness. The domain size of $L_x = L_y = 2$ cm is the same as used for the two-dimensional strained setup described in Section 5.2.2. The flame is perturbed with a multi-wavelength perturbation with initial amplitude $A_0 = 0.02\delta_f$, and the dispersion relation in the linear regime is reconstructed following the polychromatic methodology in Al Kassar *et al.* [75]. Results are reported in Figure 5.3, and compared to those in the literature for the same burning regime [74, 75, 85]. As observed, the dispersion relation obtained in OpenFOAM is within the range expected from the other literature studies, indicating that the methodology used in the present work is suitable to study thermodynamically unstable flames.

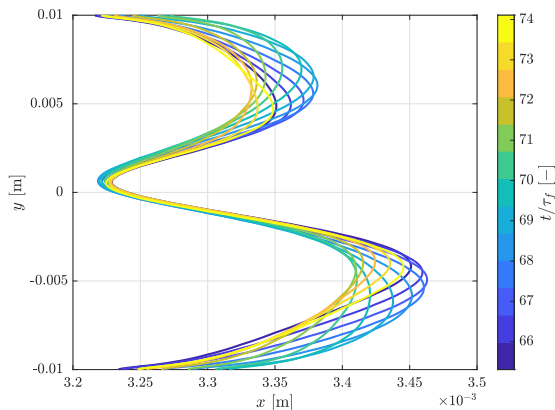


Figure 5.4: Low strain rate case a500. Evolution of the flame front as a function of time. Note the different x and y axis scale.

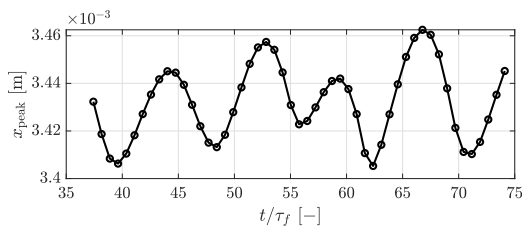


Figure 5.5: Low strain rate case a500. Evolution of the x position of the lower flame tip as a function of time.

5.4. 2D SIMULATION RESULTS

5.4.1. FLAME DYNAMICS WITHOUT IMPOSED PERTURBATIONS

The two-dimensional flame dynamics at different applied strain rates without imposing any perturbation yet is discussed first to have a base reference. At the lowest strain rate, case a500 of Table 5.1, the flame front does not reach any steady state after an initial transient. As shown in Figure 5.4, the flame front is curved and its tips feature a small-amplitude, undamped sequential onset and suppression pattern in time. This unsteady sequential pattern can be further observed in Figure 5.5, showing the variation in time of the flame position (reported only at the lower boundary for simplicity). This unstable sequential pattern is not observed for the other strain rate cases, where after a numerical transient the flame achieves a steady shape in time, which is reported in Figure 5.6. Note that, although a steady state is reached for those cases, their respective flame fronts exhibit a mild curvature (observe that the axes in the figure are not uniform). This is however due to some variation in the velocity field near the outlet boundaries, rather than being an intrinsic effect of the flame dynamics. On the contrary, the unsteady a500 case shows an opposite concavity with respect to the other cases. Here, the instantaneous, positively curved flame front $\kappa > 0$ (concave towards the products) near the domain centreline is located more upstream than for the higher strain rate cases at any time,

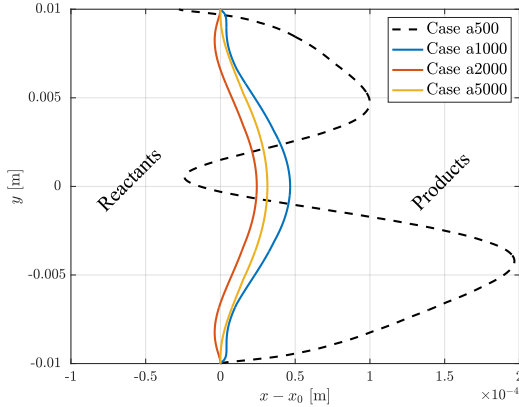


Figure 5.6: Steady flame front shape achieved at moderate to high strain rate cases (case a1000 to a5000, solid lines). Comparison to an instantaneous unsteady flame front at low strain rate (case a500, dashed line). Note the different x and y axis scale.

implying that the flame is propagating locally at a higher speed. Conversely, the negatively curved flame fronts $\kappa < 0$ (concave towards the reactants) at $y \approx \pm 5$ mm are located more downstream at any time step as compared to the higher strain rate cases, indicating that the flame speed is slower at these locations. These differences for the a500 case with respect to the cases at higher strain rate are the result of the occurrence of intrinsic flame instabilities due to thermodiffusive effects. However, this behaviour is different from that of an unstrained thermodiffusively unstable case, where the flame fingers would keep developing in time, and which is not expected to exhibit the sequential onset and suppression pattern highlighted in Figures 5.4 and 5.5. Indeed, the aforementioned sequential pattern is a characteristic feature of the counterflow configuration, where the velocity at the reactants side decreases (about linearly) in the streamwise direction. This implies that when a positively (negatively) curved flame front, due to its higher (lower) flame speed, propagates upstream (downstream) towards the reactants (products), it will also encounter a higher (lower) velocity and lower tangential strain, both counteracting the propagation effect of increased (decreased) flame speed. For this case, the intrinsic instability onset and the (stabilising) effect of the counterflow configuration are of similar magnitude, so that the unsteady sequential pattern described earlier is achieved. For the higher strain rate cases the velocity gradient in the streamline direction is stronger, implying that the stabilising effect is dominant over the onset of intrinsic instabilities, thus a steady flame front is achieved.

The above results suggest that for sufficiently high strain levels the counterflow configuration stabilises hydrogen flames that would be thermodiffusively unstable in unstretched conditions. This point will be further discussed in the following sections.

5.4.2. PERTURBED FLAME FRONT DYNAMICS

The steady flame front obtained for cases a1000, a2000, and a5000 of Table 5.1 discussed in the previous section was perturbed with a single-wavelength or mono-chromatic

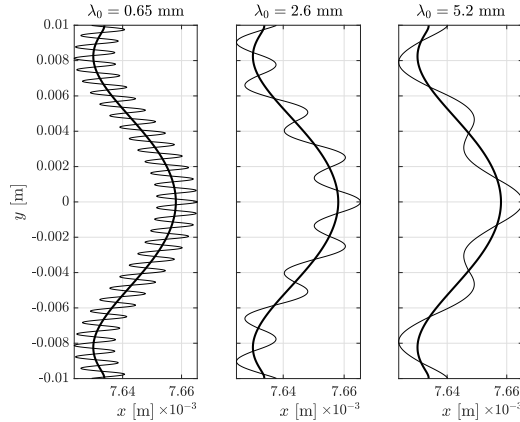


Figure 5.7: Basic state flame front (thick line) vs perturbed flame front (thin line) at different perturbation wave lengths λ_0 for case a2000 of Table 5.1.

5

signal, and the response of the flame to this perturbation is discussed here. The initial range of perturbation wavelength λ_0 is chosen such that the corresponding wave number $k_0 = 2\pi/\lambda_0$ falls within the unstable modes in the dispersion relation of unstretched flames for the conditions investigated (see Fig. 5.3). For completeness, one case ($\lambda_0 = 0.65$ mm) is also chosen in the negative growth rate dispersion relation region. The applied perturbations are summarised in Table 5.2. The normalised wave number $k_0\delta_f$ is also reported as a mean of comparison to the dispersion relation for freely propagating flame in Figure 5.3. The perturbation signal is given to all fields with a cosine function to preserve

Table 5.2: Perturbations applied to the basic state flame for cases a1000, a2000 and a5000. λ_0 is the initial perturbation wavelength, k_0 is the corresponding wave number and δ_f is the unstretched flame thickness.

λ_0 [mm]	k_0 [1/mm]	$k_0\delta_f$ [-]
0.65	9.67	3.91
1.3	4.83	1.96
2.6	2.42	0.978
3.9	1.61	0.652
5.2	1.21	0.489
6.5	0.967	0.391

the flame front symmetry, with an initial amplitude of $A_0 = 0.02\delta_f$ (similar to previous studies [74]). An example of how the steady state flame front (basic state) is perturbed in the chosen range of λ_0 is given in Figure 5.7. Once the flame is perturbed, as one would expect the initial (imposed) wavelength increases in time due to the effect the velocity along the y direction of the counterflow domain (see Fig. 5.1), which is responsible for flame tangential strain. To better visualise this phenomenon, the reader is referred to Appendix C.3.

Before discussing the evolution in time of λ , it is however convenient to derive an

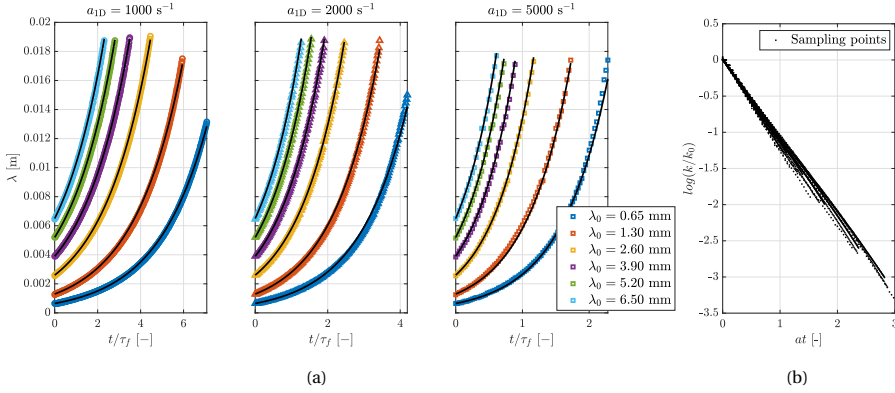


Figure 5.8: (a) Comparison between the numerical values of wave length λ and the pseudo-analytical expression $\lambda = \lambda_0 e^{K_s t}$ for different perturbation wave lengths λ_0 and strain rates. (b) Collapsing sampling points in $at - \log(k/k_0)$ space at all perturbation wave lengths λ_0 and strain rates investigated.

analytical formulation for its expected shape function. Considering that $A_0 \ll \delta_f$, the local tangential strain rate K_s for the opposed-jet configuration can be reduced to that of a flat flame front, $K_s = \frac{\partial u_y}{\partial y}$. Let's also assume that K_s is about constant in time along the flame front during its evolution post-perturbation, which is confirmed by the numerical results (see Appendix C.4). By replacing $y = \lambda/2$ and recalling that $u_y \approx \frac{dy}{dt} = y'$ for small perturbations, one then obtains

$$\lambda(t) = \lambda_0 e^{K_s t}, \quad (5.7)$$

and in terms of wave number

$$k(t) = k_0 e^{-K_s t}. \quad (5.8)$$

In order to compare this solution with the simulation data, an estimate of the exponential factor K_s is necessary. By noting that $K_s = \frac{d(\log(\lambda/\lambda_0))}{dt}$ and recalling that $K_s \approx \text{const}$ in time, the exponential factor is obtained by linear interpolation of the function $\log \frac{\lambda(t)}{\lambda_0}$ obtained from the simulations. A comparison between the analytical Equation (5.7) with fitted K_s and the simulation data for $\lambda(t)$ is shown in Figure 5.8a. One can observe a very close agreement between the pseudo-analytical expression and the simulation data, implying the assumptions used for the analytical derivation hold. It is worth to note that K_s is directly proportional to the applied strain rate a . In fact

$$\log k(t) = \log k_0 - K_s t \Rightarrow \log(k/k_0) = -K_s t, \quad (5.9)$$

and thus $\log \frac{k}{k_0}$ as a function of $(K_s t)$ is a straight line with slope -1 for all the investigated cases. Should K_s be directly proportional to a , the same straight line would be obtained when plotting $\log \frac{k}{k_0}$ as a function of (at) . This is confirmed with very good approximation by the plot in Figure 5.8b. This aspect is important as it demonstrates that the mono-chromatically perturbed flame front in a counterflow configuration yields an exponentially increasing wavelength in time with applied strain rate as amplification factor. Some deviations from the pseudo-analytical expression are found because the

local K_s shows moderate variations depending on the local perturbations, which are locally affecting the flow field on the small scales. Yet, the fit remains linear with very good approximation if the global applied strain rate is considered. Note that this exponential wavelength growth found in this simplified laminar case should be considered as fundamental knowledge to analyse the effect of strain on thermodiffusive instabilities. Indeed, in turbulent settings, shear-driven turbulence can establish local random velocity gradients tangential to the flame front, thus significantly altering the instantaneous local strain rate experienced by the flame. In such conditions, an exponential growth of λ should not be expected.

5.4.3. PERTURBATION GROWTH RATE

The behaviour of the perturbation growth rate ω is investigated in this section for the three stable cases of Table 5.1 (a1000 to a5000). The growth rate is defined as:

$$\omega = \frac{d(\log A)}{dt} = \frac{1}{A} \frac{dA}{dt}, \quad (5.10)$$

where A is the time-evolving amplitude. Growth rates are shown for different initial wavelengths and applied strain rates in Figure 5.9 as a function of the wave number. The dispersion relation for the unstretched case is also reported for comparison purposes (dashed lines). Note that in order to suppress some noise from the simulation data, the counterflow curves in the figure have been smoothed out using a fifth-order polynomial fit over the sampling points, which are the same as shown in Figure 5.8a (one every 0.01 ms). The lowest value of k on the x -axis in the plots represents the computed wavelength at the time the last remaining crest reaches the upper outlet of the domain. It is worth mentioning that these plots do not display a dispersion relation. An unstretched premixed flame under a similar monochromatic perturbation exhibits a constant wave number over time in the initial linear regime, corresponding to a constant growth rate and thus enabling the construction of a dispersion relation. However, in strained configurations, k decreases in time according to Equation (5.8). Consequently, ω is also not constant for a given λ_0 , as no initial linear regime can be identified due to this mode shift. Note that this is also why a fourth-order polynomial, which is generally used to fit a dispersion relation curve [74] following theoretical findings [77], did not provide here a good fit for $\omega(k)$.

For all cases, similar growth rate patterns can be recognised: ω initially exhibits negative values for high values of k (recall that in time the graph should be read from right to left) and increases with (decreasing) k until it becomes positive and reaches a maximum for a certain value k^* . For lower values of k , i.e. further progressing in time, ω is then observed to decrease until it becomes negative again. This result indicates that, after an initial and temporary growth, any perturbation in the flame-tangential, vertical direction is always damped in the 2D counterflow configuration as long as sufficient time has passed. In other words, sufficiently high applied strain rates (let's recall that case a500 of Table 5.1 does not reach a steady state) suppress the intrinsic instability onset, regardless of the initial perturbation wavelength. Note that the temporary positive growth rate region is relatively short, as it spans over a time up to $7\tau_f$.

Further insight on the role of strain rate in suppressing the intrinsic instabilities onset

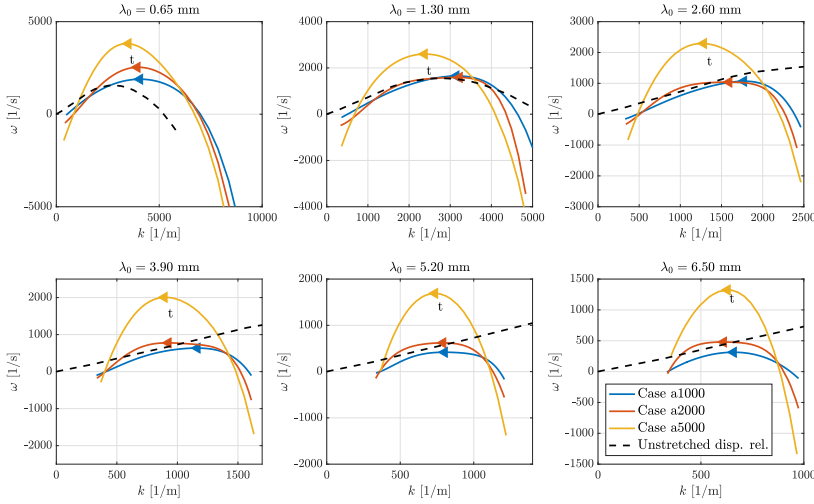


Figure 5.9: Growth rate ω as a function of the wave number k at different strain rates and different initial perturbation wave lengths λ_0 .

is provided next. By combining Eqs. (5.10) and (5.8), the growth rate can be rewritten as

$$\omega = \frac{1}{A} \frac{dA}{dk} \frac{dk}{dt} = -\frac{1}{A} \frac{dA}{dk} K_s k. \quad (5.11)$$

The above expression indicates that the growth rate in k space would vary linearly with the strain K_s if the derivative $\frac{dA}{dk}$ is independent of strain. To assess whether this is the case, one can compute the roots of k at zero growth rate, $k(\omega = 0)$. By looking at Equation (5.11), since for the cases investigated K_s and k are always greater than zero, $\omega = 0$ only for $\frac{dA}{dk} = 0$. The values of k at zero growth rate, $k(\omega = 0)$, are plotted for the corresponding time $t(\omega = 0)$ in Figure 5.10. At each initial perturbation λ_0 there corresponds a pair of $k(\omega = 0)$ points on the graph. Furthermore, two distinct sets of points can be identified. On the left-hand side, the ‘earlier’ roots of $\omega(k)$ are shown, which correspond to the points in Figure 5.9 where the growth rate transitions in time from negative to positive. In contrast, the ‘later’ roots are located at the bottom-right, corresponding to the points in Figure 5.9 where the growth rate shifts from positive to negative, ultimately suppressing the instabilities over time. The region enclosed by the iso-line (shaded in Fig. 5.10) represents the range of modes and times for which the growth rate is positive.

This figure highlights that the region of instability at the two higher strain rates, cases a2000 and a5000 of Table 5.1, almost perfectly overlap, while the same region of instability is broader at the lower strain rate case. In particular, the ‘later’ roots are closer to $k = 0$ in the a1000 case. This suggests that a further decrease of applied strain would virtually shift the values of $k(\omega = 0)$ at $k < 0$, meaning that there would not be any stabilisation over time. This is consistent with the discussion in the previous section, where an unsteady evolution of the flame front (which can be considered equivalent to a random perturbation) was

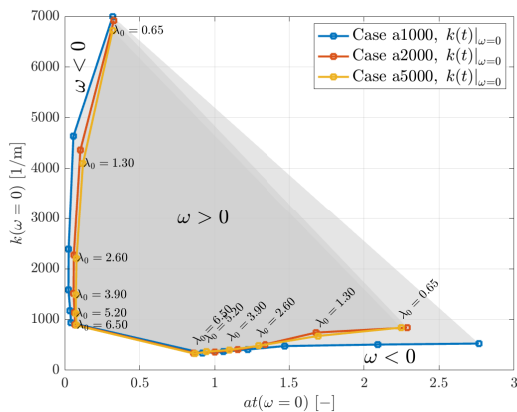


Figure 5.10: Isolines of growth rate $\omega = 0$ in the $at - k$ space for different strain rates and initial perturbation wave lengths λ_0 [mm]. The set of points on the left-hand-side of the figure represent the ‘earlier’ roots of $\omega(k)$ (refer to the roots on the right of $\omega(k)$ in Fig. 5.9), while the set of points on the bottom-right side represent the ‘later’ roots (refer to the roots on the left of $\omega(k)$ in Fig. 5.9).

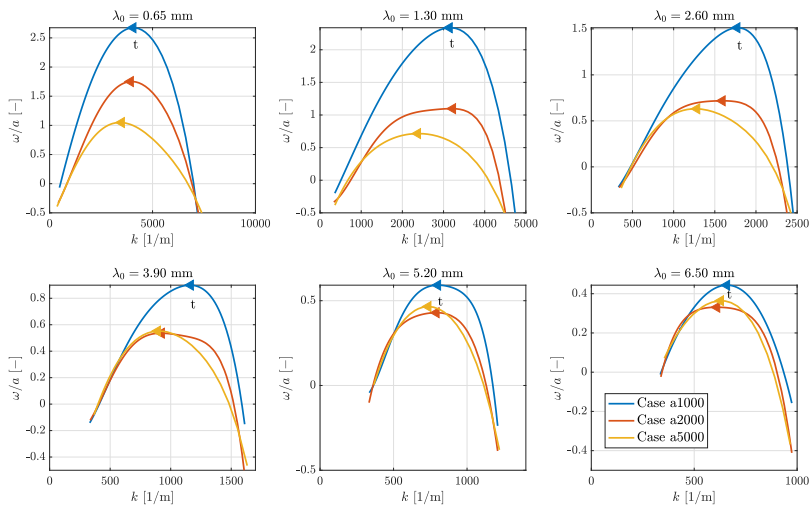


Figure 5.11: Growth rate ω as a function of the wave number k normalized by the applied strain rate a at different initial perturbation wave lengths λ_0 .

observed for the relatively low strain case (case a500 of Table 5.1). In that case, in fact, strain is not sufficiently high and a succession of positive and negative growth rates occurs as time progresses, as shown by Figure 5.5 where the amplitude of the local bumps in the flame front is observed to alternatively grow (due to intrinsic instabilities) and shrink (due to the stabilising effect of the flow field in the counterflow). As suggested by means of analytical analyses by Sivashinsky *et al.* [87] for stagnation point flames, a further decrease in strain levels is expected to result in growing instabilities similar to the unstretched premixed flame case. However, this instability would exhibit a non-linear onset due to the influence, albeit not dominant, of the tangential velocity component. Note that, although Sivashinsky *et al.* [87] analyse a different configuration, similar behaviours to those in the reactants-to-products setup can be expected at low strain, as the flame remains sufficiently distant from the wall or stagnation plane. However, at higher strain rates, stagnation point flame analyses may not be reliable due to unpredictable flame-wall interactions, as discussed in Section 2.6. For sufficiently high strain rates, instead, the observed growth rate pattern characterised by the shift of modes triggered by the tangential velocity becomes increasingly dominant over the single-mode constant growth rates typical of unstretched conditions, resulting in the stabilisation of the flame.

It is also worth noting that the collapse of the $\omega = 0$ iso-lines in the $k - at$ space for the two higher strain rate cases (a2000 and a5000) implies that the equation $\frac{dA}{dk} = 0$ is independent of strain in the limit of high applied strain rates. This suggests that $\omega(k)$ may become a linear function of K_s or a (recall Eq. (5.11)) in this limit. This consideration can be verified by looking at the growth rates normalised by the applied strain rate in Figure 5.11. The figure shows that for the two higher strain rates, the curves overlap for the majority of the λ_0 cases, whereas no such overlap is observed for the lower strain rate case a1000. This observation confirms that at sufficiently high strain rate, the growth rate in k space becomes a linear function of strain rate itself, with the derivative $\frac{dA}{dk}$ becoming independent on K_s or a . Hence, for a given initial perturbation λ_0 , a characteristic $\omega(k)$ proportional to the applied strain rate can be identified in the counterflow configuration.

To understand the physics behind this phenomenon, it is convenient to define two distinct time scales. The rate of change of the wavelength due to the counterflow characteristic velocity in y direction, $\frac{d\lambda}{dt}$, defines a mode-shifting time scale, τ_{MS} . Meanwhile, τ_{DR} represents the time required for a given mode to adapt its growth rate to its characteristic unstretched dispersion relation $\omega(k)$. At high strain levels $\frac{d\lambda}{dt}$ is very high and determines a τ_{MS} that is much shorter than τ_{DR} . This implies that before a perturbation can be affected by the characteristic $\omega(k)$ at unstretched conditions, it has already transitioned to another mode, and $\omega(k)$ will thus follow a characteristic pattern uniquely defined by the counterflow configuration at the given λ_0 and applied strain rate. In the a1000 case, instead, $\frac{d\lambda}{dt}$ is still low enough to allow the unstretched characteristic $\omega(k)$ to partially sum up to the characteristic counterflow growth rate and ultimately affect the total $\omega(k)$, triggering overall higher transient growth rates in the region of instability. Note that, for the two lowest λ_0 cases, one can observe a non-perfect scaling also for the a2000 case when $k \gtrsim 1500 \text{ m}^{-1}$. This can be explained by the fact that, at earlier times, smaller initial perturbations exhibit lower values of $\frac{d\lambda}{dt}$ compared to wider initial perturbations (see Fig. 5.8a), resulting in a larger τ_{MS} even at higher strain rates.

Overall, the analysis carried in the present study shows that from moderate strain rate

upwards, intrinsic instabilities in the flame-tangential direction are always damped after sufficient time in a 2D counterflow configuration. At further increased strain rates, the transient shape of $\omega(k)$ becomes completely unaffected by the characteristic growth rate of each mode in unstretched conditions, and is uniquely determined by the applied strain rate and the initial imposed perturbation wavelength.

5.4.4. DISCUSSION

In previous subsections, the flame response to perturbations of varying wavelengths along the vertical flame-tangential direction was analysed in a two-dimensional counterflow configuration. Overall, the following regimes can be identified considering the onset of intrinsic instabilities:

- At very low strain rates, the mode shift time scale is greater than the dispersion relation time scale ($\tau_{MS} > \tau_{DR}$). As suggested analytically by Sivashinsky *et al.* [87] for stagnation point flames, intrinsic instabilities always grow similarly to an unstretched premixed flame case at the same conditions, because the perturbation has enough time at a given mode to be strongly influenced by the destabilising growth rate of the dispersion relation $\omega_{DR}(k)$. However, ω would still follow a non-linear onset due to the counterflow-characteristic presence, albeit not dominant, of a flame-tangential velocity component triggering a slow mode shifting.
- At low to moderate strain rates, the mode shift time scale is comparable to the dispersion relation time scale $\tau_{MS} \approx \tau_{DR}$. Here, the intrinsic instabilities onset triggered by the destabilising growth rates from the unstretched dispersion relation and the stabilising effect of the mode shifting in the counterflow define an unstable equilibrium, where a sequential pattern is established featuring first a growth and then a damping of the perturbation.
- At moderate to high strain rates, the mode shift time scale is smaller than the dispersion relation time scale $\tau_{MS} < \tau_{DR}$. From this level of strain onward, any forced perturbation is damped after sufficient time, as the perturbation switches from a mode to another before the mode has time to adapt its growth rate to the one of the unstretched dispersion relation. Nevertheless, ω_{DR} maintains a mild destabilising influence on the growth rate in k space, such that $\omega(k)$ is not yet a linear function of strain.
- At high to very high strain rates, the mode shift time scale is much smaller than the dispersion relation time scale $\tau_{MS} \ll \tau_{DR}$. Here, not only any perturbation is always damped after sufficient time, but also the transitory growth rate evolution is independent on ω_{DR} , establishing a pattern that is uniquely defined by the perturbation wavelength and linearly dependent on the applied strain rate.

5.5. 3D SIMULATION RESULTS

In this section, the results obtained with the three-dimensional counterflow setup described in Section 5.2.3 are examined. Unlike the previous section, where the perturbation

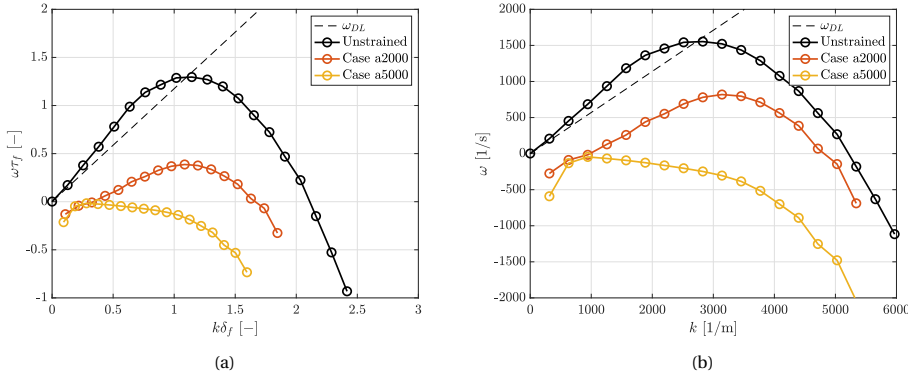


Figure 5.12: Dispersion relation with non-dimensional (a) and dimensional (b) axes for unstrained and different strained three-dimensional counterflow lean premixed hydrogen flames.

was imposed along the same direction as the flame-tangential velocity gradient established to strain the flame, the perturbation is now applied perpendicular to that gradient (along the z direction). Since the ‘extruded’ counterflow configuration features a zero velocity component in the z direction $u_z = 0$, any perturbation applied to the flame along this direction will not be affected by the velocity field and will not feature any mode shift. This allows to perform a classical linear stability analysis and reconstruct a dispersion relation like in a freely propagating flame, which was not possible for perturbations applied along the y direction of the counterflow analysed in the previous section. The purpose of this analysis is to determine whether sufficiently high strain suppresses thermodiffusive instabilities regardless of the direction of the imposed velocity gradients established to strain the flame, thereby generalising the findings of the previous section. Note that due to the prohibitive computational time to let flame fingers develop in the non-linear growth regime, the analysis in this study is limited to the linear growth regime.

The dispersion relations for the two cases a2000 and a5000 of Table 5.1 are reported in Figure 5.12a. For comparison, the dispersion relation of an unstrained 2D freely propagating flame is also reported in Figure 5.12a, as obtained in Section 5.3. Note that despite this reference unstrained flame is two-dimensional, there is no coupling between multi-dimensional perturbations in the linear regime, and thus the dispersion relations obtained from a 2D and a 3D setting would be coincident for this specific setup. Also note that since the flame thickness and chemical time scales are different at different strain rates (see Table 5.1), the same graph is also reported using dimensional units in Figure 5.12b. The graph shows that the dispersion relation curve is shifted downwards with increasing strain. This means that for a given perturbation mode, the associated growth rate is reduced by strain. Furthermore, in the lower strain rate case, some of the low wave number and higher wave number modes that are unstable in unstretched conditions become stable, displaying negative growth rates. More interestingly, for the highest strain rate case all the modes become stable, showing that strain plays a role in suppressing thermodiffusive instabilities. Overall, these results generalise the findings of Section 5.4 by showing that thermodiffusive instabilities are suppressed regardless of the direction of

the tangential velocity gradient applied to strain the flame. Indeed, here the tangential velocity gradient is established across the y direction in the counterflow configuration, while the perturbation is applied along the z direction. Ultimately, combining these results with those obtained in Section 5.4 for perturbations along the direction of the velocity gradient, it is demonstrated that sufficiently high strain rate can turn intrinsically unstable lean premixed hydrogen flames into stable.

5.6. SUMMARY

Detailed chemistry, two-dimensional and three-dimensional simulations have been conducted on pure hydrogen lean premixed flames in counterflow configuration at different strain rates. The main findings are summarised below.

- Different strain regimes have been identified considering the flame response to perturbations with ranging wavelengths along the direction of the flame-tangential velocity gradient. Across these regimes, strain progressively becomes the dominant parameter governing the onset of intrinsic flame instabilities.
- At sufficiently high applied strain rate, intrinsic instabilities growing along the direction of the flame-tangential velocity gradient are always suppressed, following a transient onset uniquely defined by both the initial perturbation and the applied strain itself.
- Higher strain rates systematically reduce the growth rates in the linear regime of all perturbation modes when perturbations are applied perpendicular to the direction of the flame-tangential velocity gradient. At sufficiently high strain rates, these perturbations are stabilised entirely.

Overall, this chapter demonstrates for the first time using high-fidelity numerical simulations that intrinsic instabilities in a counterflow configuration are suppressed by sufficiently high applied strain rates regardless of the direction of the imposed perturbation and of the tangential velocity gradients applied to strain the flame. Ultimately, this proves that intensive strain rate can stabilise lean premixed hydrogen flames that would be otherwise intrinsically unstable in unstrained conditions.

6

ASSESSMENT OF TABULATED CHEMISTRY MODELS FOR LEAN PREMIXED STRAINED HYDROGEN FLAMES WITH LOW-DIMENSIONAL MANIFOLDS

*The wrong view of science betrays itself in the craving to be right;
for it is not his possession of knowledge, of irrefutable truth,
that makes the man of science,
but his persistent and recklessly critical quest for truth.*

Karl Popper

6.1. INTRODUCTION

The investigations in previous chapters have revealed significant benefits of strain on lean premixed hydrogen flames, including reduced NO_x emissions (Chapter 3), mitigated preferential diffusion effects (Chapter 4), and inhibition of thermodiffusive instabilities (Chapter 5). These findings demonstrate strain's potential for improving hydrogen combustion performance and stability while maintaining reduced emissions. However, as discussed in Chapters 1 and 2, current tabulated chemistry LES models typically assume unity Lewis numbers, failing to capture hydrogen's differential and preferential diffusion phenomena and their interaction with strain, which are crucial for accurate predictions.

To finally address to the main research question outlined in Section 1.3, this chapter focuses on developing improved modelling strategies capable of predicting these distinctive phenomena within Large Eddy Simulation (LES) contexts. By enhancing these models, the advantages of strained hydrogen combustion can be leveraged in practical system design, ultimately advancing the development of safe and low-emission hydrogen combustors.

This chapter presents a comprehensive *a priori* analysis of various tabulated chemistry models applied to both laminar and turbulent lean premixed hydrogen flames. In order to limit both tabulation complexity and memory requirements, this work specifically aims to evaluate manifolds to simulate lean premixed hydrogen flames without increasing their dimensionality beyond progress variable and mixture fraction space. Two novel solutions to reduce model errors are proposed. The first solution corrects the consumption speed predicted by unstretched flamelet manifolds in turbulent cases using an efficiency function. The second introduces a novel counterflow flamelet manifold at fixed-strain and varying equivalence ratio. Indeed, mean strain rate has been recognized as the main driver of the increased overall flame reactivity experienced in turbulent lean premixed hydrogen flames as it triggers an enrichment of the conditional mean of mixture fraction over the progress variable [46]. Unlike previous works where the total mean strain rate was solely a function of shear-driven turbulence [99], this study employs a counterflow premixed flame configuration with a varying applied strain rate. This configuration offers two main advantages: it allows extrapolation of the effect of increasing mean strain rate on model error in laminar flame analyses, and enables isolation of turbulence-driven and configuration-driven mean strain effects in turbulent settings. Nevertheless, the generalities of the present analysis would apply to most turbulent and intrinsically unstable lean premixed hydrogen flames, as they all feature strain-induced increased reactivity also when a mean positive strain is not directly imposed [see 46, for example].

This chapter is organised as follows: Section 6.2 describes the computational setup and tested tabulated chemistry models for both laminar and turbulent cases. Section 6.3 presents the *a priori* analysis results, including local reaction rate errors and consumption speed predictions, with separate discussions for laminar (Sec. 6.3.1) and turbulent flames (Sec. 6.3.2). Section 6.3.3 provides guidance on how to choose the fixed-strain rate for manifolds of strained flamelets. Section 6.3.4 details the proposed correction method for unstretched flamelets. Finally, Section 6.4 summarises key findings and their implications for hydrogen combustion modelling.

6.2. COMPUTATIONAL SETUP AND TABULATED CHEMISTRY MODELS

A priori analyses are performed using existing laminar two-dimensional data from Chapter 5 and turbulent three-dimensional data from Fathi *et al.* [160]. These two simulations are chosen because they both consist of the same strained counterflow configuration with the same inflow conditions (and thus flame setup), and similar ranges of strain rates are established, thus allowing for a meaningful comparison between the laminar and the turbulent cases. Note that the solvers used in both cases do not include Soret effect to simplify the numerical setup. While this may lead to underestimated flame speeds, this choice does not affect the overall trends in terms of flame structure interplay with strain and turbulence, which this work aims to model [160, 161]. The flame setups are described in detail below.

6.2.1. 2D LAMINAR SETUP

The laminar DNS setup consists of a two-dimensional counterflow flame in reactants-to-products configuration as sketched in Figure 5.1. Lean conditions are established at an equivalence ratio $\phi = 0.5$ and the reactants temperature and pressure are fixed respectively to $T_r = 300$ K and $p = 1$ atm. Detailed kinetic data of reactions are taken from the Conaire chemical mechanism [146]. The nominal applied strain rate is defined according to Equation (5.6). Three levels of nominal strain rates are considered in this study: $a = 706.85$ s⁻¹, $a = 1447.5$ s⁻¹, and $a = 3633.5$ s⁻¹, which correspond to cases a1000, a2000, and a5000 in Table 5.1, respectively. Further information on the solver and the setup can be found in Chapter 5. Despite this flame is intrinsically unstable in unstretched conditions, it was shown in Chapter 5 that thermodiffusive instabilities are suppressed at these levels of strain rate, resulting in a planar flame front once steady state is achieved [153]. The *a priori* analysis is performed for each case at different applied strain rates over a sample steady-state, planar simulation snapshot. Note, however, that variations with respect to the states of an unstretched laminar flame are still present due to the presence of different strain rates, leading to super-adiabatic temperatures (see Fig. 5.1) and super-equilibrium products, thus still challenging the tested models.

6.2.2. 3D TURBULENT SETUP

The turbulent DNS setup consists of a three-dimensional counterflow flame in reactants-to-products configuration. A cross-section of the setup can be observed in Figure 6.1. The setup features periodic boundary conditions over the z axis, so that the complete computational domain should be considered an ‘extrusion’ of the counterflow section reported by $L_z = 3$ mm. Unlike laminar cases where small domains may suppress thermodiffusive instabilities [114, 158], here thermodiffusive structures do not grow freely but are instantaneously shaped by local turbulent eddies, for which the domain is suitably sized [160]. The reacting compressible Navier-Stokes equations are solved with the finite-volume DNS code INCA [162] on a uniform mesh of 576x192x144 cells with grid spacing $\Delta x = 2 \cdot 10^{-5}$ m. The diffusion velocity is modelled similarly to the laminar case (see Eq. (5.2a) and (5.3) in Sec. 5.2.1 of Chapter 5), except for the constant non-unity Lewis number approximation employed to obtain the species diffusion coefficients ($D_k = \alpha / Le_k$,

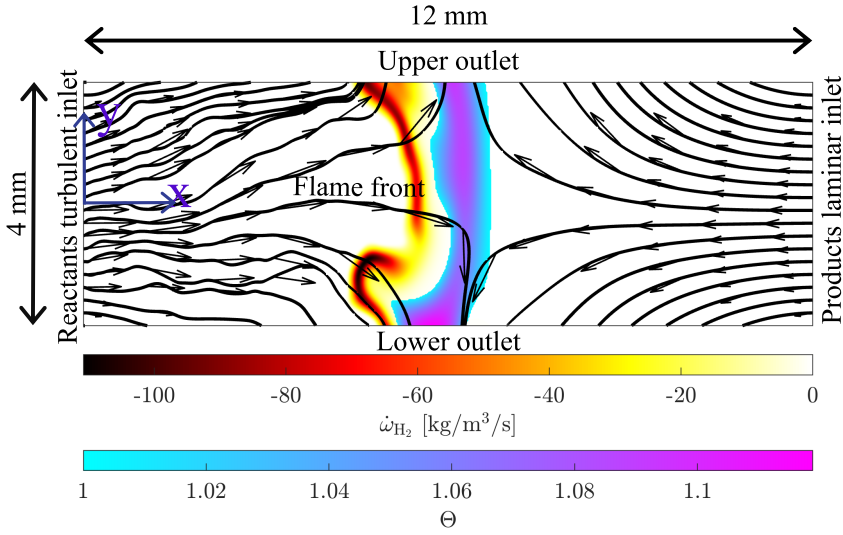


Figure 6.1: Cross-section sketch at the mid cutting plane of the three-dimensional turbulent counterflow setup at a sample timestep, showing a snapshot of the flame solution at $a = 2000 \text{ s}^{-1}$ [160]. The flame front is identified by the contour of hydrogen source term $\dot{\omega}_{H_2}$, and super-adiabatic temperatures are visible in the region of super-unity temperature progress variable Θ .

6

where Le_k is a constant value for the species k obtained from 1D simulations). The same equivalence ratio, reactants temperature, and pressure conditions are considered as in the laminar case, while detailed kinetic data of reactions are taken from a combination of the hydrogen skeletal mechanism from Sanchez and Williams [163] and the NO_x module from Capurso *et al.* [138]. The selected equivalence ratio ($\phi = 0.5$) enables the occurrence of the synergistic interplay between turbulence and thermodiffusive instabilities [98].

An inflow boundary with homogeneous isotropic turbulence is superimposed using the digital filter method [164] at the reactants side of the counterflow. The average inflow velocity is kept fixed at all cases to 10 m/s, such that a Karlovitz number of $Ka = (l_t / \delta_f)^{-1/2} (u' / S_L)^{3/2} = 3.143$ is achieved, where l_t is the integral length scale, δ_f is the unstretched laminar flame thickness, u' is the root-mean-square velocity, and S_L is the laminar flame speed. Additional parameters to identify the turbulent and combustion regimes are reported in Appendix D.1. The total tangential strain rate experienced locally by the flame front is given by the combination of turbulence-driven and configuration-driven strain rate. The configuration-driven nominal applied strain rate, also referred to as "bulk" strain rate, is changed by adjusting the products inlet velocity (see Eq. (5.6)), whose inflow is kept laminar. This way it is possible to globally increase the tangential strain rate through the bulk strain rate while keeping unaffected the level of turbulence withstood by the flame. Two different levels of bulk strain rate are considered in this study, $a=2000 \text{ s}^{-1}$ and $a=5000 \text{ s}^{-1}$. A three-dimensional, characteristic-based boundary condition is used at the upper and lower outlets to prevent wave reflections in the domain that are likely to occur when a compressible solver is used to simulate a counterflow

setup. For the same reason, a non-reflecting boundary condition is also prescribed at the products laminar inflow. For a complete description of the solver and the setup, along with the simulation results analysis, the reader is referred to Fathi *et al.* [160].

The *a priori* analysis is performed over an instantaneous field at a sample time step. Given the three-dimensional flame setup counting ~ 16 millions grid points, a single time step is sufficient to collect statistically representative thermochemical state sampling.

6.2.3. FILTERING OF DNS DATASET

The DNS dataset is filtered using a spatial convolution with a homogeneous isotropic filter function [165]:

$$\bar{\phi}(\mathbf{x}, t) = \int_{-\infty}^{\infty} \phi(\mathbf{x} - \mathbf{r}, t) G(\mathbf{r}; \Delta) d\mathbf{r}, \quad (6.1)$$

where the filter function G is taken as a Gaussian filter, and depends on the filter width Δ . In order to be consistent with LES formulations, the Favre filtering for a generic quantity ϕ is introduced as $\tilde{\phi} = \rho\phi/\bar{\rho}$. The Favre-filtering is then applied to progress variable c and mixture fraction z , while the density and the reaction rates (in Kg/s/m³) are filtered using the conventional Reynolds filter. A range of filters widths around the laminar flame thickness is applied to the DNS dataset. This range is reported in Table 6.1 for the different cases at different applied strain rates analysed in this work, along with corresponding flame thicknesses. Note that the same ratio Δ/δ_f is kept for different cases. Also, the largest filter size used in the laminar cases of $\Delta = 8\delta_f$ could not be achieved for the turbulent cases due to the smaller domain size in the latter, leading to a very coarse filtered grid.

Table 6.1: Range of filter widths applied to the different DNS datasets with the corresponding laminar flame thicknesses δ_f .

Case name	a [s ⁻¹]	Δ [mm]	δ_f
Laminar flames			
a707L	706.85	$\delta_f, 2\delta_f, 4\delta_f, 8\delta_f$	0.371
a1448L	1447.5	$\delta_f, 2\delta_f, 4\delta_f, 8\delta_f$	0.346
a3634L	3633.5	$\delta_f, 2\delta_f, 4\delta_f, 8\delta_f$	0.299
Turbulent flames			
a2000T	2000	$\delta_f, 2\delta_f, 4\delta_f$	0.285
a5000T	5000	$\delta_f, 2\delta_f, 4\delta_f$	0.239

6.2.4. TABULATION APPROACH

In this work, three different types of flamelet manifolds are considered as follows, and summarised in Table 6.2.

- A single counterflow reactants-to-products strained flamelet at the nominal equivalence ratio $\phi = 0.5$ (1DS). On the unfiltered grid, this one-dimensional manifold is parametrised with a progress variable c . The applied strain rate in the flamelet is the same as that of the DNS for the 2D laminar cases, both computed with Eq. (5.6). In the turbulent cases the total tangential strain rate experienced by the flame varies

in space and time as it is a combination of applied and turbulence-driven strain. Therefore, the applied strain rate on the flamelet is chosen so that the tangential strain on the flamelet is close to the conditional mean estimated from the DNS [see 160, Fig. 10];

- A manifold of 300 unstretched premixed flamelets with equivalence ratio varying from $\phi = 0.3$ to $\phi = 1$ (2DU). On the unfiltered grid, two-dimensional manifold is parametrised with a progress variable c and a mixture fraction z .
- A manifold of 300 reactants to products counterflow flamelets at the same fixed applied strain rate and with equivalence ratio varying from $\phi = 0.3$ to $\phi = 1$ (2DFS). The value of applied strain rate is chosen here as for the 1DS case. On the unfiltered grid, the resulting two-dimensional manifold is parametrised with a progress variable c and a mixture fraction z .

Table 6.2: Summary of the tested flamelet manifolds.

Manifold name	Manifold type
1DS	Fixed-strain counterflow flamelet at $\phi = 0.5$
2DU	Unstretched flamelets with varying ϕ
2DSF	Fixed-strain counterflow flamelets with varying ϕ

Note that while higher dimensional manifolds are possible, they are not considered in the present work where the objective is to ensure that potential LES based on these manifolds remain efficient in terms of computational time and memory requirements (note that the manifold dimension will increase in the case of filtered meshes, see Secs. 6.2.4 and 6.2.4). Additionally, further expanding the manifold could introduce empty zones or non-linear thermochemical variables distributions, particularly when varying strain rate is involved, which promote tabulation errors and necessitate additional tabulation points.

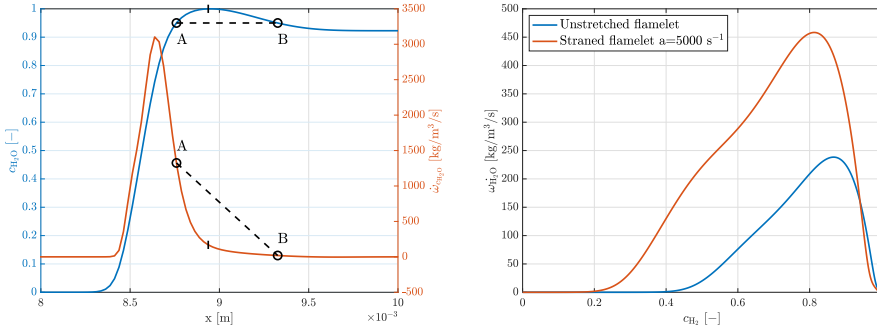
The flamelet manifolds are computed with Chem1D [53]. Soret effect is neglected to ensure consistency with the DNS solvers. Note that in the counterflow cases, unlike the setup in Chapter 3 (Eq. (3.3c)), a rearranged formulation for the transport equation of the local strain stretch rate is employed to closely mimic the DNS setup [166]

$$\frac{\partial \rho K}{\partial t} + \rho u_x \frac{\partial K}{\partial x} = \frac{\partial}{\partial x} \left(\mu \frac{\partial K}{\partial x} \right) - \rho K^2, \quad (6.2)$$

with $K(x \rightarrow \pm\infty) = 0$ as a Dirichlet boundary condition. The mass flow rate at the reactants and products inlet are kept fixed. With this formulation, the inlet reactants and products velocities are computed from the imposed fixed strain rate a as:

$$u_r = \frac{aL}{1 + \frac{\rho_r}{\rho_p}}, \quad u_p = u_r \frac{\rho_r}{\rho_p}, \quad (6.3)$$

where $L = 2$ cm is the domain length and subscripts r and p refer to reactants and products streams respectively.



(a) Water-based progress variable and progress variable reaction rate across the centerline of the a3634L case.

(b) Product reaction rate as a function of fuel-based progress variable for an unstretched flamelet (blue line) and strained flamelet at $a=5000 \text{ s}^{-1}$ (red line). Both at $\phi = 0.5$.

Figure 6.2: Relative error of the H_2 source term $\dot{\omega}_{\text{H}_2}$ over the resolved grid and with increased filter width obtained with the 2DU-type manifolds. The filtered fields are reconstructed with the β -FDF (a) and with the F-TACLES (b) subgrid models.

As parametrising variables for the tabulated quantities, the Bilger mixture fraction according to Equation (2.7) and a progress variable are used. Two possible definitions of progress variables are explored, one based on water and one based on the hydrogen fuel:

$$c_{\text{H}_2\text{O}} = \frac{Y_{\text{H}_2\text{O}}}{Y_{\text{H}_2\text{O},\text{max}}} ; \quad c_{\text{H}_2} = 1 - \frac{Y_{\text{H}_2}}{Y_{\text{H}_2,r}}. \quad (6.4)$$

where $Y_{\text{H}_2,r}$ denotes the mass fraction of hydrogen in the reactants at the nominal equivalence ratio. It is well known, however, that lean hydrogen flames exhibit super-equilibrium products in correspondence of positively-strained or positively-curved flame fronts (see for example Fig. 4.3 in Chapter 4). This leads to a non-monotonic water-based progress variable across the flame front, as shown for the a3634L case in Figure 6.2. As a consequence, one might have two different values of reaction rate at the same value of progress variable which makes direct parametrisation with $c_{\text{H}_2\text{O}}$ not feasible (see for example points A and B where $c_{\text{H}_2\text{O}} = 0.95$ in Figure 6.2a). Berger *et al.* [118] found a way to tackle this problem in a presumed-FDF LES framework by re-interpolating the manifold in $c_{\text{H}_2\text{O}}$ space after the flamelet integration is performed over c_{H_2} and its variance. However, this walk-around only works with an unstretched flamelet manifolds, where $c_{\text{H}_2\text{O}}$ is monotonic. In a strained flamelets manifold, instead, the non-monotonicity of $c_{\text{H}_2\text{O}}$ is experienced by the flamelet itself, making also this walk-around ineffective. In light of these arguments, only the hydrogen-based progress variable c_{H_2} will be used in this *a priori* study, and will be indicated generically with c in the remainder of the Chapter. A known weakness of progress variables based on fuel, particularly in hydrocarbon fuel, is that it can sometime reach value one before all the reactions are completed. However, this is not the case in lean hydrogen combustion thanks to its shorter combustion reaction chain and overall faster chemistry. This behaviour is demonstrated for both an unstretched flamelet and a strained flamelet example at $\phi = 0.5$ in Figure 6.2b, which shows that when $c_{\text{H}_2} = 1$, the product reaction rate $\dot{\omega}_{\text{H}_2\text{O}}$ has already reached zero.

Additional controlling variables are needed when the DNS dataset is filtered, emulating the subgrid turbulence-flame interaction in a LES. This work mainly evaluates the presumed filtered density function (FDF) approach with β -FDF with additional comparisons to the performance of the filtered tabulated chemistry approach for LES (F-TACLES) in the context of 2DU-type manifolds. These approaches are discussed next.

PRESUMED FDF APPROACH

The performance of different manifolds based on the presumed FDF approach for LES is assessed *a priori*. The filtered reaction rate in the presumed FDF approach can be written as [95]:

$$\bar{\omega} = \bar{\rho} \int_0^1 \int_0^1 \frac{\dot{\omega}(\zeta, \eta)}{\rho(\zeta, \eta)} \tilde{P}(\zeta, \eta; \tilde{c}, \tilde{z}, \sigma_{c,\text{sgs}}^2, \sigma_{z,\text{sgs}}^2) d\zeta d\eta, \quad (6.5)$$

where ζ and η are the sample space variables of progress variable and mixture fraction, respectively, $\sigma_{c,\text{sgs}} = \tilde{c}^2 - \bar{c}^2$ and $\sigma_{z,\text{sgs}} = \tilde{z}^2 - \bar{z}^2$ represent the subgrid variance of c and z , respectively, and $\tilde{P}(\zeta, \eta; \tilde{c}, \tilde{z}, \sigma_{c,\text{sgs}}^2, \sigma_{z,\text{sgs}}^2)$ is their joint FDF (sometimes referred to as subgrid probability density function, PDF). In LES of hydrocarbon fuels z only describes the local mixing of fuel and oxidizer, and c and z can be treated as statistically independent [167]. However, this is not the case in hydrogen flames, where local fluctuations of mixture fraction across the flame front are present due to preferential diffusion. Following the methodology proposed by Berger *et al.* [118], it is therefore convenient to introduce a flamelet index ϕ_{FL} . For every flame state described by (c, z) , ϕ_{FL} represents the nominal equivalence ratio of the corresponding flamelet in the chosen manifold, so that $\phi_{\text{FL}} = f(c, z)$ is a bijective function and can be tabulated from the manifold itself. Unlike the mixture fraction, this quantity is conveniently independent on the progress variable, as it is basically a 'label' of each 1D flamelet forming the manifold. This allows to assume statistical independence between c and ϕ_{FL} :

$$\tilde{P}(\zeta, \xi; \tilde{c}, \tilde{\phi}_{\text{FL}}, \sigma_{c,\text{sgs}}^2, \sigma_{\phi_{\text{FL}},\text{sgs}}^2) = \tilde{P}(\zeta; \tilde{c}, \sigma_{c,\text{sgs}}^2) \tilde{P}(\xi; \tilde{\phi}_{\text{FL}}, \sigma_{\phi_{\text{FL}},\text{sgs}}^2), \quad (6.6)$$

where ξ is the sample space variable of the flamelet index. The validity of this assumption has been also confirmed with good approximation from the DNS data of this study (not reported) and previous works (e.g. see [118]). In the present study, the β shape is tested as presumed FDF for the progress variable space, as it showed good performance in the thickened reaction zone regime of the Borghi's diagram [95] (which is the regime for the turbulent flames here), while other choices are remanded to future studies. A delta-function is chosen instead for $\tilde{P}(\xi)$ since the subgrid variance of mixture fraction is negligible for the cases under investigation. Therefore, the tabulated filtered reaction rate is expressed as $\bar{\omega}(\tilde{c}, \sigma_{c,\text{sgs}}^2, \tilde{\phi}_{\text{FL}})$.

Note that, since $\tilde{\phi}_{\text{FL}}$ is implicitly determined by \tilde{z}

$$\tilde{z} = \int_0^1 z(\zeta, \tilde{\phi}_{\text{FL}}) \beta(\zeta; \tilde{c}, \sigma_{c,\text{sgs}}^2) d\zeta, \quad (6.7)$$

then the filtered reaction rate in Equation (6.5) still depends on the set of initial parametrization variables \tilde{c} , $\sigma_{c,\text{sgs}}^2$ and \tilde{z} . Also, since \tilde{z} increases monotonically with $\tilde{\phi}_{\text{FL}}$, the latter can be re-interpolated in the functional form $\bar{\omega}(\tilde{c}, \sigma_{c,\text{sgs}}^2, \tilde{z})$. After this final re-interpolation,

the reaction rate is tabulated as a function of the initial parametrisation variables, where the variations of the mixture fraction at different filtered grids are correctly taken into account through Equation (6.7). The importance of this final step, which has been controversially omitted in some of the existing studies [see 119, 120, 168, for example], is discussed extensively in Section 6.3.1.

F-TACLES APPROACH

In this approach the filtered reaction rate in a LES is obtained by spatially pre-filtering the reaction rate from the laminar solution [102, 114], i.e.

$$\bar{\omega} = \Xi(\Delta)\bar{\omega}^*(\tilde{c}, \tilde{z}, \Delta), \quad (6.8)$$

where $\bar{\omega}^*$ denotes the pre-filtered laminar reaction rate and Δ is the chosen LES filter width. To account for the subgrid wrinkling at the filtered scales in the turbulent flames, the subgrid scale wrinkling factor Ξ is introduced, which is found from the filtered DNS data as [30]:

$$\Xi(\Delta) = \frac{\overline{\rho s_d |\nabla c|}}{\rho_u S_L |\nabla \tilde{c}|}, \quad (6.9)$$

where ρ and $s_d = \frac{1}{|\nabla c|} \frac{Dc}{Dt}$ [160] are the local density and displacement speed, respectively, ρ_u is the density of the unburnt reactant mixture, and S_L is the laminar flame speed of the unstretched flamelet at $\phi = 0.5$.

It is worth noting that, since counterflow flamelets are a 1D representation of the 2D laminar counterflow case, applying this approach using the spatially pre-filtered reaction rate from strained flamelets would result in the same 2D laminar setting at the same filtered grid and strain rate. Attempts to incorporate counterflow strained flamelets within the F-TACLES approach are documented in literature for non-premixed [169] and partially premixed [170] setups. However, they are not applicable in the framework of this work assessing fully premixed counterflow flamelet manifolds. Therefore, this approach is only employed in the context of unstretched flamelet manifolds, which is well-established in literature also for hydrogen flames [170].

6.3. RESULTS

6.3.1. LAMINAR FLAMES

The 2D DNS dataset of laminar flames is assessed first in order to evaluate the robustness of the tabulation approaches proposed in Section 6.2 without turbulence, and with increasing strain rate to mimic the increase of reactivity and upward shift in the conditional mean of mixture fraction typical of turbulent, intrinsically unstable setups. Note that as the filter size increases, $\sigma_{c,sgs}^2 > 0$ even in the case the flame is laminar. The full list of cases assessed is provided in Table 6.3.

FIXED-STRAIN FLAMELET

In this section, the ability of the fixed-strain manifold (first three cases in Table 6.3) to reproduce the states of a two-dimensional laminar and strained lean premixed hydrogen flame is tested. The fuel source term $\dot{\omega}_{H_2}^M$, filtered and unfiltered, is reconstructed by

Table 6.3: Summary of tested models over the laminar setup with nomenclature. Recall that the flamelet strain rate in the 1DS manifolds are the same as the nominal strain rate of the corresponding case.

Tested model name	Case nominal strain rate [s ⁻¹]	Manifold type	Subgrid model	parametrisation variables
a707L-1DS- β FDF	706.85	1DS	β -FDF	$\tilde{c}, \sigma_{c,sgs}^2$
a1448L-1DS- β FDF	1447.5	1DS	β -FDF	$\tilde{c}, \sigma_{c,sgs}^2$
a3634L-1DS- β FDF	3633.5	1DS	β -FDF	$\tilde{c}, \sigma_{c,sgs}^2$
a707L-2DU- β FDF	706.85	2DU	β -FDF	$\tilde{c}, \sigma_{c,sgs}^2, \tilde{z}$
a1448L-2DU- β FDF	1447.5	2DU	β -FDF	$\tilde{c}, \sigma_{c,sgs}^2, \tilde{z}$
a3634L-2DU- β FDF	3633.5	2DU	β -FDF	$\tilde{c}, \sigma_{c,sgs}^2, \tilde{z}$
a707L-2DU-FT	706.85	2DU	F-TACLES	$\tilde{c}, \tilde{z}, \Delta$
a1448L-2DU-FT	1447.5	2DU	F-TACLES	$\tilde{c}, \tilde{z}, \Delta$
a3634L-2DU-FT	3633.5	2DU	F-TACLES	$\tilde{c}, \tilde{z}, \Delta$
a707L-2DSF- β FDF	706.85	2DSF	β -FDF	$\tilde{c}, \sigma_{c,sgs}^2, \tilde{z}$
a1448L-2DSF- β FDF	1447.5	2DSF	β -FDF	$\tilde{c}, \sigma_{c,sgs}^2, \tilde{z}$
a3634L-2DSF- β FDF	3633.5	2DSF	β -FDF	$\tilde{c}, \sigma_{c,sgs}^2, \tilde{z}$

entering the flamelet manifold with the controlling variables indicated in Table 6.3. The modelled consumption speed is thus computed as

$$S_c^M = -\frac{1}{\rho_u Y_{H_2,u} L_y} \int_A \dot{\omega}_{H_2}^M dA, \quad (6.10)$$

where $L_y = 2$ cm is the stream transversal length of the domain, and is compared to the one obtained directly from the DNS data, $S_{c,DNS}$. Results are shown in Figure 6.3 for increasing filter widths and three levels of applied strain. The graph shows that the relative error is below 5% for filter sizes up to $\Delta = 2\delta_f$. This is somewhat expected, since the used flamelet is a one-dimensional representation of the two-dimensional flame at the given strain. The small discrepancies observed are attributed to the numerical errors in the different solvers used. The error rapidly increases for filter sizes $\Delta > 2\delta_f$, which is due to the limitations of the β -FDF in mimicking the asymptotic bimodal behaviour at large filter sizes [171]. Interestingly, this overestimate appears to be reducing at increasing strain rates, the reasons for which are discussed in Appendix D.2.

UNSTRETCHED FLAMELETS

In this section, the ability of a manifold of unstretched flamelets at varying equivalence ratio to reproduce the states of the two-dimensional laminar and strained lean premixed hydrogen flame front is assessed for three levels of applied strain (fourth to ninth case in Table 6.3). For this manifold type, results from the presumed FDF are compared to those of the F-TACLES subgrid model to distinguish whether the observed errors stem from parametrisation inaccuracies or from the subgrid closure itself. The results are shown in Figure 6.4. Unlike the cases with fixed-strain manifold discussed in Section 6.3.1, the modelled consumption speed shows a 20% overestimate already on the unfiltered mesh ($\Delta \rightarrow 0$). This indicates that even if the correct variation of z due to preferential diffusion

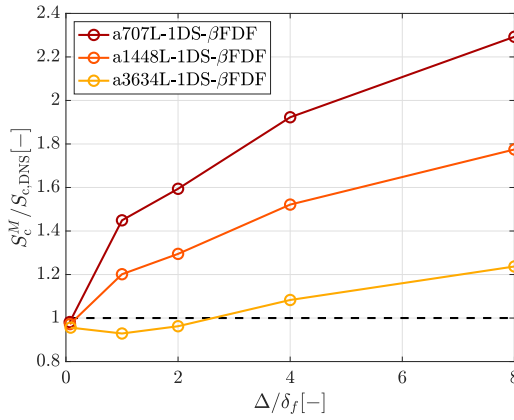


Figure 6.3: Ratio of modelled versus DNS consumption speed for the first three cases of Table 6.3 (IDS manifolds), for increasing filter widths.

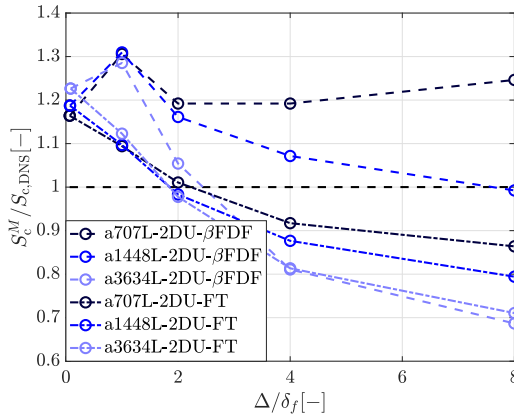


Figure 6.4: Ratio of modelled versus DNS consumption speed for cases four to nine of Table 6.3 (2DU manifolds), for increasing filter widths.

and stretch is predicted in the reacting flow, thermochemical states of strained flames are not well represented by unstretched manifolds even in laminar conditions. Except for the case at lowest applied strain and presumed FDF approach, the error on filtered meshes overall tends to decrease for increasing filter sizes either with using the β presumed FDF or with the F-TACLES approach. Although this might seem as an improvement at moderate filter sizes, for all these cases the ratio between modelled and DNS consumption speed becomes eventually smaller than unity and keeps decreasing as the filter size increases. This suggests that the small error found for $\Delta \approx 2\delta_f$, in particular for the F-TACLES cases, is rather due to compensation of effects. Note also that the ratio of consumption speeds in the cases of the β -FDF becomes negative for the two highest applied strain cases despite the known tendency of the β -FDF methods to overestimate S_c , suggesting that the errors introduced by the unstretched thermochemical states play a stronger role.

In order to understand what regions of space across the flame contribute more to the discrepancies on the consumption speed, the relative error between the fuel reaction rate from the DNS (unfiltered, $\dot{\omega}_{\text{H}_2}^{\text{ref}}$, or filtered, $\overline{\dot{\omega}}_{\text{H}_2}^{\text{ref}}$) and that reconstructed from the manifold, is shown in Figure 6.5. The relative error is computed as

$$\epsilon_{rel}(\dot{\omega}_{\text{H}_2}) = \frac{|\dot{\omega}_{\text{H}_2}^M| - |\dot{\omega}_{\text{H}_2}^{\text{ref}}|}{\max|\dot{\omega}_{\text{H}_2}^{\text{ref}}|}. \quad (6.11)$$

6

The reader can find further comparisons between reference and reconstructed fuel reaction rate profiles along the centreline of the domain in Appendix D.3. For the unfiltered mesh, the overestimate of the reaction rate is stronger in the region of higher progress variable (more downstream to the right in the contour plots), which corresponds to the region of super-equilibrium products, where the mixture fraction in a lean strained flame also goes above its nominal value (see Chapter 4). This suggests that within an unstretched flamelet manifold, the mixture fraction variations, which correspond to transitions toward richer flamelets, fail to accurately capture the strain-induced reaction rate changes, resulting in an overestimation of reaction rate. Similar considerations can be extended to the reaction rate changes in a positively-curved flame front, which exhibit an overshoot of z at high progress variables similar to that induced by strain.

For filtered meshes ($\Delta > 0$) a similar overestimate of the modelled reaction rate is observed for large values of progress variable. However, an underestimation is also observable for both presumed FDF and F-TACLES approaches at low values of progress variables (more upstream to the left in the contour plots), corresponding to regions where the mixture fraction falls below the nominal value in lean strained flames [145]. These regions of underestimation of reaction rate compensate for the overestimation in the region of super-equilibrium (and superadiabaticity), explaining the relatively small errors on the consumption speed at moderate filter sizes observed in Figure 6.4. The region of underestimate becomes dominant at larger filter sizes and higher strain rates, leading to larger and larger underestimation of the consumption speed. Since the same behaviour is observed for both presumed FDF and F-TACLES models, this suggests that the error stems from fundamental parametrisation limitations at filtered grids rather than subgrid model inaccuracies. Moreover, these errors, together with the resulting consumption speed, appear to be filter dependent.

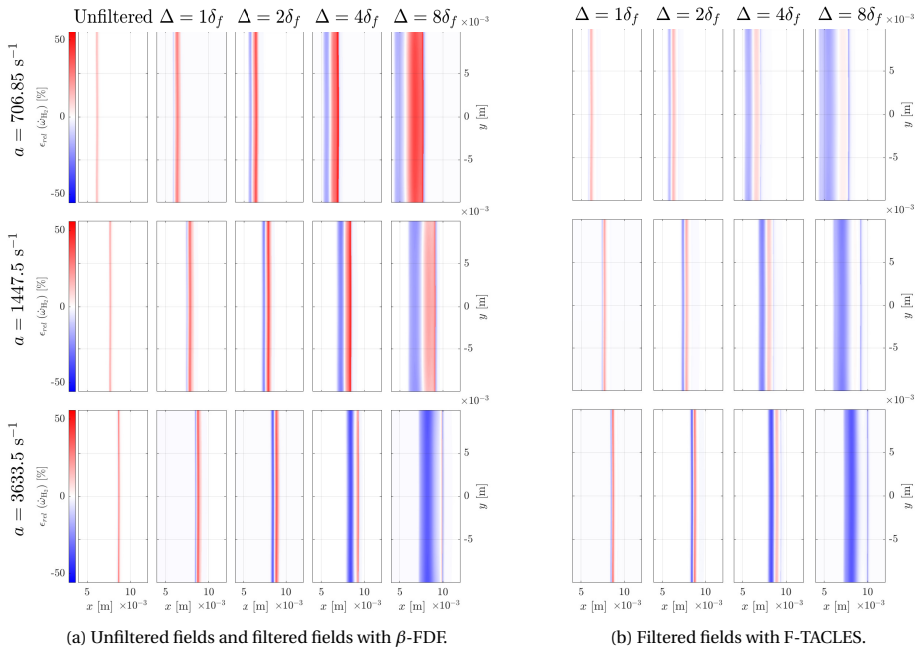


Figure 6.5: Relative error of the H_2 source term $\dot{\omega}_{H_2}$ over the resolved grid and with increased filter width obtained with the 2DU-type manifolds. The filtered fields are reconstructed with the β -FDF (a) and with the F-TACLES (b) subgrid models.

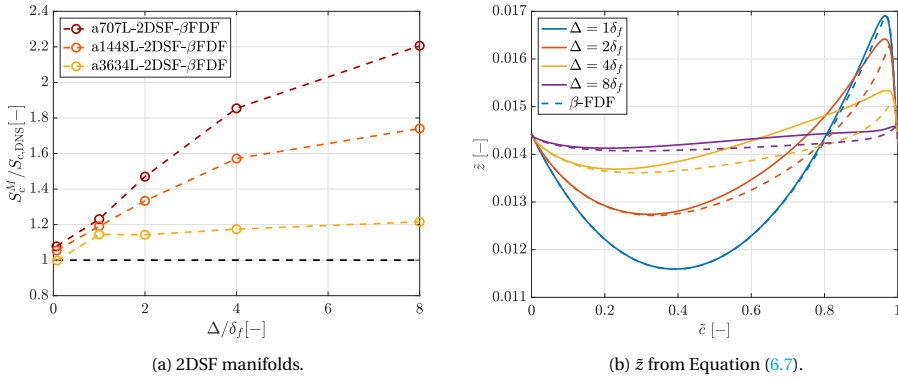


Figure 6.6: (a) Ratio of modelled versus DNS consumption speed for cases ten to twelve in Table 6.3 (2DSF manifolds), for increasing filter widths. (b) Comparison of filtered mixture fraction \bar{z} (solid lines) with the one reconstructed with the β -FDF model (dashed lines, Eq. (6.7)) of the strained flamelet a3634L at varying filter width Δ .

Overall, this *a priori* analysis on the laminar flame showed the limitations of manifolds made of unstretched flamelets in mimicking the local changes of reaction rate due to differential/preferential diffusion and strain, at both unfiltered and filtered grids and regardless of the subgrid model used. This suggests that a correction is necessary in turbulent LES settings to account for the inaccurate thermochemical states provided by this type of manifold and correctly predict the flame properties cross-grid, which is discussed in Section 6.3.4.

FIXED-STRAIN FLAMELETS WITH VARYING EQUIVALENCE RATIO

The ability of a manifold of fixed-strain flamelets at varying equivalence ratio (2DSF) to mimic the behaviour of the 2D laminar strained lean hydrogen flame is assessed in this section for three levels of applied strain (tenth to twelfth case in Table 6.3). The ratios between modelled and DNS consumption speeds are presented in Figure 6.6a for increasing filter sizes. Introducing variable equivalence ratio with the additional controlling variable z , while not necessary in planar laminar flames, is essential to capture local strain and curvature effects in turbulent flames with differential/preferential diffusion.

For the unfiltered DNS mesh, the results for the laminar flame are expected to match those of the 1DS manifold (see Fig 6.3), since each couple (c, z) in a laminar strained flame would correspond to the same flamelet. This is indeed the case, despite some negligible discrepancies attributable to the numerical errors of the different solvers being amplified by the additional controlling variable z . However, at filtered grids, computing $\bar{z}(\bar{c}, \sigma_{c,sgs}^2)$ with Equation (6.7) results in an underestimate of the filtered mixture fraction across the strained flamelets of the manifold, as shown in Figure 6.6b. As this underestimated \bar{z} is used as a controlling variable for the manifold, this could result in locally accessing richer flamelets and thus overestimating reaction rates. Assessing the impact of this parametrisation inaccuracy gives scope to the present analysis.

Indeed, comparing Figure 6.6b with Figure 6.3 reveals an overestimated consumption speed with the 2DSF manifold, particularly at smaller filters. However, the overall error

decreases substantially with increasing strain rate, the reasons for which will be discussed in Appendix D.2. Additionally, in the limit of high strain rate, the consumption speed achieves a substantial filter independence, which represents an improvement with respect to the 2DU manifold, for instance.

Overall, this *a priori* analysis on the laminar flame highlighted that manifolds made of single (see Sec. 6.3.1) or multiple strained flamelets at a fixed strain rate show improved performance with respect to unstretched flamelets, particularly in the limit of high strain, giving scope to further tests in turbulent settings.

IMPORTANCE OF RE-INTERPOLATING THE MANIFOLD OVER \tilde{z} IN β -FDF CLOSURES

While performing the *a priori* analysis, the authors noted a significant dependence of the predicted consumption speed at filtered grids on whether the manifold source term is re-interpolated over \tilde{z} obtained with Equation (6.7) or not. This re-interpolation was introduced by Berger *et al.* [118] in a presumed-FDF modelling framework to be able to assume statistical independence between the FDF of the progress variable and that of a quantity uniquely-related to the mixture fraction. However, in other LES studies [see 119, 120, 168, for example] this re-interpolation is not performed, even though the same statistical independence is assumed, and good results are still ensured. Note that the re-interpolation also importantly serves to consider the effect of the changing cross-flame mixture fraction at different filters (and so different progress variable variance $\sigma_{c,sgs}^2$) over the tabulated reaction rates. This means that in studies where this step is not performed in the tabulation, the correct $\bar{\omega}(\tilde{c}, \tilde{z})$ is found in the table at the wrong value of mixture fraction, and a different and inherently wrong $\bar{\omega}$ is referenced with the values \tilde{c} and \tilde{z} transported in a LES framework. Note that this effect occurs only for premixed cases with preferential diffusion, such as hydrogen/air flames, where the mixture fraction is not constant as a function of the progress variable. In this section, the quantitative impact of this re-interpolation is clarified once for all *a priori*.

A point A is now taken across the flame front of the a3634L simulation at $y = 0$ (centerline) and $c = 0.8$, which is very close to the cross-flame peak reaction rate. Note that this flame front is representative of any premixed flame front with varying local mixture fraction due to preferential diffusion, regardless of whether laminar or turbulent, or whether curved or strained. This point is placed in the map of H_2 source term obtained from an unstretched flamelet manifold [as used in 118–120, 168] at $\sigma_{c,sgs}^2 = 0$. The position of the point within the manifold, as well as the unstretched flamelet it belongs to, is shown in Figure 6.7. The relative error $\epsilon_{rel,A}$ of the obtained modelled H_2 source term by mass $\dot{\omega}_{H_2,A}^M / \rho_A^M$ with respect to the reference one $\dot{\omega}_{H_2,A}^{ref} / \rho_A$ is reported in the first row of Table 6.4, showing an overestimate as discussed in Section 6.3.1 for this manifold type.

The same point at $y = 0$ and $\tilde{c} = 0.8$ is taken from the filtered DNS field at $\Delta = 2\delta_f$, namely A' . The properties of this point are reported in the second row of Table 6.4. The comparison with point A shows that $\tilde{z}_{A'} > z_A$ and $\bar{\omega}_{H_2,A'}^{ref} / \rho_{A'} < \dot{\omega}_{H_2,A}^{ref} / \rho_A$, as expected due to the scalar redistribution over the thickened filtered flame. Hence, point A' is placed over a manifold (\tilde{c}, \tilde{z}) map at $\sigma_{c,sgs,A'}^2$ with (Figure 6.8a) and without (Figure 6.8b, point A'') re-interpolation. In the first case, the graph shows that point A' falls very close to the flamelet with the same nominal mixture fraction (or the same flamelet index ϕ_{FL}) as point A, despite a small local error. The upward shift of the point in the map

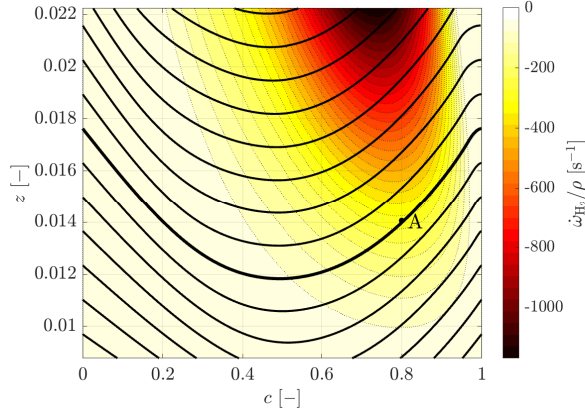


Figure 6.7: Map of tabulated H_2 source term $\dot{\omega}_{H_2}/\rho$ at $\sigma_{c,sgs}^2 = 0$ as a function of progress variable c and Bilger mixture fraction z .

Table 6.4: Reference (ref) and modelled (M) hydrogen source terms $\dot{\omega}_{H_2}$ in points A (unfiltered grid), A' and A'' (filtered grid).

Point	c [-]	$\sigma_{c,sgs}^2$ [-]	z [-]	$\dot{\omega}_{H_2}^{ref}/\rho$ [s^{-1}]	$\dot{\omega}_{H_2}^M/\rho$ [s^{-1}]	$\epsilon_{rel}(\dot{\omega}_{H_2}^M/\rho)$ [%]
A	0.8	0	0.0141	-212	-266	25.5
A'	0.8	0.048	0.0148	-105	-102	-2.86
A''	0.8	0.048	0.0148	-105	-142	35.2

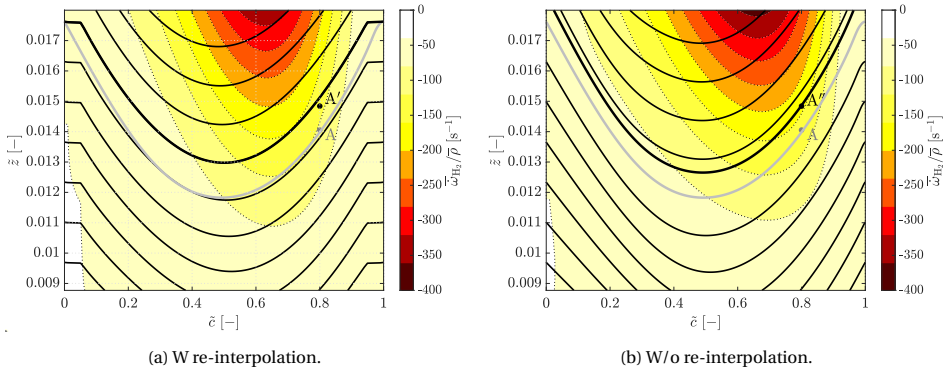


Figure 6.8: Map of tabulated filtered H_2 source term $\bar{\omega}_{H_2}/\bar{\rho}$ at $\sigma_{c,sgs}^2 = 0.048$ as a function of filtered progress variable \tilde{c} and filtered Bilger mixture fraction \tilde{z} (note rescaled range with respect to Figure 6.7). With (a) and without (b) re-interpolation over \tilde{z} from Eq 6.7 in the manifold according to Berger *et al.* [118].

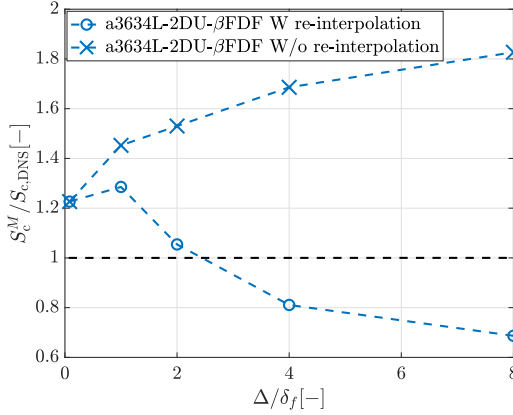


Figure 6.9: *A priori* consumption speeds for the case a3634L-2DU- β FDF case (see Table 6.3) over the unfiltered grid (first point from the left of each line) and with increasing filter width, with and without re-interpolation over \tilde{z} in the manifold tabulation.

correctly corresponds to an upward shift of the local \tilde{z} of the same flamelet, and thus to an accordingly upward shift of the reaction rate map. This upward map shift occurs thanks to the re-interpolation over \tilde{z} . In the second case, on the other hand, the point A'' is shifted over a richer flamelet, i.e. at a higher nominal equivalence ratio. This leads to an overestimate of the corresponding reaction rate at the same \tilde{z} .

The H_2 source terms obtained through the two different tabulation methods along with their errors are reported in the second and third row of Table 6.4. The table shows that failing to re-interpolate the manifold leads to an overestimate of the H_2 source term by more than 35%. With a correct re-interpolation, instead, the error drops to around 2% for this specific point. Considering integral quantities like the consumption speed, the overestimate is even more pronounced, leading to an overestimate of up to a factor two at the largest filter, as shown in Figure 6.9. This evidence remarks the importance of the re-interpolation over \tilde{z} in the manifold tabulation and questions the reliability of existing models tested neglecting this step, despite good results being still achieved. The author believes that a compensatory mechanism occurs involving an overestimated progress variable variance, but further investigation is required to prove this hypothesis, which is left to future work.

6.3.2. TURBULENT FLAMES

The 3D DNS dataset of turbulent flames is now assessed in order to evaluate how the tabulation approaches proposed in Section 6.2 perform when the flame is turbulent. The full list of cases assessed is provided in Table 6.5. Note that the nominal applied strain rate in the DNS differs from the one imposed in the manifold because turbulent eddies induce a mean (positive) tangential strain on the flame [160], therefore the total amount of strain experienced by the flame increases. This amount was directly estimated from the DNS [see 160, Fig. 7]. However, since the strain on the flame changes in space and time in the turbulent cases, multiple manifold strain levels have been tested for each DNS case

Table 6.5: Summary of the cases analysed and manifold strategy used for the turbulent strained flames.

Tested model name	Case nominal strain rate [s ⁻¹]	Manifold type	Manifold strain rate a [s ⁻¹]	Subgrid model	Parametrisation variables
a2000T-1DSa5000- β FDF	2000	1DS	5000	β -FDF	$\tilde{c}, \sigma_{c,sgs}^2$
a2000T-1DSa10000- β FDF	2000	1DS	10000	β -FDF	$\tilde{c}, \sigma_{c,sgs}^2$
a5000T-1DSa5000- β FDF	5000	1DS	5000	β -FDF	$\tilde{c}, \sigma_{c,sgs}^2$
a5000T-1DSa10000- β FDF	5000	1DS	10000	β -FDF	$\tilde{c}, \sigma_{c,sgs}^2$
a2000T-2DU- β FDF	2000	2DU	-	β -FDF	$\tilde{c}, \sigma_{c,sgs}^2, \tilde{z}$
a5000T-2DU- β FDF	5000	2DU	-	β -FDF	$\tilde{c}, \sigma_{c,sgs}^2, \tilde{z}$
a2000T-2DSFa5000- β FDF	2000	2DSF	5000	β -FDF	$\tilde{c}, \sigma_{c,sgs}^2, \tilde{z}$
a2000T-2DSFa10000- β FDF	2000	2DSF	10000	β -FDF	$\tilde{c}, \sigma_{c,sgs}^2, \tilde{z}$
a2000T-2DSFa15000- β FDF	2000	2DSF	15000	β -FDF	$\tilde{c}, \sigma_{c,sgs}^2, \tilde{z}$
a5000T-2DSFa5000- β FDF	5000	2DSF	5000	β -FDF	$\tilde{c}, \sigma_{c,sgs}^2, \tilde{z}$
a5000T-2DSFa10000- β FDF	5000	2DSF	10000	β -FDF	$\tilde{c}, \sigma_{c,sgs}^2, \tilde{z}$
a5000T-2DSFa15000- β FDF	5000	2DSF	15000	β -FDF	$\tilde{c}, \sigma_{c,sgs}^2, \tilde{z}$
a2000T-2DU-FT	2000	2DU	-	F-TACLES w/o Ξ	$\tilde{c}, \tilde{z}, \Delta$
a5000T-2DU-FT	5000	2DU	-	F-TACLES w/o Ξ	$\tilde{c}, \tilde{z}, \Delta$
a2000T-2DU-FTWF	2000	2DU	-	F-TACLES w Ξ	$\tilde{c}, \tilde{z}, \Delta$
a5000T-2DU-FTWF	5000	2DU	-	F-TACLES w Ξ	$\tilde{c}, \tilde{z}, \Delta$

around the total value estimated from the DNS, and further considerations are provided in Section 6.3.3.

6

IRREDUCIBLE ERROR

An irreducible error is introduced to evaluate how accurately a given set of input parameters can be employed to reproduce different flame states (identified by the fuel reaction rate in the present analysis). The irreducible error is defined as [172, 173]

$$\epsilon_{irr}^2 = \frac{\langle (\dot{\omega}_{H_2} - \langle \dot{\omega}_{H_2} | \Psi \rangle)^2 | c \rangle}{\max(\langle \dot{\omega}_{H_2} | c \rangle)^2}, \quad (6.12)$$

where Ψ is a set of input parameters, and quantifies the fluctuations of reaction rate with respect to its mean value. Only for this case, the irreducible error is calculated by sampling DNS data points at two different time steps (nominally $t = t_1$ and $t = t_2$) to improve the accuracy. Figures 6.10 and 6.11 show respectively midplane reaction rate contours at the two time steps, and the corresponding irreducible errors, for both unfiltered data and filtered data with increasing Δ . Only the case at nominal applied strain rate $a = 5000 \text{ s}^{-1}$ is reported as the lower strain rate case yields similar outcomes.

For the unfiltered mesh (Figure 6.11a), using only the progress variable as controlling parameter results in $\dot{\omega}_{H_2}$ fluctuations that reach 15% of the mean value at $c = 0.7$. Although this value is smaller than those reported in existing leaner and low-strain cases (e.g. see $\phi = 0.4$ in Figure 2 of [118]), where the error reaches up to 70%, it still indicates substantial reaction rate fluctuations due to the combination of differential/preferential diffusion effects and local strain and curvature induced by turbulence. When mixture fraction is added to the controlling parameters the maximum irreducible error on the unfiltered mesh reduces to as low as 2%. This suggests that, unlike the planar laminar case (see Sec. 6.3.1), a manifold made of fixed-strain flamelets with varying equivalence ratio featuring z as additional controlling variable is expected to strongly improve the performance of tabulated chemistry models in the turbulent setting.

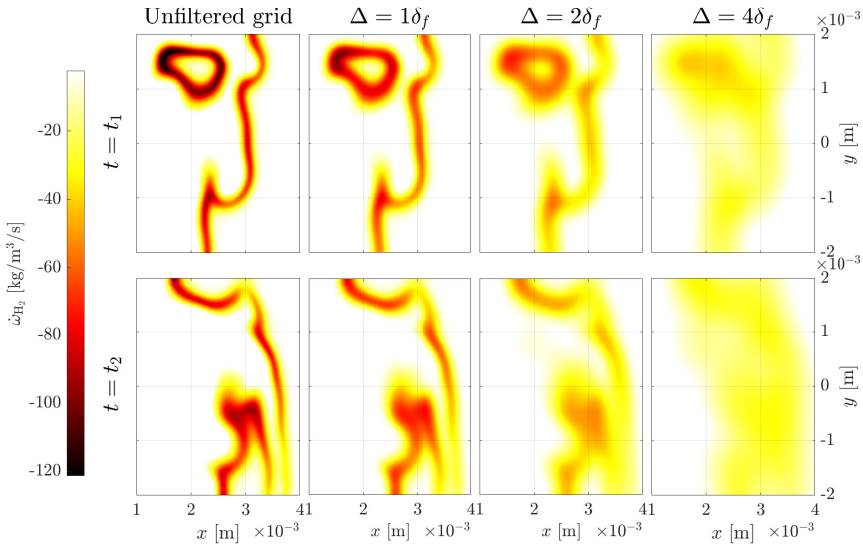


Figure 6.10: Snapshots at $t = t_1$ (first row) and $t = t_2$ (second row) of H_2 source term at the mid-plane of the a5000T simulation over the unfiltered field and with increasing filter width.

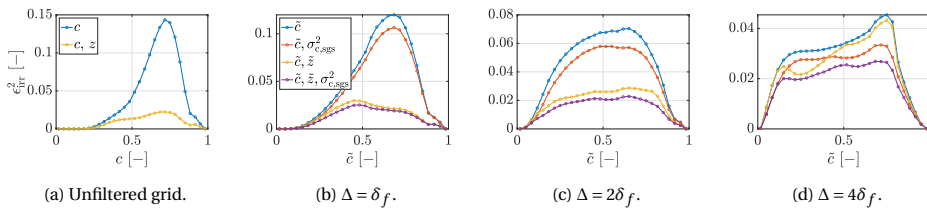


Figure 6.11: Irreducible error of the H_2 source term $\dot{\omega}_{H_2}$ over the unfiltered grid (a) and with increased filter width (b-d) for the case a5000T. Points are sampled at both $t = t_1$ and $t = t_2$.

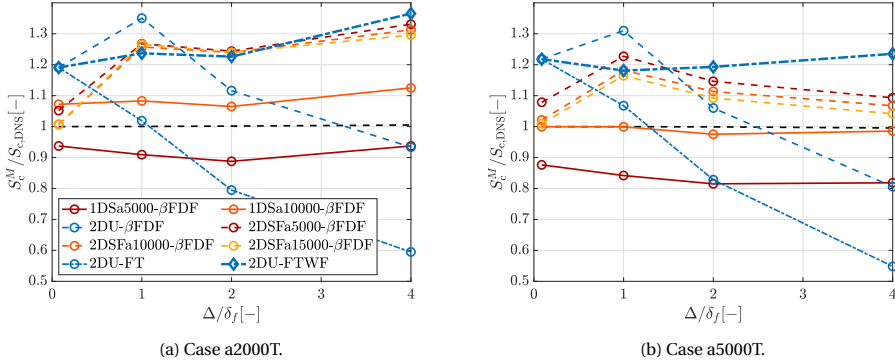


Figure 6.12: Ratio of modelled versus DNS consumption speed obtained using the manifold approaches of Table 6.5, for increasing filter widths and for values of nominal applied strain of $a = 2000 \text{ s}^{-1}$ (a) and $a = 5000 \text{ s}^{-1}$ (b).

When the mesh is filtered, combinations of input parameters including also the progress variable variance are considered. From Figures 6.11b-6.11d, it can be observed that the error remains always below 5% when considering a manifold parametrised with \tilde{c} and \tilde{z} , and it decreases further below 3% when introducing $\sigma_{c,sgs}^2$ among the controlling variables (presumed-FDF approach), although this introduction has a moderate impact at moderate filter sizes. This suggests that subgrid models not considering the variance as a parameter, like the F-TACLES model, may perform slightly worse solely due to the reduced accuracy of the parametrisation, particularly at coarser grids.

Interestingly, the error reduction due to including mixture fraction among the controlling variables becomes less strong as the filter width increases. This is due to the fact that mixture fraction variation are solely caused by preferential diffusion effects in the studied flames, and filtering the results reduces mixture fraction gradients thus reducing the reaction rate scatter across the mixture fraction space.

ERROR ON CONSUMPTION SPEED

In this section, the ability of the different manifold approaches of Table 6.5 to predict the consumption speed of a turbulent and strained lean premixed hydrogen flame is assessed. The consumption speed is computed as:

$$S_c^M = - \frac{1}{\rho_u Y_{H_2,u} L_y L_z} \int_V \dot{\omega}_{H_2} dV, \quad (6.13)$$

where $L_y = 4 \text{ mm}$ and $L_z = 3 \text{ mm}$ are the vertical and transversal length of the turbulent domain, respectively. The results presented in Figures 6.12 show data for the cases with nominal applied strain of $a = 2000 \text{ s}^{-1}$ and $a = 5000 \text{ s}^{-1}$. The manifolds based on unstretched flamelets with varying equivalence ratios (blue lines in Figure 6.12) lead to an overestimation of consumption speed of about 20% on the unfiltered grid, similarly to the laminar cases (see Sec. 6.3.1). Furthermore, the strong filter dependence observed in the laminar is also observed for the turbulent cases presented here, when the presumed FDF

approach with β -FDF is used. This dependence is instead somewhat relaxed when the F-TACLES approach is used with a wrinkling factor, which is computed in this study directly from the DNS dataset using Equation (6.9). In particular, the modelled consumption speed is overestimated up to 40% at small filter sizes and underestimated at large filter sizes when the presumed-FDF approach is used. When the F-TACLES approach (without wrinkling factor) is used, on the other hand, the consumption speed is underestimated at all filter sizes by up to 50% due to the absence of a subgrid wrinkling factor. Introducing the wrinkling factor still results in a remaining systematic overestimation of above 20%. Overall, these results indicate that manifolds based on unstretched flamelets introduce significant errors on consumption speed, which would be difficult to minimise due to the observed dependency on filter width.

Let's now consider the manifolds based on a fixed-strain flamelet (1DS in Table 6.5). The first observation is that in this case the consumption speed ratio is observed to be mainly independent of the filter width. The quantitative error depends on chosen value for the fixed-strain rate on the flamelet, which as explained earlier varies on the turbulent flame due to the effects of turbulent eddies. For this reason, for each nominal applied strain rate in the turbulent case, two manifolds are tested, respectively with imposed strain on the flamelet of $a = 5000 \text{ s}^{-1}$ and $a = 10000 \text{ s}^{-1}$, which are representative of the actual values observed from the DNS data. As observed in Figure 6.12 the error on the consumption speed is observed to be below or slightly above 10% for the lower strain case, and almost zero for the higher strain case when flamelets at $a = 10000 \text{ s}^{-1}$ are used. This is somewhat expected, since, the total strain rate experienced by the lower- and higher-strain flames in the DNS are approximately $7000\text{-}8000 \text{ s}^{-1}$ and $10000\text{-}11000 \text{ s}^{-1}$, respectively. Nevertheless, results also show that mispredicting the value of strain rate to apply on the flamelet up to 50% (e.g. see Fig. 6.12b, moving from $a = 10000 \text{ s}^{-1}$ to $a = 5000 \text{ s}^{-1}$ on the flamelet) produces an error on consumption speed below 20% at any filter width, which is still below the maximum error observed for the unstretched manifolds. Overall, these results indicate that a single strained flamelet can quantitatively reproduce the flame speed in flames subject to differential and preferential diffusion effects and potential subgrid thermodiffusive instabilities, as long as the fixed-strain value is imposed within a reasonable range.

Let's now consider the manifolds based on a fixed-strain flamelets with varying equivalence ratio (2DSF in Table 6.5). The application of varying equivalence ratio in the manifold stems from the fact that turbulent eddies and induced strain and curvature might affect the thermochemical state within the flame. By looking at the consumption speed ratio in Figure 6.12, one can notice that the error now depends again on the filter width, although more weakly than the 2DU-type manifolds, and its maximum value ranges from 20% to 30% for the lower strain case (see Fig. 6.12a), and reduces to below 20% for the higher strain case (see Fig. 6.12b). Nevertheless, the error in this case is much less sensitive to the choice of the fixed-strain level imposed on the flamelets.

MODELLING ERROR

Additional insight on the performance of the various manifold approaches of Table 6.5 is provided by quantifying the conditionally averaged modelling error for the fuel reaction

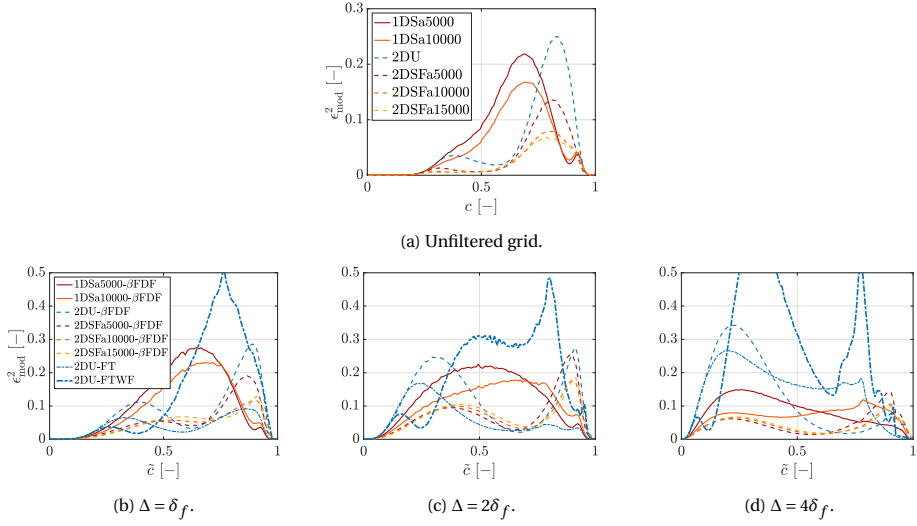


Figure 6.13: Conditionally averaged modelling error at a random time $t = t_1$ of the turbulent DNS flame with applied strain rate $a = 5000 \text{ s}^{-1}$, for unfiltered (top) and filtered (bottom) mesh at different filter widths. The nomenclature in the legend refer to Table 6.5.

6

rate, which is defined as [118]:

$$\epsilon_{mod}^2 = \frac{\langle (\dot{\omega}_{\text{H}_2}^M - \dot{\omega}_{\text{H}_2}^{\text{ref}})^2 | c \rangle}{\max(\langle \dot{\omega}_{\text{H}_2}^{\text{ref}} | c \rangle)^2}. \quad (6.14)$$

This definition allows to assess how the modelling error as compared to the peak mean reaction rate varies across the flame front. The error variation in filtered progress variable space is shown in Figs. 6.13a and 6.13b-6.13d respectively for the unfiltered and filtered (at different Δ) meshes. Midplane contour plots of the relative error according to Equation (6.11) are further shown in Figure 6.14 for a subset of cases in Table 6.5. Only the DNS case with applied strain rate $a = 5000 \text{ s}^{-1}$ is shown as similar observations could be made for the case at $a = 2000 \text{ s}^{-1}$. Consistently with the laminar flames analysis (Section 6.3.1) and the turbulent flame consumption speed assessment, the manifold of unstretched flamelets exhibits the highest modelling error on the unfiltered grid (see Fig. 6.13a), with an average deviation from the DNS reaction rate of about 25%. Accordingly, the highest relative errors are observed in space in the contour plots of Figure 6.14. The modelling error seems to only mildly reduce when the single fixed-strain flamelet is employed (even with the imposed strain rate of $a = 10000 \text{ s}^{-1}$ giving the smallest error on consumption speed). The error seems to reduce more significantly, instead, when a manifold of fixed-strain flamelets with varying equivalence ratio is used. The error peak in this case (see $\tilde{c} \approx 0.7$ in Fig. 6.13) reduces further when increasing the applied strain rate in the flamelets from $a = 5000 \text{ s}^{-1}$ to $a = 10000 \text{ s}^{-1}$, but shows negligible additional improvement for $a = 15000 \text{ s}^{-1}$, the reasons for which are discussed in the next subsection.

When the mesh is filtered, the modelling error for the unstretched flamelets manifold

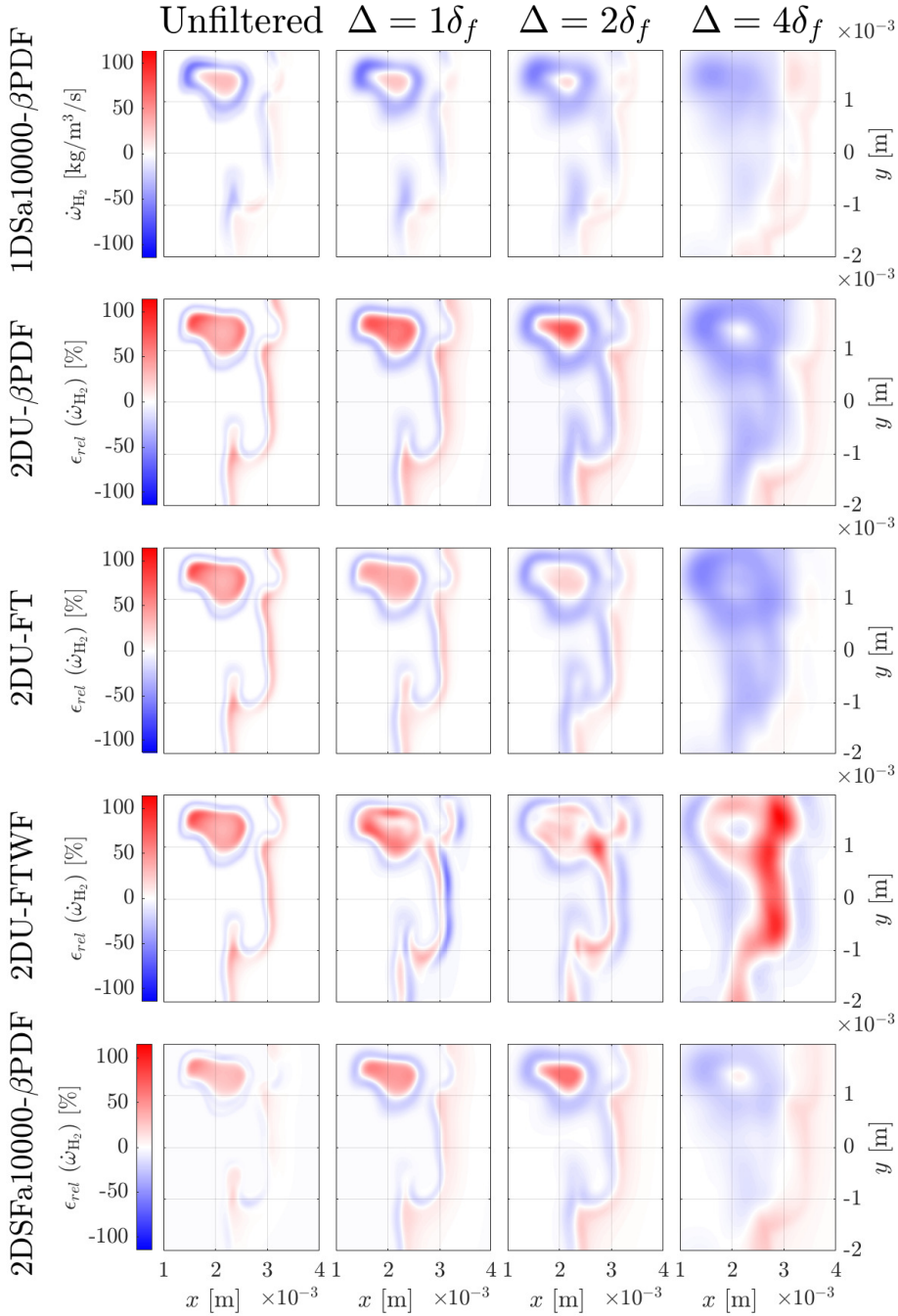


Figure 6.14: Midplane contours of relative error of the H_2 source term $\dot{\omega}_{\text{H}_2}$ (Eq. (6.11)) for increasing filter widths and some of the manifold approaches of Table 6.5.

and presumed β -FDF reaches values of about 30% at all filter widths. Furthermore, two peaks are observed, respectively at low values of progress variable (corresponding to underestimation of reaction rate, see Sec. 6.3.1) and high values of progress variable (corresponding to overestimation of reaction rate). In detail, the reaction rate is overall more overestimated at small filter sizes ($\Delta = \delta_f$, the error peak is stronger for large values of progress variable), and underestimated at large filter sizes (see $\Delta = 4\delta_f$, where the error peaks is stronger at low values of progress variable) confirming the strong filter-dependence of this manifold approach. At intermediate filter widths ($\Delta = 2\delta_f$), the two peaks are observed to be of the same magnitude, suggesting that the errors might compensate each other in this case, leading to about correct consumption speed observed for Figure 6.12.

When the F-TACLES approach is used without wrinkling factor (with the unstretched flamelets manifold), the modelling error is observed to remain below 10% for small filter sizes ($\Delta = \delta_f$), but the peak for low values of progress variable (underestimation of reaction rate) significantly increases to values above 20% for larger filter sizes. Unlike for the observation on the consumption speed in Section 6.3.2, however, introducing the wrinkling factor does not reduce the modelling error of Equation (6.14), and instead results in sharp peaks of about 50%. Consistently, the contour plots of Figure 6.14, show that for increasing filter sizes the relative error increases in magnitude in the F-TACLES approach when the wrinkling factor is introduced. However, this errors corresponds to both regions of overestimation and underestimation of reaction rate, which apparently compensate for each other when integrating the reaction rate to compute the consumption speed. This suggests that the wrinkling factor would introduce limitations in mimicking the correct local behaviour in terms of differential and preferential diffusion effects.

Let's now consider the performance of fixed-strain single-flamelet manifold with presumed β -FDF at increasing filter widths. Here the modelling error exhibits a similar behaviour to that observed for the irreducible error examined in Section 6.3.2. The error peak in this case is relatively high, between 20% and 30%, for the smallest filter width ($\Delta = \delta_f$), but decreases to values around 10% for $\Delta = 4\delta_f$. Note that the error is lower when a strain rate of $a = 10000\text{s}^{-1}$ is applied on the flamelet since this value is closer to the value experienced by the turbulent flame. The higher error at smaller filter sizes is explained by the fact that a single flamelet is not able alone to capture the correct thermochemical states in correspondence of the local leaning and enrichment of mixture fraction induced by preferential and differential diffusion effects in strained and curved regions of the flame, corresponding to modified local reactivity. The fact that the error in the consumption speed is still very low for this manifold is therefore probably due to compensating overestimation and underestimation of reaction rates in correspondence of leaner and richer regions, respectively. The improvement at larger filter sizes is due to the fact that these local phenomena are moved more and more to subgrid scales at increased filter widths, allowing to observe at the resolved scales only the related overall increased flame reactivity induced synergistically by thermodiffusive instabilities and turbulence [see 46, for example]. As proved by this analysis, this globally increased flame reactivity can be captured with tabulated chemistry models by simply tuning the applied strain rate of a single flamelet.

Lastly, the manifold with fixed-strain flamelets of varying equivalence ratio is assessed.

This manifold approach leads to the smallest modelling error peaks among the cases of Table 6.5, which are observed in Figure 6.13a to be overall contained around 10% or below. Similar considerations can be driven by inspecting the contour plot of the relative error for this manifold in Figure 6.14. This suggests that this approach, unlike the others, has potential to mimic an about correct local behaviour in terms of differential and preferential diffusion effects in strained and curved regions. The fact that other manifold approaches lead to reduced errors on the consumption speed at specific meshes is thus to be interpreted as compensation of errors in the parametrisation as demonstrated by the present analysis (a part from the IDS-type manifold at large filters discussed in the previous paragraph). A stronger sensitivity to the choice of the value of the fixed-strain level in the manifold is observed as compared to the results for the consumption speed (which is generally not known *a priori* in a LES context). This dependence is further investigated in the next section.

6.3.3. CHOICE OF FIXED STRAIN RATE VALUE

Although improved performance was observed in the *a priori* analyses of fixed-strain flamelets manifolds with varying equivalence ratio for both laminar and turbulent conditions (Tables 6.3 and 6.5 respectively), the values of strain imposed on the flamelets in these analyses could be chosen by inspection of the DNS data. Although some methods to estimate the flame strain have been proposed for hydrocarbon fuels [174], generally it is not straightforward to find such a value in the context of a LES, especially in hydrogen flames. An analysis is thus conducted here to assess how the choice of the fixed-strain value influences the reconstructed reaction rate. For this purpose the stretch factor $I_0 = S_c/S_L$ of a laminar flamelet at the nominal equivalence ratio $\phi = 0.5$ across different strain rates is computed, and presented in Figure 6.15. As observed, the stretch factor exhibits a peak value of approximately 1.55 in the strain rate range of 7000 s^{-1} to 8000 s^{-1} , indicating a 55% increase in consumption speed as compared to the laminar unstretched flame speed. Notably, the stretch factor shows a steep increase with strain rate up to values of about $a = 3600 \text{ s}^{-1}$, followed by a more gradual variation in the region near the peak. For values of strain rate ranging between about 3600 s^{-1} to 15000 s^{-1} (shaded area in the figure), a misprediction of applied strain rate would lead to a maximum 10% error in the stretch factor. This range includes the strain rates of all tested manifolds of strained flamelets in the turbulent setting. This result suggests that imposing any strain rate on the flamelet within this range would lead to similar predictions, at least for integral quantities like the consumption speed, which is consistent with the observations in Figure 6.12.

This outcomes suggests that, at least for the ranges of turbulence and strain investigated in this study, relatively low-dimensional manifolds consisting of a single strained flamelet can be used in a LES with relatively large filter sizes to predict, with limited errors, integral quantities such as consumption speed, even in presence of preferential and differential diffusion effects. A set of flamelets with varying equivalence ratio, but still with fixed value of strain, might be accurate enough to further predict local fluctuations of reaction rates induced by preferential and differential diffusion effects, such as strain and curvature effects and the onset of thermodiffusive instabilities. This represents an important simplification for flamelets-like models as strained flamelets with varying levels of strain, implying a higher-dimensional manifold, might be avoided. However, this

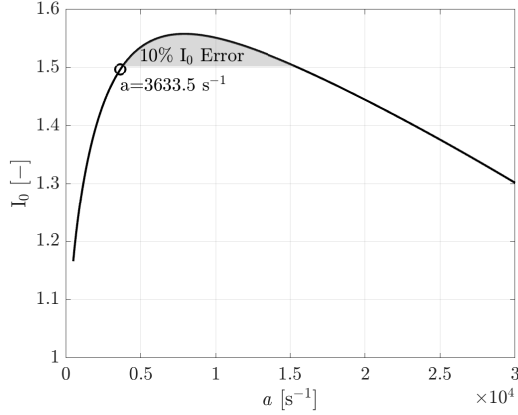


Figure 6.15: Stretch factor of a laminar flamelet as a function of the applied strain rate.

should be ultimately assessed *a posteriori* in future works.

6.3.4. UNSTRETCHED FLAMELETS CORRECTION

Previous sections have demonstrated both poor *a priori* performance and strong filter dependence in models based on manifolds constructed from unstretched flamelets. Specifically, unlike strained flamelets, unstretched flamelets provided a poor prediction of the consumption speed already in laminar conditions, showing a counter-intuitive systematic decrease with increasing filter width. This systematic decrease was more significant at higher simulation strain rates, suggesting that the reaction rate map it provides is not a good picture of the thermochemical states of lean premixed and turbulent hydrogen flames, as later proved in Section 6.3.2. In light of this, a correction for the predicted turbulent consumption speed is proposed here based on the results of the laminar analysis.

At the highest tested strain rate, the predictions in the laminar analysis from both subgrid closures exhibited perfect agreement (see Fig. 6.4). This level of strain is marked in Figure 6.15, showing that its corresponding stretch factor belongs to the 10% band from the peak. A correction function $f(\Delta/\delta_f)$, valid for the range of strain rate considered, can therefore be derived from these laminar data, such that

$$\frac{S_c^*}{S_{c,DNS}} = f\left(\frac{\Delta}{\delta_f}\right) \frac{S_c^{2DU}}{S_{c,DNS}}, \quad (6.15)$$

where S_c^{2DU} represents the consumption speed reconstructed using the 2DU manifold, and S_c^* denotes the corrected consumption speed. The correction function is defined as

$$f\left(\frac{\Delta}{\delta_f}\right) = \left(\frac{S_c^{2DU,lam}}{S_{c,DNS}^{ref,lam}}\right)^{-1}, \quad (6.16)$$

and is obtained from the 2DU manifold applied to laminar simulations at $a = 3633.5 \text{ s}^{-1}$. To determine this function, a double exponential fit is performed using combined data

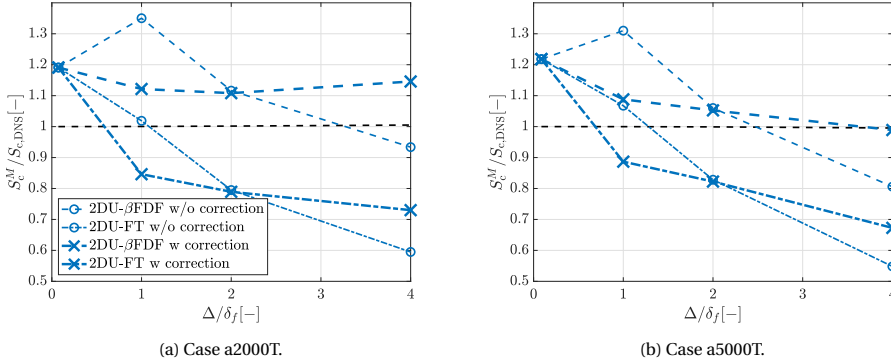


Figure 6.16: *A priori* consumption speeds for the turbulent cases obtained with 2DU type manifolds, with and without the proposed correction with increasing filter width. The reader is referred to Table 6.5 to interpret the graph legend. For a single snapshot of case a2000T (a) and a5000T (b).

points from both the β -FDF and F-TACLES models across all tested filtered grids. Note that the 2DU-FTWF tabulation with the wrinkling factor has not been corrected here due to the limitations highlighted in Section 6.3.2.

This correction is applied to both the 2DU- β FDF and 2DUFT tabulation predictions, with the results shown in Figures 6.16a and 6.16b for the cases a2000T and a5000T, respectively. The figures show that the correction significantly improves the 2DU- β FDF tabulation predictions. In both the a2000T and a5000T cases, the corrected consumption speed exhibits markedly reduced filter dependence, thereby addressing the primary limitation of this tabulation identified in previous sections. Moreover, the error decreases to below 15% in the lower strain rate case and to below 5% in the higher strain rate case. These results demonstrate that the weaknesses observed in 2DU manifold predictions stem solely from intrinsic tabulation errors rather than inaccuracies in the way the β -FDF subgrid model captures turbulence-chemistry interactions. Although these inaccuracies originate from incorrectly reconstructed local reaction rates, they can be effectively corrected at the integral level, corresponding to the grid cell scale in finite-volume CFD solvers, with a methodology similar to that suggested by Nilsson *et al.* [171] - through a correction derived from laminar simulations at strain rates near the peak stretch factor. This correction will be tested *a posteriori* in a future work.

Considering the 2DU-FT tabulation, on the other hand, the correction is not as effective. Although there is a moderate improvement, the prediction of the consumption speed remains substantially dependent on the width of the filter, and an underestimate above 20% remains. This proves that the proposed correction is not able alone to correct the reaction rate to account for subgrid wrinkling, but only for the intrinsic tabulation error of manifolds made of unstretched flamelets. Indeed, to further improve the predictions, this correction should be combined with an appropriate wrinkling factor. Some correction was proposed in this regard by combining a "laminar" and "turbulent" wrinkling factor [72, 117], where a similar correction to the one proposed here is applied for the former. Nevertheless, while such an approach is expected to improve predictions, the

analysis of Section 6.3.2 suggests that further improvements might still be necessary.

6.4. SUMMARY

This study presents a comprehensive *a priori* assessment of various tabulated chemistry models for lean premixed hydrogen combustion with differential and preferential diffusion, with particular focus on addressing the challenges posed by the synergistic effect of thermodiffusive instabilities and turbulence in strained counterflow settings. The main findings obtained through systematic analysis of both laminar and turbulent flame configurations are summarised below.

- **Limitations of Unstretched Flamelet Manifolds:** The investigation highlights significant inaccuracies in the thermochemical states parametrisation based on unstretched flamelet manifolds. These manifolds exhibit systematic overestimation of reaction rates at high progress variables and underestimation at low progress variables. While in some cases correct predictions are obtained by compensation of these effects, the consumption speed obtained through this manifold are overall unreliable, and worsen with increasing strain rates and filter widths, thus requiring and *ad hoc* correction.
- **Effectiveness of Strained Flamelet Approaches:** Fixed-strain flamelet manifolds demonstrate improved performance compared to unstretched counterparts. When the flamelet strain rate matches the total strain rate of the simulated flame, the single strained flamelet manifold shows a remarkably low modelling error at large filter sizes. The novel strained flamelets manifold, combining fixed strain with varying equivalence ratio, offers enhanced ability to reconstruct the local reaction rates determined synergistically by thermodiffusive instabilities and turbulence at all tested filter sizes.
- **Critical Importance of Manifold Re-interpolation:** The study highlights the crucial role of re-interpolating manifolds over filtered mixture fractions in β -FDF closures. Failure to perform this re-interpolation leads to significant overestimation errors (up to 100%) in reaction rates, particularly at filtered grids. This finding calls into question the reliability of previous simulations that omitted this step.
- **Strain Rate Selection Guidelines:** Analysis of the stretch factor reveals a wide range of strain rates (3500-15000 s⁻¹) where the corresponding stretch factor changes by less than 10%. The strain rate for fixed-strain flamelets manifolds should be selected within this range to ensure the model predictions remain relatively consistent in a LES framework, where the simulation strain rate is unknown *a priori*.
- **Correction Methodology for Unstretched Manifolds:** A novel correction function derived from laminar simulations significantly improves the predictions *a priori* of integral quantities such as the consumption speed of unstretched flamelet manifolds, reducing filter dependence. While effective for β -FDF models, this correction proves less successful for F-TACLES implementations, suggesting the need for combined approaches with wrinkling factors.

Overall, for coarse grid simulations, ultra-light manifolds consisting of single strained counterflow flamelets with appropriate strain rates and β -FDF subgrid closures offer computationally efficient and reliable solutions to capture the increased reactivity at subgrid scales determined by tothermodiffusive instabilities, turbulence, and strain. However, it's important to note that this approach works effectively only at coarser grids, as finer resolutions would reveal the model's inability to capture local mixture fraction and reaction rate oscillations, potentially leading to poor *a posteriori* performance. For higher fidelity requirements across multiple grid resolutions, both the corrected unstretched flamelets manifold and the novel manifold with fixed strain and varying equivalence ratio with β -FDF closure provides reliable predictions of integral quantities such as the consumption speed. Ultimately, the novel strained manifold shows the best performance among all the tabulations tested in reconstructing the local reaction rates.

Unlike previous works, this study achieves modelling improvements without increasing the dimensionality of the manifolds, thereby maintaining computational efficiency and keeping memory costs unchanged. This work advances the understanding of tabulated chemistry modelling for lean hydrogen combustion, and showcases new modelling strategies for designing lean premixed hydrogen combustion devices that leverage the emission reduction and improved stability of strained hydrogen combustion.

7

CONCLUSIONS AND OUTLOOK

*E quindi uscimmo a riveder le stelle
And then we emerged to see the stars again*

Dante Alighieri

This thesis investigated lean premixed hydrogen flames under intensive strain through detailed numerical simulations. The conclusions achieved can be split into two main blocks. The first block sheds light on the unexplored fundamental features of lean premixed hydrogen flames in strained conditions, particularly considering flame stability and NO_x emissions. The second block leverages the gathered fundamental knowledge to formulate and test novel and affordable computational fluid dynamics modelling approaches that are able to accurately predict the structure and the dynamics of strained hydrogen flames. The insights obtained concerning these two blocks are summarised in Sections 7.1 and 7.2 of this Chapter, respectively. The outlook and societal impact of the work performed in this thesis is discussed in Section 7.3. Finally, recommendations for future works to advance the research in strained hydrogen combustion modelling towards practical hydrogen combustion systems are given in Section 7.4.

7.1. FUNDAMENTAL FEATURES OF STRAINED LEAN PREMIXED HYDROGEN FLAMES

Detailed chemistry analyses have been conducted on pure hydrogen-air lean premixed and strained flamelets in a counterflow reactants-to-products configuration. The studies explored one-, two-, and three-dimensional configurations across a wide range of strain rates. The main conclusions obtained considering the effect of increasing strain on the emissions, the structure, and the dynamics of lean premixed hydrogen flames are summarised below.

1. **Suppression of NO_x emissions.** Chapter 3 demonstrated that NO_x is significantly suppressed across the thermal route as the strain rate increases, despite the hydrogen flame becoming more reactive, thereby addressing key question # 1. This effect persists across a range of lean equivalence ratios and elevated pressures, and remains effective up to very high strain rates, unlike hydrocarbon flames which would instead extinguish. The suppression mechanism is not connected to a temperature reduction, but is rather attributed to a local redistribution of radicals involved in NO_x formation.
2. **Mitigation of preferential diffusion effects.** Through a careful analysis of the transport terms of the flamelet governing equations, it was demonstrated in Chapter 4 that preferential diffusion effects are mitigated by increasing strain. Key question #2 was thereby addressed by showing that strain establishes a differential transport of species on the flame-tangential direction which leads to a global flame enrichment, and which is limiting the impact of cross-flame preferential diffusion effects.
3. **Stabilisation of intrinsic flame instabilities.** By performing a stability analysis of counterflow flames in Chapter 5, it was demonstrated that intrinsic flame instabilities are suppressed at sufficiently high strain rate regardless of the direction of the imposed perturbation and of the tangential velocity gradients applied to strain the flames, thereby addressing key question #3.

Overall, this thesis revealed the potential of strain in reducing the emissions and improve the stability of lean premixed hydrogen combustion, and collected useful insights on

the structure and the dynamics of such flames that helped develop novel computational models, as it will be discussed in the next section.

7.2. ADVANCEMENTS IN AFFORDABLE CFD MODELLING FOR LEAN PREMIXED AND STRAINED HYDROGEN FLAMES

Collecting the insights obtained from the preceding chapters, novel modelling strategies were proposed in Chapter 6 for simulating lean premixed hydrogen combustion devices that leverage the advantages of strained hydrogen combustion previously discovered, thereby addressing key question #4 and the main research question. Indeed, while reduction of emissions and improved stability have been observed at increasing strain with direct numerical simulations in simplified canonical setups, existing tabulated chemistry models are not able to predict the response of lean premixed hydrogen flames to strain in a large eddy simulation framework, particularly in turbulent conditions. Detailed chemistry LES models, on the other hand, are computationally expensive and thus inconvenient to design practical combustion systems. The novel modelling approaches proposed are summarised below, along with the main conclusions drawn from their *a priori* testing at different filter sizes on a turbulent, lean premixed hydrogen flame in a counterflow configuration at varying strain rate.

1. **Corrected consumption speed with unstretched flamelets manifold.** Improved predictions *a priori* of the turbulent flame integral quantities and a reduction of their filter dependence have been achieved by correcting the consumption speed obtained with unstretched flamelet manifolds with a function derived from laminar simulations. This approach was successful when coupled with the β -FDF subgrid closure, while requires further improvement in the F-TACLES framework.
2. **Improved local reaction rates with fixed-strain counterflow flamelets manifold with varying equivalence ratio.** When coupled with the β -FDF subgrid closure, this manifold demonstrated improved performance across multiple grid resolutions with respect to the unstretched flamelets manifold, provided that the manifold strain rate is chosen within the correct range. Among all the manifolds tested, it showed the best performance in reconstructing the local reaction rates in a turbulent and intrinsically unstable lean premixed hydrogen flame undergoing both preferential and differential diffusion and strain effects.
3. **Reliable prediction from ultra-light single-strain counterflow flamelet manifold.** When coupled with the β -FDF subgrid closure, a manifold made of a single counterflow strained flamelet was proved to capture at coarse grids ($\Delta > 2\delta_f$) the increased reactivity at subgrid scales determined by thermodiffusive instabilities, turbulence, and strain. This solution delivers reliable predictions at a fraction of the computational cost, provided the flamelet strain rate is appropriately selected close enough to the strain conditions experienced by the turbulent flame.

Unlike previous works, the modelling approaches proposed and studied in this work do not increase the manifold dimensionality and thus maintain computational efficiency and limited memory costs. Ultimately, this thesis advanced the understanding and the

performance of tabulated chemistry models for lean premixed hydrogen combustion under strained conditions. This potentially enables more accurate simulations of practical hydrogen combustion systems leveraging the reduced emissions and improved stability of strained regimes. The proposed approaches, however, require *a posteriori* validation before they can be actually employed for combustor design, as it will be discussed in Section 7.4.

7.3. OUTLOOK

The findings of this thesis bridge a critical gap between fundamental flame physics and practical hydrogen combustion technologies. By demonstrating that intensive strain suppresses NO_x emissions and stabilises intrinsic flame instabilities, this work not only advances our scientific understanding but also unlocks new opportunities for the design of low-emissions and stable hydrogen combustion systems.

Furthermore, the novel modelling strategies proposed here offer a pathway to affordable large eddy simulations of lean premixed hydrogen flames, for which existing LES models are not suited due to hydrogen's differential and preferential diffusion effects. Unlike the recently proposed approaches that rely on computationally expensive detailed chemistry or high-dimensional manifolds, these strategies maintain efficiency and accuracy while capturing the complex interactions between strain, turbulence, and thermodiffusive instabilities. This balance between accuracy and computational feasibility is essential for industrial applications such as aviation, where rapid design iterations and optimisation are required to meet stringent performance and safety requirements. By enabling more reliable simulations of strained hydrogen flames, this research supports the development of next-generation gas turbines, industrial burners, and propulsion systems that can operate with minimal emissions and maximal stability, thereby helping advance the TRL of hydrogen propulsion and energy technologies.

From a broader perspective, the advancements presented in this thesis contribute to accelerating the adoption of hydrogen as a sustainable fuel. Hydrogen combustion holds immense promise for decarbonising sectors where electrification is challenging such as power generation, heavy industry and particularly aviation, where battery-electric and hybrid-electric solutions are limited by energy density and weight constraints. However, emissions, flame stability, and computational modelling remain a major obstacle for its implementation and for the design of practical hydrogen combustion systems, which are currently still at a low TRL. The strategies developed in this thesis address these challenges directly, paving the way for the design of safe and clean hydrogen combustion technologies, thereby helping to meet global climate targets. Recommendations for future work to further advance research in this direction are provided in the next section.

7.4. RECOMMENDATIONS FOR FUTURE WORK

This thesis contributes to enhance the understanding of lean premixed and strained hydrogen flames, and to advance state-of-the-art simulation modelling solutions that are able to predict their interaction with turbulence. In order to enable the practical and cross-application use of the developed models, the following follow up investigations are recommended.

- ***A posteriori* testing.** The main caveat to the use of the proposed modelling approaches into practical combustor design is that their capabilities have been tested *a priori* in this thesis. Indeed, additional potential sources of inaccuracies are introduced when running an actual large eddy simulation, which can impact the reliability of the results. For instance, the subgrid variance of the progress variable should be estimated through an additional transport equation in a *a posteriori* applications, which involves additional modelling assumptions in some of its terms, unlike *a priori* where it is found from the filtered DNS progress variable field. Furthermore, scalar and velocity gradients are found from the resolved fields in LES setups, thereby potentially neglecting or inaccurately modelling possible subgrid effects on the resolved scales, unlike *a priori* where the gradients are found directly by filtering those obtained from the DNS fields. In light of this, future works should focus on validating the proposed modelling approaches into practical *a posteriori* LES setting, in order to provide a conclusive assessment of their reliability.
- **Improved manifold fixed strain rate estimation.** In this thesis, manifolds based on fixed strain counterflow flamelets have been proposed and tested in Chapter 6, and this approach allowed to reduce substantially the modelling error when the flamelets strain rate was close enough to the total strain rate of the simulated flame. Although general guidelines have been provided to select the manifold strain rate based on the stretch factor, future work should focus on improving the correct strain rate selection in absence of DNS data. For instance, it is well known from literature that the turbulent burning velocity is strongly dependent on the length scale ratio in turbulent flames with unity Lewis number, as it alters the flame surface area generation due to tangential strain rate [175]. This relationship could be further explored in hydrogen flames, and the length scale ratio in turbulent settings could be related to an appropriately scaled strain rate in laminar flamelets which mimics the increase in turbulent flame speed. Another viable strategy would be to directly define a correlation function for the stretch factor in turbulent flames with the the turbulent integral length scale by means of DNS data, as performed by Attili *et al.* [174] for lean premixed methane flames. Developing a similar correlation for hydrogen flames would allow to estimate the stretch factor in a turbulent flame *a priori*. Hence, the flamelet strain rate can be selected such that the same stretch factor is achieved.
- **Improved correction methodology for F-TACLES subgrid model.** In Chapter 6, the proposed correction of the consumption speed obtained with unstretched flamelet manifolds proved successful in turbulent settings only when using the β -FDF closure. Future work should focus on coupling the proposed correction methodology with an appropriate subgrid wrinkling factor formulation to improve the consumption speed predicted with F-TACLES subgrid closures.
- **Fixed curvature manifolds.** In Chapter 6 of this thesis, manifolds of flamelets at fixed strain rate have been tested with good success to capture the increased reactivity determined by thermodiffusive instabilities, turbulence, and strain. A similar increase in the tabulated reaction rates due to stretch could be in principle also

observed for manifolds at fixed curvature, obtained for instance through cylindrical flamelets. Testing this manifold type could be object of future works.

- **Effect of strain on enthalpy distribution and differential diffusion.** In this thesis, the effect of strain on the mixture fraction distribution has been addressed in Chapter 4, thereby discussing its implications on preferential diffusion effects. As a follow up, a similar analysis could be conducted on the enthalpy distribution and transport, to understand whether also differential diffusion effects are mitigated or they are enhanced by strain. Furthermore, the effect of shear-driven turbulence on enthalpy distribution could be assessed to understand whether it mimics the effect of strain, as it is the case for the mixture fraction distribution. If this was the case, one could also consider testing enthalpy as a controlling variable for the flamelet manifolds in tabulated chemistry models.
- **Soret effect.** In the simulations performed in Chapters 3, 5, and 6 of this thesis, Soret effect (or thermal diffusion) was not considered in the transport models to reduce the computational cost of direct numerical simulation setups with detailed chemistry. Multiple recent works, however, remarked the importance of Soret effect inclusion in both high-fidelity detailed chemistry and tabulated chemistry simulations to correctly predict the increased global consumption speed in thermodynamically unstable flames [66, 73]. While the assumption of negligible Soret does not affect the generality of the conclusions of this thesis regarding the effect of strain and improved tabulated chemistry modelling, future work should focus on including Soret effect in both detailed and tabulated chemistry formulations to enable more accurate quantitative predictions, possibly through simplified and computationally efficient modelling solutions [see 103, for example].
- **NO_x implementation in tabulated chemistry models.** The prediction of NO_x is a well known weakness of flamelet-based tabulated chemistry models regardless of whether simulating hydrogen or another fuel. Indeed, since NO is a slow-forming species, it keeps forming in the post-flame zone at high temperatures, where the commonly defined progress variable based on major species has already reached one. A possible walk-around would be to transport the NO mass fraction in the LES equations and tabulate its source term, instead of tabulating the mass fraction directly. However, this approach was not tested in the analysis of tabulated chemistry approaches in Chapter 6, and it is therefore left to future works to enable accurate predictions of NO_x emissions while designing strained hydrogen combustion devices.
- **Partially premixed flames.** Real flames in practical settings are never perfectly premixed, and this means that the flame can experience mixture fraction gradients not only due to preferential diffusion effects and turbulence, but also due to imperfect mixing between fuel and oxidizer, or due to local air dilution. Therefore, the approaches proposed in this thesis should be expanded and tested to non-perfectly premixed turbulent settings such as stratified flames [105], where multiple combustion modes are present.

- **Increased pressure setups.** While this work obtained valuable fundamental and modelling insights for atmospheric flames, real gas turbines operate at elevated pressure. Therefore, the proposed modelling approaches should be tested at increased pressure setups, where it is known that more favorable conditions are established for the onset of thermodiffusive instabilities [73] and for elevated NO_x emissions (see Sec. 3.4.5).
- **Fuel blends.** Due to the slow implementation of the hydrogen production and supply infrastructure and to its consequent unprofitable price, recent works in the combustion community focused on blending hydrogen with other fuels like ammonia [176], methane [42], or kerosene [177]. This way, one can reduce the carbon footprint of the fuel mixture while limiting the operational costs. In this thesis, only pure hydrogen fuel was considered due to its distinctive response to strain. Considering hydrogen blends, however, the stability and the emissions of the flame along with its response to strain and the tabulated chemistry modelling accuracy can vary depending on the hydrogen content. These aspects should be investigated in future works.

ACKNOWLEDGEMENTS

The research outcomes of this PhD journey are the result of contributions from everyone I have interacted with. Creativity in science is nurtured not only by hard work but also by the moments of inspiration and restoration shared with my partner, family, friends, and colleagues, both inside and outside the academic world. To all those who have been part of this journey, thank you for shaping my work and my growth.

First, I would like to express my deepest gratitude to my supervisor, Dr Ivan Langella, for his unwavering support throughout my PhD journey. His guidance during technical discussions, his trust in my abilities from the very beginning, and the freedom he gave me to shape my research and take ownership of my work have been invaluable. I am also grateful for the social events we organised within the research group. It has been inspiring to see the group grow in size, talent, and enthusiasm over the years, and I am proud to remain a part of it as a postdoc. I also thank my promotor, Prof Arvind Gangoli Rao, for his role as a cohesive group leader, fostering a strong sense of community within the entire combustion group. I especially appreciate the inspiring philosophical conversations we shared, often accompanied by some 'biofuels'.

I would like to thank all the friends and colleagues I met during these years for creating such a friendly and inspiring working environment. A special thanks to Gioele for being my older brother in research and for patiently discussing combustion modelling with me, especially when I was just starting out. To Davide, for the sport discussions and bike rides; to Federica, for the laughs at the coffee machine; and to Marisa, for bringing new energy to our group. Emanuele, thank you for hosting football games, and Antonio, for bringing enthusiasm and fun as a visiting researcher. Blanca, thank you for the laughs as my first office desk mate when I began my PhD, and Hugo, for being the only person I could talk football with in the faculty for a while. Nitish, thanks for the bike rides. To my fellow numerical pyromaniacs—Boris, Francesco Fico, Emre, Pablo, Mihnea, Turhan, Vittorio, Vaibhav, and Mohamad—and to all other pyromaniacs: Andre, Kaushal, Rishikesh, Alam, and Sarah. I also want to thank the Italian office crew—all the Francescos, Lorenzo, Andrea, Fabio (for the table tennis lunch games), Matteo, and Alessandro C.—and all my other colleagues who shared talks and fun activities with me: Ruben, Evert (for correcting my abstract in Dutch), Wessel, Floyd, Nikki, Kilian, Ankit, Alessandro B., and Dabo.

During my PhD journey, I had the fantastic opportunity to undertake a visiting period at Sapienza University. I would like to thank Dr Pasquale Lapenna for being a supportive and patient supervisor, and Prof Francesco Creta for warmly welcoming me into his group. I am also deeply grateful to all my colleagues and friends at Sapienza who made me feel at home with their warmth and laughter: Jacopo and Matteo, for sharing both the pain and joy of being Roma supporters; Chiara and Davide C. for the invaluable technical discussions; and Davide S. and Stefano. Thanks for making my time at Sapienza so special.

I would like to thank my friend Filippo for being my mate during the move from Sweden to the Netherlands and for sharing all these years as friends in Delft. My heartfelt

thanks also go to all my Delft friends—some of whom have come and gone—Daniele, Melania, Rossella, Francesco M., Marco, Antonio (for being a great housemate and for the inspiring aeronautics discussions), and Sara.

I would like to thank my lifelong friends from Italy for all the unforgettable experiences we shared together in Vicenza and across Europe during my PhD journey. A special thank you to Lori and Suns for being my best friends, always there when I needed you. To Galva, for the invaluable geopolitical and philosophical discussions that helped shape the ideas in this thesis, and for all the trips to London exploring Championship stadiums. Ale Zezza, thank you for the music conversations and the endless laughs over fantacalcio and sport curiosities. Casa, thank you for all the ‘pizzette in taverna’, for always organising ways for us to be together, and for the sport conversations. Ercolino, for your grit and energy in every challenge and activity. Rollia, thank you for the laughter and fun we’ve always shared. And Gaspa, for all your extravagant yet uniquely memorable initiatives and discussions. Having most of you here for this occasion means a lot to me. Finally, thank you to all my school friends—Gre, Roger, Ila, Cate, and Fibby—for the joyful gatherings that have brightened these years.

To my parents Mario and Chiara, for your unconditional support and love, and for the educational values you instilled in me, which have shaped me as a person. To Apo for being the brother I could always count on, and for challenging me in Aerospace related conversations (and dining disputes). To my grandparents: Nonna Margherita, for teaching me the importance of humanistic knowledge and the pursuit of culture; Nonno Nino, for his humour and for embodying charity and service, showing me the meaning of giving; Nonna Chiara, for her delicious meals and for teaching me the joy of welcoming others with warmth and a smile; and Nonno Renzo, for sharing his life stories with me as a child and for teaching me the importance of attention to detail and responsibility. I am also deeply grateful to all my aunts, uncles, and cousins for their support and the meaningful conversations we’ve shared along the way.

Last but not least, thank you, Elena, for being my partner through all the joys and challenges. Thank you for travelling across Europe to see each other, for the unforgettable experiences we’ve shared at home and around the world, and for listening to me with patience and love during every high and low of my research journey. Your presence has been my greatest strength.

BIBLIOGRAPHY

1. IEA. *Global Energy Review 2025* tech. rep. [accessed 30 May 2025] (IEA, 2025).
2. IEA. *World energy outlook* tech. rep. [accessed 30 May 2025] (IEA, 2024).
3. IEA. *World electricity generation in the Stated Policies Scenario* tech. rep. [accessed 30 May 2025] (IEA, 2024).
4. IEA. *OECD share of electricity generation by source* tech. rep. [accessed 30 May 2025] (IEA, 2024).
5. IEA. *CO2 Emissions in 2023* tech. rep. [accessed 30 May 2025] (IEA, 2024).
6. IEA. *Global CO2 emissions from energy combustion and industrial processes and their annual change, 1900-2023* tech. rep. [accessed 30 May 2025] (IEA, 2025).
7. IEA. *Annual change in energy-related CO2 emissions, 1900-2024* tech. rep. [accessed 30 May 2025] (IEA, 2025).
8. UNFCCC. *The Paris Agreement* tech. rep. [accessed 13 June 2025] (UNFCCC, 2018).
9. A. R. Masri. Challenges for turbulent combustion. *Proceedings of the Combustion Institute* **38**, 121–155 (2021).
10. IEA. *Hydrogen* tech. rep. [accessed 30 May 2025] (IEA, 2024).
11. IEA. *Global Hydrogen Review 2024* tech. rep. [accessed 30 May 2025] (IEA, 2024).
12. icograms.com. *The colors of hydrogen* tech. rep. [accessed 30 May 2025] (2025).
13. J. A. Turner. Sustainable hydrogen production. *Science* **305**, 972–974 (2004).
14. S. H. Jensen, P. H. Larsen & M. Mogensen. Hydrogen and synthetic fuel production from renewable energy sources. *International Journal of Hydrogen Energy* **32**, 3253–3257 (2007).
15. IEA. *Electrolysers* tech. rep. [accessed 30 May 2025] (IEA, 2024).
16. M. Lehner, R. Tichler, H. Steinmüller, M. Koppe, M. Lehner, R. Tichler, H. Steinmüller & M. Koppe. Methanation. *Power-to-Gas: Technology and Business Models*, 41–61 (2014).
17. C. Malins. What role is there for electrofuel technologies in European transport's low carbon future. *Cerology Report* (2017).
18. C. Tornatore, L. Marchitto, P. Sabia & M. De Joannon. Ammonia as green fuel in internal combustion engines: state-of-the-art and future perspectives. *Frontiers in Mechanical Engineering* **8**, 944201 (2022).
19. M. K. Singla, P. Nijhawan & A. S. Oberoi. Hydrogen fuel and fuel cell technology for cleaner future: a review. *Environmental Science and Pollution Research* **28**, 15607–15626 (2021).

20. C. White, R. Steeper & A. E. Lutz. The hydrogen-fueled internal combustion engine: a technical review. *International Journal of Hydrogen Energy* **31**, 1292–1305 (2006).
21. R. L. Speth & A. F. Ghoniem. Using a strained flame model to collapse dynamic mode data in a swirl-stabilized syngas combustor. *Proceedings of the Combustion Institute* **32**, 2993–3000 (2009).
22. W. Xu, L. Z. Liu, M. Loizidou, M. Ahmed & I. G. Charles. The role of nitric oxide in cancer. *Cell research* **12**, 311–320 (2002).
23. Y. Huang & V. Yang. Dynamics and stability of lean-premixed swirl-stabilized combustion. *Progress in Energy and Combustion Science* **35**, 293–364 (2009).
24. S. Ducruix, T. Schuller, D. Durox & S. Candel. Combustion dynamics and instabilities: Elementary coupling and driving mechanisms. *Journal of Propulsion and Power* **19**, 722–734 (2003).
25. Y. Hu & R. Kurose. Large-eddy simulation of turbulent autoigniting hydrogen lifted jet flame with a multi-regime flamelet approach. *International Journal of Hydrogen Energy* **44**, 6313–6324 (2019).
26. B. Johannessen, A. North, R. Dibble & T. Løvås. Experimental studies of autoignition events in unsteady hydrogen–air flames. *Combustion and Flame* **162**, 3210–3219 (2015).
27. K. R. Dinesh, H. Shalaby, K. Luo, J. Van Oijen & D. Thévenin. High hydrogen content syngas fuel burning in lean premixed spherical flames at elevated pressures: Effects of preferential diffusion. *International Journal of Hydrogen Energy* **41**, 18231–18249 (2016).
28. P. E. Lapenna, L. Berger, F. Creta & H. Pitsch. in *Hydrogen for Future Thermal Engines* 93–139 (Springer, 2023).
29. H. Pitsch. The transition to sustainable combustion: Hydrogen-and carbon-based future fuels and methods for dealing with their challenges. *Proceedings of the Combustion Institute* **40**, 105638 (2024).
30. T. Poinso & D. Veynante. *Theoretical and numerical combustion* (RT Edwards, Inc., 2005).
31. E. Abbasi-Atibeh & J. M. Bergthorson. Differential diffusion effects in counter-flow premixed hydrogen-enriched methane and propane flames. *Proceedings of the Combustion Institute* **37**, 2399–2406 (2019).
32. F. H. Vance, Y. Shoshin, L. de Goey & J. A. van Oijen. Quantifying the impact of heat loss, stretch and preferential diffusion effects to the anchoring of bluff body stabilized premixed flames. *Combustion and Flame* **237**, 111729 (2022).
33. W. T. Ashurst, N. Peters & M. Smooke. Numerical simulation of turbulent flame structure with non-unity Lewis number. *Combustion Science and Technology* **53**, 339–375 (1987).
34. D. Haworth & T. Poinso. Numerical simulations of Lewis number effects in turbulent premixed flames. *Journal of Fluid Mechanics* **244**, 405–436 (1992).

35. M. Baum, T. Poinso, D. Haworth & N. Darabiha. Direct numerical simulation of H₂/O₂/N₂ flames with complex chemistry in two-dimensional turbulent flows. *Journal of Fluid Mechanics* **281**, 1–32 (1994).
36. G. S. Jackson, R. Sai, J. M. Plaia, C. M. Boggs & K. T. Kiger. Influence of H₂ on the response of lean premixed CH₄ flames to high strained flows. *Combustion and Flame* **132**, 503–511 (2003).
37. E.-S. Cho & S. H. Chung. Improvement of flame stability and NO_x reduction in hydrogen-added ultra lean premixed combustion. *Journal of Mechanical Science and Technology* **23**, 650–658 (2009).
38. J. Van Oijen, A. Donini, R. Bastiaans, J. ten Thije Boonkamp & L. De Goey. State-of-the-art in premixed combustion modeling using flamelet generated manifolds. *Progress in Energy and Combustion Science* **57**, 30–74 (2016).
39. Y. M. Marzouk, R. L. Speth & A. F. Ghoniem. *Combined Effects of Curvature and Strain on Hydrogen Enriched Lean Methane Flames*. tech. rep. (Sandia National Lab. (SNL-CA), Livermore, CA (United States), 2005).
40. D. Ning, A. Fan & H. Yao. Effects of fuel composition and strain rate on NO emission of premixed counter-flow H₂/CO/air flames. *International Journal of Hydrogen Energy* **42**, 10466–10474 (2017).
41. T. Reichel, K. Goeckelera & O. Paschereit. Investigation of lean premixed swirl-stabilized hydrogen burner with axial air injection using OH-PLIF imaging. *Journal of Engineering for Gas Turbines and Power* **137**, 111513 (2015).
42. S. Link, K. Dave, F. F. de Domenico, A. G. Rao & G. Eitelberg. Experimental analysis of dual-fuel (CH₄/H₂) capability in a partially-premixed swirl stabilized combustor. *International Journal of Hydrogen Energy* **101**, 427–437 (2025).
43. W. Liang, F. Wu & C. K. Law. Extrapolation of laminar flame speeds from stretched flames: Role of finite flame thickness. *Proceedings of the Combustion Institute* **36**, 1137–1143 (2017).
44. E. Varea, J. Beeckmann, H. Pitsch, Z. Chen & B. Renou. Determination of burning velocities from spherically expanding H₂/air flames. *Proceedings of the Combustion Institute* **35**, 711–719 (2015).
45. D. Bradley, C. Sheppard, R. Woolley, D. Greenhalgh & R. Lockett. The development and structure of flame instabilities and cellularity at low Markstein numbers in explosions. *Combustion and Flame* **122**, 195–209 (2000).
46. L. Berger, A. Attili & H. Pitsch. Synergistic interactions of thermodiffusive instabilities and turbulence in lean hydrogen flames. *Combustion and Flame* **244**, 112254 (2022).
47. Y. B. Zeldvich. The oxidation of nitrogen in combustion and explosions. *Acta Physicochimica* **21**, 577 (1946).
48. J. Blauwens, B. Smets & J. Peeters. *Mechanism of “prompt” NO formation in hydrocarbon flames in Symposium (International) on Combustion* **16** (1977), 1055–1064.

49. S. J. Klippenstein, L. B. Harding, P. Glarborg & J. A. Miller. The role of NNH in NO formation and control. *Combustion and Flame* **158**, 774–789 (2011).
50. S. Liu & W. Zhu. A comprehensive review on the significant role of nitrous oxide in the transformation of nitrogen oxides during combustion. *Journal of the Energy Institute* **116**, 101678 (2024).
51. E. L. Merryman & A. Levy. *Nitrogen oxide formation in flames: the roles of NO₂ and fuel nitrogen in Symposium (international) on combustion* **15** (1975), 1073–1083.
52. C. K. Law. *Combustion physics* (Cambridge university press, 2010).
53. Eindhoven University of Technology. *CHEM1D. A one dimensional laminar flame code* 2021.
54. M. E. Morsy & J. Yang. The instability of laminar methane/hydrogen/air flames: Correlation between small and large-scale explosions. *International Journal of Hydrogen Energy* **47**, 29959–29970 (2022).
55. R. Bilger. *The structure of turbulent nonpremixed flames in Symposium (international) on combustion* **22** (1989), 475–488.
56. R. Bilger, S. Stårner & R. Kee. On reduced mechanisms for methane-air combustion in nonpremixed flames. *Combustion and Flame* **80**, 135–149 (1990).
57. A. Masri & R. Barlow. On conserved scalars that preserve stoichiometric mixture fraction. *Combustion and Flame* **260**, 113224 (2024).
58. M. Matalon & B. J. Matkowsky. Flames as gasdynamic discontinuities. *Journal of Fluid Mechanics* **124**, 239–259 (1982).
59. S. M. Candel & T. J. Poinsot. Flame stretch and the balance equation for the flame area. *Combustion Science and Technology* **70**, 1–15 (1990).
60. S. H. Chung & C. Law. An invariant derivation of flame stretch. *Combustion and Flame* **55** (1984).
61. T. M. Vu, M. S. Cha, B. J. Lee & S. H. Chung. Tip opening of premixed bunsen flames: Extinction with negative stretch and local Karlovitz number. *Combustion and Flame* **162**, 1614–1621 (2015).
62. A. Scholtissek, P. Domingo, L. Vervisch & C. Hasse. A self-contained progress variable space solution method for thermochemical variables and flame speed in freely-propagating premixed flamelets. *Proceedings of the Combustion Institute* **37**, 1529–1536 (2019).
63. J. Bechtold & M. Matalon. The dependence of the Markstein length on stoichiometry. *Combustion and Flame* **127**, 1906–1913 (2001).
64. M. Matalon, C. Cui & J. Bechtold. Hydrodynamic theory of premixed flames: effects of stoichiometry, variable transport coefficients and arbitrary reaction orders. *Journal of Fluid Mechanics* **487**, 179–210 (2003).
65. P. Pelce & P. Clavin. in *Dynamics of curved fronts* 425–443 (Elsevier, 1988).
66. M. R. Acquaviva, A. Porcarelli & I. Langella. Influence of Soret effect on flame structure and NO_x emissions in highly strained lean premixed counterflow hydrogen flames. *Fuel* **395**, 134939 (2025).

67. J. Beeckmann, R. Hesse, J. Schaback, H. Pitsch, E. Varea & N. Chaumeix. Flame propagation speed and Markstein length of spherically expanding flames: Assessment of extrapolation and measurement techniques. *Proceedings of the Combustion Institute* **37**, 1521–1528 (2019).
68. Z. Huang, Y. Zhang, K. Zeng, B. Liu, Q. Wang & D. Jiang. Measurements of laminar burning velocities for natural gas–hydrogen–air mixtures. *Combustion and Flame* **146**, 302–311 (2006).
69. G. K. Giannakopoulos, A. Gatzoulis, C. E. Frouzakis, M. Matalon & A. G. Tomboulides. Consistent definitions of “Flame Displacement Speed” and “Markstein Length” for premixed flame propagation. *Combustion and Flame* **162**, 1249–1264 (2015).
70. L.-Q. Wang, Y. Ge & H.-H. Ma. Revisiting effective Lewis number of combustible mixtures. *Fuel* **343**, 127909 (2023).
71. J. D. Regele, E. Knudsen, H. Pitsch & G. Blanquart. A two-equation model for non-unity Lewis number differential diffusion in lean premixed laminar flames. *Combustion and Flame* **160**, 240–250 (2013).
72. P. E. Lapenna, R. Lamioni & F. Creta. Subgrid modeling of intrinsic instabilities in premixed flame propagation. *Proceedings of the Combustion Institute* **38**, 2001–2011 (2021).
73. L. Berger, A. Attili & H. Pitsch. Intrinsic instabilities in premixed hydrogen flames: parametric variation of pressure, equivalence ratio, and temperature. Part 2–Non-linear regime and flame speed enhancement. *Combustion and Flame* **240**, 111936 (2022).
74. L. Berger, A. Attili & H. Pitsch. Intrinsic instabilities in premixed hydrogen flames: Parametric variation of pressure, equivalence ratio, and temperature. part 1–dispersion relations in the linear regime. *Combustion and Flame* **240**, 111935 (2022).
75. S. A. Kassar, L. Berger, P. E. Lapenna, F. Creta, H. Pitsch & A. Attili. Efficient and accurate calculation of dispersion relations for intrinsically unstable premixed flames. *Combustion and Flame* **269**, 113640 (2024).
76. M. L. Frankel & G. I. Sivashinsky. On effects due to thermal expansion and Lewis number in spherical flame propagation. *Combustion science and technology* **31**, 131–138 (1983).
77. G. Sivashinsky. Diffusional-thermal theory of cellular flames. *Combustion Science and Technology* **15**, 137–145 (1977).
78. S. Chung & C. Law. An integral analysis of the structure and propagation of stretched premixed flames. *Combustion and Flame* **72**, 325–336 (1988).
79. L. De Goeij, R. Mallens & J. T. T. Boonkamp. An evaluation of different contributions to flame stretch for stationary premixed flames. *Combustion and Flame* **110**, 54–66 (1997).
80. L. De Goeij & J. ten Thijsse Boonkamp. A flamelet description of premixed laminar flames and the relation with flame stretch. *Combustion and Flame* **119**, 253–271 (1999).

81. L. De Goeij & J. ten Thijsse Boonkamp. Mass burning rate of premixed stretched flames: integral analysis versus large-activation-energy asymptotics. *Journal of Engineering Mathematics* **62**, 67–84 (2008).
82. J. D. Buckmaster & G. S. S. Ludford. Theory of laminar flames. *Cambridge, New York* (1982).
83. F. Creta, P. E. Lapenna, R. Lamioni, N. Fogla & M. Matalon. Propagation of premixed flames in the presence of Darrieus–Landau and thermal diffusive instabilities. *Combustion and Flame* **216**, 256–270 (2020).
84. C. Matteucci, F. D’Alessio, A. Nicolai, P. E. Lapenna & F. Creta. Marginal stability of thermodynamically unstable circular expanding flames. *Proceedings of the Combustion Institute* **41**, 105920 (2025).
85. C. E. Frouzakis, N. Fogla, A. G. Tomboulides, C. Altantzis & M. Matalon. Numerical study of unstable hydrogen/air flames: shape and propagation speed. *Proceedings of the Combustion Institute* **35**, 1087–1095 (2015).
86. F. H. Vance, Y. Shoshin, P. de Goeij & J. van Oijen. Flame stabilization and blow-off of ultra-lean H₂-air premixed flames. *Energies* **14**, 1977 (2021).
87. G. I. Sivashinsky, C. K. Law & G. Joulin. On stability of premixed flames in stagnation-point flow. *Combustion Science and Technology* **28**, 155–159 (1982).
88. T. F. Xie & P. Y. Wang. Analysis of NO Formation in Counterflow Premixed Hydrogen-Air Flame in *Applied Mechanics and Materials* **284** (2013), 601–607.
89. P. Nilsson & X.-S. Bai. Effects of flame stretch and wrinkling on CO formation in turbulent premixed combustion. *Proceedings of the Combustion Institute* **29**, 1873–1879 (2002).
90. E. R. Hawkes & J. H. Chen. Comparison of direct numerical simulation of lean premixed methane–air flames with strained laminar flame calculations. *Combustion and Flame* **144**, 112–125 (2006).
91. W. Polifke, P. Flohr & M. Brandt. Modeling of inhomogeneously premixed combustion with an extended TFC model. *J Eng Gas Turbine Power* **124**, 58–65 (2002).
92. P. A. Libby & F. A. Williams. Structure of laminar flamelets in premixed turbulent flames. *Combustion and Flame* **44**, 287–303 (1982).
93. N. Darabiha, S. Candel & F. Marble. The effect of strain rate on a premixed laminar flame. *Combustion and Flame* **64**, 203–217 (1986).
94. H. Kolla & N. Swaminathan. Strained flamelets for turbulent premixed flames, I: Formulation and planar flame results. *Combustion and Flame* **157**, 943–954 (2010).
95. I. Langella & N. Swaminathan. Unstrained and strained flamelets for LES of premixed combustion. *Combustion Theory and Modelling* **20**, 410–440 (2016).
96. T. Sattelmayer, W. Polifke, D. Winkler & K. Döbbeling. NO_x-abatement potential of lean-premixed GT combustors. *Journal of Engineering for Gas Turbines and Power* **120**, 48–59 (1998).
97. A. Alqallaf, M. Klein & N. Chakraborty. Effects of Lewis number on the evolution of curvature in spherically expanding turbulent premixed flames. *Fluids* **4**, 12 (2019).

98. P. E. Lapenna, G. Troiani, F. D'Alessio & F. Creta. Synergistic interplay of thermodiffusive instability and turbulence in premixed flames. *Proceedings of the Combustion Institute* **40**, 105499 (2024).
99. L. Berger, A. Attili, M. Gauding & H. Pitsch. Effects of Karlovitz number variations on thermodiffusive instabilities in lean turbulent hydrogen jet flames. *Proceedings of the Combustion Institute* **40**, 105219 (2024).
100. C. Law. *Dynamics of stretched flames* in *Symposium (international) on combustion* **22** (1989), 1381–1402.
101. I. Langella. *Large eddy simulation of premixed combustion using flamelets* PhD thesis (University of Cambridge, 2016).
102. B. Fiorina, R. Vicquelin, P. Auzillon, N. Darabiha, O. Gicquel & D. Veynante. A filtered tabulated chemistry model for LES of premixed combustion. *Combustion and Flame* **157**, 465–475 (2010).
103. J. Schlup & G. Blanquart. Reproducing curvature effects due to differential diffusion in tabulated chemistry for premixed flames. *Proceedings of the Combustion Institute* **37**, 2511–2518 (2019).
104. J. de Swart, R. Bastiaans, J. van Oijen, L. de Goey & R. Cant. Inclusion of preferential diffusion in simulations of premixed combustion of hydrogen/methane mixtures with flamelet generated manifolds. *Flow, Turbulence and Combustion* **85**, 473–511 (2010).
105. E. Pérez-Sánchez, E. Fortes & D. Mira. Assessment of the Flamelet Generated Manifold method with preferential diffusion modeling for partially premixed hydrogen flames. *Combustion and Flame* **277**, 114141 (2025).
106. E. Fortes, E. Pérez-Sánchez, A. Both, T. Grenga & D. Mira. Analysis of thermodiffusive instabilities in hydrogen/air premixed flames using a tabulated flamelet model. *International Journal of Hydrogen Energy* **137**, 247–259 (2025).
107. N. Mukundakumar, D. Efimov, N. Beishuizen & J. van Oijen. A new preferential diffusion model applied to FGM simulations of hydrogen flames. *Combustion Theory and Modelling* **25**, 1245–1267 (2021).
108. A. Scholtissek, P. Domingo & L. V. C. Hasse. A self-contained progress variable space solution method for thermochemical variables and flame speed in freely-propagating premixed flamelets. *Proceedings of the Combustion Institute* **37**, 1529–1536 (2019).
109. A. Scholtissek, P. Domingo & L. V. C. Hasse. A self-contained composition space solution method for strained and curved premixed flamelets. *Combustion and Flame* **207**, 342–355 (2019).
110. X. Wen, T. Zirwes, A. Scholtissek, H. Böttler, F. Zhang, H. Bockhorn & C. Hasse. Flame structure analysis and composition space modeling of thermodiffusively unstable premixed hydrogen flames—Part I: Atmospheric pressure. *Combustion and Flame* **238**, 111815 (2022).

111. X. Wen, T. Zirwes, A. Scholtissek, H. Böttler, F. Zhang, H. Bockhorn & C. Hasse. Flame structure analysis and composition space modeling of thermodiffusively unstable premixed hydrogen flames—Part II: Elevated pressure. *Combustion and Flame* **238**, 111808 (2022).
112. H. Böttler, X. Chen, S. Xie, A. Scholtissek, Z. Chen & C. Hasse. Flamelet modeling of forced ignition and flame propagation in hydrogen-air mixtures. *Combustion and Flame* **243**, 112125 (2022).
113. H. Böttler, H. Lulic, M. Steinhausen, X. Wen, C. Hasse & A. Scholtissek. Flamelet modeling of thermo-diffusively unstable hydrogen-air flames. *Proceedings of the Combustion Institute* **39**, 1567–1576 (2023).
114. P. E. Lapenna, L. Berger, A. Attili, R. Lamioni, N. Fogla, H. Pitsch & F. Creta. Data-driven subfilter modelling of thermo-diffusively unstable hydrogen-air premixed flames. *Combustion Theory and Modelling* **25**, 1064–1085 (2021).
115. P. E. Lapenna, A. Remiddi, D. Molinaro, G. Indelicato & F. Creta. A-posteriori analysis of a data-driven filtered wrinkled flamelet model for thermodiffusively unstable premixed flames. *Combustion and Flame* **259**, 113126 (2024).
116. A. Remiddi, P. E. Lapenna, D. Cavalieri, D. Schintu, G. Indelicato, A. Attili, L. Berger, H. Pitsch & F. Creta. Data-driven modeling of resolved and filtered thermo-diffusively unstable hydrogen-air flames. *Proceedings of the Combustion Institute* **40**, 105713 (2024).
117. V. S. Wehrmann, N. Chakraborty, M. Klein & J. Hasslberger. On Local Equivalence Ratio Dependence of the Burning Rate in Premixed Turbulent Lean Hydrogen/Air Flames: A Direct Numerical Simulation Analysis. *Flow Turbulence and Combustion* **116**, 19 (2026).
118. L. Berger, A. Attili, M. Gauding & H. Pitsch. LES combustion model for premixed turbulent hydrogen flames with thermodiffusive instabilities: a priori and a posteriori analysis. *Journal of Fluid Mechanics* **1003**, A33 (2025).
119. R. Kai, T. Tokuoka, J. Nagao, A. L. Pillai & R. Kurose. LES flamelet modeling of hydrogen combustion considering preferential diffusion effect. *International Journal of Hydrogen Energy* **48**, 11086–11101 (2023).
120. G. Ferrante, G. Eitelberg & I. Langella. Differential diffusion modelling for LES of premixed and partially premixed flames with presumed FDF. *Combustion Theory and Modelling*, 1–36 (2024).
121. H. Böttler, D. Kaddar, T. J. P. Karpowski, F. Ferraro, A. Scholtissek, H. Nicolai & C. Hasse. Can flamelet manifolds capture the interactions of thermo-diffusive instabilities and turbulence in lean hydrogen flames?—An a-priori analysis. *International Journal of Hydrogen Energy* **56**, 1397–1407 (2024).
122. A. Porcarelli, B. Kruljević & I. Langella. Suppression of NO_x emissions by intensive strain in lean premixed hydrogen flamelets. *International Journal of Hydrogen Energy* **49**, 413–431 (2024).

123. H. G. Weller, G. Tabor, H. Jasak & C. Fureby. A tensorial approach to computational continuum mechanics using object-oriented techniques. *Journal of Computational Physics* **12**, 620–631 (1998).
124. B. E. Poling, J. M. Prausnitz & J. P. O'connell. *Properties of gases and liquids* (McGraw-Hill Educ, 2001).
125. S. Chapman & T. G. Cowling. *The mathematical theory of non-uniform gases: an account of the kinetic theory of viscosity, thermal conduction and diffusion in gases* (Cambridge Univ press, 1990).
126. V. Novaresio, M. García-Camprubí, S. Izquierdo, P. Asinari & N. Fueyo. An open-source library for the numerical modeling of mass-transfer in solid oxide fuel cells. *Computer Physics Communications* **183**, 125–146 (2012).
127. G. Smith et al. *GRI-MECH 3.0* <http://combustion.berkeley.edu/gri-mech/version30/text30.html>. [accessed 12 July 2023]. 2000.
128. T. Jaravel, E. Riber, B. Cuenot & P. Pepiot. Prediction of flame structure and pollutant formation of Sandia flame D using Large Eddy Simulation with direct integration of chemical kinetics. *Combustion and Flame* **188**, 180–198 (2018).
129. Q. Cazeres. *Analysis and reduction of chemical kinetics for combustion applications* PhD thesis (Toulouse, INPT, 2021).
130. A. Konnov. Implementation of the NCN pathway of prompt-NO formation in the detailed reaction mechanism. *Combustion and Flame* **156**, 2093–2105 (2009).
131. N. Lamoureux, P. Desgroux, A. El Bakali & J.-F. Pauwels. Experimental and numerical study of the role of NCN in prompt-NO formation in low-pressure CH₄-O₂-N₂ and C₂H₂-O₂-N₂ flames. *Combustion and Flame* **157**, 1929–1941 (2010).
132. F. Contino, H. Jeanmart, T. Lucchini & G. D'Errico. Coupling of in situ adaptive tabulation and dynamic adaptive chemistry: An effective method for solving combustion in engine simulations. *Proceedings of the Combustion Institute* **33**, 3057–3064 (2011).
133. W. Ramaekers. *Development of flamelet generated manifolds for partially-premixed flame simulations* PhD thesis (Technische Universiteit Eindhoven, 2011).
134. B. Somers. *The simulation of flat flames with detailed and reduced chemical models* PhD thesis (Gastec NV NL, 1994).
135. B. Rogg. Response and flamelet structure of stretched premixed methane-air flames. *Combustion and Flame* **73**, 45–65 (1988).
136. T. Zirwes, F. Zhang, P. Habisreuther, M. Hansinger, H. Bockhorn, M. Pfitzner & D. Trimis. Quasi-DNS dataset of a piloted flame with inhomogeneous inlet conditions. *Flow, Turbulence and Combustion* **104**, 997–1027 (2020).
137. Q. Cazères, P. Pepiot, E. Riber & B. Cuenot. A fully automatic procedure for the analytical reduction of chemical kinetics mechanisms for computational fluid dynamics applications. *Fuel* **303**, 121247 (2021).
138. T. Capurso, D. Laera, E. Riber & B. Cuenot. NO_x pathways in lean partially premixed swirling H₂-air turbulent flame. *Combustion and Flame* **248**, 112581 (2023).

139. R. J. Kee, F. M. Rupley & J. A. Miller. *Chemkin-II: A Fortran chemical kinetics package for the analysis of gas-phase chemical kinetics* tech. rep. (Sandia National Lab.(SNL-CA), Livermore, CA (United States), Sept. 1989). <https://www.osti.gov/biblio/5681118>.
140. G. J. Rørtveit, J. E. Hustad, S.-C. Li & F. A. Williams. Effects of diluents on NO_x formation in hydrogen counterflow flames. *Combustion and Flame* **130**, 48–61 (2002).
141. N. A. Samiran, C. T. Chong, J.-H. Ng, M.-V. Tran, H. C. Ong, A. Valera-Medina, W. W. F. Chong & M. N. M. Jaafar. Experimental and numerical studies on the premixed syngas swirl flames in a model combustor. *International Journal of Hydrogen Energy* **44**, 24126–24139 (2019).
142. T. C. Williams, C. R. Shaddix* & R. W. Schefer. Effect of syngas composition and CO₂-diluted oxygen on performance of a premixed swirl-stabilized combustor. *Combustion Science and Technology* **180**, 64–88 (2007).
143. S. de Persis, M. Idir, J. Molet & L. Pillier. Effect of hydrogen addition on NO_x formation in high-pressure counter-flow premixed CH₄/air flames. *International Journal of Hydrogen Energy* **44**, 23484–23502 (2019).
144. A. Masucci, A. Porcarelli, T. Ghisu & I. Langella. Investigation of tangential strain rate impact on NO emissions in turbulent premixed hydrogen flames using the Eulerian Stochastic Fields approach. *Combustion and Flame* **287**, 114887 (2026).
145. A. Porcarelli & I. Langella. Mitigation of preferential diffusion effects by intensive strain in lean premixed hydrogen flamelets. *Proceedings of the Combustion Institute* **40**, 105728 (2024).
146. M. Ó. Conaire, H. Curran, J. Simmie, W. Pitz & C. Westbrook. A comprehensive modeling study of hydrogen oxidation. *International Journal of Chemical Kinetics* **36**, 603–622 (2004).
147. Z. Zhou, F. E. Hernández-Pérez, Y. Shoshin, J. A. van Oijen & L. P. de Goey. Effect of Soret diffusion on lean hydrogen/air flames at normal and elevated pressure and temperature. *Combustion Theory and Modelling* **21**, 879–896 (2017).
148. A. Ern & V. Giovangigli. *Multicomponent transport algorithms* (Springer Sc. & Business Media, 1994).
149. H. C. Lee, P. Dai, M. Wan & A. N. Lipatnikov. Lewis number and preferential diffusion effects in lean hydrogen–air highly turbulent flames. *Physics of Fluids* **34** (2022).
150. L. Berger, M. Grinberg, B. Jürgens, P. E. Lapenna, F. Creta, A. Attili & H. Pitsch. Flame fingers and interactions of hydrodynamic and thermodiffusive instabilities in laminar lean hydrogen flames. *Proceedings of the Combustion Institute* **39**, 1525–1534 (2023).
151. F. H. Vance, P. de Goey & J. A. van Oijen. The effect of thermal diffusion on stabilization of premixed flames. *Combustion and Flame* **216**, 45–57 (2020).
152. N. Peters. Fifteen lectures on laminar and turbulent combustion. *Ercoftac summer school* **1428**, 245 (1992).

153. A. Porcarelli, P. E. Lapenna, F. Creta & I. Langella. Stability analysis of thermodynamically unstable counterflow lean premixed hydrogen flames. *Proceedings of the Combustion Institute* **41**, 105906 (2025).
154. J. O. Hirschfelder, C. F. Curtiss & R. B. Bird. *The molecular theory of gases and liquids* (John Wiley & Sons, 1964).
155. A. J. Fillo, J. Schlup, G. Blanquart & K. E. Niemeyer. Assessing the impact of multi-component diffusion in direct numerical simulations of premixed, high-Karlovitz, turbulent flames. *Combustion and Flame* **223**, 216–229 (2021).
156. B. Naud, M. Arias-Zugasti & A. Cuoci. Complete multicomponent versus mixture-averaged calculations of a laminar H₂/N₂ diffusion flame including heat transfer at the burner and Soret effects. *International Journal of Hydrogen Energy* (2025).
157. A. Evlampiev. *Numerical combustion modeling for complex reaction systems* PhD thesis (Technische Universiteit Eindhoven, 2007).
158. L. Berger, K. Kleinheinz, A. Attili & H. Pitsch. Characteristic patterns of thermodynamically unstable premixed lean hydrogen flames. *Proceedings of the Combustion Institute* **37**, 1879–1886 (2019).
159. A. Porcarelli, P. E. Lapenna, F. Creta & I. Langella. Assessment of tabulated-chemistry models for lean premixed strained hydrogen flames with low-dimensional manifolds. *Combustion Theory and Modelling*, 1–27 (2026).
160. M. Fathi, S. Hickel, N. A. K. Doan & I. Langella. Effects of intense strain on flame structure and NO_x generation in turbulent counterflow lean-premixed hydrogen flames. *Combustion and Flame* **282**, 114459 (2025).
161. M. X. Yao & G. Blanquart. Isolating effects of large and small scale turbulence on thermodynamically unstable premixed hydrogen flames. *Combustion and Flame* **269**, 113657 (2024).
162. M. Fathi, S. Hickel & D. Roekaerts. Large eddy simulations of reacting and non-reacting transcritical fuel sprays using multiphase thermodynamics. *Physics of Fluids* **34** (2022).
163. A. Sánchez & F. Williams. Recent advances in understanding of flammability characteristics of hydrogen. *Progress in Energy and Combustion Science* **41**, 1–55 (2014).
164. L. Laguarda & S. Hickel. Analysis of improved digital filter inflow generation methods for compressible turbulent boundary layers. *Computers & Fluids* **268**, 106105 (2024).
165. S. B. Pope. Turbulent flows. *Measurement Science and Technology* **12** (2001).
166. A. Iyer. *Investigation of unsteady stretch effects using premixed counterflow flames* PhD thesis (Technische Universiteit Eindhoven, 2018).
167. Z. X. Chen, N. A. K. Doan, S. Ruan, I. Langella & N. Swaminathan. A priori investigation of subgrid correlation of mixture fraction and progress variable in partially premixed flames. *Combustion Theory and Modelling* **22**, 862–882 (2018).

168. E. Fortes, E. Pérez-Sánchez, T. Grenga, M. Gauding, H. Pitsch & D. Mira. Large-eddy simulations of a lean premixed turbulent jet flame with tabulated chemistry. *Proceedings of the 13th Mediterranean Combustion Symposium, under review* (2025).
169. S. Dillon, R. Mercier & B. Fiorina. Controlling the resolved flame thickness of non-premixed flames in LES with filtered tabulated chemistry. *Proceedings of the Combustion Institute* **40**, 105294 (2024).
170. S. Dillon, R. Mercier & B. Fiorina. A new filtered tabulated chemistry model for multi-regime combustion: A priori validation on a laminar triple flame. *Proceedings of the Combustion Institute* **40**, 105301 (2024).
171. T. Nilsson, I. Langella, N. Doan, N. Swaminathan, R. Yu & X. Bai. A priori analysis of sub-grid variance of a reactive scalar using DNS data of high Ka flames. *Combustion Theory and Modelling* **23**, 885–906 (2019).
172. A. Morea, O. Teytaud & J. Bertoglio. Optimal estimation for large-eddy simulation of turbulence and application to the analysis of subgrid models. *Physics of Fluids* **18** (2006).
173. L. Berger, K. Kleinheinz, A. Attili, F. Bisetti, H. Pitsch & M. Mueller. Numerically accurate computational techniques for optimal estimator analyses of multi-parameter models. *Combustion Theory and Modelling* **22**, 480–504 (2018).
174. A. Attili, S. Luca, D. Denker, F. Bisetti & H. Pitsch. Turbulent flame speed and reaction layer thickening in premixed jet flames at constant Karlovitz and increasing Reynolds numbers. *Proceedings of the Combustion Institute* **38**, 2939–2947 (2021).
175. A. R. Varma, U. Ahmed, M. Klein & N. Chakraborty. Effects of turbulent length scale on the bending effect of turbulent burning velocity in premixed turbulent combustion. *Combustion and Flame* **233**, 111569 (2021).
176. F. D'Alessio, C. Matteucci, P. E. Lapenna & F. Creta. Intrinsic instability of lean hydrogen/ammonia premixed flames: Influence of Soret effect and pressure. *Fuel Communications* **19**, 100110 (2024).
177. K. Dave, S. Link, F. De Domenico, F. Schrijer, F. Scarano & A. G. Rao. Kerosene-H₂ blending effects on flame properties in a multi-fuel combustor. *Fuel Communications* **23**, 100139 (2025).
178. M. Klein, A. Herbert, H. Kosaka, B. Böhm, A. Dreizler, N. Chakraborty, V. Papadopolou, H. G. Im & J. Hasslberger. Evaluation of flame area based on detailed chemistry DNS of premixed turbulent hydrogen-air flames in different regimes of combustion. *Flow, Turbulence and Combustion* **104**, 403–419 (2020).
179. H. Lee, P. Dai, M. Wan & A. N. Lipatnikov. A DNS study of extreme and leading points in lean hydrogen-air turbulent flames-part II: local velocity field and flame topology. *Combustion and Flame* **235**, 111712 (2022).
180. L. Berger, R. Hesse, K. Kleinheinz, M. J. Hegetschweiler, A. Attili, J. Beeckmann, G. T. Linteris & H. Pitsch. A DNS study of the impact of gravity on spherically expanding laminar premixed flames. *Combustion and Flame* **216**, 412–425 (2020).

181. J. F. Driscoll, J. H. Chen, A. W. Skiba, C. D. Carter, E. R. Hawkes & H. Wang. Premixed flames subjected to extreme turbulence: Some questions and recent answers. *Progress in Energy and Combustion Science* **76**, 100802 (2020).

A

APPENDIX A

A.1. GRID CONVERGENCE STUDY

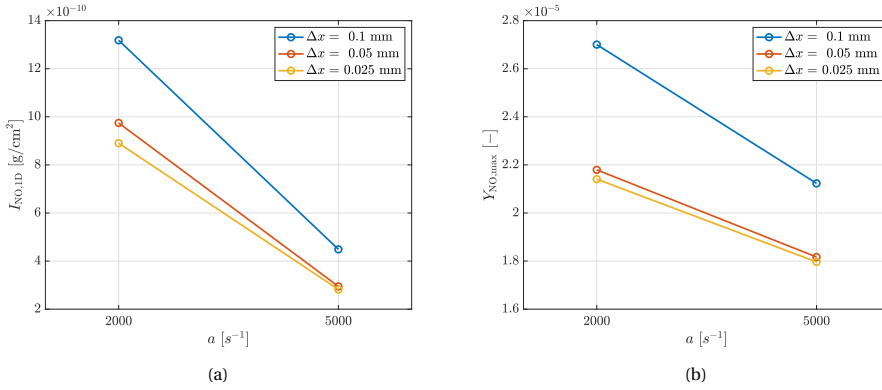


Figure A.1: Variation of peak NO mass fraction $Y_{\text{NO,max}}$ (a) and density weighted NO integral $I_{\text{NO},1\text{D}}$ (b) with strain rate a for 2D simulations of hydrogen-air flames at equivalence ratio $\phi = 0.7$ with different grid refinements.

Two-dimensional simulations are performed in Chapter 3 in order to enhance the physical understanding of the 1D results, and particularly to verify the NO_x emission behaviour with strain observed in the 1D simulations. For this reason, it is important to check that NO_x emission trends resulting from 2D simulations are mesh-independent. Figure A.1a and A.1b show the results of the two-dimensional simulations for different grid refinements in terms of peak NO mass fraction and density weighted NO integral, respectively. Data are shown for three mesh resolutions in terms of the longitudinal grid spacing, respectively 0.1 mm, 0.05 mm and 0.025 mm. Results show that a decreasing emission trend with strain is observed for any refinement. Furthermore, very close quantitative results are found for the two more refined configurations, showing that the results are grid-independent once a good level of local refinement is achieved.

The minimum cell spacing for the most refined mesh is calculated as $\Delta x_{\text{min}} = 0.2/2^3 = 0.025$ mm, which ensures at least 12 cells are present within the flame thickness at any of the conditions investigated. This resolution is similar to that found in previous DNS and quasi-DNS studies on reacting flows [136, 178–180]. Therefore, this refinement is chosen for the study performed in Chapter 3. The resulting total cell count for all the cases investigated with the most refined mesh is around 40000, and varies slightly depending on the width of the refined region at different strain rates.

A.2. FLAME TEMPERATURE PLOT

In Section 3.4.2 it is shown that the strongest decrease of NO production at higher strain rate is associated to the thermal pathway. In contrast to what one could generally expect, however, this phenomenon is not associated to a decrease in temperature. In fact, Figure A.2 shows that higher peak temperatures are observed for any strained flamelet in comparison to the unstrained flamelet case. Furthermore, temperature shows an increasing trend with strain following the increase of peak reaction rate (see Section A.3). Note

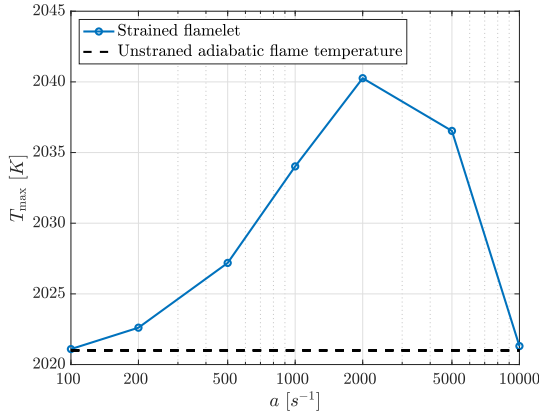


Figure A.2: Variation of peak flame temperature T_{max} with strain rate a for 1D simulations of hydrogen-air flamelets at equivalence ratio $\phi = 0.7$.

that the increasing trend is inverted only at very high strain rate because of the proximity of the flame to the stagnation plane due to high local convection, but the decreased NO_x emissions are observed for any range of strain rate with a similar trend, and are thus not dependent to this peak temperature variation. Hence, the reason behind the observed NO suppression is not imputable to a change in the flame temperature despite the dominant mechanism being the thermal one, and it should be searched instead in the local radical redistribution as discussed in Chapter 3.

A.3. REACTION RATE PLOT

As discussed in Section 3.4.3, increasing reaction rates are expected with increasing strain rate in lean hydrogen flames. This is confirmed by the flamelet results which are reported in Figure A.3 for the 1D setup of Chapter 3. The peaks of reaction rates can be clearly seen to be higher when strain rate is increased, and this is a consequence of the combination of hydrogen's high reactivity due to its chain-branching consumption and its high diffusivity.

A.4. RADICAL PLOTS IN METHANE FLAMELETS

The main radicals concentration across the flamelet at $\phi = 0.8125$ are plotted for different strain rates in Figure A.4. Unlike what observed for hydrogen, the peaks of radicals decrease with strain. Moreover, the amount of radicals also decrease with strain in the further downstream region of the domain, similarly to the hydrogen case. This behaviour triggers a similar trend for the NO source term, i.e. $\dot{\omega}_{NO}$ is decreasing with increasing strain rate at any flamelet position.

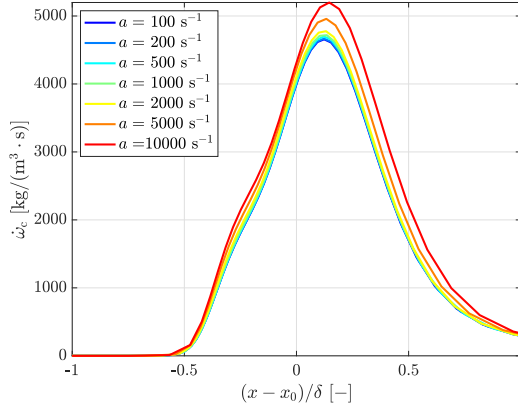


Figure A.3: Reaction rate of normalised, water-based progress variable $\dot{\omega}_c$ across an hydrogen-air flamelet at equivalence ratio $\phi = 0.7$, for different strain rates a .

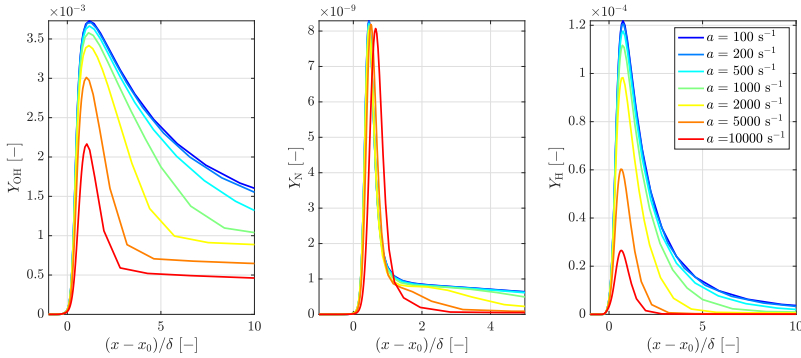


Figure A.4: Distribution of OH, N, and H radicals mass fraction Y_k across a methane-air flamelet at $\phi = 0.8125$ and for different values of applied strain rates.

B

APPENDIX B

B.1. BILGER MIXTURE FRACTION

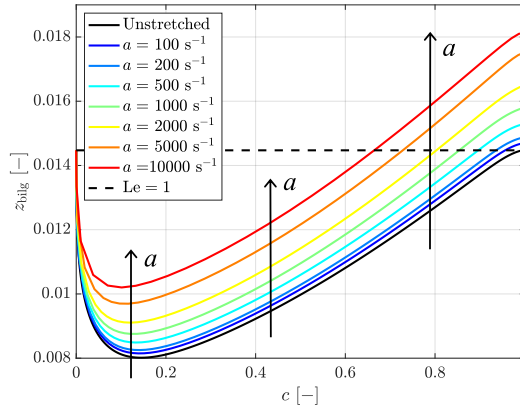


Figure B.1: Distribution of Bilger's mixture fraction at different strain rates in progress variable space obtained with multicomponent diffusion and $Le = 1$ model.

In order to accurately monitor the local leaning and enrichment of the flame due to the combination of hydrogen preferential diffusion and strain, one can define a mixture fraction based on the elemental mass fractions of monoatomic hydrogen (\mathcal{Y}_H) and oxygen (\mathcal{Y}_O) as the one in Equation (2.7) (see Sec. 2.2) according to Bilger *et al.* [55]. The definition of Bilger *et al.* [55] is more rigorous than the one of Regele *et al.* [71], because it considers all the species containing oxygen and hydrogen instead of only considering H_2 and O_2 . The distribution of mixture fraction as defined in Equation (2.7) across the flamelet, computed with the multicomponent and $Le = 1$ diffusion model, is shown in Figure B.1. For the case at $Le = 1$ the Bilger's mixture fraction remains perfectly constant across the flamelet as one would expect from theory, while some local variation was observed in Figure 4.3 (see Sec. 4.3.2), where the approximate expression of Regele *et al.* [71] was used, and this variation is caused by the locally different burning rates of H_2 and O_2 . On the other hand, when the multicomponent model is used, the same pattern is observed with both the mixture fraction definitions, with a local leaning of the mixture for relatively low values of progress variable, and an enrichment of the flame with increasing strain rate. Therefore, it can be concluded that the discussion in Chapter 4 on mixture fraction trends with increasing strain rate is valid regardless of the choice of the mixture fraction definition.

B.2. CONSTANT LEWIS NUMBER DIFFUSION MODEL

In this section, the difference between constant non-unity Lewis number (Le_{const}) and multicomponent diffusion modelling approach is discussed. Figures B.2a and B.2b respectively show the distribution of H radical mass fraction and of progress variable reaction rate as a function of the flame-centered, flame-thickness-normalised longitudinal flamelet coordinate at different strain rates computed with the constant non-unity and unity Lewis number approaches. These figures can be directly compared to Figures 4.1

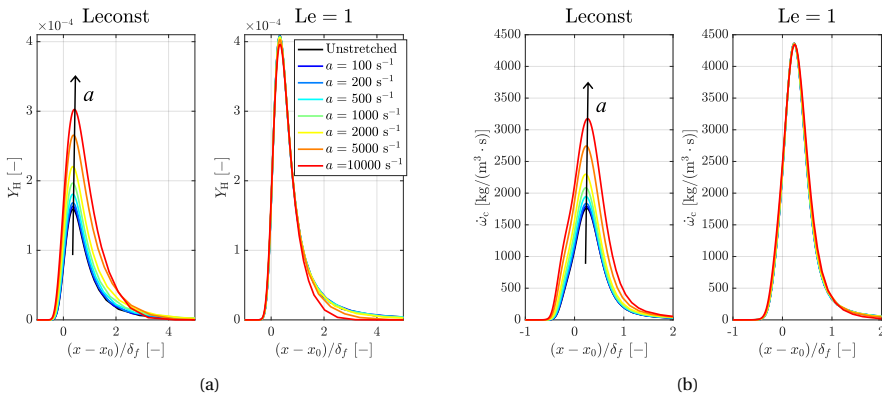


Figure B.2: Distribution of H radicals mass fraction (a) and progress variable reaction rate (b) at different strain rates obtained with constant non-unity Lewis number diffusion model (left) and Le = 1 model (right).

and 4.2 (see Sec. 4.3.1), respectively, where the multicomponent diffusion model is used. The comparison indicates that while the quantitative values of the peaks at high strain rate values as predicted by the two approaches are slightly different, the trend with increasing strain rate are the same when preferential diffusion is taken into account, regardless of the choice of modelling approach (multicomponent or constant Lewis number). In particular, in both cases the values of H radicals and reaction rate are observed, as strain increases, to approach the distribution obtained when preferential diffusion is not taken into account. The distribution across the flamelet of mixture fraction, as defined in Equation (4.1), computed with constant non-unity Lewis number approach, is also plotted as a function of the normalised flamelet progress variable in Figure B.3. This figure can be directly compared to Figure 4.3 (see Sec. 4.3.2), where the multicomponent diffusion model is used. The comparison again indicates that the same behaviour is predicted by the two

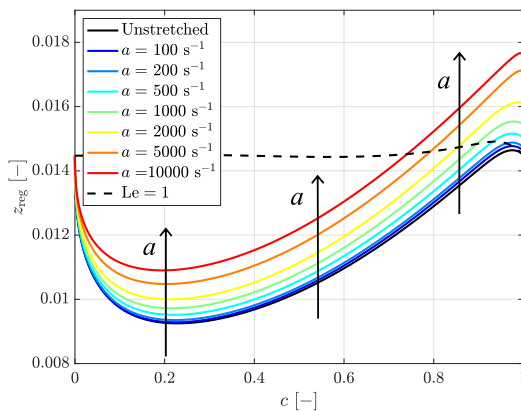


Figure B.3: Distribution of mixture fraction at different strain rates obtained with constant non-unity Lewis number diffusion model as a function of the progress variable.

diffusion models, with a local leaning of the mixture at relatively low values of progress variable, an enrichment with increasing strain rate.

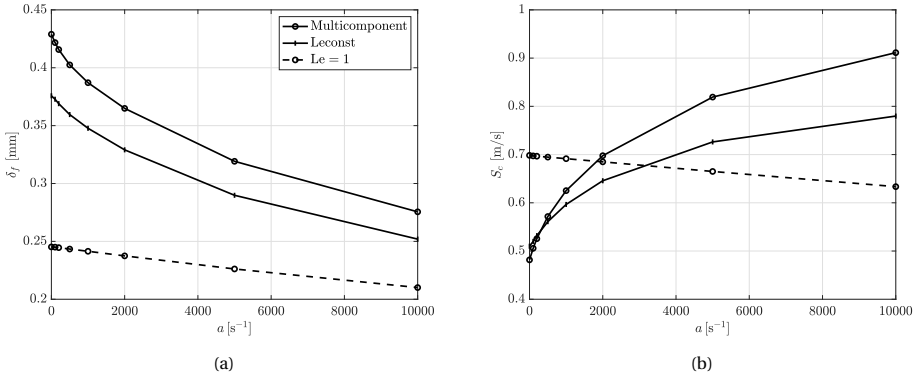


Figure B.4: Flame thickness (a) and consumption speed (b) as a function of strain rate with different diffusion models: multicomponent, constant non-unity Lewis number, and constant unity Lewis number.

The flame thickness and consumption speed as a function of strain rate are further plotted in Figs. B.4a and B.4b, as obtained with multicomponent, constant non-unity Lewis number, and constant unity Lewis number diffusion models. Considering the flame thickness, very similar values are predicted by the two approaches where preferential diffusion is taken into account (multicomponent and Leconst models). Moreover, as strain increases to relatively large values, both these predictions seem to converge to those of the case without preferential diffusion. A different behaviour is observed for the consumption speed. For this quantity the behaviour predicted by the two preferential diffusion models is similar at low values of strain, but the two curves tend to diverge with increasing strain rate. Still, both models preserve the prediction of the negative Markstein length. On the other hand, as expected, the slope of the curve of consumption speed with strain is inverted when preferential diffusion is not taken into account, implying the Markstein length would be severely mispredicted in this case.

Overall, the results reported in this section show that the analysis in Section 4.3.3, where a constant non-unity Lewis number diffusion modelling is used to reconstruct a simplified mixture fraction transport equation, do not lose generality, as all trends with increasing strain rate are preserved if compared to the multicomponent diffusion model.

B.3. INFLUENCE OF REACTANTS TEMPERATURE

In this section, the influence of the reactants temperature is assessed by testing a new setup with $T_r = 400$ K for both the multicomponent and Le = 1 diffusion models. Figure B.5a shows the distribution of progress variable reaction rate as a function of the flame-centered, flame-thickness-normalised longitudinal flamelet coordinate at different strain rates computed with the multicomponent and unity Lewis number approaches. The mixture fraction distribution as a function of the progress variable at different strain rates is also reported in Figure B.5b. These figures can be directly compared to the base-

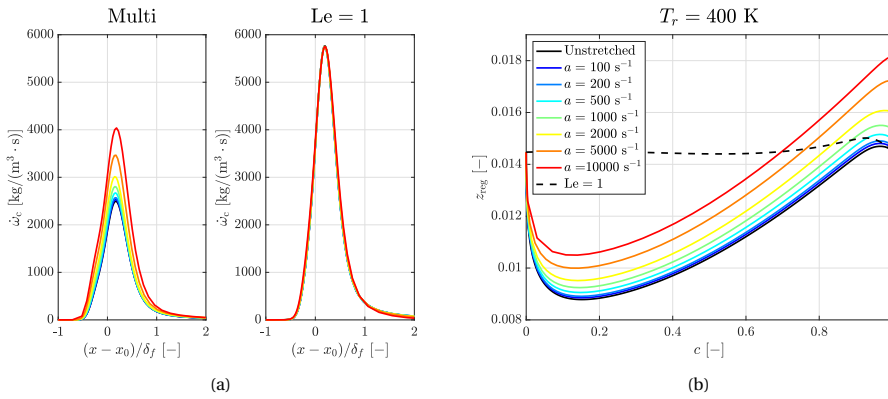


Figure B.5: Distribution of progress variable reaction rate (a) and mixture fraction (b) across the flamelet at different strain rates obtained at $T_r = 400$ K with multicomponent and $Le = 1$ diffusion models.

line case where $T_r = 300$ K reported in Figures 4.2 and 4.3 (see Secs. 4.3.1 and 4.3.2), respectively. This increased preheat temperature setup shows overall very similar patterns and trends with increasing strain rate as compared to the baseline case. By comparing Figure B.5b with Figure 4.3 in Chapter 4, it can be observed that the dip of mixture fraction in the unstretched case is slightly less substantial, suggesting that preferential diffusion effects are weaker in these conditions. This observation agrees with previous findings in literature [73]. In both Figures B.5a and B.5b it can be seen that the effect of strain in increasing the peak reaction rate is still retained, but is less strong compared to the baseline case due to the discussed globally weaker preferential diffusion effects.

B.4. INFLUENCE OF EQUIVALENCE RATIO

In this section, the influence of the equivalence ratio is assessed by testing a new setup with $\phi = 0.7$ for both the multicomponent and $Le = 1$ diffusion models. This setup is chosen such that the mixture is richer than the baseline case, but still lean so that preferential diffusion effects are still present. Figure B.6a shows the distribution of progress variable reaction rate as a function of the flame-centered, flame-thickness-normalised longitudinal flamelet coordinate at different strain rates computed with the multicomponent and unity Lewis number approaches. The mixture fraction distribution as a function of the progress variable at different strain rates is also reported in Figure B.6b. These figures can be directly compared to the baseline case where $\phi = 0.5$ reported in Figures 4.2 and 4.3 (see Secs. 4.3.1 and 4.3.2), respectively. It can be seen that when the two transport models are compared in unstretched conditions, the peak of reaction rate is still diminished in the multicomponent case due to preferential diffusion effects, but much less significantly if compared to the case where $\phi = 0.5$ (see Fig. 4.2). This suggests that preferential diffusion effects are weaker in these conditions, and this finding agrees with previous studies in literature [73]. Furthermore, this increased equivalence ratio setup has a weaker dependence on strain, with the peak of reaction rate still increasing with strain but less substantially. Similar considerations hold for the mixture fraction, where

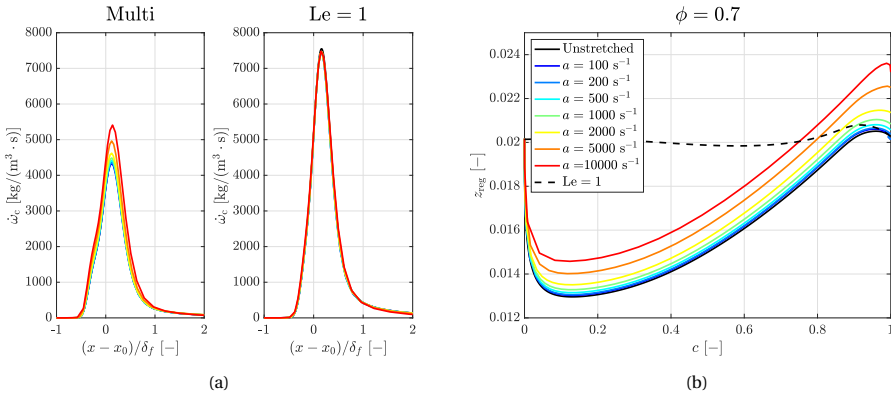


Figure B.6: Distribution of progress variable reaction rate (a) and mixture fraction (b) across the flamelet at different strain rates obtained at $\phi = 0.7$ K with multicomponent and $Le = 1$ diffusion models.

the dip due to preferential diffusion effect is still increased by strain but less significantly as compared to the baseline leaner case due to the discussed globally weaker preferential diffusion effects.

B.5. KARLOVITZ NUMBER CALCULATION AND COMPARISON TO TURBULENT FLOW

In order to provide a more general classification of the strain rates investigated, and to make them comparable to practical flame regimes, it could be convenient to relate strain rates to a Karlovitz number. For a one-dimensional premixed flat flame, a so-called Karlovitz integral Ka_k can be defined for each species as [38]:

$$Ka_k = \frac{Le_k}{m_b^0} \int_{x_u}^{x_b} \rho K \tilde{Y}_k dx, \quad (B.1)$$

where $\tilde{Y}_k = \frac{Y_k - Y_{k,u}}{Y_{k,b} - Y_{k,u}}$ is a scaled mass fraction, and m_b^0 is the mass burning rate in unstretched conditions that can be found as [38]:

$$m_b^0 = \frac{1}{|Y_{k,b} - Y_{k,u}|} \sqrt{2 \int_{Y_{k,u}}^{Y_{k,b}} \frac{1}{Le_k} \frac{\lambda}{c_p} \dot{\omega}_k dY_k}. \quad (B.2)$$

Unburnt and burnt flame conditions are denoted with the pedices u and b , respectively. The quantity Ka_k expresses the relative change of mass fraction of the species k over the flamelet path due to flame stretch [38]. The Karlovitz integral considering hydrogen (fuel) mass fraction Ka_{H_2} computed at each corresponding applied strain rate of Chapter 4 for both the transport models is reported in Table B.1. At the highest applied strain rate, a value of Ka significantly beyond the ranges previously investigated in literature is found [38], further remarking hydrogen's very high resistance to high strain rate regimes. The consumption speed for the two transport model cases is further re-plotted as a

a [s^{-1}]	100	200	500	1000	2000	5000	10000
Ka_{H_2} [-] Multi	0.022	0.052	0.151	0.284	0.600	1.147	1.778
Ka_{H_2} [-] Le = 1	0.032	0.057	0.169	0.354	0.803	1.303	1.961

Table B.1: Karlovitz integral for H_2 at each applied strain rate and with the two transport models computed with the formula from Van Oijen *et al.* [38].

function of Ka_{H_2} in Figure B.7, proving that the same patterns are recognizable regardless of the quantity used to quantify strain.

Although one might immediately relate these values to the thin reaction zone regime

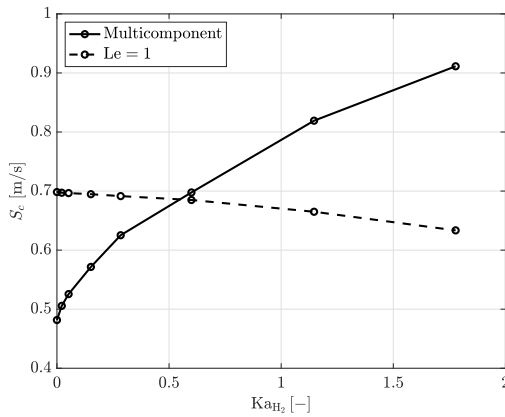


Figure B.7: Evolution of the consumption speed with the two transport models as a function of the Karlovitz integral for H_2 computed with the formula from Van Oijen *et al.* [38].

in turbulent combustion, it is important to distinguish conceptually the macroscopic response of the flame to mean strain rate in laminar conditions investigated in Chapters 4 and 5 and the local flame response to strain due to turbulence, which is a microscopic and inherently unsteady effect. Therefore, the results of Chapters 4 and 5 are solely intended to pave the way to the exploration of turbulent flame configurations where the flow field is designed to establish strong mean velocity gradients tangential to the flame to limit the growth of thermodiffusive instabilities (further interacting with turbulence), thus making the lean premixed hydrogen flame more stable and controllable in practical applications.

C

APPENDIX C

C.1. COMPUTATIONAL SETUP BOUNDARY CONDITIONS

The boundary conditions for the 2D counterflow reactants-to-products setup employed in this study are shown in Figure C.1. The inlet velocities imposed at the reactants and

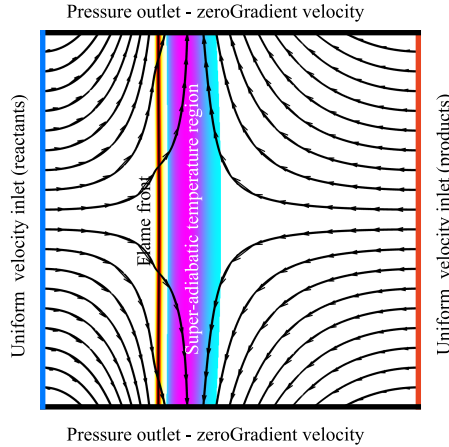


Figure C.1: Sketch of the two-dimensional reactants-to-products counterflow setup with the prescribed boundary conditions.

products inlets to achieve the strain rates reported in Table 5.1 in Chapter 5 are reported for completeness in Table C.1. As one can notice from the figure, the flame stabilises

Table C.1: Inlet velocity boundary conditions assigned at the reactants (u_r) and products (u_p) side of two-dimensional simulations for the four cases investigated (see Table 5.1 in Chapter 5).

Case name	a [s^{-1}]	u_r [m/s]	u_p [m/s]
a500	331.3	1.134	-5.492
a1000	706.85	3.166	-10.971
a2000	1447.5	7.3	-21.65
a5000	3633.5	19.65	-53.02

sufficiently far from the inlets to avoid numerical effects. It is worth noting that the outlet boundary condition allows a potential perturbation to be convected out of the domain freely. Only the local tangential strain rate in the proximity of the outlets varies slightly from the nominal value due to the imposed boundary condition, thereby potentially influencing the propagation of the perturbation along the flame. Nevertheless, in Section 5.4.2 in Chapter 5 constant tangential strain rate has been assumed all across the flame in time, and this assumption was proved correct by the validation of the pseudo-analytical expression obtained with the numerical results (see Fig. 5.8a in Chapter 5). Therefore, the overall effect of the outlet boundaries on the propagation of the perturbation can be considered negligible.

C.2. 1D FLAME VALIDATION

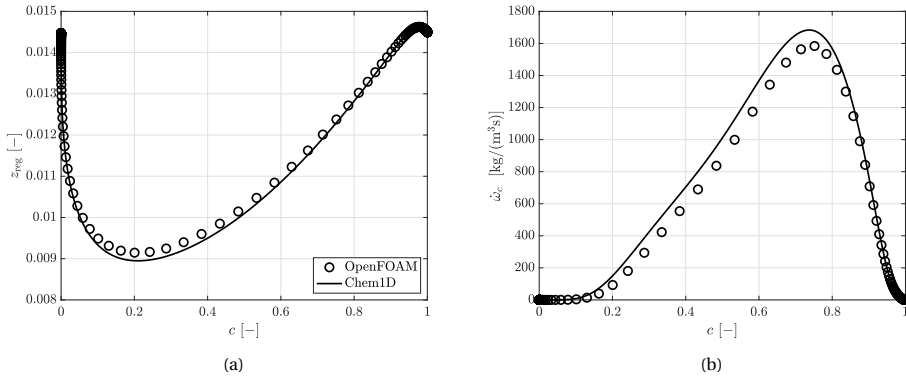


Figure C.2: Validation of mixture fraction (a) and reaction rate (b) distribution across a 1D flame against Chem1D solution.

In this section, the validation results of the custom version of the reactingFoam solver employed in Chapter 5 are reported for a one-dimensional setup. The solution of a one-dimensional, laminar, freely propagating premixed flame setup with hydrogen fuel at an equivalence ratio of $\phi = 0.5$ is compared to the flamelet obtained with Chem1D [53]. The transport properties and diffusion model in Chem1D are the same as described in Section 5.2.1 for the OpenFOAM simulation. The reader can find further details in [38, 133, 157]. The only discrepancy between the two compared computational models lies in the molecular weight gradients within the diffusion velocity formulation, which are neglected in OpenFOAM (see Eq. (5.2a) in Chapter 5) and retained in Chem1D. This means that there is an additional term in the diffusion velocity expression proportional to the gradient of molar mass. The OpenFOAM simulation is carried over a highly-refined grid featuring around 32 cells within the unstretched laminar flame thickness δ_f . The comparison of the obtained mixture fraction z profile and progress variable reaction rate $\dot{\omega}_c$ in progress variable c space are reported in Figures C.2a and C.2b, respectively. The mixture fraction is defined according to Equation (4.1), and the progress variable is based on the mass fraction of water: $c = Y_{\text{H}_2\text{O}}/Y_{\text{H}_2\text{O},\text{max}}$. The graphs show an overall good agreement of the quantities between the two simulations. Both the mixture fraction dip and the reaction rate peak are slightly underestimated by the OpenFOAM simulation within a reasonable range. This discrepancy may raise from the approximation used in the diffusion model. To get a quantitative gap between the two solutions, the flame consumption speed (see Eq. (4.9)) and thermal thickness (see Eq. (2.5)) are further compared in Table C.2. The

Table C.2: Comparison of the obtained global 1D flame parameters to Chem1D results.

	OpenFOAM	Chem1D	% Error
S_c [m/s]	0.485	0.515	5.7%
δ_f [mm]	0.405	0.424	4.47%

table shows again a very close estimate of both the properties, with a relative mismatch of approximately 5%.

C.3. TIME EVOLUTION OF A SAMPLE FLAME FRONT

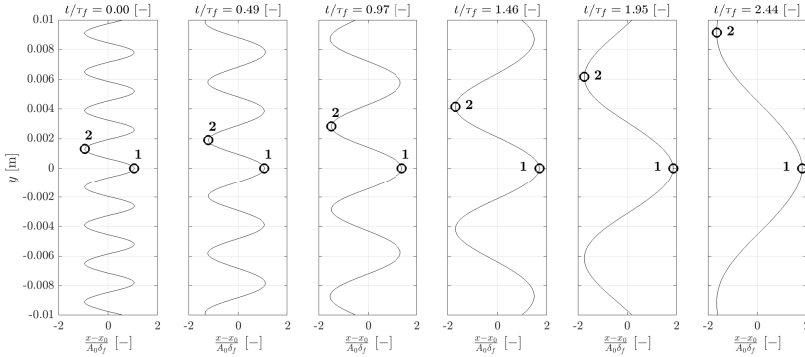


Figure C.3: Evolving perturbed flame front and perturbation tracking points at different simulation times, $\lambda_0 = 2.6$ mm, and $a = 1447.5$ s⁻¹.

As discussed in Section 5.4.2 of Chapter 5, after the perturbation is started, one can expect that there will be a variation of wavelength in time due to the local vertical component of the flow field featured by the counterflow configuration. To better visualise this phenomenon, the flame front shape (after subtraction of the basic flame front shape, see Fig. 5.6) is reported at different times in Figure C.3 for a sample case ($\lambda_0 = 2.6$ mm, case a2000 of Table 5.1). The figure clearly highlights a wavelength increase in time due to the vertical velocity component. In the analysis performed in Chapter 5, the wavelength is tracked in time by measuring the vertical distance between the fixed cosine crest at $y_1 = 0$ (point 1 in Fig. C.3) and the moving closest upper crest at $y_2 = y_2(t)$, such that $\lambda(t) = 2(y_2(t) - y_1)$ and thus $y(t) = \lambda/2$.

C.4. LOCAL TANGENTIAL STRAIN RATE IN TIME

In the pseudo-analytical derivation for $\lambda(t)$ performed in Section 5.4.2 of Chapter 5, it has been assumed that the local tangential strain rate K_s is about constant in time along the flame front during its evolution post-perturbation. In this section, this assumption is verified using the numerical results of a sample simulation. The relative variation of the local tangential strain rate of a perturbed flame front K_s^p at a given time step with respect to that of the unperturbed flame front K_s^u is defined as:

$$\epsilon_{\text{err}}(K_s) = \frac{K_s^p - K_s^u}{K_s^u}. \quad (\text{C.1})$$

In Figure C.4, the relative error obtained from case a2000 of Table 5.1 is plotted along the flame (y direction) at different time instants. The figure shows that some variations

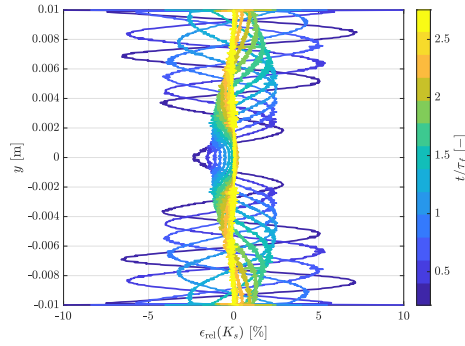


Figure C.4: Relative variation of the local tangential strain rate at different time instants of case a2000.

of local tangential strain rates are present over the crests of a perturbed flame front. However, these variations are kept below 5% at most times and never exceed 10%. In light of this verification, it can be concluded that the assumption of constant K_s in time across the flame front performed in Section 5.4.2 of Chapter 5 is acceptable, as this moderate variations of local tangential strain rate have a negligible influence on the validity of the pseudo-analytical expression presented. Indeed, the wavelength evolution found with the pseudo-analytical expression agrees very well with that observed within the simulation data, as shown in Figure 5.8a.

D

APPENDIX D

D.1. 3D TURBULENT SETUP COMBUSTION REGIME AND ADDITIONAL FLAME PARAMETERS

Additional parameters describing the 3D turbulent flame setup of Fathi *et al.* [160] used to perform the *a priori* analysis in Chapter 6 are reported in Table D.1. In the Table,

Table D.1: Flame parameters of 3D turbulent flame setup (see Sec. 6.2.2) used to perform the *a priori* analysis in Chapter 6 [160].

Parameter and dimension	Value
δ_f [mm]	0.400
s_L [m/s]	0.568
$\delta = \nu_0 / s_L$ [mm]	0.028
l_λ / δ [-]	7.057
l_t / δ [-]	35.28
u' / s_L [-]	7.038
$Da = (l_t / \delta)(u' / s_L)^{-1}$ [-]	5.013
$Ka = (l_t / \delta)^{-1/2}(u' / s_L)^{3/2}$ [-]	3.143
$Re = Da^2 Ka^2 = u' l_t / \nu_0$ [-]	248.3
$Ka_T = (l_t / \delta_f)^{-1/2}(u' / s_L)^{3/2}$ [-]	11.81
$Ka_K = (\delta_f / \eta_k)^2$ [-]	626.6

the unstretched laminar flame thickness is referred to as δ_f , while the turbulent flame thickness is indicated with the symbol δ and is estimated using the unity flame Reynolds number assumption [30] and the kinematic viscosity ν_0 of air at 300 K. The unstretched laminar flame speed, the Taylor length scale, the integral length scale, the root-mean-square velocity, and the Kolmogorov length scale are represented respectively with the symbols s_L , l_λ , l_t , u' , and η_k . The following non-dimensional numbers are computed to identify the turbulent and combustion regime as reported in the table: Damköhler number (Da), Karlovitz number (Ka), turbulent Reynolds number (Re), turbulent Karlovitz number (Ka_T), and Karlovitz number defined using the Kolmogorov length scale (Ka_K). Fathi *et al.* [160] collocated the investigated setup in the "moderate" turbulence regime according to the classification in [181] and in the high Karlovitz number regime according to the classification in [99].

D.2. IMPROVEMENT OF β -FDF PREDICTIONS AT INCREASING STRAIN RATE

In Section 6.3.1 in Chapter 6, improved performance of the 1DS-type manifolds has been observed with increasing strain rate at larger filters, where the β -FDF shows limitations in mimicking the asymptotic bimodal behaviour [171]. In this appendix, the reasons behind this improvement are discussed. In Figure D.1 the filtered H_2 source term obtained by filtering three different strained flamelets (first three cases in Table 6.3) is compared to the one reconstructed through the β -FDF at different filter sizes. As expected, the reaction rate is increasingly overestimated at larger filter sizes for all three levels of strain rate. However, the gap between the filtered source term and the one obtained from the β -FDF

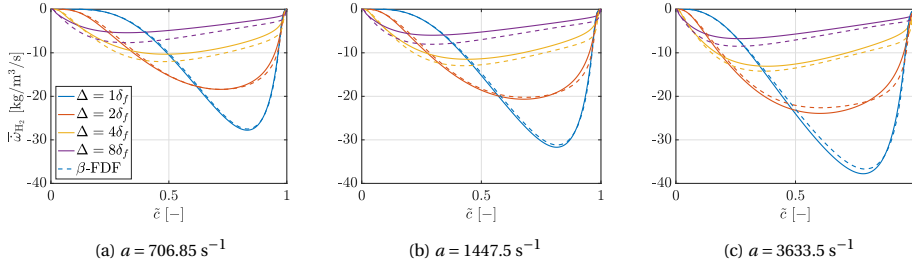


Figure D.1: Comparison of filtered hydrogen source term $\bar{\dot{\omega}}_{\text{H}_2}$ (solid lines) with the one reconstructed with the β -FDF model (dashed lines) of the strained flamelets employed in the 1DS manifolds (see Sec. 6.3.1) at varying filter width Δ .

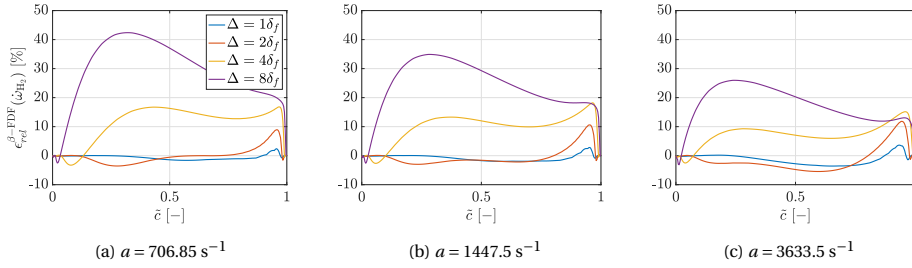


Figure D.2: Relative error of filtered hydrogen source term reconstructed with the β -FDF model $\epsilon_{rel}^{\beta\text{-FDF}}(\dot{\omega}_{\text{H}_2})$ of the strained flamelets employed in the 1DS manifolds (see Sec. 6.3.1) at varying filter width Δ .

appears to decrease at increasing strain rate. To quantify this improvement of the β -FDF, the relative error in the reconstruction of the filtered H_2 source term is quantified as:

$$\epsilon_{rel}^{\beta\text{-FDF}}(\dot{\omega}_{\text{H}_2}) = \frac{\bar{\dot{\omega}}_{\text{H}_2} - \bar{\dot{\omega}}_{\text{H}_2}^{\beta\text{-FDF}}}{\max|\bar{\dot{\omega}}_{\text{H}_2}|}. \quad (\text{D.1})$$

This quantity is reported in Figure D.2 for the three flamelets of Figure D.1 at different filter sizes. The figure proves that the error in reconstructing the filtered reaction rate through the β -FDF decreases substantially with increasing strain. Although the errors are still not negligible at the largest filter size ($\Delta = 8\delta_f$), they are pushed below 10% in all the other cases ($\Delta \leq 4\delta_f$). This suggests that the capability of the β -FDF model in mimicking the filtered reaction rate profile of highly-strained flame fronts is improved. This is probably due to the way the unfiltered reaction rate itself is re-distributed across the flame at increased strain rate, shaping a profile which, when filtered, is easier to mimic through the β -FDF model.

As a last note, a similar overall improvement at increasing strain of the consumption speed predicted through the β -FDF with the 2DSF-type manifold has been observed in Section 6.3.1 of Chapter 6, despite an additional overestimation compared to the 1DS-type manifold attributed to the additional controlling variable \bar{z} . This improvement can be similarly ascribed to the enhanced performance of the β -FDF in reconstructing the

filtered reaction rate profile of strained flamelets in the limit of high strain.

D.3. CROSS-FLAME REACTION RATE PLOTS IN THE LAMINAR SETTING OBTAINED WITH UNSTRETCHED FLAMELETS MANIFOLD

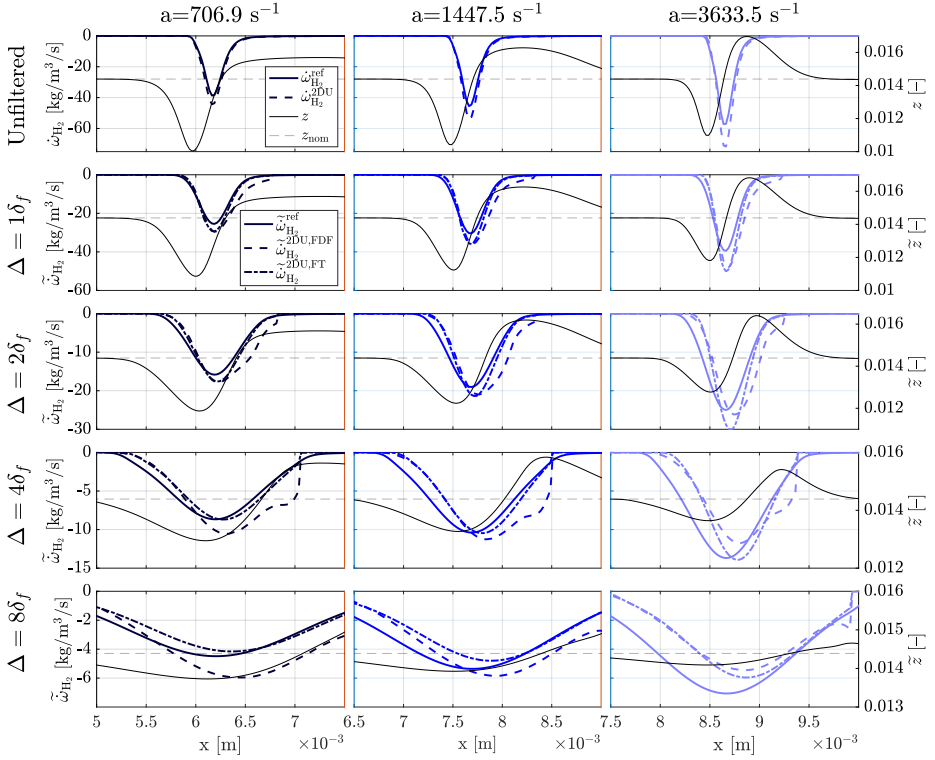
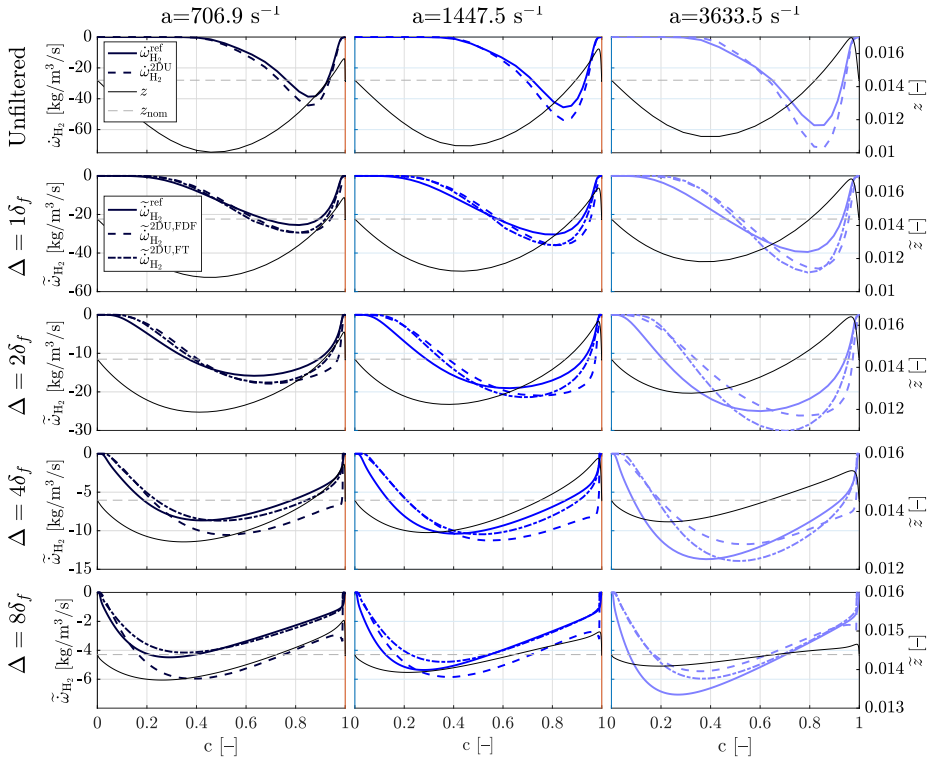


Figure D.3: Left y axis: reference ($\dot{\omega}_{\text{H}_2}^{\text{ref}}$, solid lines) and reconstructed ($\dot{\omega}_{\text{H}_2}^{2\text{DU}}$) fuel source term across the horizontal centreline of the 2D laminar domain at different applied strain rates and over the unfiltered and filtered grids. The reconstructed source term is obtained with the 2DU-type manifolds with both β -FDF (dashed blue lines) and F-TACLES (FT, dash-dot blue lines) subgrid models. Right y axis: distribution of mixture fraction z across the flame (solid black line) and mixture fraction nominal value z_{nom} (dashed black line).

In Section 6.3.1 of Chapter 6, the limitations of any approach using a manifold of unstretched flamelets in predicting the consumption speed and the local reaction rates of a laminar counterflow setting have been highlighted through the analysis of contour plots of the relative error in the reconstructed fuel reaction rate. To further support the analysis and better identify the regions where reaction rates are under- or over-predicted across the flame, this section presents comparisons between reference ($\dot{\omega}_{\text{H}_2}^{\text{ref}}$) and reconstructed ($\dot{\omega}_{\text{H}_2}^{2\text{DU}}$) fuel source term profiles along the horizontal centreline of the 2D laminar domain



D

Figure D.4: Same as Fig. D.3, but with cross-flame plots against progress variable c .

($y = 0$). The plots against the spatial coordinate x and the progress variable c are reported in Figures D.3 and D.4, respectively. The distribution of mixture fraction z is also reported for each case alongside its nominal value z_{nom} for reference.

CURRICULUM VITÆ

Alessandro PORCARELLI

19-02-1998 Born in Vicenza, Italy.

EXPERIENCE

- Oct 2021 Doctoral Researcher (PhD Candidate)
Apr 2026 TU Delft, Faculty of Aerospace Engineering, Delft, Netherlands
Fundamental analysis and modelling of highly strained hydrogen combustion for stable and low NO_x premixed flames
Promotor: Prof. dr. A. Gangoli Rao
Supervisor: Dr. I. Langella
- Aug 2024 Visiting Doctoral Researcher
Oct 2024 Sapienza University of Rome, Rome, Italy
Obtained Short Term Scientific Mission (STSM) grant to perform a stability analysis of counterflow lean premixed and laminar hydrogen flames at Sapienza University
- Nov 2019 CFD Engineer (ancillary)
Mar 2025 neptech AB, Stokholm, Sweden (remotely)
Conducted and team-led meshing & high-fidelity flow CFD simulation projects with a variety of application domains, including aeronautics, drones, and process engineering
Interacted with international industrial partners and customers
Provided technical support to Scandinavian Pointwise users
- Sept 2019 Graduate researcher
Sept 2021 DENERG, Polytechnic University of Turin, Turin, Italy (remotely)
Performed simulations of heat transfer to assess thermal effects on helicoidal channels cooling systems in solar parks

Oct 2018 Aerodynamicist Intern and in Student Team
 Sept 2021 Green Raven Project and KTH Hyperloop Team, Stockholm, Sweden
 Agom Engineering Sas di Marmo Oreste & C. and Team ICARUS
 PoliTO, Turin, Italy

Preprocessed complex CAD geometries for CFD meshing
 Run external flow simulations on a UAVs, cargo model aircrafts, vac-
 trains and car restyling concepts with commercial solvers
 Suggested aerodynamic design improvements and partnered with
 cross functional engineering teams

EDUCATION

2019–2021 MSc Aerospace Engineering
 KTH – Royal Institute of Technology
 Stockholm, Sweden

Thesis: Development of a CFD model and methodology for
 the internal flow simulation in a hydrogen-powered
 UAV

Examiner: Prof. dr. R. Mariani

Supervisor: Prof. dr. L. Brandt

2016–2019 BSc Aerospace Engineering
 PoliTO – Polytechnic University of Turin
 Turin, Italy

Thesis: Calculation of the aerodynamic characteristics of a
 wing in a competition model aircraft

Supervisor: Prof. dr. D. D'Ambrosio

AWARDS

May 2025 Best Poster Award at the 2nd Cypher General Meeting

LIST OF PUBLICATIONS

JOURNAL ARTICLES

9. **A. Porcarelli**, P.E. Lapenna, F. Creta and I. Langella, *Suppression of intrinsic instabilities by strain in thermodynamically unstable hydrogen flames*, Proceedings of the Combustion Institute, under review.
8. **A. Porcarelli**, P.E. Lapenna, F. Creta and I. Langella *Assessment of tabulated-chemistry models for lean premixed strained hydrogen flames with low-dimensional manifolds*, [Combustion Theory and Modelling](#), 1–27 (2026).
7. A. Masucci, **A. Porcarelli**, T. Ghisu and I. Langella *Impact of tangential strain rate on NO emissions in turbulent premixed hydrogen flames using LES with Eulerian stochastic fields approach*, [Combustion and Flame](#) **287**, 114887 (2026).
6. **A. Porcarelli**, P.E. Lapenna, F. Creta and I. Langella, *Stability analysis of thermodynamically unstable counterflow lean premixed hydrogen flames*, [Proceedings of the Combustion Institute](#) **41**, 105906 (2025).
5. M.R. Acquaviva, **A. Porcarelli** and I. Langella, *Influence of Soret effect on flame structure and NOx emissions in highly strained lean premixed counterflow hydrogen flames*, [Fuel](#) **395**, 134939 (2025).
4. **A. Porcarelli** and I. Langella, *Mitigation of preferential diffusion effects by intensive strain in lean premixed hydrogen flamelets*, [Proceedings of the Combustion Institute](#) **40**, 105728 (2024).
3. **A. Porcarelli**, B. Kruljević and I. Langella, *Suppression of NOx emissions by intensive strain in lean premixed hydrogen flamelets*, [International Journal of Hydrogen Energy](#) **49**, 413–421 (2024).
2. S. Suewatanakul, **A. Porcarelli**, A. Olsson, H. Grimler, A. Chiche, R. Mariani and G. Lindbergh, *Conceptual design of a hybrid hydrogen fuel cell/battery blended-wing-body unmanned aerial vehicle—an overview*, [Aerospace](#) **9**(5), 275 (2022).
1. K.E.T. Giljarhus, **A. Porcarelli** and J. Apeland, *Investigation of rotor efficiency with varying rotor pitch angle for a coaxial drone*, [Drones](#) **6**(4), 91 (2022).

CONFERENCE PROCEEDINGS

13. **A. Porcarelli** *Highly Strained Lean Premixed Hydrogen Flames for Sustainable Aviation*, TU Delft Clean Tech Conference, Delft, Netherlands, 17 March 2026.

12. **A. Porcarelli**, P.E. Lapenna, F. Creta and I. Langella *Modelling turbulent lean premixed hydrogen flames under intensive strain rate*, 20th International Conference on Numerical Combustion, Rome, Italy, 14-17 October 2025.
11. **A. Porcarelli**, P.E. Lapenna, F. Creta and I. Langella *Stability analysis of thermodiffusively unstable counterflow lean premixed hydrogen flames*, 13th Mediterranean Combustion Symposium, Corfu, Greece, 1-5 June 2025.
10. **A. Porcarelli**, P.E. Lapenna, F. Creta and I. Langella, *Two-dimensional flamelet manifolds for turbulent and thermodiffusively unstable hydrogen flames: an a-priori analysis*, 2nd Cypher General Meeting, Krakow, Poland, 19-21 May 2025.
9. **A. Porcarelli**, G. Ferrante and I. Langella, *Soret effect modelling in flamelet-based LES with presumed FDF for lean premixed hydrogen flames*, 19th International Conference on Numerical Combustion, Kyoto, Japan, 7-10 May 2024.
8. M.R. Acquaviva, B. Cassese, **A. Porcarelli** and I. Langella, *Numerical investigation of a water droplet interacting with an hydrogen/air counterflow flame*, 19th International Conference on Numerical Combustion, Kyoto, Japan, 7-10 May 2024.
7. B. Cassese, **A. Porcarelli** and I. Langella, *Combined effect of strain and water injection in lean premixed hydrogen flamelets*, ERCOFTAC Bulletin 136 and Combura 2023, Eindhoven, Netherlands, 23-24 October 2023.
6. R. Khanduja, **A. Porcarelli** and I. Langella, *Effect of ammonia blending in strained lean premixed hydrogen flamelets*, Combura 2023, Eindhoven, Netherlands, 23-24 October 2023.
5. **A. Porcarelli** and I. Langella, *Limiting effect of strain on the impact of differential diffusion on hydrogen lean premixed flamelets*, 15th International Conference on Combustion Technologies for a Clean Environment, Lisbon, Portugal, 25-29 June 2023.
4. **A. Porcarelli**, B. Kruljević and I. Langella, *NO_x emissions trends in hydrogen lean premixed flamelets at high strain*, 12th Mediterranean Combustion Symposium, Luxor, Egypt, 26-26 January 2023.
3. **A. Porcarelli**, G. Ferrante and I. Langella, *Influence of water droplets injection on NO_x emission trends with strain in H₂ lean premixed flames*, 8th International workshop on Turbulent Combustion of Sprays, Luxor, Egypt, 22 January 2023.
2. **A. Porcarelli**, B. Kruljević and I. Langella, *NO_x emissions trends in hydrogen lean premixed flamelets at high strain*, Combura 2022, Soesterberg, Netherlands, 23-24 November 2022.
1. **A. Porcarelli**, *Development of a CFD model and methodology for the internal flow simulation in a hydrogen-powered UAV*, 33rd Congress of the International Council of Aeronautical Sciences (ICAS 2022), Stockholm, Sweden, 4-9 September 2022.

